ANDRIUS GINEIKA

SYNTHESIS, PROPERTIES AND APPLICATION OF WOLLASTONITE AND CUSPIDINE

DOCTORAL DISSERTATION

Kaunas
2023

KAUNAS UNIVERSITY OF TECHNOLOGY

ANDRIUS GINEIKA

SYNTHESIS, PROPERTIES AND APPLICATION OF WOLLASTONITE AND CUSPIDINE

Doctoral dissertation
Technological Sciences, Chemical Engineering (T 005)

2023, Kaunas

This doctoral dissertation was prepared at Kaunas University of Technology, Faculty of Chemical Technology, Department of Silicate Technology during the period of 2019–2023.

Scientific Supervisor
Prof. Dr. Kęstutis BALTAKYS (Kaunas University of Technology, Technological Sciences, Chemical Engineering, T 005).

Edited by: English language editor Dr. Armandas Rumšas (Publishing House *Technologija*), Lithuanian language editor Aurelija Gražina Rukšaitė (Publishing House *Technologija*)

Dissertation Defense Board of Chemical Engineering Science Field:
Prof. Dr. Eugenijus VALATKA (Kaunas University of Technology, Technological Sciences, Chemical Engineering, T 005) – **chairperson**;

Assoc. Prof. Dr. Joana BENDORAITIENĖ (Kaunas University of Technology, Technological Sciences, Chemical Engineering, T 005);

Prof. Dr. Rimvydas KAMINSKAS (Kaunas University of Technology, Technological Sciences, Chemical Engineering, T 005);

Assoc. Prof. Dr. Jolanta ROUSSEAU (Artois University, France, Natural Sciences, Chemistry, N 003);

Dr. Rimvydas STONYS (Vilnius Gediminas Technical University, Technological Sciences, Materials Engineering, T 008).

The official defense of the dissertation will be held at 10 a.m. on the 12 September, 2023 at the public meeting of the Dissertation Defense Board of Chemical Engineering Science Field in the Rectorate Hall at Kaunas University of Technology.

Address: K. Donelaičio 73-402, Kaunas, LT-44249, Lithuania.
Phone: (+370) 608 28 527; email doktorantura@ktu.lt

The doctoral dissertation was sent out on 11 August, 2023.
The doctoral dissertation is available on the internet at http://ktu.edu and at the library of Kaunas University of Technology (K. Donelaičio 20, Kaunas, LT-44239, Lithuania).

© A. Gineika, 2023

KAUNO TECHNOLOGIJOS UNIVERSITETAS

ANDRIUS GINEIKA

VOLASTONITO IR KUSPIDINO SINTEZĖ, SAVYBĖS IR PANAUDOJIMAS

Daktaro disertacija
Technologijos mokslai, chemijos inžinerija (T 005)

2023, Kaunas

Disertacija rengta 2019–2023 metais Kauno technologijos universiteto Cheminės technologijos fakultete, Silikatų technologijos katedroje.

Mokslinis vadovas:
prof. dr. Kęstutis BALTAKYS (Kauno technologijos universitetas, technologijos mokslai, chemijos inžinerija, T 005).

Redagavo: anglų kalbos redaktorius Armandas Rumšas (leidykla „Technologija“), lietuvių kalbos redaktorė Aurelija Gražina Rukšaitė (leidykla „Technologija“)

Chemijos inžinerijos mokslo krypties disertacijos gynimo taryba:
prof. dr. Eugenijus VALATKA (Kauno technologijos universitetas, technologijos mokslai, chemijos inžinerija, T 005) – **pirmininkas**;

doc. dr. Joana BENDORAITIENĖ (Kauno technologijos universitetas, technologijos mokslai, chemijos inžinerija, T 005);

prof. dr. Rimvydas KAMINSKAS (Kauno technologijos universitetas, technologijos mokslai, chemijos inžinerija, T 005);

doc. dr. Jolanta ROUSSEAU (Artua (Artois) universitetas, Prancūzija, gamtos mokslai, chemija, N 003);

dr. Rimvydas STONYS (Vilniaus Gedimino technikos universitetas, technologijos mokslai, medžiagų inžinerija, T 008).

Disertacija bus ginama viešame Chemijos inžinerijos mokslo krypties disertacijos gynimo tarybos posėdyje 2023 m. rugsėjo 12 d. 10 val. Kauno technologijos universiteto Rektorato salėje.

Adresas: K. Donelaičio g. 73-402, Kaunas, LT-44249, Lietuva
Tel. (+370) 608 28 527; el. paštas doktorantura@ktu.lt

Disertacija išsiųsta 2023 m. rugpjūčio 11 d.
Su disertacija galima susipažinti interneto svetainėje http://ktu.edu ir Kauno technologijos universiteto bibliotekoje (K. Donelaičio g. 20, Kaunas LT-44239).

© A. Gineika, 2023

Table of Contents

List of tables 7
List of figures 8
List of abbreviations 15
Introduction 17
1. Literature review 20
1.1. Classification and general properties of calcium silicates 20
1.2. Wollastonite 22
1.2.1. The crystal structure of wollastonite 22
1.2.2. The synthesis methods of wollastonite 24
1.2.3. The influence of additives on the physical properties of wollastonite 26
1.3. The application of wollastonite 27
1.3.1. Wollastonite additive in concrete 27
1.3.2. CO_2-cured (carbonated) wollastonite binders 28
1.3.3. Wollastonite-polymer composites 30
1.3.4. 3D-printed wollastonite and wollastonite-based scaffolds 32
1.4. Silane coupling 33
1.4.1. The synthesis of silane copupling agents 34
1.4.2. The hydrolysis of silane coupling agents 35
1.4.2. The coupling of surfaces 36
1.5. Cuspidine 37
2. Materials and methods 39
2.1. Materials 39
2.2. Methods 43
2.2.1. Synthesis 43
2.2.2. Analysis 46
3. Results and discussion 50
3.1. Two-step synthesis of wollastonite in the CaO- $SiO_2 \cdot nH_2O$-H_2O system 50
3.2. Two-step synthesis of wollastonite in the CaO-silica gel waste-H_2O system 61
3.2.1. Hydrothermal synthesis of the precursors in unstirred suspensions and calcination 61
3.2.2. Direct (single-step) synthesis of the initial mixture 67
3.2.3. Hydrothermal synthesis of the precursors in stirred suspensions and calcination 69
3.3. Two-step synthesis of wollastonite in the CaO-$SiO_2 \cdot nH_2O$-AlF_3-H_2O system 77
3.3.1. Application of saturated AlF_3 solution for the calcium silicate hydrate synthesis 77
3.3.2. Direct (single-step) synthesis of wollastonite using the dry initial mixture 81
3.3.3. Hydrothermal synthesis of the precursors in stirred suspensions and calcination 83

3.4. The influence of temperature on the formation of wollastonite via two-step synthesis 87
3.5. The application of wollastonite samples 95
3.5.1. CO_2-curing of wollastonite 95
3.5.2. Silane coupling and polymer composites 100
3.5.3. 3D printed silicate-polymer scaffolds 103
3.6. The formation of cuspidine in the $CaO\text{-}SiO_2 \cdot nH_2O\text{-}CaF_2\text{-}H_2O$ system 106
3.7. The formation of cuspidine in the CaO-silica gel waste-CaF_2-H_2O system. 111
3.8. Direct synthesis and calcination of hydrothermally synthesized precursors of cuspidine 114
3.8.1. Direct synthesis of cuspidine 114
3.8.2. Calcination of the synthetic precursors 117
3.9. Investigation of binding properties of synthetic cuspidine samples 121
3.9.1. Hydration of synthetic cuspidine samples 121
3.9.2. CO_2-curing of synthetic cuspidine sample 125
4. Conclusions 129
5. Santrauka 131
5.1. Įvadas 131
5.2. Eksperimentinė dalis 133
5.2.1. Naudotos medžiagos 133
5.2.2. Metodai 133
5.3. Rezultatai ir aptarimas 134
5.3.1. Vienos ir dviejų stadijų volastonito sintezė 139
5.3.2. Sintetinio volastonito panaudojimas 139
5.3.3. Dviejų stadijų kuspidino sintezė 147
5.3.4. Kuspidino rišamosios savybės 155
5.4. Išvados 161
References 163
Curriculum Vitae 183
List of scientific publications 184
Acknowledgments 186
Appendices 187

List of tables

Table 2.1. The composition of the suspensions for DLP of scaffolds 45
Table 3.1. The intensity of the main peaks of lime, larnite, wollastonite, and quartz in the products of direct synthesis in the $CaO/CaCO_3$-$SiO_2 \cdot nH_2O$ systems 53
Table 3.2. Thermal characteristics of the synthesis products formed at different durations of hydrothermal synthesis in the CaO-$SiO_2 \cdot nH_2O$-H_2O system at 200 °C under stirring 56
Table 3.3. The results of dilatometric analysis of synthesis products formed at different durations of hydrothermal synthesis at 200 °C under stirring in the CaO-$SiO_2 \cdot nH_2O$-H_2O system 58
Table 3.4. The intensity of representative peaks of lime, larnite, wollastonite, cuspidine and fluorite in the products of direct synthesis in CaO-silica gel waste system 68
Table 3.5. Thermal characteristics of the synthesis products formed at different durations of hydrothermal synthesis in mixtures of silica gel waste and calcium oxide 71
Table 3.6. Dilatometry data of synthesis products formed at different durations of hydrothermal synthesis in a mixture of silica gel waste and calcium oxide 73
Table 3.7. The intensity of the main peaks of lime, larnite, wollastonite, cuspidine and fluorite in the products of direct synthesis in the CaO-$SiO_2 \cdot nH_2O$-AlF_3 system82
Table 3.8. Thermal characteristics of the synthesis products formed at different durations of hydrothermal synthesis in mixtures of amorphous silicon dioxide, calcium oxide, and aluminium fluoride 84
Table 3.9. Dilatometry data of synthesis products formed at different durations of hydrothermal synthesis in the CaO-$SiO_2 \cdot nH_2O$-AlF_3 system 86
Table 3.10. Calculated parameters of the samples of hydrothermal synthesis at 130 °C under stirring in CaO-silica gel waste-H_2O system, determined by BET analysis 93
Table 3.11. The results of thermogravimetric analysis of the green bodies 104
Table 3.12. The visual appearance of scaffolds before and after sintering. 105
Table 3.13. Products of hydrothermal synthesis in the CaO-$SiO_2 \cdot nH_2O$-CaF_2-H_2O system 110
5.1 lentelė. Karkasų 3D spausdinimui naudotų suspensijų sudėtis 137
5.2 lentelė. Karkasų išvaizda prieš ir po degimo 1100–1300 °C temperatūroje 154

List of figures

Fig. 1.1. $CaO\text{-}SiO_2$ phase diagram [7]..... 20
Fig. 1.2. $CaSiO_3$ phase diagram [10]..... 21
Fig. 1.3. The crystal lattice of pseudowollastonite: a – two-layer polytype, b – four-layer polytype [19] 23
Fig. 1.4. The structure of the most common wollastonite polytypes: a – 1T, b – 2M (parawollastonite), c – schematic explanation of slab stacking and displacement in 1T, 2M, 3T, 4T, and 4M wollastonite polytypes. 24
Fig. 1.5. The silane coupling: a – the formation of covalent bond between the silane molecule and the surface, b – a schematic illustration of a modified surface [110]. 36
Fig. 1.6. Crystall lattice of cuspidine [136] 37
Fig. 2.1. Analysis data of silica gel waste: a – XRD pattern; b – particle size distribution (1 – cumulative, 2 – relative); c – STA curves (1 – TG, 2 – DSC,)..... 39
Fig. 2.2. Analysis data of calcium oxide: a – XRD pattern; b – particle size distribution (1 – cumulative, 2 – relative) 40
Fig. 2.3. Analysis data of amorphous hydrated silica: a – XRD pattern; b – particle size distribution (1 – cumulative, 2 – relative) 40
Fig. 2.4. Analysis data of aluminium fluoride: a – XRD pattern; b – particle size distribution (1 – cumulative, 2 – relative). 41
Fig. 2.5. Analysis data of calcium oxide: a – XRD pattern; b – particle size distribution (1 – cumulative, 2 – relative) 41
Fig. 2.6. Grain size distribution of sand according to EN 196-1: 1 – relative, 2 – cumulative 42
Fig. 3.1. XRD patterns (a) and STA (b) curves (solid line – DSC; dashed line – TG) of hydrothermal synthesis products obtained in the $CaO\text{-}SiO_2\cdot nH_2O\text{-}H_2O$ system at 200 °C without stirring after: 1 – 4 h, and 2 – 48 h. 51
Fig. 3.2. XRD pattern of the synthesis products in the $CaO\text{-}SiO_2\cdot nH_2O\text{-}H_2O$ system without stirring for: a – 4 h, b – 48 h and calcined at 900°C for 1 h. 52
Fig. 3.3. XRD patterns of direct synthesis products after 1 h in: a – $CaO\text{-}SiO_2\cdot nH_2O$ system, b – $CaCO_3$- $SiO_2\cdot nH_2O$ system. Curves 1 – calcination at 900 °C, 2 – 1000 °C, and 3 – 1100 °C. 53
Fig. 3.4. XRD patterns (a) and STA (b) curves (solid line – DSC; dashed line – TG) of hydrothermal synthesis products obtained in the $CaO\text{-}SiO_2\cdot nH_2O\text{-}H_2O$ system under stirring: 1 – 4 h, 2 – 12 h, and 3 – 48 h. 56
Fig. 3.5. The FT-IR spectra of synthetic samples in the $CaO\text{-}SiO_2\cdot nH_2O\text{-}H_2O$ system at 200 °C under stirring: 1 – 4 h, 2– 12 h, and 3 – 48 h..... 57
Fig. 3.6. Dilatometric analysis curves (a, solid line– relative length change; dashed line– differential length change) of the synthesis products obtained after 12 h of hydrothermal synthesis at 200 °C under stirring; and b – XRD patterns of the synthesis product calcined (12 h) at a temperature of 900°C for 1 h in the $CaO\text{-}SiO_2\cdot nH_2O\text{-}H_2O$ system. 58
Fig. 3.7. Adsorption isotherm of N_2 in BET plots of synthetic (a) and calcined (b) samples of the $CaO\text{-}SiO_2\cdot nH_2O\text{-}H_2O$ system under stirring for 12 h 59

Fig. 3.8. Adsorption (1) and desorption (2) isotherms of N_2 for synthetic (a) and calcined (b) samples of the $CaO\text{-}SiO_2 \cdot nH_2O\text{-}H_2O$ system under stirring for 12 h ... 60
Fig. 3.9. The SEM images of sample of $CaO\text{-}SiO_2 \cdot nH_2O\text{-}H_2O$ system: a – hydrothermally obtained (200 °C, 12 h), and b –after calcination at 900 °C for 1 h 60
Fig. 3.10. XRD patterns (a) and STA curves (b) of hydrothermal synthesis (200 °C, without stirring) products in the CaO-silica gel waste-H_2O system: 1 – 4 h, 2 – 16 h, 3 – 72 h. 62
Fig. 3.11. XRD patterns after calcination at: 1 – 800 °C, 2 – 900 °C; 3 – 1100 °C of synthetic precursors obtained after 72 h of isothermal treatment at 200 °C..... 63
Fig. 3.12. Analysis curves of defluorinated silica gel waste: a – XRD pattern; b – STA curves of the raw material: 1 – TG, 2 – DSC. 64
Fig. 3.13. Analysis curves of: a – XRD pattern of the hydrothermally synthesised precursor, b – STA curves (1 – TG, 2 – DSC) of the precursor, c – produced wollastonite sample (WD). 65
Fig. 3.14. The white concrete tiles: 1 – White A, 2 – White A+, 3 – XD, 4 – WD . 66
Fig. 3.15. The compressive strength of white concrete tiles 66
Fig. 3.16. The amount of adsorbed carbon dioxide by concrete samples under different conditions: 1 – white cement, sand and water, 2 – white cement, sand and water with plastifier (1 %), 3 – white cement with 10 mass% WD additive, sand and water with plastifier (1 %) 67
Fig. 3.17. XRD patterns of direct synthesis products: a – CaO-silica gel waste system, b – $CaCO_3$-silica gel waste system: 1 – 900 °C, 2 – 1000 °C, 3 – 1100 °C. 68
Fig. 3.18. XRD patterns (a) and STA (b) curves (solid line – DSC; dashed line – TG) of the hydrothermal synthesis products obtained in the CaO-silica gel waste after: 1 – 4 h, 2 – 12 h, 3 – 48 h. 70
Fig. 3.19. The FT-IR spectra of synthetic samples in CaO-silica gel waste-H_2O system: 1 – 4 h, 2– 12 h, and 3 – 48 h 72
Fig. 3.20. Dilatometry curves (a, solid line– relative length change; dashed line– differential length change) of the synthesis products obtained after 12 h of hydrothermal synthesis; XRD patterns (b) of the calcined synthesis product (12 h) at different temperatures (1 – 900 °C, 2 – 1000 °C, 3 – 1100 °C) for 1 h. 73
Fig. 3.21. Adsorption isotherms of N_2 in BET plots of synthetic (a) and calcined (b) samples 75
Fig. 3.22. Adsorption (1) and desorption (2) isotherms of N_2 for synthetic (a) and calcined (b) samples of the 75
Fig. 3.23. The SEM images of samples of CaO-silica gel waste-H_2O system: a – hydrothermally obtained (200 °C, 12 h), and b –after calcination at 900 °C for 1 h 76
Fig. 3.24. Neutralisation of saturated AlF_3 solution: a – pH values after neutralisation by $CaO/SiO_2 \cdot nH_2O$ mixture; b – XRD patterns of the products from obtained suspensions after hydrothermal curing at 200 °C for 12 h without stirring: 1 – 0 vol% AlF_3 solution, 2 – 25 vol%, 3 – 50 vol%, and 4 – 100 vol%. 78
Fig. 3.25. XRD patterns of natural $CaCO_3$-bearing rocks: a – opoka, b – limestone 79
Fig. 3.26. The neutralisation curves of saturated AlF_3 solution with additives: a – only carbonaceous additives, b – after neutralisation by carbonaceous additives and further addition of $CaO/SiO_2 \cdot nH_2O$ 80

Fig. 3.27. The XRD patterns of residue that formed after neutralisation of saturated AlF_3 solution with additives: a – only carbonaceous additives, b – after neutralisation by carbonaceous additives (1 – opoka, 2 – limestone, and 3 – $CaCO_3$) and further addition of $CaO/SiO_2 \cdot nH_2O$ mixture and hydrothermal treatment at 200 °C for 12 h without stirring..... 80
Fig. 3.28. XRD patterns of direct synthesis products: a – $CaO\text{-}SiO_2 \cdot nH_2O\text{-}AlF_3$ system, b – $CaCO_3$- $SiO_2 \cdot nH_2O\text{-}AlF_3$ system..... 81
Fig. 3.29. XRD patterns (a) and STA (b) curves (solid line – DSC; dashed line – TG) of the hydrothermal synthesis products obtained in the $CaO\text{-}SiO_2 \cdot nH_2O\text{-}AlF_3$ system: 1 – after 4 h, 2 – 12 h, 3 – 48 h..... 83
Fig. 3.30. The FT-IR spectra of synthetic samples in $CaO\text{-}SiO_2 \cdot nH_2O\text{-}AlF_3\text{-}H_2O$ system: 1 – 4 h, 2– 12 h, and 3 – 48 h 85
Fig. 3.31. Dilatometry curves (a, solid line– relative length change; dashed line– differential length change) of the synthesis products obtained after 12 h of hydrothermal synthesis; b – XRD patterns of the calcined synthesis product (12 h) at different temperatures (1 – 900 °C, 2 – 1000 °C, 3 – 1100 °C) for 1 h..... 86
Fig. 3.32. XRD patterns of hydrothermal synthesis at 95 °C products after: 1 – 0 h; 2 – 4 h; 3 – 48 h..... 88
Fig. 3.33. XRD patterns of hydrothermal synthesis at 130 °C products after: 1 – 4 h; 2 – 8 h; 3 – 24 h; 4 – 48 h..... 89
Fig. 3.34. STA curves (solid – DSC, dashed – TG) of the hydrothermal synthesis at 130 °C products after: a) 1 – 0 h, 2 – 4 h, and 3 – 8 h, b) 1 – 12 h, 2 – 24 h, and 3 – 48 h 90
Fig. 3.35. The FT-IR spectra of hydrothermally synthesised products at: a – 95 °C within 1 – 0 h, 2 – 4 h, and 3 – 48 h; b – 130 °C within 1 – 0 h, 2 – 8 h, and 3 – 48 h 91
Fig. 3.36. Adsorption isotherms of N_2 in BET plots of synthetic samples after a – 8 h, b – 24 h, and c – 48 h of isothermal curing at 130 °C under stirring..... 92
Fig. 3.37. Adsorption (1) and desorption (2) isotherms of N_2 of synthetic samples after a – 8 h, b – 24 h, and c – 48 h of isothermal curing at 130 °C under stirring... 92
Fig. 3.38. Intensity of the main peak of wollastonite (d = 0.2980 nm) in XRD patterns of calcined products. Hydrothermal synthesis temperature: a – 95 °C, b – 130 °C..... 93
Fig. 3.39. XRD patterns of calcined (900 °C 1 h) hydrothermal synthesis (130 °C, under stirring, CaO-silica gel waste-H_2O system) products after: 1 – 4 h; 2 – 12 h and 3 – 48 h. 94
Fig. 3.40. The image of the prepared binder-sand samples..... 95
Fig. 3.41. Analysis data of wollastonite type 1: XRD patterns (a): 1 – before curing, 2 – after CO_2 curing, granulometric composition (b), and STA curves (c; dashed line – TG, solid line – DSC) after curing for 24 h at 45 °C and 15 bar CO_2 (without sand, powdered)..... 96
Fig. 3.42. Compressive strength of cured sand-binder (wollastonite type 1) samples dependency on: a – amount of binding material, b – compaction pressure, c – curing duration. (a and b – cured for 24 h; b and c – 25 mass% of binding material)..... 97

Fig. 3.43. Particle size distribution of synthetic wollastonite type 2, which was used for CO_2-curing 98
Fig. 3.44. Compressive strength (a) and degree of carbonation (b) of binder-sand (1:3 ratio by mass, wollastonite type 2) samples 99
Fig. 3.45. XRD patterns (a) and STA curves (b; dashed – TG, solid – DSC) of the wollastonite type 2 after curing for 1 – 2 h, 2 – 24 h at 45 °C and 15 bar CO_2 (without sand, powdered). 100
Fig. 3.46. FT-IR curves of: 1 – acryloxypropyltrimethoxysinane, and the modified fillers: 2 – W-C and 3 – WS-C 101
Fig. 3.47. STA curves (1 – TG, 2 – DSC) of the modified fillers: a – W-C, and b – WS-C 101
Fig. 3.48. The mechanical properties of wollastonite-polymer composite samples: a – viscosity of uncured resin, b – Young's (elastic) modulus, c – tensile strength, and d – elongation at break 103
Fig. 3.49. Thermal analysis results of the green bodies: a – TG, and b – DTG 104
Fig. 3.50. The influence of sintering temperature on the properties of the printed scaffolds: a – volume change, b – compressive strength 106
Fig. 3.51. XRD patterns of synthetic cuspidine samples synthesised for: a – 4 h (1 – 95 °C, 2 – 150 °C, 3 – 170 °C) and b – 12 h (1 – 130 °C, 2 – 150 °C, 3 – 200 °C) in the $CaO\text{-}SiO_2\cdot nH_2O\text{-}CaF_2\text{-}H_2O$ system 107
Fig. 3.52. Area (a) of the main peak of fluorite (*d*-spacing 0.3157 nm) and cuspidine (*d*-spacing 0.3051 nm) in XRD patterns and STA (b, DSC – solid line, TG – dashed line) curves of synthetic cuspidine samples in the $CaO\text{-}SiO_2\cdot nH_2O\text{-}CaF_2\text{-}H_2O$ system: 1 – 130 °C 12 h, 2 – 170 °C 12 h and 3 – 200 °C 12h 108
Fig. 3.53. FT-IR curves (a) of hydrothermally synthesised samples at 1 – 95 °C, 2 – 130 °C, 3 – 200 °C for 12 h from $CaO\text{-}SiO_2\cdot nH_2O\text{-}CaF_2$ mixture; and SEM image (b) of the hydrothermally synthesised sample at 200 °C for 12 h from the mentioned mixture 109
Fig. 3.54. BET analysis results of the hydrothermally synthesised sample (200 °C, 12 h): a – adsorption (1) and desorption (2) isotherms of N_2; b) – adsorption isotherm of N_2 in BET plots. 110
Fig. 3.55. XRD (a) and STA (b, DSC – solid line, TG – dashed line) curves of hydrothermally synthesised samples at 200 °C for 1 – 12 h, 2 – 48 h from CaO-silica gel waste-CaF_2-H_2O system. 112
Fig. 3.56. Area of the main peak of fluorite (*d*-spacing 0.3157 nm) and cuspidine (*d*-spacing 0.3051 nm) in XRD patterns (CaO-silica gel waste-CaF_2-H_2O system) 112
Fig. 3.57. FT-IR curves (a) of hydrothermally synthesised samples at 200 °C for 1 – 12 h, 2 – 48 h from CaO-silica gel waste-CaF_2-H_2O system; and SEM image (b) of the hydrothermally synthesised sample at 200 °C for 12 h from the aforementioned mixture 113
Fig. 3.58. XRD patterns of calcined mixtures for 1 h in: a) $CaO\text{-}SiO_2\cdot nH_2O\text{-}CaF_2$, b) CaO-silica gel waste-CaF_2 systems at 1 – 900 °C, 2 – 1000 °C, and 3 – 1100 °C. 114
Fig. 3.59. SEM images of products obtained after direct synthesis at 1100 °C for 1 h of mixtures: a) $CaO\text{-}SiO_2\cdot nH_2O\text{-}CaF_2$, b) CaO-silica gel waste-CaF_2 115

Fig. 3.60. XRD patterns of calcined mixtures for 1 h: a) $CaCO_3$-$SiO_2{\cdot}nH_2O$-CaF_2, b) $CaCO_3$-silica gel waste-CaF_2 systems at 1 – 900 °C, 2 – 1000 °C, and 3 – 1100 °C. 116
Fig. 3.61. SEM images of products obtained after direct synthesis at 1100 °C for 1 h of mixtures: a) $CaCO_3$-$SiO_2{\cdot}nH_2O$-CaF_2, b) $CaCO_3$-silica gel waste-CaF_2..... 116
Fig. 3.62. XRD patterns (a) of: 1 – hydrothermally synthesised at 95 °C for 12 h and calcined at 900 °C for 1 h, 2 – 130 °C-12 h and 900 °C-1 h, 3 – 200 °C-12 h and 900 °C-1 h, 4 – 200 °C-12 h and 1100 °C-1 h; b – SEM image of 200 °C-12 h and 900 °C-1 h; c – 200 °C-12 h and 1100 °C-1 h; using CaO-$SiO_2{\cdot}nH_2O$-CaF_2 system. 118
Fig. 3.63. Area of the main peak of cuspidine (*d*-spacing 0.3051 nm) in the CaO-$SiO_2{\cdot}nH_2O$-CaF_2 system : a – hydrothermal synthesis for 4 h, b – 12 h 119
Fig. 3.64. a – XRD patterns of hydrothermally synthesised at 200 °C for: 12 h and calcined at 900 °C for 1 h, 2 – 48 h and 900 °C 1 h, 3 – 12 h and calcined at 1100 °C for 1 h, 4 – 48 h and 1100 °C 1 h; b – SEM image of 200 °C 12 h and 900 °C 1 h; c – 200 °C 12 h and 1100 °C 1 h; using CaO-silica gel waste-CaF_2 system..... 120
Fig. 3.65. Area of the main peak of cuspidine (*d*-spacing 0.3051 nm) in the CaO-silica gel waste-CaF_2 system 121
Fig. 3.66. Heat evolution rate (a) and cumulative heat (b) of calcined synthetic cuspidine samples. Curve 1 – CSF-r-900, 2 – CSF-w-900, 3 – CSF-r-1100 and 4 – CSF-w-1100 122
Fig. 3.67. XRD patterns of hydrated (72 h) cuspidine samples: a – CaO-$SiO_2{\cdot}n$$H_2O$-$CaF_2$ mixture: 1 – CSF-r-900 and 2 – CSF-r-1100; b – CaO-silica gel waste-CaF_2 mixture: 1 – CSF-w-900 and 2 – CSF-w-1100..... 123
Fig. 3.68. DSC curves of hydrated samples for 72 h: a – CSF-r-900, b – CSF-r-1100, c – CSF-w-900 and d – CSF-w-1100 125
Fig. 3.69. Particle size distribution of synthetic cuspidine sample (CSF-w-900) .. 126
Fig. 3.70. Compressive strength (a) of CO_2-cured cuspidine samples (with sand, at ratio 1:3, powdered) and XRD patterns (b) of the synthetic cuspidine after curing for 1 – 2 h, 2 – 24 h at 15 bar CO_2 and 45 °C (without sand, powdered)..... 127
Fig. 3.71. STA curves (1 – TG, 2 – DSC) of CO_2-cured cuspidine samples (without sand, powdered) after curing for: a – 2 h, b – 24 h at 15 bar CO_2 and 45 °C 128

5.1 pav. Vienos stadijos sintezės (1 h) produktų RSDA kreivės: a – CaO-$SiO_2{\cdot}nH_2O$ sistema, b – CaO-užteršto silikagelio sistema. Kreivės: 1 –900 °C, 2 – 1000 °C, ands 3 – 1100 °C. 140
5.2 pav. Hidroterminės sintezės CaO-$SiO_2{\cdot}nH_2O$-H_2O sistemoje produktų (200 °C, maišant) produktų RSDA (a) ir VTA (b, vientisa linija – DSK, punktyrinė linija – TG) kreivės: 1 – po 4 h, 2 – 12 h, 3 – 48 h. 142
5.3 pav. Hidroterminės sintezės CaO-$SiO_2{\cdot}nH_2O$-H_2O sistemoje produktų (200 °C, 12 h, maišant) dilatometrijos kreivės (a, vientisa linija – santykinis ilgio pokytis, punktyrinė linija – diferencinis ilgio pokytis), išdegto 900 °C temperatūroje 1 h bandinio RSDA kreivė (b). 143

5.4 pav. SEM nuotraukos: a – bandinio po hidroterminės sintezės ($CaO\text{-}SiO_2 \cdot nH_2O\text{-}H_2O$ sistema, 200 °C, 12 h, maišant), b – bandinį išdegus 900 °C temperatūroje 1 h. 144
5.5 pav. Hidroterminės sintezės CaO-užteršto silikagelio-H_2O sistemoje produktų (200 °C, maišant) produktų RSDA (a) ir VTA (b, vientisa linija – DSK, punktyrinė linija – TG) kreivės: 1 – po 4 h, 2 – 12 h, 3 – 48 h. 145
5.6 pav. Hidroterminės sintezės CaO-užteršto silikagelio-H_2O sistemoje produktų (200 °C, 12 h, maišant) dilatometrijos kreivės (a, vientisa linija – santykinis ilgio pokytis, punktyrinė linija – diferencinis ilgio pokytis), išdegto 900 °C temperatūroje 1 h bandinio RSDA kreivė (b). 146
5.7 pav. SEM nuotraukos: a – bandinio po hidroterminės sintezės (CaO-užteršto silikagelio-H_2O sistema, 200 °C, 12 h, maišant), b – bandinį išdegus 900 °C temperatūroje 1 h. 147
5.8 pav. V1-smėlio bandinių stiprumo gniuždant priklausomybė nuo: a – rišamosios medžiagos kiekio, b – presavimo jėgos, c – kietinimo trukmės. (a ir b – kietinti 24 h, b ir c- 25 % rišamosios medžiagos) 148
5.9 pav. V2-smėlio (santykis 1:3) bandinių gniuždomasis stipris (a) ir karbonizacijos laipsnis (b) 149
5.10 pav. Kalcio hidrosilikatų pagrindu paruošto priedo (prototipas XD) sudėtis: a – mineralinė, b – granuliometrinė (1 – santykinis kiekis, 2 – absoliutusis kiekis). 150
5.11 pav. Kalcio silikatų (volastonito) pagrindu paruošto priedo (prototipas WD) sudėtis: a – mineralinė, b – granuliometrinė (1 – santykinis kiekis, 2 – absoliutusis kiekis). 150
5.12 pav. Gamybinio bandymo metu pagamintos plokštės: 1 – White A, 2 – White A+, 3 – su priedu XD, 4 – su priedu WD 151
5.13 pav. Skirtingos sudėties baltojo betono plokščių gniuždomojo stiprio priklausomybė nuo kietėjimo trukmės 151
5.14 pav. Skirtingomis kietinimo sąlygomis sugerto anglies dioksido masės dalis bandiniuose: 1 – baltasis cementas, smėlis ir vanduo, 2 – baltasis cementas, smėlis ir vanduo su plastifikatoriumi (1 %), 3 – baltasis cementas su 10 % WD priedu, smėlis ir vanduo su plastifikatoriumi (1 %) 152
5.15 pav. Mechaninės volastonito-polimerų kompozitų savybės: a – nesutinklintos dervos klampa, b – Jungo (tampros) modulis, c – tempiamasis stipris, d – pailgėjimas prieš trūkį 153
5.16 pav. Hidroterminės sintezės $CaO\text{-}SiO_2 \cdot nH_2O\text{-}CaF_2\text{-}H_2O$ sistemoje produktų produktų (12 h, maišant) RSDA (a) ir VTA (b, vientisa linija – DSK, punktyrinė linija – TG) kreivės: 1 – 130 °C, 2 – 150 °C, 3 – 200 °C. 156
5.17 pav. Hidroterminės sintezės CaO-užteršto silikagelio-CaF_2-H_2O sistemoje produktų (200 °C, maišant) produktų RSDA (a) ir VTA (b, vientisa linija – DSK, punktyrinė linija – TG) kreivės: 1 – po 4 h, 2 – 12 h. 157
5.18 pav. Bandinių, gautų po hidroterminės sintezės (12 h) ir išdegtų (1 h) $CaO\text{-}SiO_2 \cdot nH_2O\text{-}CaF_2$ sistemoje RSDA kreivės (a): 1 – 95 °C ir 900 °C, 2 – 130 °C ir 900 °C, 3 – 200 °C ir 900 °C, 4 – 200 °C ir 1100 °C; b – 200 °C ir 900 °C bandinio SEM nuotrauka, c – 200 °C ir 1100 °C bandinio SEM nuotrauka. 158

5.19 pav. Sintetinių kuspidino bandinių hidratacijos metu išsiskyrusios šilumos srautas (a) ir bendras šilumos kiekis (b): 1 – CSF-r-900, 2 – CSF-w-900, 3 – CSF-r-1100 and 4 – CSF-w-1100 160
5.20 pav. CO_2 aplinkoje sukietintų kuspidino-smėlio (santykiu 1:3) bandinių gniuždomasis stipris (a) ir RSDA kreivės (b): 1 – kuspidinas prieš kietinimą, 2 – po kietinimo. 161

List of abbreviations

DSC – differential scanning calorimetry,

FT-IR – Fourier-transform infrared spectroscopy,

OPC – ordinary Portland cement,

S_{BET} – specific surface area of a sample calculated with BET equation,

SEM – scanning electron microscopy,

STA – simultaneous thermal analysis,

TG – thermogravimetry,

XRD – X-ray power diffraction.

Indices in the X-ray powder diffraction patterns:

A – C-S-H(I) – $Ca_{0.8\text{-}1.3}SiO_2 \cdot 1.3H_2O$ /C-S-H(II) – $Ca_{1.3\text{-}2.0}SiO_2 \cdot 1.3H_2O$,

Al – aluminium hydroxofluoride hydrate – $Al_8(OH)_{12}F_{12} \cdot 3H_2O$,

Af – β aluminium fluoride – β-AlF_3,

B – kumtyubeite – $Ca_5Si_2O_8F_2$,

C – calcite – $CaCO_3$,

Co – calcio-olivine – γ-Ca_2SiO_4,

Cr – cristobalite – SiO_2,

D – dolomite – $CaMg(CO_3)_2$,

F – fluorite – CaF_2,

G – gibbsite – $Al(OH)_3$,

H – gehlenite – $Ca_2Al_2SiO_7$,

Hl – halloysite – $Al_2Si_2O_5(OH)_4$,

K – katoite – $Ca_3Al_2(SiO_2)_{0.5}(OH)_{10}$,

L – larnite – β-Ca_2SiO_4,

M – fluormayenite – $Ca_{12}Al_{14}O_{32}F_2$,

N – calcium carboaluminate hydrate – $Ca_4Al_4O_9(CO_3) \cdot 11H_2O$,

O – lime – CaO,

P – portlandite – $Ca(OH)_2$,

Pr – prosopite – $CaAl_2(OH)_4F_4$,

Q – quartz – SiO_2,

R – rosenbergite – $AlF_3 \cdot 3H_2O$,

S – óskarssonite – AlF_3,

T – 1.13 nm tobermorite – $Ca_5Si_6O_{17} \cdot 5.5H_2O$,

Tr – tridymite – SiO_2,

U – cuspidine $Ca_4Si_2O_7F_2$,

V – vaterite – $CaCO_3$,

W – wollastonite – $CaSiO_3$,

X – xonotlite – $Ca_6Si_6O_{18} \cdot H_2O$,

Y – gyrolite – $Ca_4Si_6O_{16} \cdot 4H_2O$.

Abbreviations of materials:

X – wollastonite precursor, $CaO\text{-}SiO_2 \cdot nH_2O\text{-}H_2O$ system ($CaO/SiO_2 = 1$), 200°C, 12 h, under stirring;

XS – wollastonite precursor, CaO-silica gel waste-H_2O system ($CaO/(SiO_2 + Al_2O_3 + F^-) = 1$), 200°C, 12 h, under stirring;

XD – wollastonite precursor, CaO-defluorinated silica gel waste-H_2O system ($CaO/(SiO_2 + Al_2O_3 + F^-) = 1$), 200°C, 12 h, without stirring;

W – wollastonite sample ($CaO/SiO_2 = 1$), obtained from precursor X after calcination at 900°C for 1 h;

WS – wollastonite-based sample ($CaO/(SiO_2 + Al_2O_3 + F^-) = 1$), obtained from precursor XS after calcination at 900°C for 1 h;

WD – wollastonite-based sample ($CaO/(SiO_2 + Al_2O_3 + F^-) = 1$), obtained from precursor XD after calcination at 900°C for 1 h;

W-C – wollastonite sample W, coupled with acryloxypropyltrimethoxysilane;

WS-C – wollastonite-based sample WS, coupled with acryloxypropyl-trimethoxysilane;

AESO – monomer, acrylated epoxidized soybean oil;

IBOMA – reactive solvent, isobornyl methacrylate;

THFMA – reactive solvent, tetrahydrofurfuryl methacrylate;

AI – resin, AESO-IBOMA mixture at ratio 40 mass%:60 mass%;

AT – resin, AESO-THFMA mixture at ratio 60 mass%:40 mass%;

GDMA – monomer, glycerol dimethacrylate;

CSF-r-900 – cuspidine sample, $CaO\text{-}SiO_2 \cdot nH_2O\text{-}CaF_2\text{-}H_2O$ system ($CaO/SiO_2/CaF_2 = 3/2/1$), obtained via two step synthesis (1st at 200°C, 12 h; 2nd at 900°C, 1 h);

CSF-w-900 – cuspidine sample, CaO-silica gel waste-CaF_2-H_2O system ($CaO/SiO_2+Al_2O_3/CaF_2 = 3/2/1$), obtained via two step synthesis (1st at 200°C, 12 h; 2nd at 900°C, 1 h);

CSF-r-1100 – cuspidine sample, $CaO\text{-}SiO_2 \cdot nH_2O\text{-}CaF_2\text{-}H_2O$ system ($CaO/SiO_2/CaF_2 = 3/2/1$), obtained via two step synthesis (1st at 200°C, 12 h; 2nd at 1100°C, 1 h);

CSF-w-1100 – cuspidine sample, CaO-silica gel waste-CaF_2-H_2O system ($CaO/SiO_2+Al_2O_3/CaF_2 = 3/2/1$), obtained via two step synthesis (1st at 200°C, 12 h; 2nd at 1100°C, 1 h).

Introduction

Wollastonite, calcium silicate $CaSiO_3$, can be a natural or an artificial material. Raw materials on the basis of this compound are widely used in ceramics, plastics, paints, paper industries, and medicine fields because of its desirable mechanical and chemical properties. These include low shrinkage, thermal stability, whiteness, hardness, and a few other features. There are many ways to synthesise wollastonite, yet two of them are the most common. The first is a single step synthesis when limestone or other calcium source is mixed with silica-rich materials (e.g. quartz) and then calcined within a temperature range of 1200–1400°C. The other way is through a two-step synthesis. The precursor may be obtained by precipitation, by using soluble Ca^{2+} and SiO_4^{4-} salts (e.g. calcium nitrate and sodium silicate). However, this method produces a lot of wastewater. Therefore, it is also possible to obtain wollastonite precursors by hydrothermal treatment of CaO and SiO_2 bearing materials in water suspension at 130–220°C to obtain such calcium silicate hydrates as xonotlite, 1.13 nm tobermorite, etc. The obtained product is calcined at 800–900°C when it recrystallises into wollastonite. When amorphous silica is used instead of crystalline silica for the initial mixture, calcium silicate hydrates are easier to form. However, the latter modification of SiO_2 is quite rare in nature; therefore, it is necessary to search for its alternative sources. One of them may be industrial waste such as the AlF_3 manufacturing by-product – silica gel – which contains 75–80 mass% of SiO_2.

During the research on the possible application of AlF_3-rich silica gel waste for the synthesis of calcium silicate, it was established that the aluminium and fluoride ions that were present in the waste promoted the formation of several minerals. One of them was cuspidine $Ca_4Si_2O_7F_2$. The possibility of applying the silica by-product of AlF_3 production for the synthesis of alternative binders would also help to solve the problem of industrial waste. Therefore, it is important to understand the formation of cuspidine and its influence on the hydration and carbonation mechanisms of binding materials and their properties.

The reduction of CO_2 emission is a major challenge for the industry of binding materials, as, in the course of production of Ordinary Portland cement, ~5% of all man-made CO_2 is emitted. An alternative to OPC could be low-lime calcium silicates, such as wollastonite $CaSiO_3$ or rankinite $Ca_3Si_2O_7$. Although wollastonite and rankinite are nonhydraulic, they react with CO_2 and harden in the presence of humidity. The advantage of wollastonite in this process is its better solubility in water, which means better interaction with CO_2 and lower carbon dioxide emissions caused by $CaCO_3$ calcination. The newly formed matrix after carbonation is composed of calcite $CaCO_3$ and amorphous SiO_2 providing similar mechanical properties to those of hydrated OPC where the matrix consists mainly of calcium silicate hydrates and calcium hydroxide.

The aim of the work is to study the formation of wollastonite or cuspidine by using aluminium fluoride production waste – silica gel or $SiO_2 \cdot nH_2O$ – in the context of synthesis methods, and to investigate the hydration and carbonation properties as well as the expedient areas of the obtained products.

The objectives of the work:

1. To determine the influence of $SiO_2 \cdot nH_2O$ or silica gel waste on the crystallisation of wollastonite via direct or two-step synthesis.
2. To investigate the microstructure, as well as the physical and chemical properties of synthetic wollastonite samples and their application in the production of CO_2-hardening binders, polymer composites, and 3D-printed scaffolds.
3. To synthesise cuspidine in the system of $CaO\text{-}SiO_2\text{-}CaF_2$ via direct and two-step synthesis.
4. To investigate the hardening of synthetic cuspidine samples in various environments.

Statements presented for the defence:

1. The mineral composition and properties of the precursor control the formation of wollastonite at 900°C.
2. Synthetic samples of cuspidine actively participate in the process of capturing and storage of CO_2.

Scientific novelty of the research

1. The synthesis method has a critical impact on the formation, structure, and texture of synthetic samples of wollastonite and cuspidine.
2. The precursors for the sintering of wollastonite or cuspidine must be $Ca(OH)_2$-free because the calcinated products contain compounds with a higher molar CaO/SiO_2 ratio – larnite or kumtyubeite.
3. It has been proven that two-step synthesis (hydrothermal synthesis at 200°C for 12 h and calcination at 900–1100°C for 1 h) is efficient to produce synthetic cuspidine.

Practical significance of the scientific research

It has been determined that AlF_3 production waste, notably, silica gel, is suitable for the manufacturing of alternative binders: wollastonite-sand samples gain compressive strength of 18 MPa during curing in CO_2 atmosphere. Meanwhile, cuspidine-sand samples reach compressive strength of 13–14 MPa during accelerated carbonation.

It has been determined that the addition of wollastonite-based fillers, either coupled with acryloxypropylsilane or uncoupled, produces harder composites than

filler-free resin samples. In addition, the developed wollastonite and soybean derived resin composites have a great potential to be a competitive alternative to the conventional petroleum-derived ones and can reduce the negative impact on the environment.

The synthesised prototype samples of calcium silicate (hydrates), which can be hardened in the carbon dioxide environment, have been used to produce white concrete tiles under industrial conditions.

Approval and publication of the research results

The results of the dissertation have been presented in 4 scientific publications included in the *Clarivate Analytics Web of Science* database: one paper has been published in *Scientific Reports*, one paper has been published in *Ceramics International*, and two papers have been published in the *Journal of Thermal Analysis and Calorimetry*.

The results have been presented at 6 scientific international conferences: *1st International Conference on Energy, Environment and Storage of Energy 2020* (ICEESEN2020), *3rd International Conference on the Chemistry of Construction Materials* (ICCCM2020), 6th *Central and Eastern European Conference on Thermal Analysis and Calorimetry* (CEEC-TAC6) – *15th Mediterranean Conference on Calorimetry and Thermal Analysis* (Medicta2021), *17 International Congress on Thermal Analysis and Calorimetry* (ICCTA), *25th International Conference – School Advanced Materials and Technologies 2022* (AMT2022), *Chemistry and Chemical Technology 2022* (CCT2022).

Contribution of the author

The selection of materials was carried out, and the research plan was outlined by Andrius Gineika and Prof. Dr. Kęstutis Baltakys. The author investigated and described the synthesis of wollastonite and cuspidine; the author also examined their carbonation hardening process and the application of synthetic wollastonite. Prof. Dr. Kęstutis Baltakys advised on the progress of the experiment and on the preparation of the manuscripts. Assoc. Prof. Dr. Tadas Dambrauskas advised on BET analysis, Prof. Dr. Raimundas Šiaučiūnas advised on the methods of synthesis, Prof. Dr. Jolita Ostrauskaitė advised on the wollastonite/resin composite research. Wollastonite-based fillers were produced in the Department of Silicate Technology of Kaunas University of Technology, whereas the composite materials were produced at the Department of Polymer Chemistry and Technology of Kaunas University of Technology. The 3D-printed scaffolds were made in Laser Research Center of Physics Faculty of Vilnius University.

Structure and content of the dissertation

The dissertation consists of introduction, literature review, experimental part, results and discussion, conclusions, and a list of references and publications on the dissertation topic. The list of references includes 221 bibliographic sources. The main results are discussed in 194 pages and illustrated in 13 tables and 71 figures.

1. LITERATURE REVIEW

1.1. Classification and General Properties of Calcium Silicates

Calcium silicates are salts of calcium and silicic acid. Their composition may be expressed as a molar ratio of calcium oxide CaO and silicon dioxide SiO_2, which varies from 0.5 to 3 (Fig. 1.1) [1–7]:

- $CaSi_2O_5$ ($CaO/SiO_2 = 0.5$),
- $CaSiO_3$ ($CaO/SiO_2 = 1$) – wollastonite, pseudowollastonite,
- $Ca_3Si_2O_7$ ($CaO/SiO_2 = 1.5$) – kilchoanite, rankinite,
- Ca_2SiO_4 ($CaO/SiO_2 = 2$) – larnite (belite), calcio-olivine,
- Ca_3SiO_5 ($CaO/SiO_2 = 3$) – hatrurite (alite).

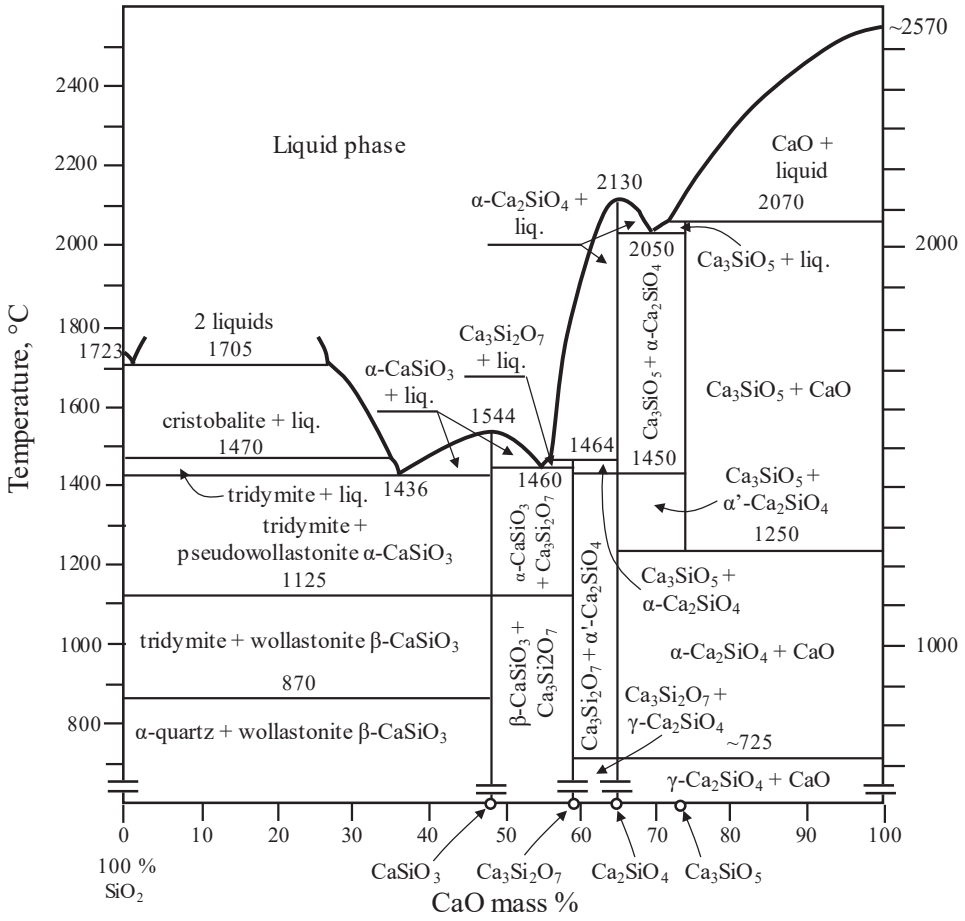


Fig. 1.1. CaO-SiO_2 phase diagram [7]

Calcium disilicate $CaSi_2O_5$ was first synthesised in 1991 by Kanzaki *et al*. [8] from wollastonite by applying additional pressure. The researchers observed a 29Si NMR peak at a chemical shift of –150 ppm, which suggested the presence of

pentacoordinated silicon. At first (Fig. 1.2.), breyite $CaSiO_3$ was observed to form under 10 GPa pressure at 1500°C. By further increment of pressure to 12 GPa, $CaSiO_3$ transformed into a mixture of Ca_2SiO_4 and $CaSi_2O_5$. Under 15 GPa, the mixture recrystallised into $CaSiO_3$ perovskite. Later research showed that perovskite phase does not undergo further recrystallisation with an additional increment of pressure [9].

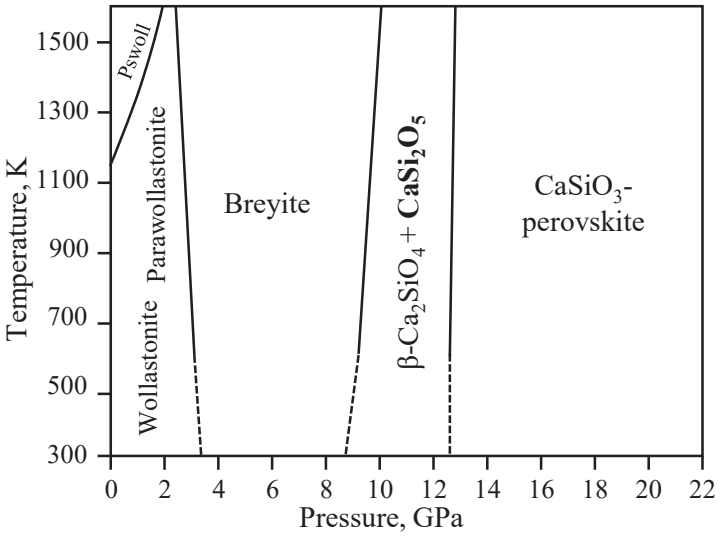
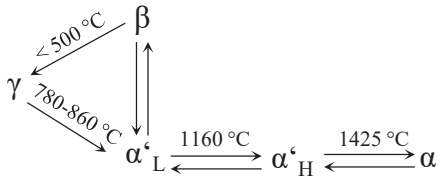


Fig. 1.2. $CaSiO_3$ phase diagram [10]

It was determined that the structure of the discovered mineral was similar to titanite $CaTiSiO_4$, where titanium is sixfold-coordinated, and silicon is fourfold-coordinated. In $CaSi_2O_5$, silicon is not only four- and sixfold-coordinated but also fivefold-coordinated, and it forms [SiO_4] tetrahedra, [SiO_6] octahedra and [SiO_5] pyramids [11].

Tricalcium disilicate $Ca_3Si_2O_7$ exhibits two crystallographic modifications – low-temperature kilchoanite and high-temperature rankinite. Although both minerals are sorosilicates, the former consists of single silicate tetrahedra and triple chains [3, 4], while the latter consists only of double chains of silicate tetrahedra [12]. Currently, these calcium silicates have little-to-no industrial application because they hydrate extremely slowly, although the application of carbon dioxide curing/hardening for tricalcium disilicate is under investigation [4, 13].

Dicalcium silicate Ca_2SiO_4 exhibits five polymorphic modifications: γ (rhombohedral), β (monoclinic), α_L' (rhombohedral), α_H' (hexagonal), and α (hexagonal):



The first modification (the natural mineral calcio-olivine) belongs to the olivine mineral group and differs most from the other modifications. Calcio-olivine does not hydrate, it does not harden and gain strength during the reaction with water, but the *γ* modification is the only variant which is stable at room temperature. The β modification – the synthetic mineral belite – is denoted by the widest industrial application as the basis for belite and related cement types. However, in order to avoid β→γ recrystallisation during production, rapid cooling is applied, or else it is doped with foreign ions that can stabilise the β modification [1,5,14].

Tricalcium silicate Ca_3SiO_5 has two names depending on its origin: the natural mineral is called hatrurite, whereas the synthetic mineral is alite. It exhibits six crystallographic modifications:

$$T_I \xleftrightarrow{600\text{-}620^\circ C} T_{II} \xleftrightarrow{920\text{-}950^\circ C} T_{III} \xleftrightarrow{970\text{-}980^\circ C} M_I \xleftrightarrow{990\text{-}1000^\circ C} M_{II} \xleftrightarrow{1050^\circ C} R$$

here: T_I, T_{II}, and T_{III} – triclinic modifications, M_I and M_{II} – monoclinic modifications, R – rhombohedral modification [1].

When exposed to water, tricalcium silicate hydrates and recrystallises into hydrated compounds – calcium silicate hydrates – which are responsible for the gain of strength. Due to this reaction, the main modern binding material Portland cement is based on synthetic alite [1,15].

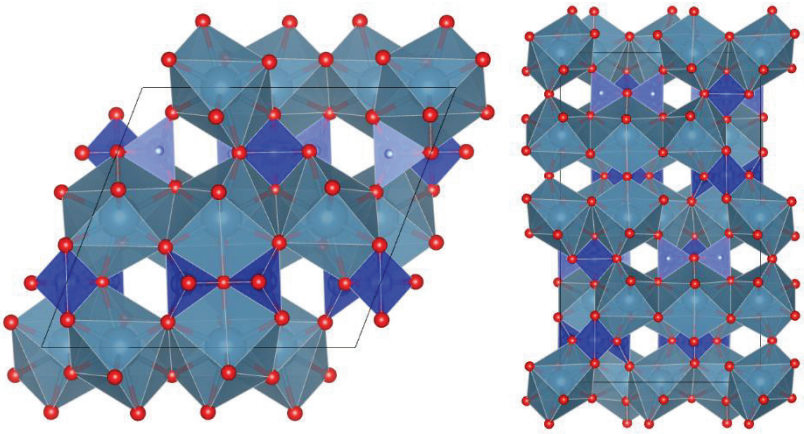
1.2. Wollastonite

1.2.1. The crystal structure of wollastonite

$CaSiO_3$ ($CaO \cdot SiO_2$) exhibits two main polymorphic modifications: α – the high-temperature one – which is called pseudowollastonite and which melts at 1544°C [16], and β – the low-temperature one – the natural mineral called wollastonite which recrystallises to the α modification at 1125°C [6,17]:

$$\beta\text{-}CaSiO_3 \xrightarrow{1125^\circ C} \alpha\text{-}CaSiO_3 \xrightarrow{1544^\circ C} \text{melt.}$$

Pseudowollastonite α-$CaSiO_3$ exhibits 3 polytypes: 2-, 4- (dominant phase), and 6-layer polytype. The structure of all polytypes has the space group C2/c. In addition, the layers remain stable at temperatures above 1400°C. Differences in pseudowollastonite polytypes are based on the different stacking sequences of the layers of ternary silicate rings [Si_3O_9] with the layers of calcium pseudooctahedra [CaO_8]. In the two-layer structure (Fig. 1.3. a), the second layer is displaced by 1/6 of a dimension compared to the first layer. In the four-layer structure (Fig. 1.3. b), the first and second silicate layers are situated directly on top of one another, while the third layer is displaced by 1/6 of the *b* axis with respect to the second layer. The fourth layer, similar to the second one, lies directly on top of the third layer [10,18,19].



a b

Fig. 1.3. The crystal lattice of pseudowollastonite: a – two-layer polytype; b – four-layer polytype [19]

β-$CaSiO_3$ is distinguished by infinite single chains of silicate tetrahedra, thus making it an inosilicate type mineral. The chains themselves consist of repeating units – three differently oriented silicate tetrahedra. The set of these repeating units is also called the *dreiketten*. The silicate chains are connected to triple columns of calcium ions: the central column consists of seven-fold coordinated calcium pseudo-octahedra [CaO_7], while the outer two are six-fold coordinated calcium octahedra [CaO_6] [18,20,21].

Because of the different sizes of the octahedral and tetrahedral units, silicate chains are slightly deformed to match the calcium columns, both of which are oriented along the *b* axis. In the wollastonite structure, each silicate chain is paired with another inversion-related chain. A single dreierketten of each chain of a pair makes up a basic slab that develops different stacking orders along the *a* axis. Following the stacking order, β-$CaSiO_3$ forms several polytypes of triclinic or monoclinic crystals: 1T, 2M (parawollastonite), 3T, 4T, 4M, 5T, and 7T (Fig. 1.4.; here: T – triclinic, M – monoclinic) [21–24]. The number of a polytype indicates the number of stacking slabs, each being about 0.77 nm thick. The crystal lattice of the 1T polytype consists of basic slabs stacking on each other, while the 2M one is made up of two slabs: a stacking one and a displaced one which is displaced by ½ along the *b* axis (Fig. 1.4. c). More complex stacking orders are observed in other polytypes and their sub-polytypes. In addition, if displacement occurs, it may only be ½ along the *b* axis [18,20].

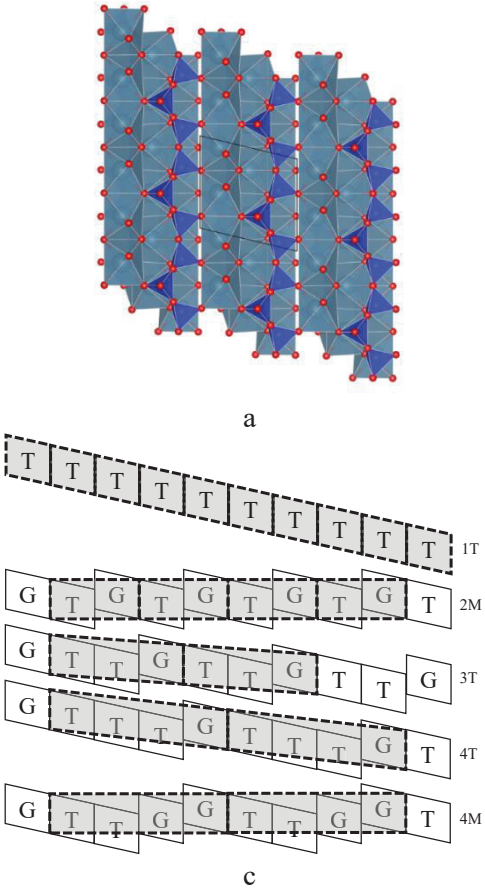


Fig. 1.4. The structure of the most common wollastonite polytypes: a – 1T; b – 2M (parawollastonite); c – schematic explanation of slab stacking and displacement in 1T, 2M, 3T, 4T, and 4M wollastonite polytypes
Here: G – a displaced slab; T – a stacking slab. The thick dashed lines show crystal lattices [23–26]

1.2.2. Synthesis methods of wollastonite

The synthesis of wollastonite was first investigated by Hedvall *et al*. back in 1931 [27] and by Jander in 1934 [28], while its production on the industrial scale started around the 1970s. Today, wollastonite is produced by solid-state sintering, calcination coupled with the sol-gel method, and hydrothermal or microwave-assisted synthesis.

Solid-state sintering

This method is based on the silica-calcium carbonate interaction which is usually carried out at temperatures above 1000°C. The reaction involves several stages: first, calcium carbonate decomposes and produces calcium oxide, and then it reacts with quartz and produces more basic calcium silicates, such as larnite or rankinite. The reaction ends when the latter compounds react with the remaining SiO_2 and produce wollastonite [20].

The early research works described the influence of the origin of the raw materials, their granulometric composition, surface area, CaO/SiO_2 molar ratio, and additives on the formation of wollastonite. The size of the quartz was determined as particles of no more than 0.1 μm, and the surface area was estimated to be around

2 m^2/g. The authors also recommended decreasing the molar ratio to 0.9, and the temperature should be 1300°C [27–30].

Nour *et al*. [6] investigated the formation of wollastonite from $CaCO_3$, amorphous silica, quartz, or waste materials (marble waste and silica fume) in the course of solid-state sintering. The research concluded that, in the temperature range of 1000–1400°C, wollastonite formed in the waste materials system which contained alkalis, MgO, and Fe_2O_3, which had a positive impact on the reaction. Furthermore, a slight decrease in the CaO/SiO_2 ratio to 0.8 also showed a positive effect on the formation. However, wollastonite failed to crystallise from pure reagents in the temperature range of 1000–1400°C. A part of lime and silica remained unreacted, and larnite formed instead. In addition, during the sintering, the amorphous silica recrystallised into cristobalite. Rashid *et al*. [7] obtained similar results when using limestone and silica sand as raw materials. At 1100°C, the formation of wollastonite was negligible, and part of quartz remained unreacted. Yet, at 1450°C, pseudo wollastonite was observed in the products with traces of calcio-olivine.

Leite *et al*. [31] performed an experiment by using waste materials, such as chamotte, which acted as a source of SiO_2, and raw or calcined avian egg shells, which were a source of CaO. It should be noted that chamotte consisted not only of 46.5wt% SiO_2 but also of 36.4wt% Al_2O_3 and 9.1wt% Fe_2O_3. In both cases (raw or calcined eggshells), after solid-state sintering of the samples at 1100°C for 24 h, the products of both systems consisted mainly of wollastonite with admixtures of rankinite, larnite and Al or Fe containing silicates, without significant differences.

Two-stage methods

Wollastonite formation from calcium silicate hydrates, such as tobermorite, xonotlite or C-S-H (I), occurs at a lower temperature compared to solid-state sintering [17, 32]. Thus, the aforementioned compounds can be considered as precursors of wollastonite. They can be synthesised by using various initial compounds and methods. One of the ways is precipitation from solutions (the sol-gel method) when Ca^{2+} and SiO_3^{2-} ions react in the soluble form. The most common initial compounds are $CaNO_3$ or $CaCl_2$ and Na_2SiO_3 or tetraethyl orthosilicate (TEOS) [33–36].

Lin *et al*. [34] synthesised wollastonite nanowires from pure calcium nitrate and sodium silicate solutions with the help of surfactants, such as cetyltrimethylammonium bromide (CTAB), n-pentanol, and n-hexane. At first, the pH value of the sodium silicate solution was adjusted to 10.8 by using ammonia solution, then mixed with the surfactants and additionally sonicated to obtain a transparent microemulsion. Calcium nitrate was added dropwise to obtain an intermediate suspension which was hydrothermally cured at 200°C for 18 h. The precursor was rinsed with water and dry ethanol, and then calcined at 800°C for 2 h. Analogous experiments were carried out without surfactants [35]. After the investigation of the hydrothermally obtained precursors, it was determined that tobermorite and xonotlite were the dominant phases.

Another way to synthesise the precursors is hydrothermal synthesis using the initial materials which are not soluble in water but are suspended in it and react at an elevated temperature and pressure. Again, the obtained precursors are calcined [37].

Pei *et al*. [38] successfully used this method for the synthesis of wollastonite from reagent-grade CaO and SiO_2. The hydrothermal synthesis was carried out at 220°C for 12 h under stirring at 10 rpm. The obtained precursor was calcined at 800°C for 1 h. It was determined that, similar to Lin's results, xonotlite was obtained during the hydrothermal treatment, which recrystallised to wollastonite.

Ismail *et al*. [37] carried out a slightly different experiment in which they used rice husk ash instead of pure silica, which contained ~90wt% SiO_2. The hydrothermal reaction was carried out at 135°C (under 0.24 MPa pressure) for 8 h. The analysis showed that the precursor contained unreacted $Ca(OH)_2$ and cristobalite SiO_2. However, after calcination at 950°C for 2 h, wollastonite dominated in the synthetic product.

1.2.3. The influence of additives on the physical properties of wollastonite

As mentioned above, in the investigations of Nour *et al*. [6] and *Lin et al*. [34], additives can have an impact on the formation of wollastonite. Additives can improve the crystallinity and quicken the formation with respect to time and/or temperature. In addition, they can increase porosity and the surface area.

Li *et al*. [39] investigated the influence of 5mol% substitution of CaO by ZnO and ZrO_2. The synthesis was carried out via the sol-gel method by using metal nitrates and TEOS. After calcination of the obtained precipitate at 950°C for 0.5 h, it was determined that zinc reacted with silicate ions and formed calcium-zinc silicate and reduced the possible amount of wollastonite. Meanwhile, the zirconium additive did not react with the silicate ions and formed zirconium oxide only; however, the intensity of the wollastonite peaks in the XRD patterns increased.

Ros-Tárraga *et al*. [40] investigated the formation of wollastonite in Na_2O-K_2O-CaO-SiO_2 and MgO-K_2O-CaO-SiO_2 systems which contained 2wt% of Na_2O/MgO additive and 1wt% of K_2O. As in the previous experiment, the synthesis was carried out via a combined sol-gel and calcination method, but the use of metal carbonates as TEOS requires hydrolysation in an acidic medium. Therefore, the carbonates were used to neutralise the obtained solution. The samples were calcined at 950°C with a ramp period of 55 h and an isothermal period of 8 h. The XRD patterns of the obtained product showed that the sample with the Na_2O additive contained not only wollastonite and pseudowollastonite, but also unreacted SiO_2 in the form of cristobalite. Meanwhile, the sample with MgO additive contained only the target product.

Obradović *et al*. [41] investigated the influence of polymer additives, such as cotton, nanocellulose, and polymethylmethacrylate, on the porosity of synthetic wollastonite. The synthesis was carried out in several steps: at first, a paste was obtained from methyl-hydrocyclosiloxane and calcium carbonate, then it was calcined at 250°C for 30°C, then, pore-forming agents were included, and, ultimately, the mixture was shaped into tablets and calcined at 900°C for 1 h. The XRD patterns showed that, in all cases, the products contained both $CaSiO_3$ and Ca_2SiO_4, but the sample with polymethylmethacrylate showed the best results. The SEM analysis demonstrated that cotton wool promoted the formation of macropores, while agglomeration was visible in the other two cases.

Bernardo *et al*. [42] used silicon resin as the source of SiO_2 and calcium carbonate filler as the CaO source, with the addition of tricalcium phosphate. Polymethylmethacrylate (PMMA) microbeads were used to create pores and a scaffold structure. The composite was sintered, and interconnected macropores of ~170 μm diameter were obtained. Liu *et al*. [43] used a similar approach with PMMA microbeads, but, in their case, the beads were impregnated with a suspension of commercial wollastonite/tricalcium phosphate suspension. They obtained macropores of 500±200 μm diameter. Kunjalukkal *et al*. [44] used a polyurethane (PU) sponge as a template that was immersed in a slurry of commercial wollastonite powders with additives and then sintered. The obtained products were similar to those of the previous work: interconnected ~500 μm diameter macropores. Xie *et al*. [45] produced wollastonite doped with magnesium by the sol-gel method from soluble salts by employing calcination. The powders were mixed with polyvinyl alcohol as a binder and then pressed in a steel mould at 200 MPa. The scaffolds with pure wollastonite reached a compressive strength of over 200 MPa, while the magnesium doping increased the value by up to 4 times.

Iljina *et al*. [46] investigated the possible use of aluminium fluoride production waste – amorphous silica – for the synthesis of calcium silicate hydrates which exhibit a CaO/SiO_2 ratio close to wollastonite. The waste material was determined to contain approx. 10wt% of fluoride and approx. 5wt% of aluminium ions. The XRD patterns of the hydrothermally synthesised samples showed that, in addition to tobermorite, admixtures of calcium alumosilicate – katoite, calcium fluorosilicate – cuspidine, and calcium fluoride formed as well. After calcination at 800–1000°C for 30 min of the obtained samples, it was observed that wollastonite formed at 1000°C, and both calcium fluoride and cuspidine remained stable up to the above mentioned temperature.

1.3. Application of Wollastonite

1.3.1. Wollastonite additive in concrete

Due to the unique fibrous nanostructure, wollastonite is used as a reinforcement material in concrete, ceramics, and plastics. Particles that are smaller than 25 μm are considered powder, 25–150 μm are referred to as microfibres, and over 150 μm is the size of fibres [47].

Zareei *et al*. [48] determined that the wollastonite additive tends to reduce the workability of fresh concrete. The measured slump values decreased by up to 34% when 50% of the cement was replaced by ~10 μm calcium silicate particles. The researchers concluded that this effect could be caused by as the two times larger specific surface area compared to cement, thus increasing the water uptake.

Wahab *et al*. [47] investigated the influence of the wollastonite additive on the hardening of Portland cement. On the one hand, it was determined that, by replacing 10, 20, and 30% of the binder with wollastonite, after 28 days of hydration, the compressive strength decreased by 12, 34, and 35%, respectively. A similar trend of a harmful effect was observed on the flexural strength: it decreased by 2, 10, and 17%, respectively. However, with the replacement of sand with wollastonite by 10, 20, and 30%, the compressive strength increased by 5, 4, 5, and 28%, respectively,

whereas the flexural strength went up by 12, 2, 8, and 15%, respectively. In addition, the replacement of cement with wollastonite tended to prolong the setting time of concrete. Ransinchung *et al*. [49] carried out a similar experiment and determined that wollastonite prolongs the start and the end of the setting time of concrete by 25 and 27%, respectively.

Soliman and Nehdi [50] received quite different results in their research on ultra-high-performance concrete. They determined that the substitution of cement with wollastonite (4 and 12vol%) improved the early compressive strength. Furthermore, the additive acted as a passive internal restraint and reduced the shrinkage strain, thus making the concrete more resistant to microcracking. Furthermore, wollastonite interacted well with organic-based shrinkage reducing agents and even reduced their deterioration.

Kalla *et al*. [51] and Mathur *et al*. [52] determined that substituting 55–60% of the cement with a mixture of wollastonite and fly ash reduced the shrinkage of the concrete during drying and reduced its water permeability. Similar results were obtained by Hamedanimojarrad *et al*. [53] and Galea *et al*. [54] when 4 μm wollastonite particles were used.

1.3.2. CO_2-cured (carbonated) wollastonite binders

The reduction of CO_2 emission is a major challenge for the binding materials as, during the production of ordinary Portland cement (OPC), ~5% of all man-made CO_2 is emitted [55]. An alternative to OPC could be low lime calcium silicates, such as wollastonite $CaSiO_3$ or rankinite $Ca_3Si_2O_7$, which also require a lower temperature to be produced [56,57].

Even though wollastonite is non-hydraulic, it can be activated by CO_2 in the presence of humidity [58]. Wollastonite is preferred for this process due to its better solubility in water, which means a faster reaction with CO_2 and less carbon dioxide emission caused by CaO production from $CaCO_3$ [59]. A newly formed matrix after carbonation is composed of calcite $CaCO_3$ and amorphous SiO_2 providing similar mechanical properties as hydrated OPC where the matrix consists mainly of calcium silicate hydrates and calcium hydroxide [60–62].

Carbonation is the formation of carbonate salts when carbonic acid reacts with salts of weaker acids. Although the atmosphere contains a small amount of carbon dioxide (about 0.04% [63]), gaseous CO_2 cannot react with dry solid materials. For the reaction to begin, carbon dioxide must dissolve in water to form carbonate CO_3^{2-} and hydrogen H^+ ions. The reaction between silicates and carbonic acid is possible because the dissociation constant (25°C) of silicic acid is $pK_a = 1.3 \cdot 10^{-10}$, while the constant of carbonic acid is $pK_a = 4.5 \cdot 10^{-7}$, which is higher, thereby making the latter a stronger acid [64]. The reaction may take place in the wet pores of silicate materials where the pore solution is available. The carbonation process can be described in three chemical Equations (1.1–1.3 [65]):

1. dissolution of CO_2 in water and formation of carbonate and hydrogen ions:
$$CO_2 + H_2O \rightleftarrows HCO_3^- + H^+ \rightleftarrows CO_3^{2-} + 2H^+; \quad (1.1)$$
2. calcium leaching from silicate material:
$$Ca_nSi_mO_{n+2m} + 2nH^+ \rightarrow nCa^{2+}\, mSiO_2\downarrow + 2H_2O; \quad (1.2)$$

3. precipitation of calcium carbonate:
$$Ca^{2+} + CO_3^{2-} \rightarrow CaCO_3\downarrow. \quad (1.3)$$

Which type of carbonate (acidic or normal) ions is formed depends on the pH value of the medium. On the surface and in the outer layers of the material, where the pore solution generally exhibits a pH value closer to 7, acidic hydrocarbonate ions are formed, while, in the deeper layers of the material, where the pore solution is more alkaline (11–13), hydrocarbonate transforms to carbonate [66].

Under natural conditions, the carbonation of silicate-based materials (rocks, concrete, etc.) takes place at a very slow rate due to the low concentration of CO_2 in the atmosphere. However, if the concentration or partial pressure is increased, it is possible to accelerate the reaction. In addition, the temperature and relative humidity have also been observed to influence carbonation [58]. Furthermore, since the reaction starts when gaseous carbon dioxide enters the pores and dissolves in the pore solution, the increasingly thick layer of the newly formed calcium carbonate tends to slow down the reaction as it becomes harder for the carbon dioxide to pass [67].

Bukowski and Berger [61] investigated the mechanical properties of a binder which contained 50% sand and 50% wollastonite. They determined that the binder reached a compressive strength of 35 MPa within 24 h in 1 bar of CO_2 when using a dynamic 1.4 L/min gas flow system (from the formation of the sample to the end of carbonation). Riman *et al*. [68] reached a compressive strength of 70 MPa from carbonated wollastonite pastes.

Liu *et al*. [69] conducted a comparative research to investigate the difference between the carbonation of α and β wollastonite. The desired polymorphs were obtained by solid-state sintering at 1100°C from calcium hydroxide and amorphous silica, followed by different cooling regimes: rapid cooling (>500°C/min) prevented α → β recrystallisation, meanwhile slow cooling (<5°C/min) allowed the transformation into the β type. In addition, after natural cooling (~100°C/min), the sample contained almost equal amounts of both polymorphs. The researchers combined the obtained powders with water at a ratio of 0.15 and formed cubic samples. The thermal analysis of the carbonated samples showed the highest sequestration of CO_2 by the rapid-cooled wollastonite and the linear dependency of the sequestration on the amount of α polymorph. Furthermore, the carbonated samples of α-wollastonite reached 60–70 MPa compressive strength (after 2 and 24 h of curing, 3 bar CO_2). The researchers suggested that the higher activity of α polymorph is related to the presence of distorted [CaO_x] polyhedra and a longer distance between the Ca and O atoms, thus making the α polymorph more prone to the leaching of Ca^{2+} ions. To confirm this theory, they investigated the dissolution of both wollastonite polymorphs in a saturated CO_2 solution (pH = 4). The results showed that the concentration of Ca^{2+} ions in the solution in the case of α-wollastonite was about 100 times higher.

Khan *et al*. [70] investigated the influence of several hydrophilic amino acids on the carbonation processes of natural wollastonite. The organic additives were dissolved in the water used to wet calcium silicate powders at concentrations of 0.13

and 0.25 mol/L The researchers observed that amino acids stabilised the metastable polymorphs of calcium carbonate: vaterite, aragonite and amorphous calcium carbonate. In addition, organic additives slightly reduced CO_2 sequestration, but prevented the 'clogging' of pores and improved the compressive strength by 35–40% and the flexural strength by ~60%. The researchers also investigated the influence of magnesium oxide addition on the properties of carbonated natural wollastonite [71]. They determined that magnesia improved the compressive strength by 44%. Furthermore, the pore volume was refined as a result of the formation of hydrated magnesium carbonates. However, the latter product caused the expansion of the samples by up to 0.1%.

1.3.3. Wollastonite-polymer composites

Polypropene

Polypropene is one of the thermoplastics that is commonly used in everyday life. It is preferred because of its low cost and sufficiently good physicochemical properties. Overall, polypropene has attracted a lot of attention when it comes to its composites with wollastonite because the plastic exhibits relatively poorer thermal properties compared to other polymers [72].

Differential Scanning Calorimetry (DSC) is the most commonly used method to investigate the thermal properties of polypropene, and many [73–80] researchers used it to observe the increase of the crystallisation temperature T_C and the degree of crystallinity X_C. Dasari *et al*. [73] determined that wollastonite particles acted as nucleation centres in the polypropene matrix and improved its crystallinity because the heat flow of the thermal melting/crystallisation effect increased by 17.5%. The investigation of the mechanical properties has shown that the filler has increased the storage modulus by 126%, and the loss modulus by 110%, thus making the plastic physically harder. Misra *et al*. [74] in their research on wollastonite-reinforced polypropene-polyethene copolymer observed that the reinforcement increased the crystallinity of the polymer from 19 to 33 %.

In a research on the polypropene-polystyrene rubber reinforcement with wollastonite [76], it was determined that the peaks of the reinforced polymer in the X-ray diffraction (XRD) patterns were narrower (the lower is the half-width of the peak, the smaller are the crystallites) than the samples of the non-reinforced polymer. Thus, it was concluded that the XRD patterns, similarly to DSC, showed that wollastonite improves the crystallinity of the polymer.

When the influence of the wollastonite filler on the thermal properties of polypropene (TC and XC) was compared with talc and mica, it was determined that wollastonite was between them: talc > wollastonite > mica [78–81].

Due to the low thermal conductivity (2.5 W/m·K), wollastonite prevents polypropene from complete incineration, thus forming char instead [82]. In addition, when the interaction between calcium metasilicate and intumescent flame retardants was investigated [83], it was determined that the formed polymer char was harder and denser, thus reducing air access and trapping the combustion products inside. Thermogravimetry was used in another work to investigate the flammability of polypropene-wollastonite composites [84]. It was determined that the additive

increased the decomposition temperature T_d for the same reason as in the aforementioned research. When the amount of filler is more than 10%, the decomposition slows down non-linearly with an increasing T_d [85]. Similar results were obtained in the works on polypropene-wollastonite composites with further additives [82,86].

The DSC curves of pure polypropene contain only one thermal effect related to melting, but, in the presence of the wollastonite additive, three effects can be observed: one is attributed to α-phase, and two to β-phase [72]. The heat flow of the melting of the latter phase decreases with the increase of the amount of the filler. Thus it is stated that wollastonite promotes the crystallisation of α-phase [87,88]. However, the data on whether wollastonite increases or decreases the melting temperature of polypropene are somewhat inconsistent [85,89–91].

As wollastonite is hydrophilic and polypropene is hydrophobic, the interaction between the mineral filler and the polymer matrix is limited [72]. To improve the interaction, wollastonite can be modified either with organic acids [87,88,92–94], or with silane/titanate coupling agents [76,92].

Polyethene

Yang *et al*. [95] investigated high-density polyethylene and wollastonite composites which contained 30 wt% of a filler (particle size ~10 μm). It was determined that the polymer did not decompose during the exposure to 110°C for 6 days. This was explained by an increase of the activation energy for the decomposition reaction because of the presence of a wollastonite additive. Furthermore, the filler increased the T_d value of the polymer from ~281 to ~288°C, and prevented it from complete combustion.

Lapčík *et al*. [96] in their research determined that the addition of wollastonite decreased the melting temperature and the degree of crystallinity of high-density polyethene. 5–10 wt% of filler addition improved the elasticity (15% increased elongation at break), but a higher amount of a filler had the opposite effect.

Tong *et al*. [97] investigated the abrasion of ultrahigh molecular weight polyethene (UHMWPE) and wollastonite composites. They determined that 10% addition of the additive showed the best performance. Furthermore, they investigated the impact of silane (vinyl-triethoxy silane) and titanate (isopropyl titanium triisostearate) coupling of wollastonite. It was determined that the modified filler showed better performance than the unmodified filler. In addition, the reduction of the particle size and their aspect ratio had a positive impact on the abrasion resistivity of the polymer. Panin *et al*. [98] in a similar research determined that the mechanical properties of ultrahigh molecular weight polyethene and wollastonite composites with 7 to 23 wt% filler increased by 1.8 times (in terms of the elastic modulus) and 1.3 times (in terms of the yield strength), while the silane coupling of wollastonite further improved the yield strength by 9% in several cases. The coupling agent *KH-550* (3-aminopropyl-triethoxy silane) was determined to be the most efficient, while *Penta-1006* (polyorgano-siloxane (a silicone) $(CH_3)_3SiO((CH_3)_2SiO)_n$-$Si(CH_3)_3$) and *OTS* (octadecyl-trimethoxy silane) had little impact on the wollastonite-polymer interaction.

Other polymers

Ma *et al*. [99,100] investigated silane-coupled wollastonite and polyetherketone (PEEK) composites. In the first work, the filler was modified with *KH-550* (3-aminopropyl-triethoxy silane), *KH-570* (3-methacryloxypropyl-trimethoxy silane) and *KH-792* (aminoethyl-aminopropyl-trimethoxy silane). In the second work, they investigated silane-terminated polyetherketones. In both works, it was determined that the wollastonite additive with or without silane modification slightly increased the decomposition temperature and the degree of crystallinity of the polymer; meanwhile, the crystallisation temperature decreased, and the melting temperature remained relatively unchanged. Furthermore, both the unmodified and modified wollastonite filler improved the flexural (~7%) and tensile (~7%) strength of the polymer composites, however, the elongation at break decreased by ~20%.

1.3.4.3D-printed wollastonite and wollastonite-based scaffolds

Wollastonite has been seen as a promising material for bone tissue regeneration due to its *in vivo* decomposition into calcium and silicate ions which stimulate the restorative processes and promote the formation and deposition of natural hydroxyapatite [101].

Wu *et al*. [100] presented one of the earliest works on 3D printed wollastonite-based scaffolds via syringe dispensing. It was also presented by Wu *et al*. [102]. In their research, calcium silicate was prepared by the sol-gel method from soluble salts, and calcination of the obtained precipitate at 800°C was employed. For the 3D-printing, an aqueous polyvinylalcohol solution (15wt% of polymer) was used as the liquid base. The solution to the wollastonite ratio was 7:8 by weight. The printed scaffolds were dried at 60°C and then heated at 180°C to cross-link the polymer. The compressive strength of the composite scaffold was ~3.6 MPa, and the *in vivo* test showed an excellent result for bone regrowth.

Shao *et al*. [103] used similar initial materials to produce magnesium and calcium phosphate-doped synthetic wollastonite-based scaffolds. But, in this case, an indirect 3D printing approach was employed, as the printed scaffolds were additionally sintered at 1120–1180°C. It was determined that the compressive strength strongly depended on porosity, and the following relationship was determined: ~45% porosity – ~140 MPa, ~55% – ~120 MPa, and ~65% – ~60 MPa. Furthermore, it was observed that the addition of calcium phosphate had a different impact regarding two aspects: it reduced the compressive strength, but it also slightly reduced the strength and the weight loss after immersion in a pH 7.4 buffer solution for up to 6 weeks. Tcanescu *et al*. [104] used the same approach to produce apatite-wollastonite scaffolds. They mixed the powder of inorganic material (55wt%) with maltodextrin powder (45wt%) and combined with zb®60 clear binder for the printing process. The prepared green bodies were sintered at 779°C (1 h) and further at 1150°C. The porosity of the sintered scaffolds was ~42%.

Elsayed *et al*. [105] used wollastonite-diopside (the W/D molar ratio in use was 1:1) glass powder for 3D printed scaffolds of different types of lattices: Kelvin, diamond, and cubic. The glass particles were <45 μm in size. To prepare a suspension for printing, the powders (41wt%) were mixed with tripropylene glycol diacrylate monomer which was cross-linked during digital light processing. The

scaffolds were rinsed in isopropanol and additionally cured in a UV furnace for 15 min. The fully polymerised scaffolds were then sintered at 550°C (3 h) and further at 1100°C (1 h). It was determined that the density and the compressive strength depended on the lattice type and increased in this sequence: Kelvin, diamond, and then cubic. The porosity decreased with the increased density. The cubic lattice reached a compressive strength of 16 MPa, while the Kelvin lattice reached ~3 MPa, and the diamond lattice yielded ~4.5 MPa.

Kamboj *et al*. [106] prepared wollastonite-silicon scaffolds (50 and 50 wt%) by using the selective laser melting method, which did not require a liquid medium. The scaffolds were determined to have a compressive strength of up to 110 MPa, which, after immersion in a buffer solution of 2-amino-2- (hydroxymethyl) propane-1,3-diol (Tris) at pH 7.3 for 14 days, decreased to 90 MPa. In a more recent work by the same authors [107], the scaffolds of the same design and a similar composition, but containing more wollastonite (70 instead of 50wt%), reached only the compressive strength which decreased to 30 MPa under the same immersion conditions.

Xu *et al*. [108] investigated the influence of magnesium doping on wollastonite scaffolds. On the one hand, it was determined that Mg ions had little-to-no effect on the linear shrinkage (~25%) and porosity (~41%). Meanwhile, magnesium doping affected the compressive strength of fresh samples and on those immersed in Tris buffer for up to 8 weeks: the fresh sample with 6mol% replacement of Ca^{2+} showed ~40 MPa, 5mol% produced ~30 MPa, whereas 4mol% withstood ~20 MPa. After 8 weeks of immersion, the values became two times lower. Moreover, the release of ions increased with the decreasing Mg doping, from which, it could be concluded that magnesium improves the general durability of the produced scaffolds.

1.4. Silane Coupling

Silane coupling agents are hybrid organic-inorganic compounds which exhibit both hydrophilic and hydrophobic properties [109]. Due to this feature, silanes offer enormous improvements for virtually all industries involving polymer/filler interactions, and, as a result, they are widely used in modifying the surface of inorganic hydrophilic fillers. The latter usually are calcium carbonate, silica, kaolin clay, talc, etc. The interaction between unmodified fillers and polymers is limited, and thus the mechanical improvement is limited as well. The modification can help to (according to [110]):

- modify surface characteristics, such as water repellence or hydrophobicity;
- improve the dispersion of the filler so that it would not agglomerate;
- control rheological properties – to allow higher loadings of the filler without an increase in viscosity;
- improve mechanical properties and high retention in adverse environments.

In addition to the physical properties, it is also possible to functionalise the surface so that the filler could participate in new chemical reactions. This modification can be achieved with functional silanes, such as those that contain thiol, acryl/methacryl, or amino groups. The coating can also participate in the polymerisation reaction with monomers and become an integral part of a polymer solid. In addition to polymer manufacturing, silane coupling agents are used to produce nanoparticles and sensors [110–113].

1.4.1. Synthesis of silane coupling agents

The synthesis of silane coupling agents can generally be separated into two stages: an inorganic precursor $SiHCl_3$ is produced in the first stage, and then it is functionalised in the second stage. The first stage can be separated into several steps: the first is the synthesis of a chlorosilane/silicon tetrachloride $SiCl_4$ precursor, and it can be carried out in several paths which differ regarding the source of silicon – it can be either silica or silicon itself [114,115]:

$$SiO_2 + C \rightarrow Si + CO_2; \quad (1.4)$$

$$Si + 2Cl_2 \rightarrow SiCl_4. \quad (1.5)$$

Next, $SiCl_4$ is hydrogenated:

$$3SiCl_4 + 2H_2 + Si \rightarrow 4SiHCl_3, \quad (1.6)$$

or

$$Si + 3HCl \rightarrow SiHCl_3 + H_2. \quad (1.7)$$

$SiHCl_3$ is the most popular precursor because it allows three hydrolysable and one functional group to form. Precursors SiH_2Cl_2 and SiH_3Cl, which are denoted by less prominent silane-silane interaction, are also available. The extreme case of SiH_4 (monosilane) would create a fully organic compound, while $SiCl_4$ would produce a fully hydrolysable silane; thus it is a precursor for orthosilicic acid [115,116].

The second stage of the synthesis starts with hydrosilylation and esterification reactions. It can be noted that the sequence of the two reactions is not important as both sequences will yield the same product. For the hydrosilylation, ω-unsaturated carbon chain alkanes are used. In case of further functionalisation of the chain, a halogen atom should be present at the opposite end of the chain. The reaction sequence – if the synthesis starts with hydrosilylation [110,114,117] – is as follows:

$$SiHCl_3 + R–CH=CH_2 \rightarrow R–(CH_2)_2–SiCl_3, \quad (1.8)$$

$$R–(CH_2)_2–SiCl_3 + 3R'–OH \rightarrow R–(CH_2)_2–Si(O–R')_3. \quad (1.9)$$

And *vice versa*:

$$SiHCl_3 + 3R'–OH \rightarrow HSi(O–R')_3, \quad (1.10)$$

$$HSi(O–R')_3 + R–CH=CH_2 \rightarrow R–(CH_2)_2–Si(O–R')_3. \quad (1.11)$$

The final product is a silicon compound with two types of ligands: the main organic group, which is attached with a stable covalent Si–C bond, and hydrolysable alcoxy groups which hydrolyse in contact with water. Hydrolysis results in the release of alcohols and the formation of active silanol groups –Si–OH which react with every other –OH group.

1.4.2. Hydrolysis of silane coupling agents

Silane coupling of fillers or surfaces starts with the hydrolysis of the agent. The interaction between the ≡Si–O–R groups and water results in the release of alcohols and the formation of the active silanol groups ≡Si–OH which react with every other –OH group. However, hydrolysis is a reverse reaction (reesterification), and, in addition, the silane silanol groups may react with each other (homocondensation) and produce silicones. Hydrolysis of the first alcoxygroup is the slowest, and it determines the total speed of the process [118–121]:

≡Si–O–R + H–O–H ⇄ ≡Si–O–H + R–O–H. (1.12)

In the meantime, other reactions are also taking place:

≡Si–O–H + H–O–Si≡ ⇄ ≡Si–O–Si≡ + H_2O, (1.13)

≡Si–O–H + R–O–Si≡ ⇄ ≡Si–O–Si≡ + H–O–R. (1.14)

The pH of the medium plays an important role in the hydrolysis reaction: the slowest rate is around the neutral values, while both the decrement and the increment increases the reaction speed due to the interaction H^+ OH^- with either Si or O atoms of the silane silanol groups, respectively [114,117].

With the elongation of the carbon chain of the alcohol molecules, its polarity and solubility in water decreases [122]. A similar effect is observable in the case of the alcoxy groups of the silane molecules: the longer is the chain, the slower is the hydrolysis reaction. This is caused by the repulsion of water molecules from the long hydrophobic carbon chain, thus preventing the water-silicon interaction and hydrolysis [114,123]. In most experiments, silanes with methoxy- and ethoxy groups are used [117].

The dependency of the polarity of the main organic group, which is connected via the Si–C bond, on the hydrolysis rate is the same as that of the alcoxygroups: the larger and less polar groups decrease the hydrolysis rate of the Si–O–C bond [124]. The experiments with silanes, which contained different amine functional groups, illustrate this dependency. It was determined that the hydrolysis rate of the silane molecules was ranked in the following sequence: primary (H_2N–R) > secondary (R–NH–R') > ternary (NR(R')(R")) [125,126].

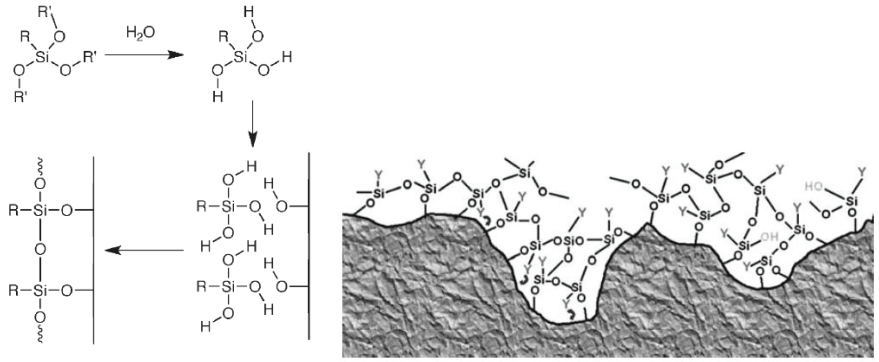
The induction effect influences the hydrolysis rate in several ways: the more electropositive groups (which tend to release electrons) hasten the reaction in acidic media. Meanwhile, the electronegative groups work in the opposite way – they increase the hydrolysis rate in the alkaline media [116, 127].

Water plays an important role in the hydrolysis of silane coupling agents. Most silane are not water-soluble, thus solvent-water mixtures are used in most cases. It was determined that the amount of water in the mixture should be limited because hydrolysis slows down as the solubility of silane decreases in such mixtures [128]. The influence of water is the strongest in acidic medium [129]. Water can be brought to silanes in several ways: the most common option is emulsion/solution; however, it also possible to use steam [130] and moisture [131]. In the case of dry conditions, traces of water can be brought from the condensation of other compounds, such as the reaction of chloroacetic acid and propanol [132].

1.4.2. The coupling of surfaces

The silane coupling of fillers and surfaces is based on the reaction between the silanol groups of silane and the hydroxyl groups of some other material (Fig. 1.5.). Thus, it is most convenient to modify the surfaces which contain a plentiful amount of –OH groups. The most suitable materials are amorphous hydrated silica, silicates (including glass), clays and similar compounds, hydroxides and oxides, or metals. Various insoluble salts, such as sulphates and carbonates, however, exhibit a weaker interaction with silane coupling agents. It should be noted that silane coupling agents can react with any hydroxyl groups, including organic molecules, such as polyalcohols and polysaccharides. Nevertheless, it is also possible to couple graphite, graphene, and soot [114].

Silane coupling starts when a silane silanol group ≡Si–OH forms a hydrogen bond with a hydroxyl group –OH of a surface. However, this bond is weak, and the silane molecule can migrate away. Afterward, the silane-material complex should be heated so that the condensation reaction could happen, and that a covalent bond between the silane and the surface could form (Fig. 1.5. a) [99,110,112,114].



a b

Fig. 1.5. Silane coupling: a – formation of a covalent bond between the silane molecule and the surface; b – schematic illustration of a modified surface [110]

The ideal silane coupling should produce a silane monolayer on the desired surface, but various irregular silane structures form due to homocondensation. The hydrolysis rate determines the size of the irregular structures – the faster the reaction happens, the earlier the molecules can interact with each other further from the surface. In such cases, the surface would be covered with various silane oligomers or polymers (silicones) – as shown in Fig. 1.5. b. It was observed that small oligomers provide better properties than single molecules, but the latter case is more favourable for even surfaces. Monoalcoxy- and monohalogensilanes may form silane dimers which further interact neither with the surface, nor with the other silanes. Therefore, they can be easily washed out [110,114,118].

1.5. Cuspidine

Cuspidine $Ca_4Si_2O_7F_2$ ($3CaO{\cdot}2SiO_2{\cdot}CaF_2$) belongs to a small group of calcium fluorosilicates together with kumtyubeite $Ca_5Si_2O_8F_2$ ($4CaO{\cdot}2SiO_2{\cdot}CaF_2$), fluorchegemite $Ca_7Si_3O_{12}F_2$ ($6CaO{\cdot}3SiO_2{\cdot}CaF_2$), and edgrewite $Ca_9Si_4O_{16}F_2$ ($8CaO{\cdot}4SiO_2{\cdot}CaF_2$) [133,134]. According to the chemical formula, cuspidine exhibits the lowest basicity in the group as its CaO/SiO_2 ratio is 1.5, while, for the others, it is 2, and, at the same time, it is the most fluorinated: the molar $CaF_2/(CaO+SiO_2)$ ratio is 1/5, while the ratios of the other members are 1/6, 1/9 and 1/12, respectively.

According to the structure which was investigated by several scientists [135,136], cuspidine is a sorosilicate-type silicate mineral due to paired silicate tetrahedra which form $[Si_2O_7]$ groups. In total, there are four types of calcium-centered polyhedra: $[CaO_5F_3]$, $[CaO_4F_3]$, $[CaO_5F]$ and $[CaO_6F]$, in which calcium ions exhibit multiple types of coordination: 6, 7, and 8. Together, these polyhedra form columns which are connected via the F^- and $[Si_2O_7]$ anions. The crystal lattice of cuspidine is monoclinic, the space group – P21/a, a = 1.0906 nm, b = 1.0521 nm and c = 0.7518 nm, β = 109.30°. Structurally, the most related minerals are tilleyite $Ca_5(Si_2O_7)(CO_3)_2$, låvenite $(Na,Ca)_2(Mn^{2+},Fe^{2+})(Zr,Ti)(Si_2O_7)(O,OH,F)_2$, and wöhlerite $NaCa_2(Zr,Nb)(Si_2O_7)(O,OH,F)_2$ [137].

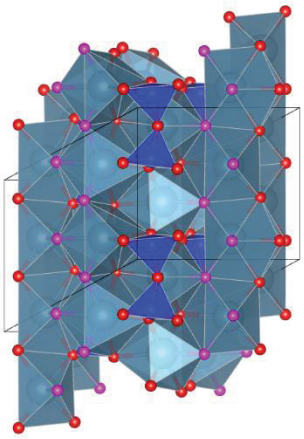


Fig. 1.6. Crystal lattice of cuspidine [136]

Naturally, cuspidine forms in the presence of volcanic activity under a low pressure and a high temperature via hydrothermal (metasomatic) transformation of skarn rocks, which contain carbonate and silicate minerals. Cuspidine, which is hosted in limestone, is found in the best-known finding location of natural cuspidine – *Monte Somma* caldera (Vesuvius volcano). A similar cuspidine-limestone composite is found in the *Upper Chegem* caldera [3,138]. Dolomite contact skarns host cuspidine in *Skye*, Scotland, UK [139].

In the industrial processes, cuspidine forms during continuous steel casting and in steel slag, and it plays an important role in metallurgy [133,138,140,141]. It was determined that the bandgap of cuspidine is ~5 eV, thus making the mineral a potent

luminescent material (phosphor) [142]. Subsequently, cuspidine was produced via solid-state sintering and was used as a carrier for rare-earth metals, such as cerium, europium, as well as manganese [142–146]. It was also determined that the dopant metal ions would replace Ca^{2+} ions. The produced phosphors showed the ability to emit various colours of light: Eu^{2+} – blue, Ce^{3+} – tuneable green-blue, Ce^{3+}/Mn^{2+} – tuneable cyan-near white-yellow, Ce^{3+}/Er^{3+} near-infrared, Eu^{2+}/Eu^{3+} – blue-red. However, the usual methods of synthesis require high temperatures of 1000–1300°C and various durations (0.5–15 h).

Earlier experiments showed that those anhydrous calcium silicates which have a similar or close CaO/SiO_2 ratio to that of cuspidine, such as kilchoanite $Ca_3Si_2O_7$ ($CaO/SiO_2 = 1.5$) or calcio-olivine γ-Ca_2SiO_4 ($CaO/SiO_2 = 2$), could be synthesised during hydrothermal treatment. Speakman *et al*. [147] observed a reaction where calcio-olivine, which was hydrothermally treated at 150–600°C, recrystallised into pavlovskyite $Ca_8Si_5O_{18}$ ($CaO/SiO_2 = 1.6$), and it later yielded kilchoanite. Mitsuda *et al*. [148] discovered that, in the mixture of lime and silicic acid, under hydrothermal treatment at 220–250°C, the initial product was γ-Ca_2SiO_4 which later recrystallised into kilchoanite and pavlovskyite $Ca_8Si_5O_{18}$.

***

To summarise the literature overview, it can be seen that wollastonite is a versatile compound. Thanks to the fibrous structure, wollastonite finds its application as a filler in concrete, plastics, paints, etc. Furthermore, this compound is under investigation as a bioactive component for bone regeneration, as well as a binding material that can be cured in carbon dioxide atmosphere. Although this mineral occurs naturally, but the different synthesis methods provide different mechanical and structural properties. Wollastonite can be produced by various methods. One of the most popular methods is solid-state sintering of calcium oxide and silicon dioxide at high temperatures. Another method is based on two-step synthesis: (1) hydrothermal synthesis of calcium silicate hydrate precursor; and (2) their calcination at relatively low temperatures (450–900°C). The two-step synthesis allows the use of various waste materials, such as silica gel from aluminium fluoride manufacturing, in the production of calcium silicates, which allows the reduction of the negative impact of solid waste on the environment. However, a specific material requires individual investigation for the application and the further properties of the product.

2. MATERIALS AND METHODS

2.1. Materials

The following materials were used:

1. AlF_3 production by-product – **silica gel waste** from chemical plant *JSC Lifosa* (Lithuania), dried at room temperature until constant mass for 2 weeks. The main elements were 39.86 mass% Si, 5.37 mass% Al (determined by using an X-ray fluorescence analyser *Bruker X-ray S8 Tiger WD* (Germany)), and 8.76 wt% F^- (determined potentiometrically by using a *Mettler Toledo* titrator *T 70* (USA) with an F− selective electrode). The main crystalline phases (Fig. 2.1. a) were gibbsite $Al(OH)_3$ (PDF No. 07-324), rosenbergite $AlF_3 \cdot 3H_2O$ (PDF No. 35-0827), and aluminium hydroxofluoride hydrate $Al_8(OH)_{12}F_{12} \cdot 3H_2O$ (PDF No. 74-0940) The silica gel waste was milled for 2.5 min at 950 rpm by using a planetary mill *Fritsch Pulverisette 9* (Germany) until specific surface area S_a = 1540 m^2/kg and density ρ = 2350 kg/m^3; the obtained particle size ranged from 0.05 to ~15 μm (Fig. 2.1. b). The STA results (Fig. 2.1. c) show two endothermal effects with mass losses: the first at 152°C, which corresponds with the dehydration of rosenbergite [149] as well as the dehydration of silica gel, and the second effect at 284°C corresponds to the dehydration of gibbsite [150].

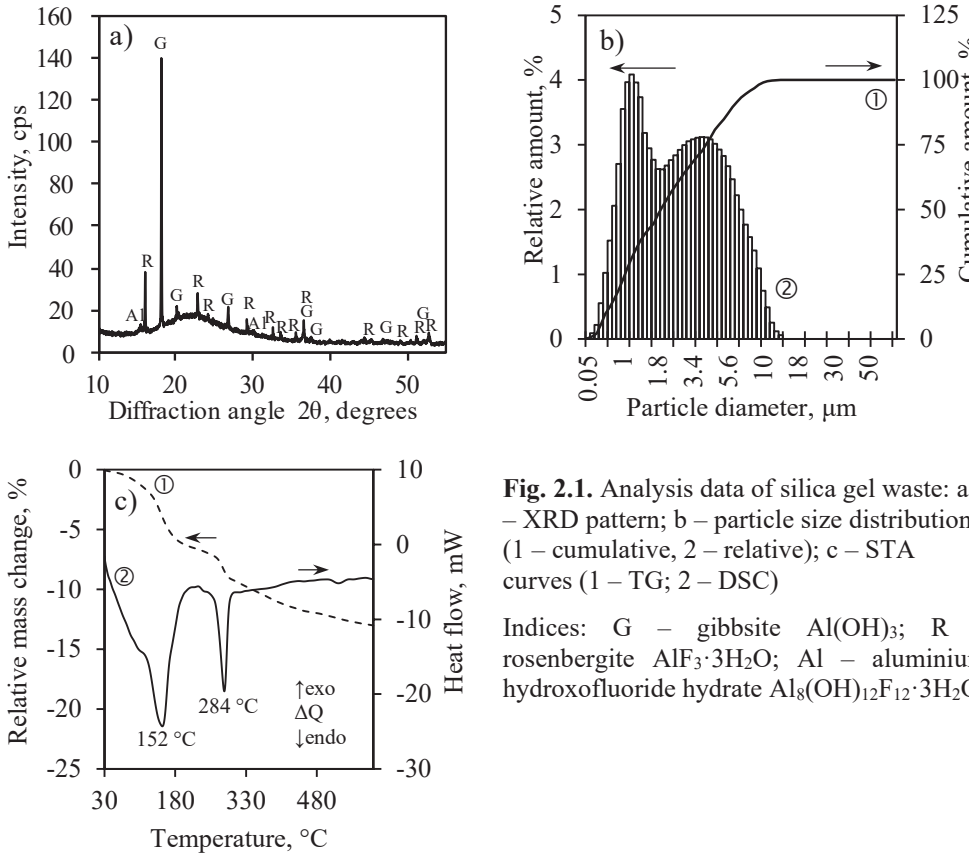


Fig. 2.1. Analysis data of silica gel waste: a – XRD pattern; b – particle size distribution (1 – cumulative, 2 – relative); c – STA curves (1 – TG; 2 – DSC)

Indices: G – gibbsite $Al(OH)_3$; R – rosenbergite $AlF_3 \cdot 3H_2O$; Al – aluminium hydroxofluoride hydrate $Al_8(OH)_{12}F_{12} \cdot 3H_2O$

2. **Calcium oxide, CaO**, was obtained by calcining calcium hydroxide (≥96%, *Honeywell*, Germany) at 550°C for 1 h and milling for 0.5 min at 950 rpm (S_a = 2076 m^2/kg, ρ = 2837 kg/m^3, free CaO – 94.22%). The only identified crystalline phase (Fig. 2.2. a) was lime CaO (PDF No. 04-0777). The obtained particle sizes ranged from 0.05 to ~50 μm (Fig. 2.2. b).

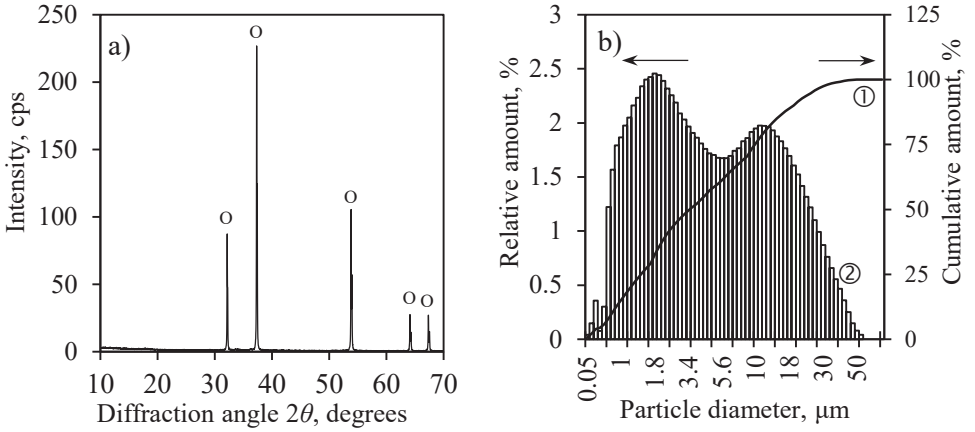


Fig. 2.2. Analysis data of calcium oxide: a – XRD pattern; b – particle size distribution (1 – cumulative, 2 – relative)
Indices: O – calcium oxide CaO

3. **Amorphous hydrated silica $SiO_2 \cdot nH_2O$** (*Reaktiv*, Russia); was ground at 950 rpm for 2.5 min, ρ = 2389 kg/m^3, S_a = 1425 m^2/kg, loss of ignition – 11.79 wt%. The XRD results (Fig. 2.3. a) showed that no crystalline phases were present in the amorphous silica. The obtained particle sizes ranged from 0.05 to ~50 μm (Fig. 2.3. b).

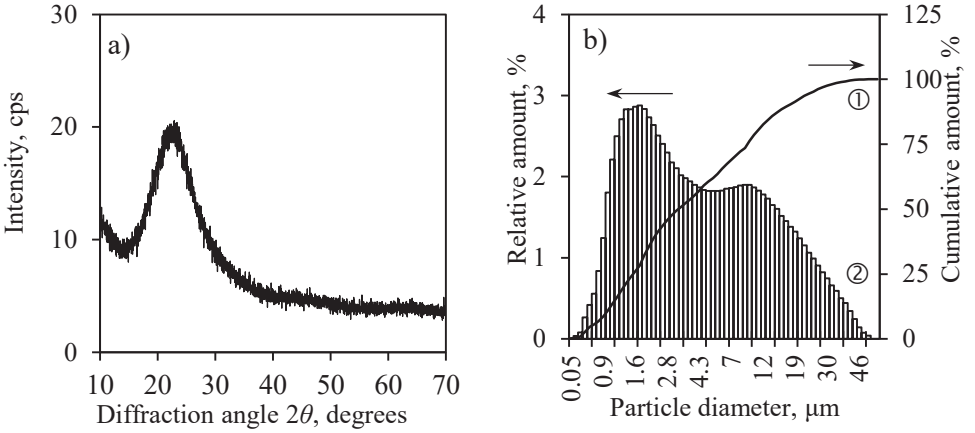


Fig. 2.3. Analysis data of amorphous hydrated silica: a – XRD pattern; b – particle size distribution (1 – cumulative; 2 – relative)

4. **Aluminium fluoride AlF_3** (*Lifosa*, Lithuania) was milled for 2.5 min at 850 rpm; ρ = 3065 kg/m^3, S_a = 2970 m^2/kg. It was determined that aluminium fluoride in the raw material existed in two crystalline forms (Fig. 2.4. a): óskarssonite (PDF No. 04-021-1079) and β-AlF_3 (01-084-1672). The obtained particle sizes ranged from 0.05 to ~80 μm (Fig. 2.4. b).

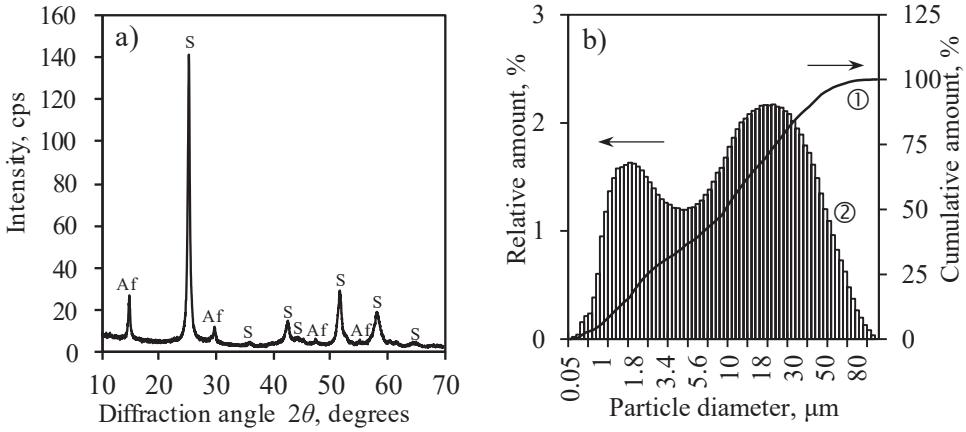


Fig. 2.4. Analysis data of aluminium fluoride: a – XRD pattern; b – particle size distribution (1 – cumulative; 2 – relative)
Indices: S – óskarssonite AlF_3, Af – β-AlF_3

5. **Calcium fluoride CaF_2** (99%, *Reaktiv*, Russia) was milled for 2.5 min at 850 rpm. Density – 3155 kg/m^3; the surface area was 2060 m^2/kg. Fluorite CaF_2 (PDF No. 00-035-0816) was the only crystalline compound in the raw material (Fig. 2.5. a). The obtained particle sizes ranged from 0.05 to ~80 μm (Fig. 2.5. b).

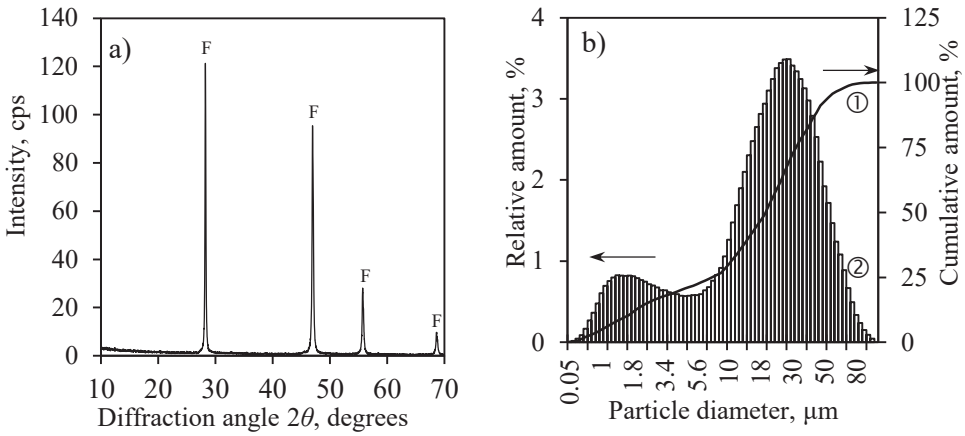


Fig. 2.5. Analysis data of calcium oxide: a – XRD pattern; b – particle size distribution (1 – cumulative; 2 – relative)
Indices: F – fluorite CaF_2

6. **CEN Standard sand** (*Normensand*, Germany). Its granulometric composition conforms to Standard DIN EN 196-1 (ISO 679) and is shown in Fig. 2.6.

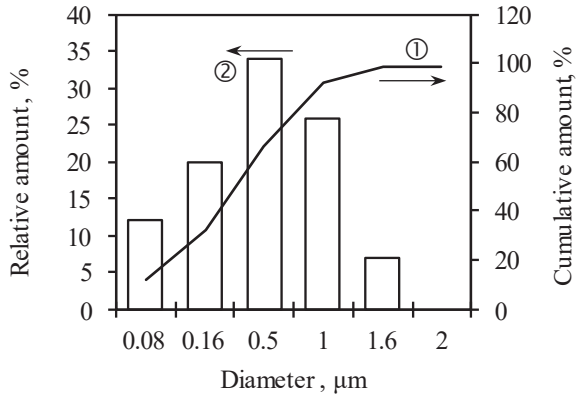


Fig. 2.6. Grain size distribution of sand according to EN 196-1: 1 – relative; 2 – cumulative

7. 3-(Acryloyloxy)propyltrimethoxysilane APTMS (94%, stab. with 100ppm BHT, *Alfa Aesar*, Germany;
8. Acrylated epoxidised soybean oil AESO (*Merck*, Germany);
9. Isobornyl methacrylate IBOMA (*Evonik Industries*, Germany);
10. Tetrahydrofurfuryl methacrylate THFMA (*Evonik Industries*, Germany);
11. Glycerol dimethacrylate, a mixture of isomers (90%, *Alfa Chemistry*, NY, USA;
12. Acrylic super-plasticiser for concrete *Dynamon XTend* (*Mapei*, Norway).

Other reagents:

1. Hydrochloric acid HCl (*Reachem Slovakia*, Slovakia), solution 1 mol/L,
2. Sodium fluoride NaF (*Reachem Slovakia*, Slovakia), solutions 1000 ppm (2.2105 g/L), 100 ppm (0.22105 g/L), 10 ppm (0.022105 g/L),
3. Sodium hydroxide NaOH (99%, *Reachem Slovakia*, Slovakia),
4. Potassium hydroxide KOH (85%, *Reachem Slovakia*, Slovakia),
5. Ammonium carbonate $(NH_4)_2CO_3$ (99%, *Riedel-de Haën*, Germany),
6. Acetic acid CH_3COOH (r.g., *Reachem Slovakia*, Slovakia)
7. Acetone (*Reachem Slovakia*, Slovakia),
8. Isopropanol (*Reachem Slovakia*, Slovakia),
9. Ethyl (2,4,6- thimethylbenzoyl) phenyl phosphinate TPOL (*Fluorochem*, United Kingdom.
10. Aerosil R972 (*Evonik*, Germany).

2.2. Methods

2.2.1. Synthesis

For the synthesis of wollastonite, three mixtures were prepared by using different raw materials:

1) A mixture of silica gel and calcium oxide with a molar ratio of CaO/(Al_2O_3+SiO_2+F^-) = 1 (48.49 wt% CaO, 42.18 wt% SiO_2, 5.01 wt% Al_2O_3, 4.32 wt% F^-).

2) A mixture of amorphous silicon dioxide, calcium oxide and aluminium fluoride with a molar ratio of CaO/(Al_2O_3+SiO_2+F^-) = 1 (48.71 wt% CaO, 43.10 wt% SiO_2, 3.87 wt% Al_2O_3, 4.32 wt% F^-).

3) A mixture of amorphous silicon dioxide and calcium oxide with a molar ratio of CaO/SiO_2 = 1 (48.28 wt% CaO, 51.72 wt% SiO_2).

For the synthesis of cuspidine, two mixtures were prepared by using different sources of silica:

1) A mixture of calcium oxide, amorphous hydrated silica and calcium fluoride with a molar ratio of CaO:SiO_2:CaF_2 = 3:2:1 (45.90 wt% CaO + 32.79 wt% SiO_2 + 21.31 wt% CaF_2).

2) A mixture of calcium oxide, silica gel waste and calcium fluoride with a molar ratio of CaO:(SiO_2 + Al_2O_3):(CaF_2+ F^-) = 3:2:1 (50.18 wt% CaO + 30.71 wt% SiO_2 + 2.69 wt% Al_2O_3 + 3.37 wt% F^- + 13.04 wt% CaF_2).

For the experiments of direct-state sintering, analogous mixtures with $CaCO_3$ instead of CaO were prepared.

The required amount of raw materials was weighted and homogenised in a *Turbula Type T2F* (Switzerland) at 49 rpm for 1 h. Subsequently, the obtained samples were mixed with distilled water to reach a suspension with a water-to-solid ratio 10 for the hydrothermal synthesis without stirring and 20 under stirring. The hydrothermal synthesis without stirring (at 200°C for 4–72 h) was carried out in 25 ml volume PTFE cells which were placed in a 1 L autoclave produced by *Parr Instruments* (Germany). The hydrothermal synthesis under stirring (100 rpm, at 95–200°C for 0–48 h) was carried out in a *Parr Instrument 4560* (USA) 600 mL autoclave, where hydrothermal synthesis was carried out in stirred suspensions. After synthesis, the suspension was filtered, and the products were rinsed with acetone (to reduce carbonation) and dried at 105 ± 0.3°C (the products which were synthesised at 95°C were dried at 80 ± 0.3°C) until constant mass.

The calcination of the hydrothermally obtained precursors and direct synthesis experiments was carried out in a high-temperature furnace *Nabertherm RT 50/250/11* (Germany) in the temperature range of 900–1100°C for 1 h, heating rate 10°C/min; the samples were cooled down naturally to room temperature.

Carbonation curing

The compressive strength test of the carbonation cured wollastonite-based binders was carried out according to modified Standard EN 196-1. The binder-sand (20, 25, 30 and 35 mass% of the binder) samples were mixed with water (water-to-binder ratio 0.35) pressed in a hydraulic press (*Test Form Mega 10 400 50*, Germany) by applying 10, 12.5, or 15 kN force. The dimensions of the cylindrical pressed samples were 36 × 36 mm. In addition, sand-free samples were formed to investigate the changes in the mineral composition during carbonation. The curing at the elevated carbon dioxide pressure was carried out at 15 bar and 45°C for 2–24 h in a *Parr Instruments* (USA) pressure reactor, model *4555*. After the curing, the compressive strength of the carbonated samples was determined by using a hydraulic press (*Test Form Mega 10 400 50*, Germany).

Production of composites

The composites were produced by using two synthetic fillers:

- W – $CaO\text{-}SiO_2 \cdot nH_2O\text{-}H_2O$ system (CaO/SiO_2 = 1); synthesised at 200°C for 12h under stirring and calcinated at 900 °C for 1 h;
- WS – CaO-silica gel waste-H_2O system ($CaO/(Al_2O_3+SiO_2+F^-)$ = 1); synthesised at 200°C for 12h under stirring and calcinated at 900°C for 1 h.

The functionalisation of synthetic calcium silicate fillers was carried out as follows. APTMS coupling agent (10 mass% of the unmodified filler weight) was added to distilled water which was acidified with acetic acid (0.1 mol/L) to reach a pH of 3–4 at 70°C. The coupling agent was left to hydrolyse for 30 min under stirring, and then the fillers were added to the solution to prepare a suspension where water to solid ratio by mass was 10. Functionalisation was carried out in stirred suspensions for 5 h at 70°C, and then the fillers were dried at 70°C until constant mass. The dried fillers were rinsed with isopropanol to remove weakly attached silane molecules and homocondensates of the silanes (silicones), and then dried again at 70°C until constant mass. In total, 2 modified fillers were produced.

Both initial and modified fillers were used to prepare composites. The resin consisted of acrylated epoxydised soybean oil AESO and a reactive solvent – either isobornyl methacrylate IBOMA or tetrahydrofurfuryl methacrylate THFMA at various ratios. The required amount of the photoinitiator TPOL was calculated from the total amount of both monomers and 3 mol.% of TPOL added to the resin. 5 mass% of the fillers was added to the resins and incorporated by using an *Ika T25* digital *Ultra Turrax* (Germany) disperser at a speed of 15000 rpm at room temperature for 2 min.

The resin-silicate composites were photo-crosslinked in a rectangular Teflon mould (70 × 10 × 1) ± 0.08 mm under the *Helios Italquartz* model *GR.E 500 W* lamp (Italy), intensity 310 mW/cm^2, at a gap of 15 cm for 5 min until solid polymer was formed.

Production of scaffolds

The scaffolds were produced by using four synthetic wollastonite-based fillers:

- W – $CaO\text{-}SiO_2 \cdot nH_2O\text{-}H_2O$ system (CaO/SiO_2 = 1); synthesised at 200°C for 12h under stirring and calcinated at 900°C for 1 h;
- WS – CaO-silica gel waste-H_2O system ($CaO/(Al_2O_3+SiO_2+F^-)$ = 1); synthesised at 200°C for 12h under stirring and calcinated at 900°C for 1 h;
- WD – CaO-defluorinated silica gel waste-H_2O system ($CaO/(Al_2O_3+SiO_2+F^-)$ = 1); synthesised at 200°C for 12h without stirring and calcinated at 900°C for 1 h.

The preparation of the resins consisted of two main steps. In the beginning, glycerol dimethacrylate was mixed with 0.1 wt% of *Aerosil R972* which was used as an anti-settling agent, and dispersed for 30 s until the mixture became homogeneous. At the second step, the photoinitiator and the precursor were added to the mixture, and the mixture was dispersed for 30 s. The composition of the suspensions is given in Table 2.1.

Table 2.1. Composition of the suspensions for DLP of scaffolds

Precursor	Precursor mass fraction	Amount of photoinitiator, mass% from monomer mass	Amount of anti-settling agent, mass% from the sum mass of precursor and monomer
-	-	0.415	-
W	0.125		0.1
WS	0.2		
WD			

Three composite materials with different wollastonite-based fillers were tested for layered optical 3D printing. An *Asiga PICO2 39 UV* optical 3D printer (Australia) was used for this experiment. 100 μm layer height was chosen for printing with an exposure time of 1 second per layer under 405 nm UV light. The first layer of 220 μm height was exposed for 6 seconds to ensure adhesion to the building platform. The chosen object to test was a woodpile-like structure consisting of 0.4x0.4 mm width and height logs arranged in the arrays with a spacing of 1.6 mm resulting in a 2 mm period. The arrays of the logs were rotated at a 60 degrees angle with respect to the previous array in order to have the internal architecture of the hexagonal arrangement. The external dimensions of the entire structure were 9.89x10.8x10 mm. 8 structures were printed per single procedure which took about 17 minutes. The structures were printed on the base plate of a thickness of 0.5 mm.

Composites with the fillers W and WS were printed without any concerns, and the manufactured objects were easily removed from the building platform and remained on the base plate. The composite with the filler WD was printed without any concerns; however, the woodpile structures had to be removed separately from

the base plate because the base plate was strongly attached to the building platform and brittle.

The printed scaffolds were placed on platinum plates and sintered at 1100, 1200, 1250 and 1300°C in a *Snol 30/1300* furnace (Lithuania) in air. The temperature increment rate was 100°C/h (1⅔°C/min), and the samples were isothermally kept at the target temperature for 3 h. After the process, the scaffolds were allowed to cool down inside the furnace naturally (approx. 8–10 h) [101,151].

2.2.2. Analysis

Determination of free CaO

~1 g of the analyte (CaO sample) was weighed (0.0001 g resolution) and placed into a 250 mL conical flask, poured with 150 mL of distilled water, and a magnetic stirrer was added. The slurry was heated and kept at a temperature just below boiling for 5 minutes. After that, the suspension was cooled down, the inner wall of the flask was washed with distilled water, and 2–3 drops of phenolphthalein indicator were added. Finally, the suspension was titrated with 1M HCl, until the pink colour disappeared. The amount of free CaO (X) in the sample was calculated by using the following Formula (2.1):

$$X = \frac{V \cdot c \cdot M}{n \cdot m} \cdot 100\% \quad (2.1)$$

where: V – volume of the consumed titrant (HCl), L; c – molar concentration of the titrant (HCl), mol/L; M – molar mass of the analyte, g/mol (M(CaO) = 56.08 g/mol); n – base/acid molar ratio in the neutralisation reaction (CaO/HCl = 2); m – mass of the analyte, g.

The analysis was carried out three times, and the average value was used.

Determination of the loss on ignition (LOI)

~10 g of the analyte (amorphous hydrated silica sample) was weighed by using an analytical balance (0.0001 g resolution) and placed into an annealed crucible. The material was calcinated to a constant weight at 1000°C for 1 h. The cooled crucible was weighed, and the loss on ignition was calculated according to Formula (2.2):

$$LOI = \frac{m - m_c}{m} \cdot 100\% \quad (2.2)$$

where: m is the initial mass of the sample, g; m_c is the mass of the sample after calcination, g.

The analysis was carried out three times, and the average value was used.

X-ray diffraction analysis (XRD)

It was performed on a *D8 Advance* diffractometer (*Bruker AXS*, Germany) operating at the tube voltage of 40 kV and the tube current of 40 mA. The X-ray beam was filtered with a Ni 0.02 mm filter to select the CuKα wavelength. The diffraction patterns were recorded in a *Bragg-Brentano* geometry by using a fast-counting detector *Bruker Lynx Eye* based on the silicon strip technology. The samples were scanned over the range of 2θ = 3–70° at a scanning speed of

0.1 degree/s by using the coupled two theta/theta scan type. *Diffrac.eva v4.3* software was used to identify the crystalline phases in the samples.

X-ray fluorescence spectroscopy (XRF)

The chemical composition analysis of the samples was performed by X-ray fluorescence spectroscopy (XRF) on a *Bruker X-ray S8 Tiger WD* spectrometer (Germany) equipped with a Rh tube with the energy of up to 60 keV. Powder samples were measured in Helium atmosphere, and the data was analysed with *SPECTRA Plus QUANT EXPRESS* standardless software.

Simultaneous thermal analysis (STA)

The simultaneous thermal analysis which consists of differential calorimetric analysis and thermogravimetry was carried out in a thermal analyser *Linseis STA PT-1000* (Germany). The flow of N_2 gas was 20 mL/min, at a heating rate of 10°C/min; the temperature ranged from RT up to 1000°C. Ceramic sample handlers and PT/10%Rh crucibles were used.

Differential scanning calorimetry (DSC)

Differential scanning calorimetry (DSC) and specific heat measurement was carried by using *Netzsch DSC 214 Polyma* (Germany). The heating rate was 5°C/min, the temperature ranged from 10°C up to 50°C; the flow of N_2 gas was 20 mL/min. Ceramic sample handlers and Al crucibles were used.

Dilatometry (DIL)

Linear thermal expansion analysis of the samples was performed with a *Linseis 75PT 1600* dilatometer (Germany) by using a corundum Al_2O_3 support tube. The temperature range was RT–1100°C, the heating rate was 10°C/min, N_2 flux was 20 mL/min. The powder samples were placed in a corundum sample holder.

Fourier transform infrared spectroscopy (FT-IR)

The FT-IR spectra of the samples were recorded with the help of a spectrometer *Perkin Elmer FT-IR* system *Spectrum X* (United Kingdom). The specimens were prepared by mixing 1 mg of the sample in 200 mg of KBr. The spectral analysis was performed in the range of 4000–400 cm^{-1} with a spectral resolution of 1 cm^{-1}.

The determination of particle size distribution

The particle size distribution of the materials was measured by using a laser particle size analyser CILAS 1090 LD with a sensitivity range from 0.04 μm to 500 μm. The dispersion phase was compressed air (2.5 bar), the distribution of solid particles in the air flow was 12–15%, and the measurement time was 15 s. The specific surface area S_A was calculated from the obtained measurement data.

Scanning electron microscopy (SEM)

The analysis was performed by using *Quanta 200 FEG* (*Fei*, The Netherlands) instrument at an accelerating voltage of 10 kV, and a working distance of 8.6 mm.

Specific surface area S_{BET} analysis

Nitrogen adsorption at 77 K was performed by using a surface area analyser *Autosorb iQ Station 1* (*Quantachrome Instruments*, USA). The specific surface area of the hydrothermal synthesis products was calculated by the BET Equation (2.3) using the data of the lower part of the N_2 adsorption isotherm ($0.05<\frac{p}{p_0}<0.35$):

$$\frac{1}{X\left(\frac{p_0}{p}-1\right)}=\frac{C-1}{X_m\cdot C}\cdot\frac{p}{p_0}+\frac{1}{X_m\cdot C} \tag{2.3}$$

where: X is the mass of the adsorbate adsorbed on the sample at a relative pressure $\frac{p}{p_0}$; p the partial pressure of the adsorbate; p_0 is the saturated vapour pressure of the adsorbate; X_m is the mass of the adsorbate adsorbed at a coverage of one monolayer; C is a constant which is a function of the heat of the adsorbate condensation and the heat of adsorption.

The BET equation yields a straight line when $\frac{1}{X\left(\frac{p_0}{p}-1\right)}$ is plotted versus $\frac{p}{p_0}$. The slope of $\frac{C-1}{X_m\cdot C}$ and the intercept of $\frac{1}{X_m\cdot C}$ were used to determine X_m and C: S=slope=$\frac{C-1}{X_m\cdot C}$ and I=intercept=$\frac{1}{X_m\cdot C}$. Solving for X_m yields $X_m=\frac{1}{S+I}$. The BET plot is usually found to be linear in the range of $\frac{p}{p_0}$ = 0.05–0.35. The total surface area of sample S_t was determined by the Equation $S_t=\frac{X_m\cdot N\cdot A_{CS}}{M}$, where: M is the molecular mass of the adsorbate; N is the Avogadro constant; A_{CS} is the cross-sectional area occupied by each nitrogen molecule ($16.2\cdot10^{-20}$ m^2). The specific surface area was obtained by the Equation $S_{BET}=\frac{S_t}{m}$, where: m is the mass of the synthesis product sample.

The total pore volume and the pore size distribution were calculated according to the corrected Kelvin equation and Orr *et al*.-developed scheme [152] using the entire N_2 desorption isotherm at 77 K. The Kelvin Equation (2.4) relates the adsorbate vapour pressure depression to the radius of a capillary which was filled with the adsorbate:

$$\ln\frac{p}{p_0}=-2\frac{\gamma\cdot V_m\cdot\cos\theta}{R\cdot T\cdot r_k} \tag{2.4}$$

where: p is the saturated vapour pressure in equilibrium with the adsorbate condensed in a capillary or a pore; p_0 is the normal adsorbate saturated vapour pressure; γ is the surface tension of nitrogen at its boiling point (γ = 8.85 ergs/cm^2 at (–195.8°C)); V_m is the molar volume of liquid nitrogen (V_m = 34.7 cm^3); θ is the wetting angle (usually taken as 0°; thus cos θ = 1); R is the ideal gas constant which is ($R = 8.134\cdot10^7\ \frac{\text{ergs}}{\text{deg}\cdot\text{mol}}$); T is the absolute temperature (in this case, T = 77 K); r_k is the Kelvin radius of a pore.

Determination of the viscosity of resins

The viscosity of the resins was measured by using a rotational *Fungilab SMART L* viscosimeter (Spain) with L2 geometry under 20 RPM at 25°C.

Determination of the mechanical properties of polymer composites

Dynamic mechanical thermal analysis (DMTA) was carried out with a *TA Instruments RSA-G2* (DE, USA) equipped with 3-point bending fixtures at a frequency of 1 Hz with a strain of 0.01% and an axial force of 0.1 N. The test was performed from 25°C to 200°C at a heating rate of 3°C/min. The mechanical properties of the synthesised polymer composites were determined with a tensile test followed by the ISO 527-3 Standard according to the procedure outlined in Ref. [153] with the use of *PWG50* grips.

Stereomicroscopy

The stereomicroscopy was carried out by using a *ZEISS SteRIO sicovery V12* microscope (Germany) with a *PlanApo S1.5x* main objective.

Statistical evaluation

All the described experiments were performed at least three times. The experimental results are calculated as a mean of at least three obtained values according to Formula (2.5):

$$\overline{X} = \frac{\sum_{i=1}^{N} X_i}{N} \tag{2.5}$$

here: $\overline{X}$ is the mean value; N is the number of samples; X_i is the result of a single sample.

The standard deviation was calculated according to Formula (2.6):

$$\sigma = \sqrt{\frac{\sum_{i=1}^{N} (\overline{X} - X_i)^2}{N-1}} \tag{2.6}$$

here: $\sum_{i=1}^{N} (\overline{X} - X_i)^2$ is the sum of the squares of deviation from the mean value of all samples.

To calculate the linear correlation of the obtained results, the linear equation was calculated by using the least squares method. The Pearson's linear correlation coefficient r was calculated according to the Formula (2.7):

$$r = \frac{n(\sum x \cdot y) - (\sum x) \cdot (\sum y)}{\sqrt{[n \sum x^2 - (\sum x)^2] \cdot [n \sum y^2 - (\sum y)^2]}} \tag{2.7}$$

here: x represents the values of the independent variable; y stands for the values of the dependant variable; n is the number of samples.

3. RESULTS AND DISCUSSION

3.1. Two-step Synthesis of Wollastonite in $CaO\text{-}SiO_2 \cdot nH_2O\text{-}H_2O$ System

In the first part of the work, the synthesis of wollastonite was carried out via two-step synthesis which consisted of hydrothermal synthesis and calcination. The former step was carried out either without stirring, or under stirring. In both cases, the obtained precursors were calcined in the temperature range of 900–1100°C for 1 h.

Hydrothermal synthesis

At the beginning of this work, experiments of hydrothermal synthesis in unstirred suspensions were performed in a system of pure calcium oxide and amorphous silica. 1.13 nm tobermorite $Ca_5Si_6O_{16}(OH)_2 \cdot 4H_2O$ (PDF No. 19-1364), xonotlite $Ca_6Si_6O_{18} \cdot H_2O$ (PDF No. 23-0125), and traces of gyrolite $Ca_4Si_6O_{16} \cdot 4H_2O$ (PDF No. 42-1452) were determined to form after 4 h of isothermal curing (Fig. 3.1. a). It is also possible for semi-crystalline C-S-H(I)/C-S-H(II) (PDF No. 03-0611) to form, but it is difficult to identify it in the XRD patterns because its peaks overlap with the peaks of other crystalline calcium silicate hydrates. It is worth noting that only the CaO/SiO_2 molar ratio of xonotlite directly corresponds to the molar ratio of the primary mixture ($CaO/SiO_2 = 1.0$). Meanwhile, the molar ratio of tobermorite is 0.83, and this value stands at 0.66 for gyrolite. The CaO/SiO_2 molar ratio of C-S-H(I)/(II) may vary from 0.83 to 1.30.

The mineralogical composition of the precursor was found to be unchanged when the duration of hydrothermal synthesis was prolonged to 48 h (Fig. 3.1 a). Similarly to another research [154], the main difference between the XRD patterns of the precursors was between 4 and 48 h is the increased intensity of the diffraction peaks of the synthetic crystalline compounds. According to the literature [155–157], tobermorite, gyrolite and C-S-H(I)/(II) are metastable in mixtures with $CaO/SiO_2 = 1.0$ and should recrystallise into a thermodynamically stable compound (xonotlite) after a long synthesis duration (> 72 h).

The STA results (Fig. 3.1 b) provided additional data to the XRD results. The first endothermic effect in the temperature range of 35–250°C can be attributed to the removal of adsorbed water and the partial dehydration of calcium silicate hydrates (Fig. 3.1 b). In addition, a shoulder-type endothermal effect at 200°C was identified in the 48 h sample which corresponds to the dehydration of tobermorite [158]. It should be noted that, when the synthesis was prolonged to 48 h, the enthalpy of the effect decreased due to the lower amount of semi-crystalline C-S-H(I)/(II). Furthermore, the DSC curves of the synthetic precursors showed an intensive exothermic effect at a temperature of 831–838°C, which is common to the recrystallisation of semi-crystalline C-S-H(I) into wollastonite [159]. The recrystallisation of gyrolite into wollastonite also incurs an exothermal effect, but it usually occurs at ~850°C. The effect was hard to observe due to the low amount of the compound. By prolonging the synthesis duration from 4 to 48 h, C-S-H(I) became metastable and recrystallised into other compounds and the enthalpy of the exothermal effect decreased from 83 to 58 J/g. An exothermic effect at 905°C was

visible in the DSC curve of 4 h sample, which, similarly to the previous effect, can be attributed to the recrystallisation of C-S-H(II) into wollastonite/larnite [159]. Furthermore, a small (1%) mass loss step without a thermal effect was observed the temperature range of 740–800°C, which is common to the dehydration of xonotlite [160]. In addition, a small endothermal effect at 447°C was detected in the 4 h sample, which is common to the dehydration of portlandite. However, the compound was not identified in the XRD pattern due to its small amount (~1.1 mass%). Traces of calcium carbonate could form during storage due to carbonation from air.

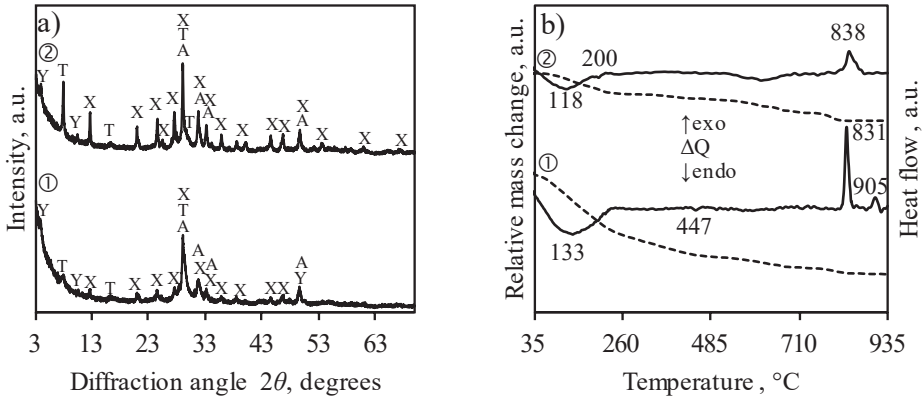


Fig. 3.1. XRD patterns (a) and STA (b) curves (solid line – DSC; dashed line – TG) of hydrothermal synthesis products obtained in $CaO\text{-}SiO_2 \cdot nH_2O\text{-}H_2O$ system at 200°C without stirring after: 1 – 4 h, and 2 – 48 h
Indices: T – 1.13 nm tobermorite; X – xonotlite; Y – gyrolite; and A – C-S-H(I)/(II)

Calcination

It was determined that all hydrothermally synthesised precursors recrystallised into wollastonite $CaSiO_3$ (PDF No. 42-0550) after calcination in the temperature range of 900–1100°C for 1 h. Although traces of semi-crystalline C-S-H(II) were identified in the 4 h sample, the compound reacted with other components, and, instead of recrystallising into larnite, it contributed to the formation of wollastonite. In addition, the duration (4–48 h) of hydrothermal synthesis was not determined to have a significant influence on the formation of the target compound during calcination (Fig. 3.2). As wollastonite was successfully produced via two-step synthesis, direct synthesis experiments of the initial mixture were performed in order to compare the obtained results.

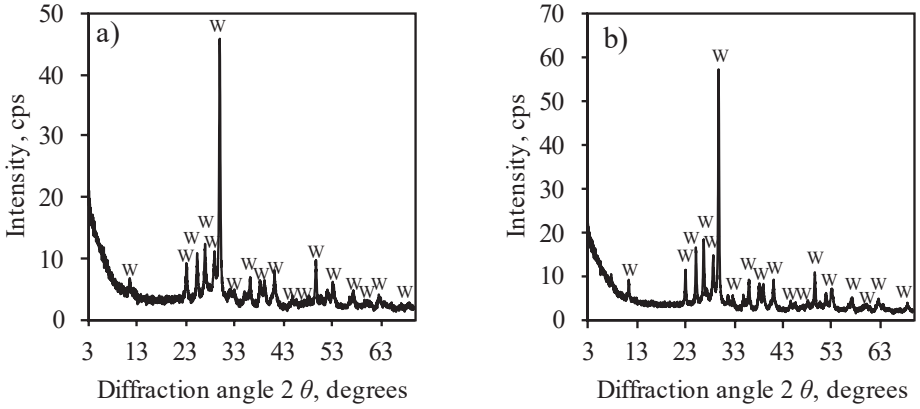


Fig. 3.2. XRD pattern of the synthesis products in $CaO\text{-}SiO_2 \cdot nH_2O\text{-}H_2O$ system without stirring for: a – 4 h; b – 48 h and calcined at 900°C for 1 h
Indices: W – wollastonite

It was observed that the composition of the precursor has a significant influence on the formation of wollastonite. During the direct synthesis at 900°C in the $CaO\text{-}SiO_2 \cdot nH_2O$ system (Fig. 3.3. a), only the formation of larnite was determined to start. This mineral exhibits a two times higher CaO/SiO_2 molar ratio than the initial mixture. The formation of wollastonite was observed at 1000°C where traces (notably, the intensity of the main peak (0.2976 nm) was 117 cps) of the target mineral were identified. A further increase in the temperature up to 1100°C slightly improved its formation (467 cps). Furthermore, lime was observed to not react completely in the entire temperature range. In addition, the recrystallisation of amorphous silica into quartz was observed, as outlined in Ref. [161] The intensity of the main peak (0.3346 nm) increased from 428 cps at 900°C to 2201 cps at 1100°C (Table 3.1).

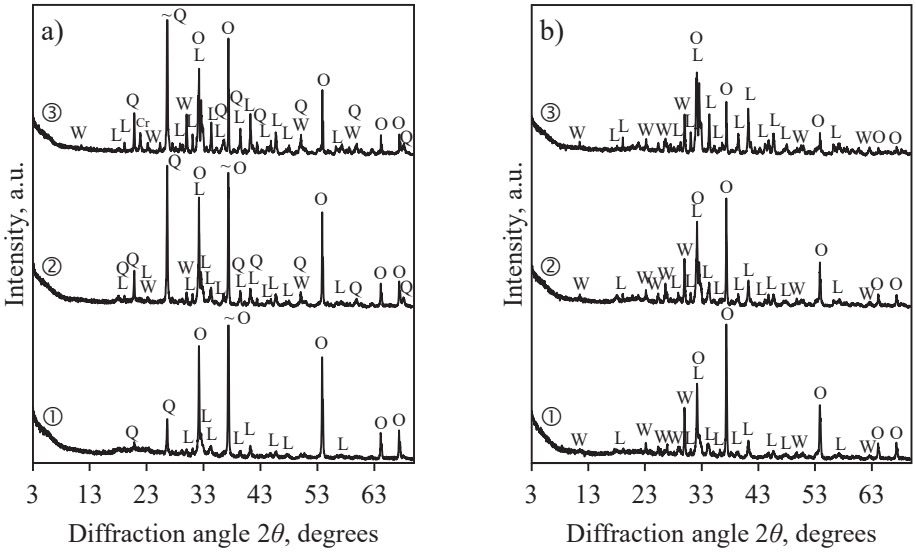


Fig. 3.3. XRD patterns of direct synthesis products after 1 h in: a – CaO-SiO_2·nH_2O system; b – $CaCO_3$- SiO_2·nH_2O system. Curves 1 – calcination at 900°C; 2 – at 1000°C; and 3 – at 1100°C

Indices: O – lime; Q – quartz; Cr – cristobalite; L – larnite; W – wollastonite

When calcium oxide was replaced with calcium carbonate for direct synthesis of wollastonite (Fig. 3.3 b), it was identified that the mineral began to form already at 900°C (560 cps, see Table 3.1), however, an increase of the temperature up to 1000–1100°C did not improve its formation. The decrement in the intensity could be caused by either insufficient activity, or by uneven distribution of SiO_2, which could allow wollastonite to react with lime rather than silica. Instead, an increase in the intensity of the larnite peaks was observed, but the intensity of the second main peak (0.2747 nm was selected because the main peak at 0.2782 nm overlapped with a CaO peak) was 245 cps at 900°C, 496 cps at 1000°C, and 845 cps at 1100°C (Table 3.1.). In addition, similarly to the system with CaO already in the initial mixture, here, lime was also identified in the products across the entire temperature range. However, the lime that forms during the decomposition of calcium carbonate during the sintering was more active than the lime which was already present in the initial mixture. Another research reports that prolonging the duration of direct synthesis up to 2 h should improve the formation of wollastonite [162].

Table 3.1. Intensity of the main peaks of lime, larnite, wollastonite, and quartz in the products of direct synthesis in CaO/$CaCO_3$-SiO_2·nH_2O systems

System	Temperature, °C	Intensity, cps			
		Lime	Larnite	Wollastonite	Quartz
		0.2406 nm	0.2747 nm	0.2976 nm	0.3346 nm
CaO-SiO_2·nH_2O	900	2896	231	0	428
	1000	2480	370	117	1699

	1100	1392	630	467	2201
$CaCO_3$-$SiO_2 \cdot nH_2O$	900	1628	245	560	0
	1000	1319	496	525	0
	1100	628	845	466	0

The summarised reactions of two-step synthesis in the CaO-$SiO_2 \cdot nH_2O$-H_2O system without stirring are given in the schemes below:

$$CaO+SiO_2 \cdot nH_2O+H_2O \xrightarrow{\text{Synthesis at 200°C, 4-48 h}} \begin{bmatrix} \text{C–S–H(I)} \\ \text{gyrolite} \\ \text{xonotlite} \\ \text{tobermorite} \end{bmatrix} \xrightarrow{\text{Calcination at 900-1100°C, 1 h}} [\text{wollastonite}.$$

The summarised reactions of direct synthesis in the CaO-$SiO_2 \cdot nH_2O$ and $CaCO_3$-$SiO_2 \cdot nH_2O$ systems in the temperature range of 900–1100°C are given in the schemes below:

$$CaO + SiO_2 \cdot nH_2O \xrightarrow{\text{sintering 900°C, 1 h}} \begin{bmatrix} \text{lime} \\ \text{larnite} \\ \text{quartz} \\ \text{amorphous silica} \end{bmatrix} \xrightarrow{\text{1000-1100°C, 1 h}} \begin{bmatrix} \text{lime} \\ \text{larnite} \\ \text{quartz} \\ \text{amorphous silica} \\ \text{wollastonite} \end{bmatrix};$$

$$CaCO_3 + SiO_2 \cdot nH_2O \xrightarrow{\text{sintering 900-1100°C, 1 h}} \begin{bmatrix} \text{wollastonite} \\ \text{lime} \\ \text{amorphous silica} \\ \text{larnite} \end{bmatrix}.$$

To sum up, it can be stated that the use of calcium silicate hydrate-based precursors allows wollastonite to form at 900°C without any initial or intermediate compounds. In the next part of this thesis, the hydrothermal synthesis was carried out under stirring to investigate whether the better interaction of the initial materials influenced the formation of the precursor and wollastonite. The literature suggests (see [7,31,162]) that a prolonged duration and an increased temperature of the direct synthesis should have a positive impact on the formation; however, this would increase the production cost and require a more advanced apparatus to withstand the conditions.

Hydrothermal synthesis of the precursors of wollastonite in stirred suspensions and their calcination

In this part of the work, hydrothermal synthesis experiments were performed under stirring. It was determined that, after 4 h of isothermal curing, C-S-H(I), 1.13 nm tobermorite and xonotlite were formed (Fig. 3.4. a). The mineralogical composition of the synthesised products was found to remain unchanged when the duration of hydrothermal synthesis was extended to 12 h and to 48 h (Fig. 3.4 a). Similarly to the synthesis without stirring, tobermorite should completely recrystallise into xonotlite after a longer duration of the synthesis (> 72 h). It should be noted that the obtained products did not contain gyrolite, as also noted in Ref. [163]. Therefore, stirred hydrothermal synthesis ensures better interaction between

the initial compounds and promotes the formation of calcium silicate hydrates which exhibit the CaO/SiO_2 molar ratio closer to the target value.

The XRD results were confirmed by the STA data. The first endothermic effect in the temperature range of 35–250°C can be attributed to the removal of adsorbed water and the partial dehydration of calcium silicate hydrates (Fig. 3.4. b). The results showed that the heat and the mass loss of this effect was significantly reduced by increasing the duration of hydrothermal synthesis. This indicates a decrease in the amount of more hydrated C-S-H(I)/(II) and physically bound water and an increase of less hydrated 1.13 nm tobermorite and xonotlite (Table 3.2). The second negligible thermal effect in the temperature range of 610–710°C corresponds to the decomposition of calcium carbonate (Fig. 3.4. b). The mass loss in the latter interval equals to 0.6–0.8 mass%, which is equivalent to ~1.5 mass% of calcium carbonate (Table 3.2). Due to the low amount of calcium carbonate, this compound was not detected in the XRD pattern. Furthermore, a small (1%) mass loss step without a thermal effect was observed the temperature range of 740–800°C which is common to the dehydration of xonotlite [160]. The DSC curves of the synthesised products obtained after 4 h of isothermal curing showed an intensive exothermic effect at a temperature of 833°C (Fig. 3.4. b and Table 3.2). According to the literature [158,160,164–166], xonotlite and tobermorite recrystallised to wollastonite without releasing heat (i.e. no exothermic effect is observed). The existence of this thermal effect indicated the occurrence of semi-crystalline calcium silicate hydrate (C-S-H(I)) in the synthesis products. In addition, a small exothermal effect at ~862–868°C indicated the presence of traces of another semicrystalline phase – C-S-H(II). At this temperature, the latter compound recrystallised into calcium silicates. It is worth emphasising that, due to the low crystallinity of the above-mentioned compounds, if other calcium silicate hydrates were present in the product, then, C-S-H(I)/(II) would be difficult to identify in the XRD patterns [154,167]. When prolonging the synthesis duration from 4 to 48 h, semicrystalline C-S-H(I)/(II) became metastable and recrystallised into other more crystalline synthesis products as the exothermic effect of heat reduction from 109 to 35 J/g (Table 3.2).

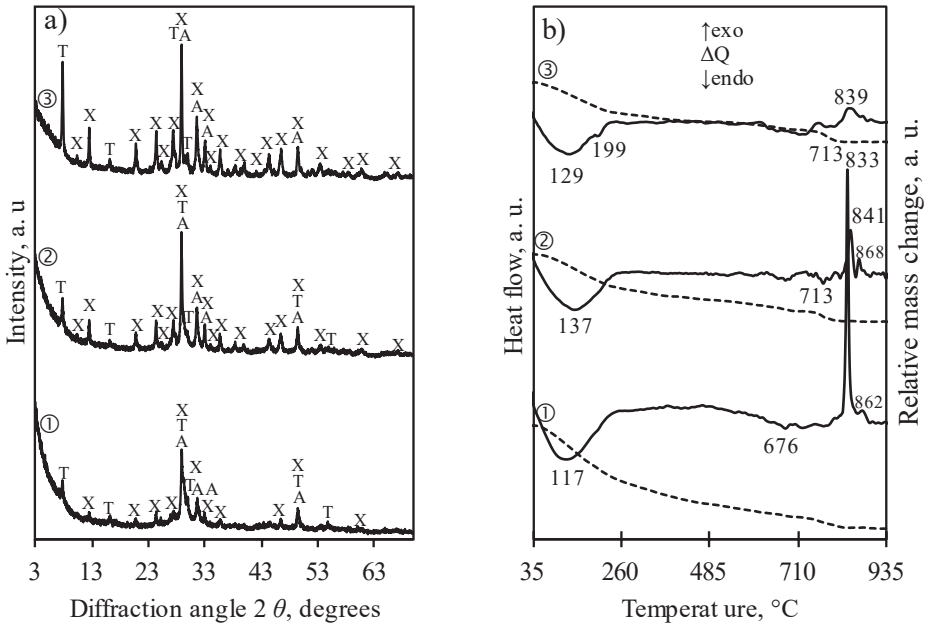


Fig. 3.4. XRD patterns (a) and STA (b) curves (solid line – DSC; dashed line – TG) of hydrothermal synthesis products obtained in $CaO\text{-}SiO_2 \cdot nH_2O\text{-}H_2O$ system under stirring: 1 – 4 h; 2 – 12 h; and 3 – 48 h
Indices: T – 1.13 nm tobermorite; X – xonotlite; A – C-S-H(I)/(II)

Table 3.2. Thermal characteristics of the synthesis products formed at different durations of hydrothermal synthesis in the $CaO\text{-}SiO_2 \cdot nH_2O\text{-}H_2O$ system at 200°C under stirring

Synthesis duration, h	Main characteristics of thermal effects		
	Temperature, °C	Enthalpy, J/g	Mass change, %
4 h	35–250	-254.69	-7.27
12 h		-233.23	-4.52
48 h		-165.64	-3.97
4 h	610–710	-	-
12 h		-15.72	-0.6
48 h		-19.2	-0.8
4 h	740–840	-	-0.86
12 h		-	-1.08
48 h		-	-1.19
4 h	840–880	109.52	~0
12 h		53.14	~0
48 h		35.66	~0

The FT-IR analysis (Fig. 3.5) provided additional information and confirmed the results of XRD and STA. A broad adsorption band in the range of 3100–3800 cm^{-1} and a peak at ~1640 cm^{-1} are common to vibration and deformation of the H–OH bond, which indicates the presence of water or the hydration of the synthetic samples. Small peaks in the range of 1450–1510 cm^{-1} are common to the bending vibration of C–O bonds in the CO_3^{2-} anions, which indicates carbonation and the presence of $CaCO_3$. A peak at ~1205 cm^{-1} is common to Si–O–Si symmetric stretching [168]. An intense peak at ~975 cm^{-1} is common to the asymmetric stretching vibration of O–Si–O bonds. A set of small peaks in the range of 670–450 cm^{-1} is common to the symmetrical vibration of Si–O–Si bonds and the deformational vibrations of O–Si–O bonds [169, 170]. A distinct peak at ~3612 cm^{-1} is common to the asymmetric vibrations of the covalent H–O (H–O^-Ca^{2+}) bond of xonotlite [171]. The appearance of the peak in the samples obtained within 12–48 h corresponds with the XRD patterns.

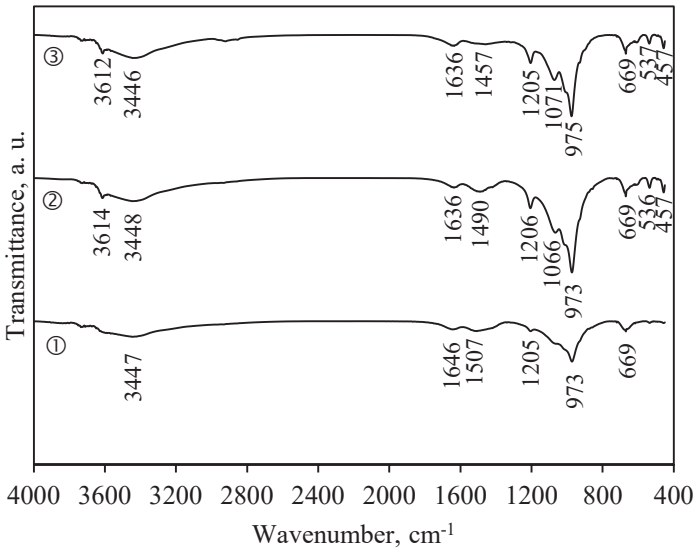


Fig. 3.5. FT-IR spectra of synthetic samples in $CaO\text{-}SiO_2 \cdot nH_2O\text{-}H_2O$ system at 200°C under stirring: 1 – 4 h; 2– 12 h; and 3 – 48 h

In order to fully describe the thermal behaviour of synthetic samples, dilatometric analysis was performed. The dilatometric curves of the samples obtained after 12 h of synthesis are given in Fig. 3.6, while the summary data of all investigated samples are given in Table 3.3. It was determined that all samples showed negligible shrinkage in the temperature range of 35–650°C (Table 3.3); however, at higher temperatures, the shrinkage depends on the duration of hydrothermal synthesis. The samples obtained after 4 h of synthesis showed the highest total shrinkage value (10.28%), which decreased to 4.52% and 1.2% by increasing the duration of hydrothermal synthesis to 12 h and 48 h, respectively. The

significant decrease in shrinkage can be explained by the decrease in the amount of C-S-H(I)/(II) in the synthesis products (Table 3.2).

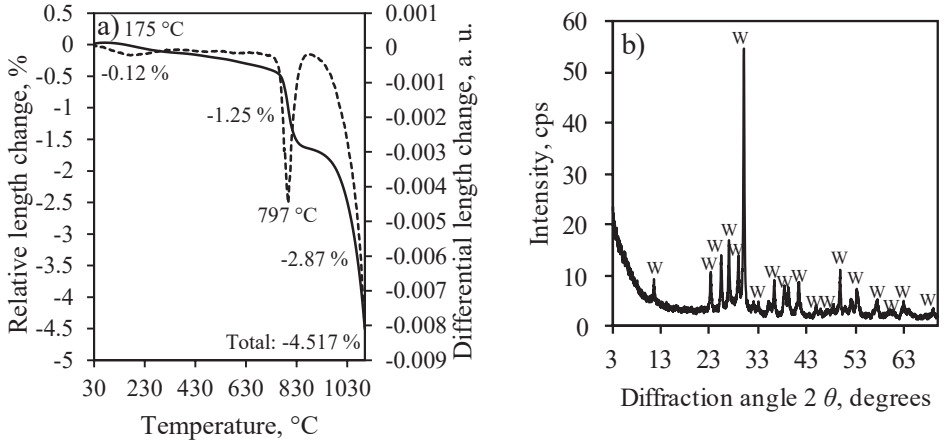


Fig. 3.6. Dilatometric analysis curves (a, solid line – relative length change; dashed line – differential length change) of the synthesis products obtained after 12 h of hydrothermal synthesis at 200°C under stirring; and b – XRD patterns of the synthesis product calcined (12 h) at a temperature of 900°C for 1 h in $CaO\text{-}SiO_2 \cdot nH_2O\text{-}H_2O$ system.
Indices: W – wollastonite

Table 3.3. Results of dilatometric analysis of synthesis products formed at different durations of hydrothermal synthesis at 200°C under stirring in $CaO\text{-}SiO_2 \cdot nH_2O\text{-}H_2O$ system

Synthesis duration, h	Temperature range, °C	Inflection point, °C	Shrinkage, %
4 h	78-323	207	0.79
	663-860	817	7.06
	941–(1100)	>1100	1.4
	Total:		10.28
12 h	76–319	175	0.12
	723–878	797	1.25
	878–(1100)	>1100	2.87
	Total:		4.52
48 h	90–345	241	0.14
	715–873	799	0.57
	873–(1100)	>1100	0.32
	Total:		1.2

The XRD pattern of the wollastonite sample obtained at 900°C is shown in Fig. 3.6 b. In addition, it was determined that neither the duration of hydrothermal synthesis, nor the calcination temperature had a significant influence on wollastonite formation during calcination of the hydrothermal synthesis products in the temperature range of 900–1100°C. The XRD analysis data showed that the main difference between the calcined products was the intensity of the diffraction peaks.

Therefore, in order to determine the specific surface area of synthetic and calcined samples, nitrogen gas adsorption was performed in combination with the Brunauer-Emmett-Teller (BET) equation. For the analysis, the samples obtained after 12 h of hydrothermal synthesis and after calcination at a temperature of 900°C were chosen.

The BET equation of synthetic and calcined samples yields a linear plot in the range of relative pressures $0.05 \leq p/p_0 \leq 0.35$ (Fig. 3.7). The correlation coefficient R^2 of the obtained lines was close to 1. According to the literature [172,173], the calculations of the specific surface area using the BET equation can be considered valid if the value of the C_{BET} constant is greater than 2 (in the ideal case, it is between 50 and 150). The calculations revealed that the values of the C_{BET} constant for synthetic and calcined samples are equal to 51.11 and 44.43, respectively, so that, in both cases, the knee of the isotherm is sharp, and the completion of monolayer formation is fairly well defined [172,174]. The specific surface area of the synthesis products obtained after 12 h of synthesis was calculated to be equal to 40.18 m^2/g, while the latter value decreased to 33.42 m^2/g during calcination at a temperature of 900°C.

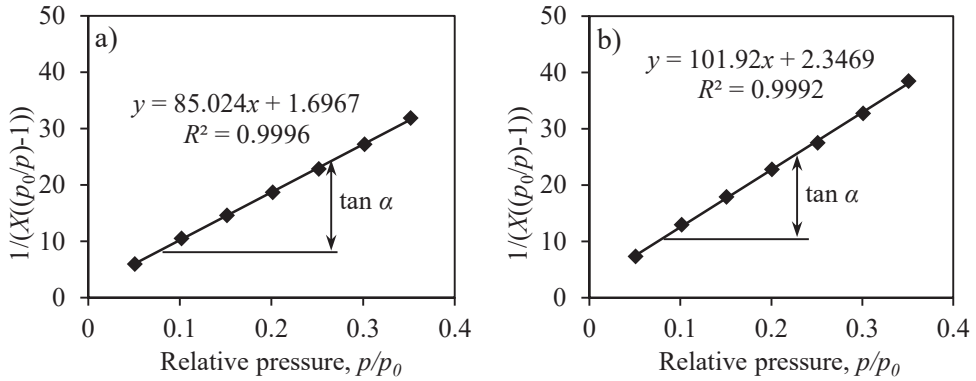


Fig. 3.7. Adsorption isotherm of N_2 in BET plots of synthetic (a) and calcined (b) samples of $CaO\text{-}SiO_2 \cdot nH_2O\text{-}H_2O$ system under stirring for 12 h

The nitrogen adsorption–desorption isotherms of both samples were determined to have no final saturation plateau, and can thus be classified as Type II [174] (Fig. 3.8). This type of the isotherm is typical of nonporous or macroporous adsorbents [174,175]. Moreover, the synthetic sample is characterised by a narrow hysteresis loop, i.e. the adsorption and desorption isotherms do not coincide (Fig. 3.8). According to the IUPAC classification [174], the hysteresis loop can be classified as Type H3, which indicates that some mesopores can be formed between the plate-like particles. It is worth highlighting that Type II adsorption isotherms can be described by the BET model.

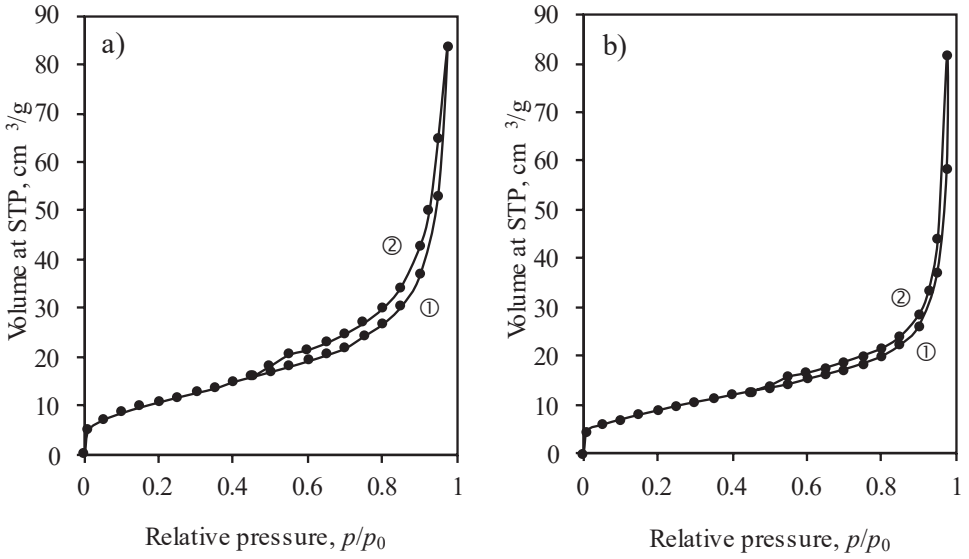


Fig. 3.8. Adsorption (1) and desorption (2) isotherms of N_2 for synthetic (a) and calcined (b) samples of $CaO\text{-}SiO_2 \cdot nH_2O\text{-}H_2O$ system under stirring for 12 h

The SEM images of the aforementioned samples (Fig. 3.9) confirmed the results which were obtained by dilatometry and BET analysis. It was observed that the fibrous and plate-like particles which are common to xonotlite and tobermorite (Fig. 3.9. a) underwent little to no changes and preserved the shape during calcination and recrystallisation into wollastonite at 900°C (Fig. 3.9. b).

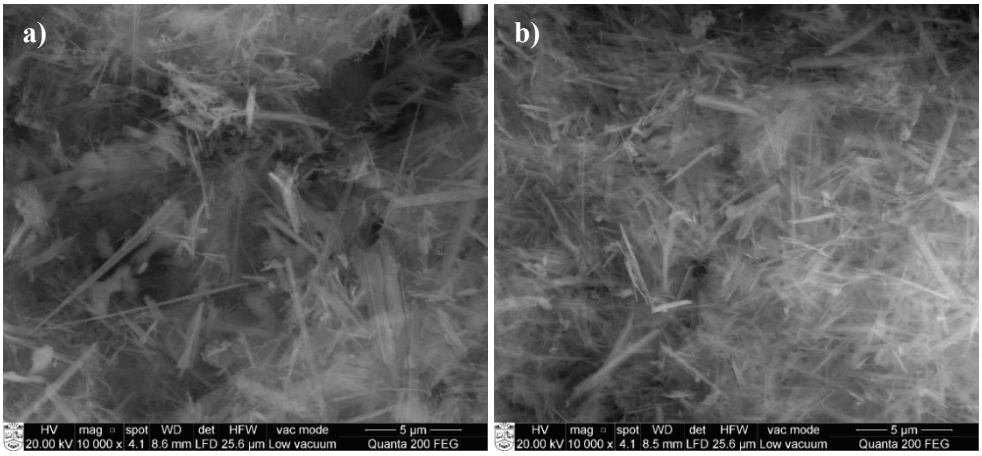


Fig. 3.9. SEM images of sample of $CaO\text{-}SiO_2 \cdot nH_2O\text{-}H_2O$ system: a – hydrothermally obtained (200°C, 12 h); and b – after calcination at 900°C for 1 h

By summarising the obtained results of hydrothermal synthesis and calcination, the formation of wollastonite and the intermediate phases in the $CaO\text{-}SiO_2 \cdot nH_2O$ mixture can be presented in the following order:

$$CaO+SiO_2\cdot nH_2O+H_2O \xrightarrow{\text{Synthesis at 200°C for 4-48 h}} \left[\begin{array}{c}\text{C–S–H(I)}\\ \text{xonotlite}\\ \text{tobermorite}\end{array}\right. \xrightarrow{\text{Calcination at 900-1100°C for 1 h}} [\text{wollastonite}.$$

When the precursor was synthesised at 200°C for 12 h under stirring, it consisted of xonotlite, tobermorite and C-S-H(I) (precursor X). Furthermore, the obtained material was mesoporous, and its specific surface area was 40.18 m^2/g. After the calcination of the precursor, it fully recrystallised into wollastonite which exhibited a specific surface area of 33.42 m^2/g, remained mesoporous and maintained the plate or fibre-like structure (sample W).

In the next part of this work, the silica gel waste containing 85.41 mass% SiO_2 with admixtures of F^- and Al^{3+} ions was used for the synthesis of wollastonite in a two-step process.

Acknowledgements:

Reprinted/Adapted by permission from *Elsevier Ltd*.: Ceramics International / Synthesis and characterisation of wollastonite with aluminium and fluoride ions / A. Gineika, T. Dambrauskas, K. Baltakys, 47(16):22900-22910. 2021 https://doi.org/10.1016/J.CERAMINT.2021.05.003

3.2. Two-step Synthesis of Wollastonite in the CaO-silica gel waste-H_2O System

An industrial waste, AlF_3 manufacturing by-product silica gel contains 75–80 mass% of SiO_2, which is amorphous (reactive). However, the fluorine-rich silica gel waste is usually stored in landfills, and fluorine compounds can dissolve in rainwater and leaks, and it pollutes the groundwater. To prevent the accumulation of industrial waste, the silica-gel waste should be investigated as a SiO_2 source for the synthesis of wollastonite.

Therefore, in the second part of the work, for the synthesis of wollastonite, reagent grade amorphous hydrated silica was replaced with silica gel waste containing Al^{3+} and F^- ions. The experiment was carried out as in the previous part of the work: via two-step synthesis which consisted of hydrothermal synthesis and calcination.

3.2.1. Hydrothermal synthesis of precursors in unstirred suspensions and calcination

It was determined that, at the beginning of hydrothermal treatment (4 h), the initial compounds containing F^- ions (rosenbergite and aluminium hydroxofluoride hydrate, Fig. 2.1 a) were unstable and decomposed. For this reason, in the synthesis products, cuspidine $Ca_4Si_2O_7F_2$ (PDF No. 76-0624) and katoite $Ca_3Al_2(SiO_2)_{0.5}(OH)_{10}$ (PDF No. 77-1713) were formed (Fig. 3.10. a). In addition, the small intensity diffraction peaks of 1.13 nm tobermorite $Ca_5Si_6O_{16}(OH)_2\cdot 4H_2O$ were also identified. The intensity of the peaks of the latter compound increased with an extension of the hydrothermal treatment up to 16 h and remained stable up

to 72 h. The formation of cuspidine during hydrothermal treatment is in good agreement with the data obtained by V. Rudelis *et al*. [176].

The previous results were confirmed by the STA data (Fig. 3.10. b). The first endothermic effect at ~191°C can be attributed to the removal of the adsorbed water and the dehydration of calcium silicate hydrates. Meanwhile, the small effect at a higher temperature (~ 340°C) corresponds to the decomposition of katoite [46]. Furthermore, the exothermic effect at ~835°C temperature can be assigned to a semi-crystalline type compound $0.83CaO{\cdot}SiO_2{\cdot}1.3H_2O$ (C-S-H(I)) recrystallisation to wollastonite [7,39]. It should be noted that it is difficult to identify (C-S-H(I)) in the XRD patterns because its diffraction maximums overlap with other calcium silicates hydrates.

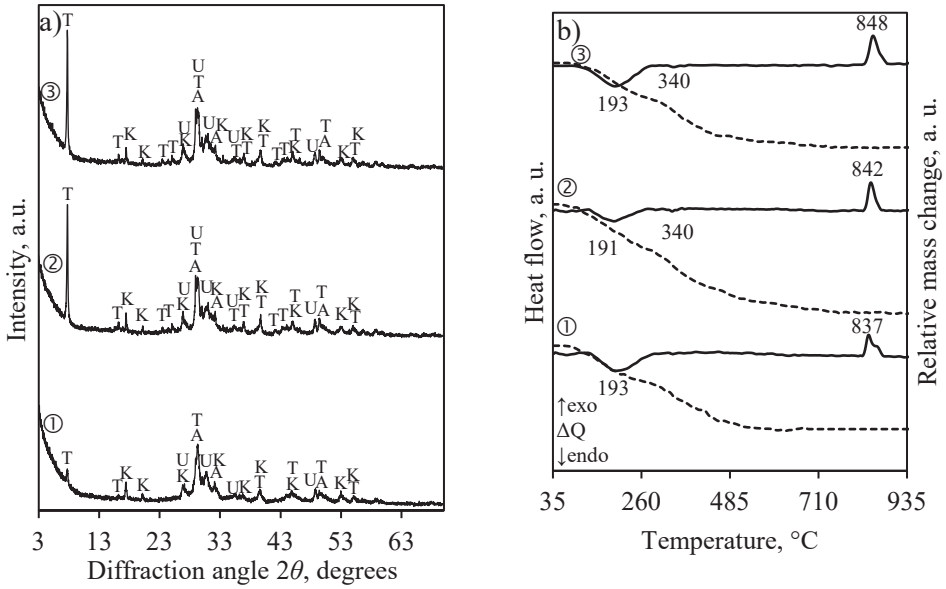


Fig. 3.10. XRD patterns (a) and STA curves (b) of hydrothermal synthesis (200°C, without stirring) products in the CaO-silica gel waste-H_2O system: 1 – 4 h; 2 – 16 h; 3 – 72 h. Indices: T – 1.13 nm tobermorite; K – katoite; U – cuspidine

In order to produce wollastonite, the synthesis products obtained after 72 h of synthesis were calcined within the 800–1100°C temperature range. This duration was chosen because 1.13 nm tobermorite formed after 72 h exhibited the highest crystal order.

It was determined that, after calcination at 800°C of the synthesis products obtained both after 4 and 72 h of hydrothermal treatment, cuspidine remained stable, while 1.13 nm tobermorite and katoite decomposed (Fig. 3.11). For this reason, fluormayenite was identified in the products; however, there is no evidence of the presence of wollastonite. The formation of fluormayenite instead of fluoride-free mayenite could be caused by the constant exposure and interaction with F^- ions in the system. The increase of the calcination temperature to 900°C positively affects the formation of wollastonite because the intense peaks of this compound were

identified in the XRD patterns (Fig. 3.11). When the calcination temperature was increased to 1100°C, the peak intensities of wollastonite and cuspidine doubled, which indicated the increased crystal order of the compounds. Furthermore, fluormayetine could no longer be identified. Instead, a new compound – gehlenite – was observed. Thus, it can be considered that fluormayenite reacted with silicate-based compounds of the system and formed a calcium alumosilicate mineral – gehlenite. It is possible that the traces of larnite could form the traces of C-S-H(II), which could form together with C-S-H(I), and which was overlapped by other silicate compounds in both the XRD and STA patterns.

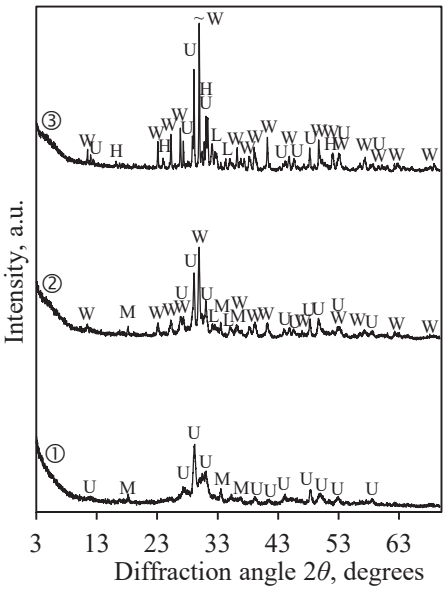


Fig. 3.11. XRD patterns after calcination at: 1 – 800°C; 2 – 900°C; 3 – 1100°C of synthetic precursors obtained after 72 h of isothermal treatment at 200°C
Indices: M – fluormayenite; U – cuspidine; W – wollastonite; H – gehlenite; L – larnite

By summarising the results, it can be stated that the characteristics of the raw materials affect the synthesis of wollastonite which occurs by the two-step method: hydrothermal treatment at 200°C for 4–72 h, and the calcination of the obtained products at 800–1100°C proceeded for 1 h. It is possible to assume that, when synthesising wollastonite by the above mentioned method, the formation of new compounds occurs in the following sequence:

$$\mathrm{CaO+Silica\ gel\ waste+H_2O} \xrightarrow{\text{hydrothermal synthesis, 4-72 h, 200 °C}} \begin{bmatrix}\text{1.13 nm tobermorite}\\ \text{C-S-H(I)/(II)}\\ \text{cuspidine}\\ \text{katotite}\end{bmatrix} \xrightarrow{\text{calcination 1h, 900 °C}} \begin{bmatrix}\text{wollastonite}\\ \text{cuspidine}\\ \text{fluormayenite}\\ \text{larnite (traces)}\end{bmatrix} \xrightarrow{\text{calcination 1h, 1100 °C}} \begin{bmatrix}\text{wollastonite}\\ \text{cuspidine}\\ \text{gehlenite}\\ \text{larnite (traces)}\end{bmatrix}.$$

Defluorinated silica gel waste

Silica gel waste usually contains 8–10% of fluoride ions, which greatly narrows the application of the waste material. Therefore, in order to reduce the formation of fluorinated compounds, such as cuspidine and fluormayenite, an additional experiment was conducted to defluorinate the silica gel waste and applied to synthesise wollastonite via two-step synthesis. The amount of F^- ions in the silica gel was reduced to less than 1% by the dynamic defluorination method [177].

It was determined that, after leaching, the waste material contained aluminium hydroxide and aluminium hydroxofluoride hydrate (Fig. 3.12. a). The STA results provided additional data about the material: an endothermal effect at 115°C is common to the dehydration of hydrated silica, and the endothermal effect at 272°C is common to the decomposition of gibbsite into alumina and water (Fig. 3.12 b). However, no distinct thermal effects that can be attributed to dehydration or decomposition of aluminium hydroxofluoride hydrate were identified, or else the effects overlapped with the dehydration of the silica.

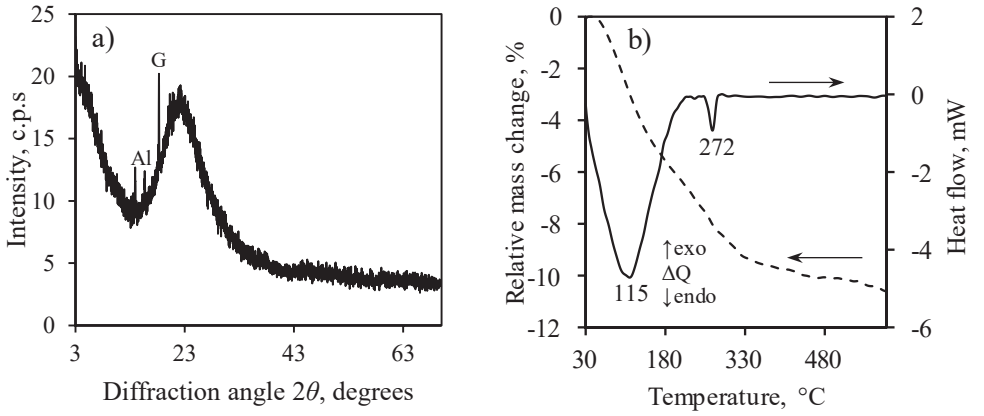


Fig. 3.12. Analysis curves of defluorinated silica gel waste: a – XRD pattern; b – STA curves of the raw material: 1 – TG; 2 – DSC
Indices: G – gibbsite; Al – aluminium hydroxofluoride hydrate

The hydrothermally prepared precursor in the CaO-defluorinated silica gel waste-H_2O mixture was determined to contain 1.13 nm tobermorite, katoite, cuspidine, C-S-H(I), and traces of calcite. In contrast to the precursors described above, the intensity and the area of the main tobermorite peak were three times smaller. The STA results were in good agreement with the XRD data. The peak of the first endothermal effect was at 123°C, and no additional endothermal effect at 200°C was identified, which indicates that C-S-H(I) dominated in the products while only a low amount of tobermorite was present in the product. The endothermal effect at 336°C is common to the decomposition of katoite, and the endothermal effect at 667°C is commonly manifested by calcite. The exothermal effect at 822°C is common to the formation of wollastonite from semi-crystalline C-S-H(I). The

high intensity and enthalpy (105 J/g) confirmed the dominance of the latter compound in the precursor.

It was determined that wollastonite was the main product after the calcination of the precursor which was obtained in the CaO-defluorinated silica gel waste-H_2O system (Fig. 3.13 a). Although katoite and calcite yield calcium oxide during their decomposition [178], the latter compound was not identified in the calcination products due to its interaction with the other components in the system. In addition to the release of calcium oxide, katoite tends to recrystallise into mayenite $Ca_{12}Al_{14}O_{33}$. However, the latter compound was not identified in the XRD pattern, and therefore it can be suggested that Al^{3+} ions – due to their low amount – intercalated into other phases instead of forming a separate one. Furthermore, the calcination revealed that a part of F^- ions did not intercalate into the silicate structure and formed a separate phase – fluorite CaF_2. The latter compound could form from the released calcium oxide and F^- ions. Cuspidine, a calcium fluorosilicate, which was identified in the precursor, remained stable.

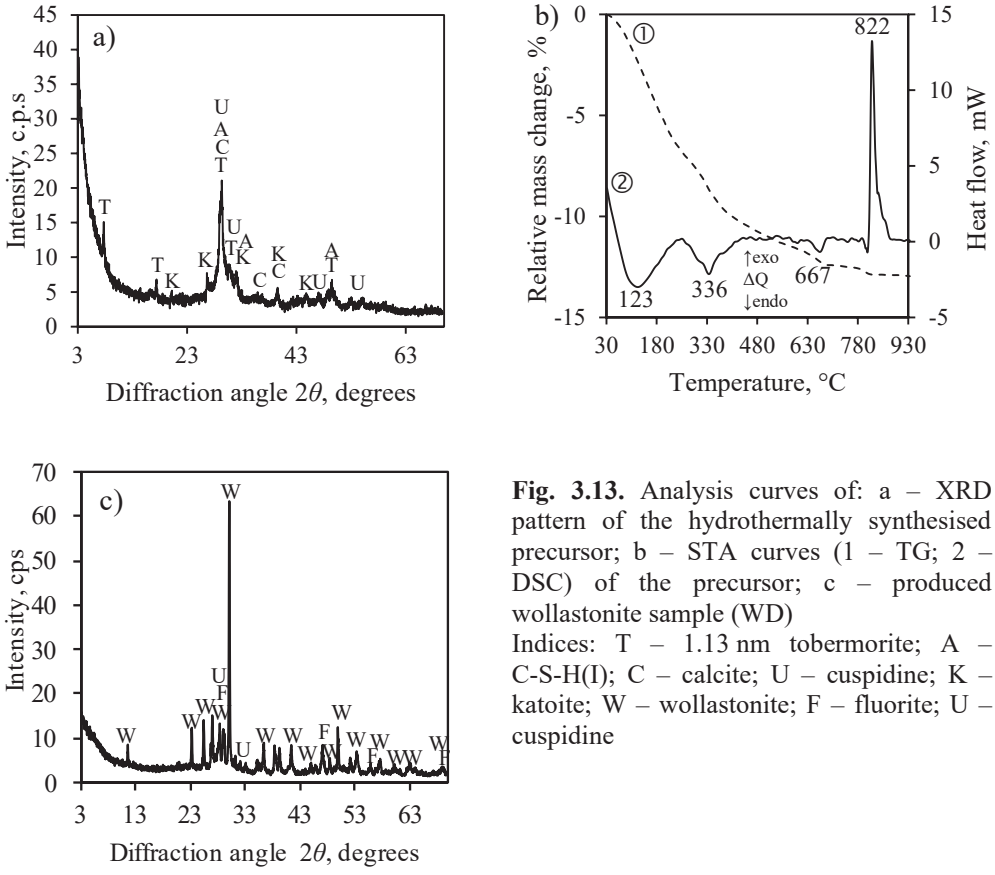


Fig. 3.13. Analysis curves of: a – XRD pattern of the hydrothermally synthesised precursor; b – STA curves (1 – TG; 2 – DSC) of the precursor; c – produced wollastonite sample (WD)
Indices: T – 1.13 nm tobermorite; A – C-S-H(I); C – calcite; U – cuspidine; K – katoite; W – wollastonite; F – fluorite; U – cuspidine

The produced samples XD and WD were applied in the production of white concrete tiles in *JSC Inhus Prefab* (see Appendix No. 1): the synthetic materials replaced the usual microfillers in the standard cement blends, and four types of tiles

were produced: 1 – White A, 2 – White A+, 3 – XD, and 4 – WD (Fig. 3.14). The concrete contained 8 mass% of microfiller additive.



Fig. 3.14. White concrete tiles (with 8 mass% of additive): 1 – White A; 2 – White A+; 3 – XD; 4 – WD

It was determined that the tiles *White A* exhibited the highest compressive strength of ~81 MPa after 28 days, meanwhile, the strength of *White A+* was 10% lower. The tiles with the WD additive exhibited ~17% lower compressive strength than *White A* at ~71 MPa, but this value was ~15% higher than the tiles with the XD additive (Fig. 3.15).

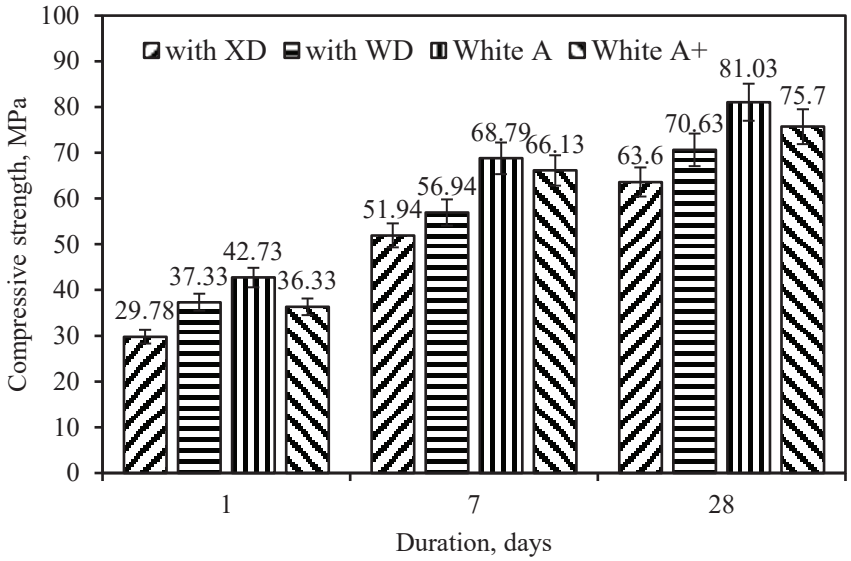


Fig. 3.15. Compressive strength of white concrete tiles

It was determined that the lowest amount of carbon dioxide was bound by the samples which were hardened under water – only 0.87–0.95%. A somewhat higher amount was adsorbed during hardening in air, specifically, 0.92–0.97%. When the samples were placed under 0.8 bar CO_2 pressure, the amount of bound carbon

dioxide was ~1.6%. Under these conditions, no distinct differences among the samples were observed (Fig. 3.16).

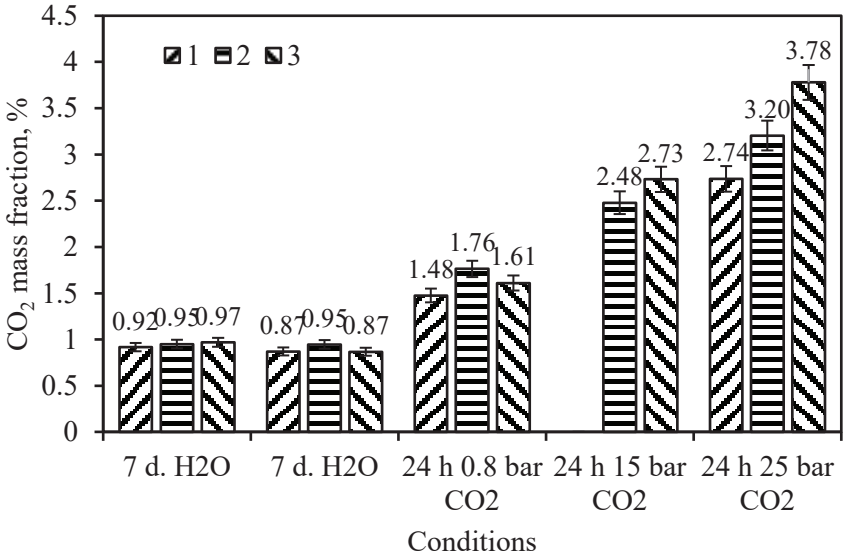


Fig. 3.16. Amount of carbon dioxide adsorbed by concrete samples under different conditions: 1 – white cement, sand, and water; 2 – white cement, sand and water with plasticiser (1%); 3 – white cement with 10 mass% WD additive, sand and water with plasticiser (1%)

After hardening under 25 bar CO_2, the WD sample adsorbed ~3.8% carbon dioxide, which was 38% more than the white concrete without additives (Fig. 3.16).

3.2.2. Direct (single-step) synthesis of the initial mixture

The interaction between the components in the initial CaO-silica gel waste mixture (Fig. 3.17 a) was determined to be low at 900°C because the main new compound was fluorite CaF_2, which is a product of the CaO-F^- interaction. Furthermore, the intense peaks of CaO (975 cps, Table 3.4) were still observable. Several silicate-based materials, which have a CaO/SiO_2 ratio of 2, did also form: larnite Ca_2SiO_4 and kumtyubeite $Ca_5Si_2O_8F_2$. In addition, it was noted that aluminium ions also reacted and promoted the formation of fluormayenite $Ca_{12}Al_{14}O_{32}F_2$. The increase in the temperature of up to 1000°C improved the CaO reactivity as the intensity of its peaks decreased by more than two times (403 cps), while the peaks of larnite increased. Furthermore, at this temperature, kumtyubeite was no longer identified, and the peaks of fluorite were less intense as well. The increase in the temperature to 1100°C also showed a positive impact on the formation of silicate materials and was favourable for the crystallisation of wollastonite $CaSiO_3$. Furthermore, cuspidine $Ca_4Si_2O_7F_2$, a compound related to kumtyubeite, was also identified, but it had a lower CaO/SiO_2 ratio (1.5).

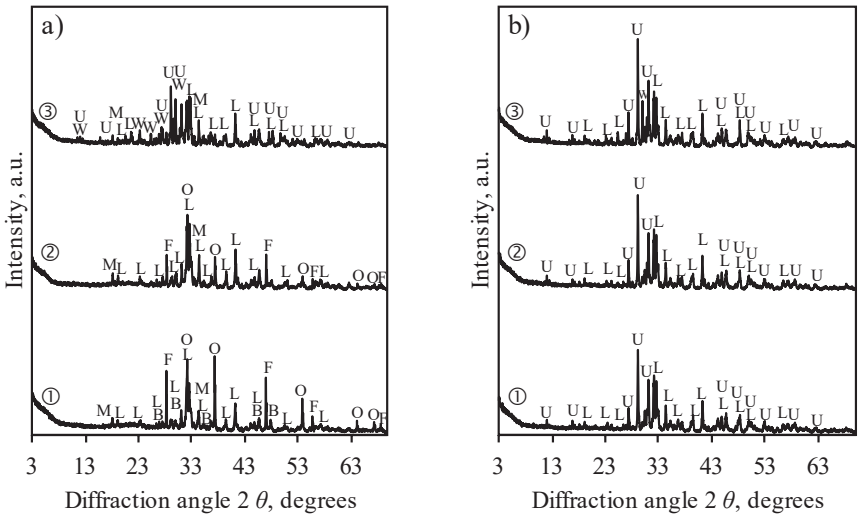


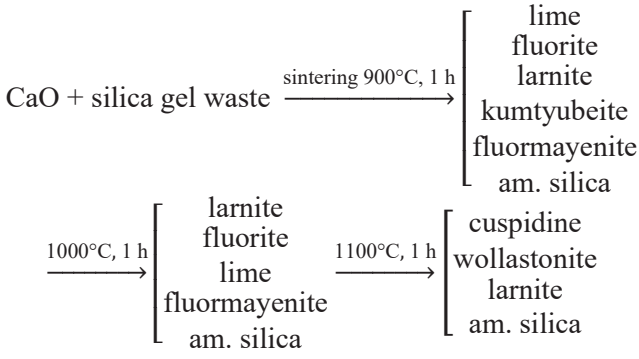
Fig. 3.17. XRD patterns of direct synthesis products: a – CaO-silica gel waste system; b – $CaCO_3$-silica gel waste system: 1 – 900°C; 2 – 1000°C; 3 – 1100°C
Indices: O – lime; F – fluorite; L – larnite; B – kumtyubeite; U – cuspidine; W – wollastonite

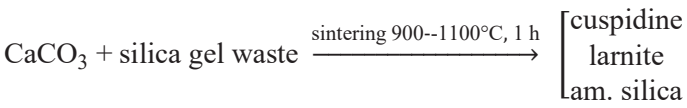
It was determined that the reaction between calcium oxide, which originated from calcium carbonate, and silica gel waste proceeds in a different way (Fig. 3.17 b) compared to the previous system. At 900°C, only silicate materials – larnite and cuspidine – were identified without fluorite and lime (Table 3.4). Additionally, no compounds containing aluminium ions, such as fluormayenite, were identified. This composition did not differ up to 1100°C. In addition, it should be noted that, in this and previous systems, the intensity of the peaks of larnite was lower after sintering at 1100°C than after 1000°C, which may indicate its meta-stability and recrystallisation into other minerals, such as wollastonite and cuspidine, due to the fluxing properties of F^- and Al^{3+} ions.

Table 3.4. Intensity of representative peaks of lime, larnite, wollastonite, cuspidine and fluorite in the products of direct synthesis in CaO-silica gel waste system

System	Temperature, °C	Intensity, cps				
		Lime	Larnite	Wollastonite	Cuspidine	Fluorite
		0.2406 nm	0.2747 nm	0.2976 nm	0.3066 nm	0.3149 nm
CaO-silica gel waste	900	975	585	0	0	760
	1000	403	818	0	107	389
	1100	0	634	578	765	139
$CaCO_3$-silica gel waste	900	0	639	0	1065	0
	1000	0	684	0	1210	0
	1100	0	608	557	1390	0

The summarised reactions of direct synthesis in the CaO-silica gel waste and $CaCO_3$-silica gel waste systems in the temperature range of 900–1100°C are given in the schemes below:





To summarise on the direct synthesis of wollastonite in the CaO-silica gel waste and $CaCO_3$-silica gel waste systems, it can be stated that the admixtures, which were present in the silica gel waste, improved the interaction between calcium oxide and the other initial compounds. However, the formed crystalline phases exhibited a higher CaO/SiO_2 molar ratio than the target compound, thus proving the necessity of a hydrothermally synthesised precursor.

3.2.3. Hydrothermal synthesis of precursors of wollastonite in stirred suspensions and calcination

The chemical composition of the primary mixture has been determined to exert a significant influence on the formation of calcium silicate hydrates under hydrothermal conditions at 200°C temperature. The X-ray diffraction analysis results show that, after 4 h of hydrothermal synthesis at a temperature of 200°C, all the primary compounds (portlandite $Ca(OH)_2$, rosenbergite $AlF_3 \cdot 3H_2O$, and gibbsite $Al(OH)_3$) were already present in the mixture of the silica gel waste and calcium oxide, thereby reacting to form two crystalline phases: 1.13 nm tobermorite and cuspidine $Ca_4Si_2O_7F_2$, which are formed in the synthesis products (Fig. 3.18. a). Similarly, under these conditions of synthesis, traces of katoite $Ca_3Al_2(SiO_2)_{0.5}(OH)_{10}$ were identified. It should be noted that, in a mixture of pure silicon dioxide and calcium oxide, only 1.13 nm tobermorite and xonotlite were formed under all experimental conditions (Fig. 3.4. a). By prolonging the duration of the synthesis to 24 h and 48 h, the composition of the synthesis products remained unchanged, despite being characterised by an increase in the intensity of the main diffraction peaks of tobermorite and a decrease in that of katoite. It is worth highlighting that there is no evidence of the formation of new aluminium-containing compounds (Fig. 3.18 a). Thus, it can be said that, by prolonging the synthesis

duration, katoite becomes metastable and starts to recrystalise into other products of synthesis.

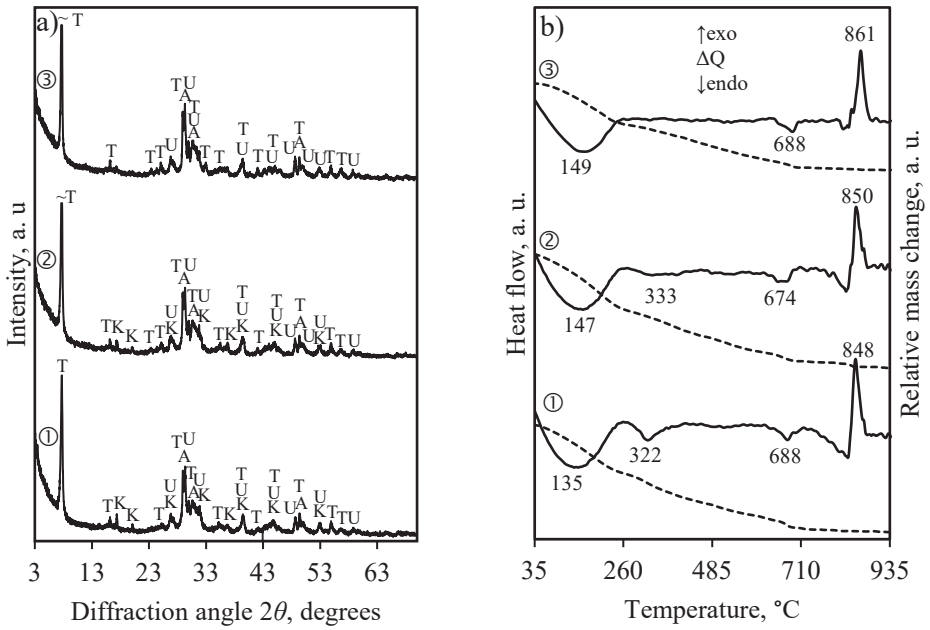


Fig. 3.18. XRD patterns (a) and STA (b) curves (solid line – DSC; dashed line – TG) of the hydrothermal synthesis products obtained in CaO-silica gel waste-H_2O system after: 1 – 4 h; 2 – 12 h; 3 – 48 h

Indices: T – 1.13 nm tobermorite; A – C-S-H(I); K – katoite; U – cuspidine

The XRD results were confirmed by the STA data (Fig. 3.18 b and Table 3). As in the previous case, the first endothermic effect, which can be attributed to the removal of the adsorbed water and the partial dehydration of semicrystalline calcium silicate hydrates and tobermorite. By increasing the duration of the hydrothermal synthesis the heat flow and the mass loss of the effect decreased, indicating the formation of less hydrtated compounds (Table 3.5). The characteristic thermal effect on katoite was observed in a temperature range of 300–350°C (Fig. 3.18 b). The obtained results showed that the heat of the latter effect was equal to 56.49 J/g after 4 h of synthesis, and the value significantly decreased (25.02 J/g) after 12 h of synthesis (Table 3.5). Finally, after 48 h of synthesis, there is no evidence of a characteristic endothermic effect on katoite (Fig. 3.18 b). The third thermal effect in a temperature range of 610–710°C corresponds to the decomposition of calcium carbonate (Fig. 3.18 b). The mass loss in the latter interval can be determined to be equal to 0.8–1.14 mass%, which is equivalent to 1.8–2.6 mass% calcium carbonate (Table 3.5). According to the literature [179], cuspidine has no thermal effect in the temperature range of 20–1000°C, so the final endothermic and exothermic effects can be attributed to the thermal conversion of calcium silicate hydrates.

Similarly, as shown in Fig. 3.4 b and suggested by the literature data [160,164,165] pure tobermorite (without intercalated additional ions in the structure) recrystallises to wollastonite at ~840°C without releasing heat, i.e. without thermal effects in the DSC curve. However, in the case of the presence of Al^{3+} ions, an intense exothermic effect can be obtained as Al^{3+} ions intervene in the formation of calcium silicate hydrates and prevent the formation of xonotlite [164,165,180]. The shape and position of this thermal effect depends on the number of Al^{3+} ions intercalated in the structure. Thus, the intense exothermic effect in the temperature range of 840–880°C can be attributed to the recrystallisation of semi-crystalline calcium silicate hydrates and Al-substituted tobermorite to wollastonite (Fig. 3.18. b and Table 3.5). It should be noted that, with the decrease of the enthalpy of katoite decomposition and the increased intercalation of aluminium ions into the silicate structure, the peak temperature of wollastonite formation increased from 848°C (4 h) to 861°C (48 h).

Table 3.5. Thermal characteristics of the synthesis products formed at different durations of hydrothermal synthesis in mixtures of silica gel waste and calcium oxide

Synthesis duration, h	The main characteristics of thermal effects		
	Temperature, °C	Enthalpy, J/g	Mass change, %
4	35–250	-287.83	-6.38
12		-262.76	-6.2
48		-228.69	-5.14
4	260–420	-56.49	-3.10
12		-25.02	-2.84
48		-	-1.9
4	610–710	-29.34	-0.96
12		-31.03	-1.14
48		-19.2	-0.8
4	840–880	72.79	~0
12		62.5	~0
48		75.23	~0

The FT-IR analysis (Fig. 3.19) provided additional information and confirmed the results of XRD and STA. A broad adsorption band in the range of 3100–3800 cm^{-1} and a peak at ~1640 cm^{-1} are common to the vibration and deformation of the H–OH bond, which indicates the presence of water or the hydration of the synthetic samples. The small peaks in the range of 1450–1510 cm^{-1} are common to bending vibration of C–O bonds in the CO_3^{2-} anions which indicate carbonation and the presence of $CaCO_3$. A peak at ~1205 cm^{-1} is common to Si–O–Si symmetric stretching [168]. An intense peak at ~975 cm^{-1} is common to the asymmetric stretching vibration of O–Si–O bonds. A set of small peaks in the range of 670–

450 cm^{-1} is common to the symmetrical vibration of Si–O–Si bonds and the deformational vibrations of O–Si–O bonds [169,170].

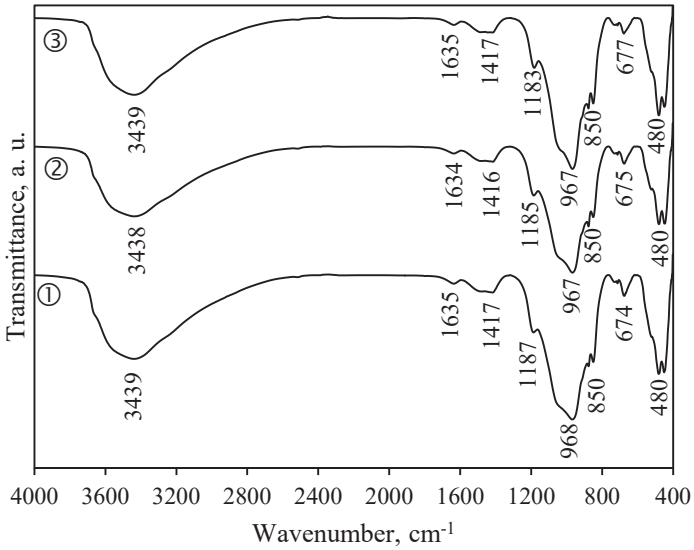


Fig. 3.19. FT-IR spectra of synthetic samples in CaO-silica gel waste-H_2O system: 1 – 4 h; 2– 12 h; and 3 – 48 h

In order to determine the influence of the calcination temperature on the sample dimensions (shrinkage), dilatometric analysis was performed. The dilatometric curves of the samples obtained after 12 h of synthesis are given in Fig. 3.20, while the summary data of all the investigated samples are given in Table 3.6. The obtained results are characterised by four interval shrinkage rates for all samples in the temperature range of 35–1100°C, which is in good agreement with the STA results (Fig. 3.18. b and Table 3.5). The first step of changes in the dimensions of the samples was carried out in the same temperature range as the removal of the adsorbed water and the partial dehydration of the synthesis products (100–450°C). During this process, the relative length changes were insignificant (~1%) for all samples (Table 3.6). The second interval of shrinkage was caused by the decomposition of calcium carbonate (Fig. 3.20. a, Table 3.6). Due to the low amount of calcium carbonate in the products (< 3 mass%), the shrinkage was negligible (Table 3.6). The temperature interval of the third shrinkage step corresponds to the final endothermic and exothermic effects (Fig. 3.18 b and Fig. 3.20. a, Table 3.6). According to the literature [164] and the previously obtained data (Table 3.3), the shrinkage of pure tobermorite is negligible up to 1000°C, while tobermorite substituted with aluminium ions is characterised by significant shrinkage. The obtained data showed that the relative length of all samples decreased by 16–19% during the final decomposition/recrystallisation interval of tobermorite (740–900°C, Table 3.6). The obtained data are in good agreement with the data from the literature [164,181]. The final step of shrinkage may be associated with some changes in the

mineralogical composition. According to calculations, the duration of hydrothermal synthesis does not affect the total shrinkage of the samples, since all samples show similar values (Table 3.6). Meanwhile, the mineralogical composition of the synthesis products has a crucial effect on the aforementioned parameter, since the total shrinkage of the synthesis products obtained in amorphous silica and calcium oxide is equal to 4.52% (after 12 h of synthesis) and 1.2% (after 48 h of synthesis), respectively, while the samples obtained in mixtures with silica gel waste have values higher by 5 and 18 times, respectively. Such prominent differences are related to the incorporation of aluminium ions into the structure of calcium silicate hydrates during the hydrothermal synthesis of silica gel waste and calcium oxide mixtures.

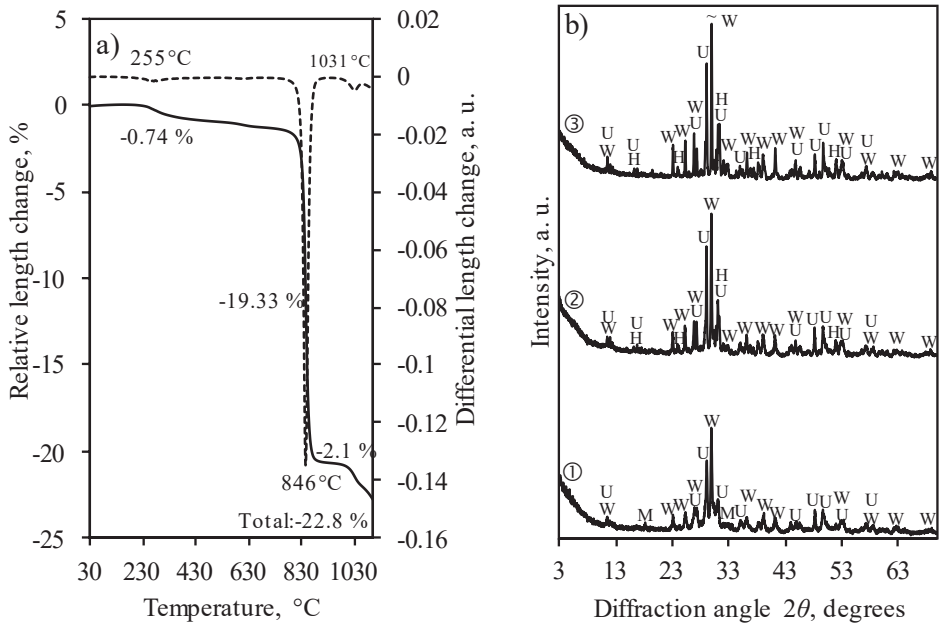


Fig. 3.20. Dilatometry curves (a, solid line – relative length change; dashed line – differential length change) of the synthesis products obtained after 12 h of hydrothermal synthesis; XRD patterns (b) of the calcined synthesis product (12 h) at different temperatures (1 – 900°C; 2 – 1000°C; 3 – 1100°C) for 1 h
Indices: W – wollastonite; U – cuspidine; M – fluormayenite; H – gehlenite

Table 3.6. Dilatometry data of synthesis products formed at different durations of hydrothermal synthesis in a mixture of silica gel waste and calcium oxide

Synthesis duration, h	Temperature range, °C	Inflection point, °C	Relative length change, %
4 h	112–424	273	-1.24
	734–905	848	-16.37
	939–(1100)	1040	-4.05
	Total:		-22.37

12 h	189–400	255	-0.74
	735–917	846	-19.33
	962–(1100)	1031	-2.1
	Total:		-22.80
48 h	206–400	271	-0.27
	759–897	850	-17.76
	965–(1100)	1024	-2.66
	Total:		-21.49

Since the primary compounds reacted after 12 h of synthesis (Fig. 3.18. a) and the duration of hydrothermal treatment had no significant effect on the thermal properties of the synthesis products (Table 3.5 and Table 3.6), the synthesis products obtained after 12 h of synthesis were calcined for 1 h at different temperatures. The obtained results suggested that, after calcination at a temperature of 900°C, the calcium silicate hydrates present in the hydrothermal synthesis products recrystallised to wollastonite, while cuspidine remained stable (Fig. 3.20. b). According to the literature [178,182], katoite recrystallised to mayenite during calcination at a temperature higher than 310°C. However, in the investigated case, traces of fluormayenite ($Ca_{12}Al_{14}O_{32}F_2$, PDF No. 87-2492) were still found (Fig. 3.20 b). This compound was probably formed due to the interaction between katoite or mayenite and the adsorbed fluoride ions by the synthesis products. At higher calcination temperatures (1000°C and 1100°C), fluormayenite reacted with other silicate-rich compounds, which resulted in the discovery of gehlenite ($Ca_2Al_2SiO_7$, PDF No. 01-6780) which has no fluoride ions in its structure. For this reason, it is not recommended to calcine the synthesis product(s) at a temperature above 1000°C. Furthermore, the final shrinkage step at > 950°C (Table 3.6) can be related to the recrystallisation process from fluormayenite to gehlenite. Eventually, the increment of the calcination temperature had a positive impact on the crystal order of both wollastonite and cuspidine as the intensity of their peaks doubled from 900 to 1100°C.

In order to determine the influence of the specific surface area on synthetic and calcined products and to compare the obtained data with the results obtained in a pure system, the synthetic (12 h, 200°C) and calcined (900°C) samples were used for nitrogen gas adsorption experiments. The BET method was determined to be valid for the calculations since a straight line with a correlation coefficient >0.999 was obtained in the BET coordination (Fig. 3.21). Likewise, in both investigated cases, the calculated values of the C_{BET} constant are equal to 46.49 (after synthesis) and 27.36 (after calcination), which indicates that the completion of the monolayer formation is fairly well defined [172,174]. The specific surface area of the synthetic sample was calculated to be equal to 67.92 m^2/g, which is 1.7 times higher compared to the surface area of the synthetic sample obtained in a mixture of amorphous silicon dioxide and calcium oxide. Furthermore, during calcination at a temperature of 900°C, the S_{BET} value decreased more than 4 times, i.e. to 16.09 m^2/g.

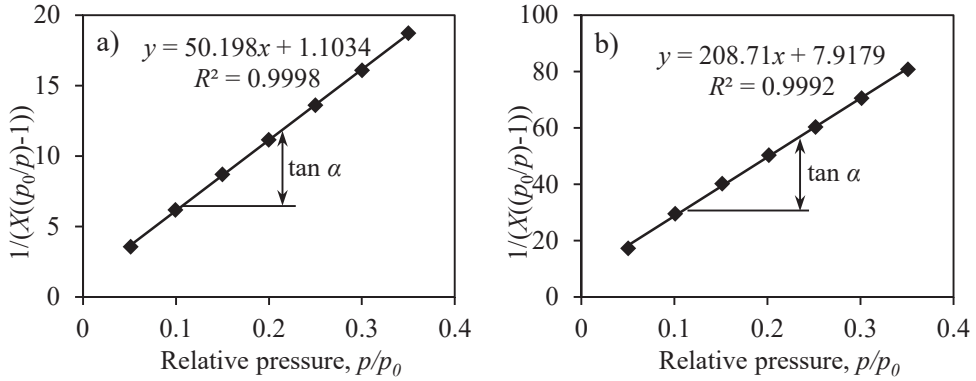


Fig. 3.21. Adsorption isotherms of N_2 in BET plots of synthetic (a); and calcined (b) samples of CaO-silica gel waste-H_2O system

As in the previous case (CaO-SiO_2·nH_2O-H_2O system, Fig. 3.8), the nitrogen adsorption–desorption isotherms of both samples do not have a final saturation plateau, but are rather characterised by a narrow hysteresis loop [174] (Fig. 3.22). The hysteresis loop of the synthetic samples can be classified as type H1, which indicates the formation of pores between cylindrical-shaped pores and spherical particles (Fig. 3.22. a). At the same time, during calcination at 900°C, the shape of the pores changed to slit-shape pores formed between particles due to the observed H3-type hysteresis (Fig. 3.22. b). It should be noted that the adsorption and desorption isotherms coincide after the calcination of the synthesis products obtained in the CaO-silica gel waste H_2O-system, which implies the non-existence of mesopores in the sample as well as in the system with amorphous silica (Fig. 3.8. b).

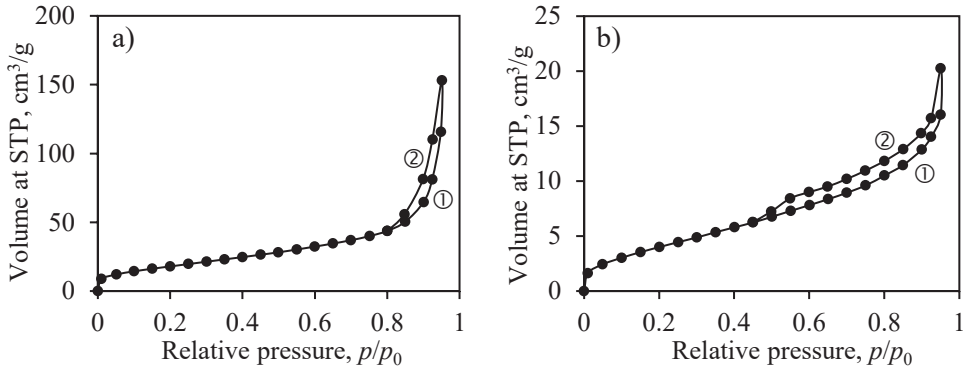


Fig. 3.22. Adsorption (1) and desorption (2) isotherms of N_2 for synthetic (a) and calcined (b) samples of CaO-silica gel waste-H_2O system

The SEM images of the aforementioned samples (Fig. 3.23) confirmed the results which were obtained by dilatometry and BET analysis. It was observed that the hydrothermally synthesised sample (Fig. 3.23. a) contained various particles, such as platelets of tobermorite, dot-like particles of katoite, and needle clusters of C-S-H(I). After calcination at 900°C for 1 h (Fig. 3.23. b), all these particles were

completely deformed and were hardly distinguishable from each other. This alteration of the sample can explain the densification of powders during the dilatometry and the loss of the surface area which was determined by using BET analysis.

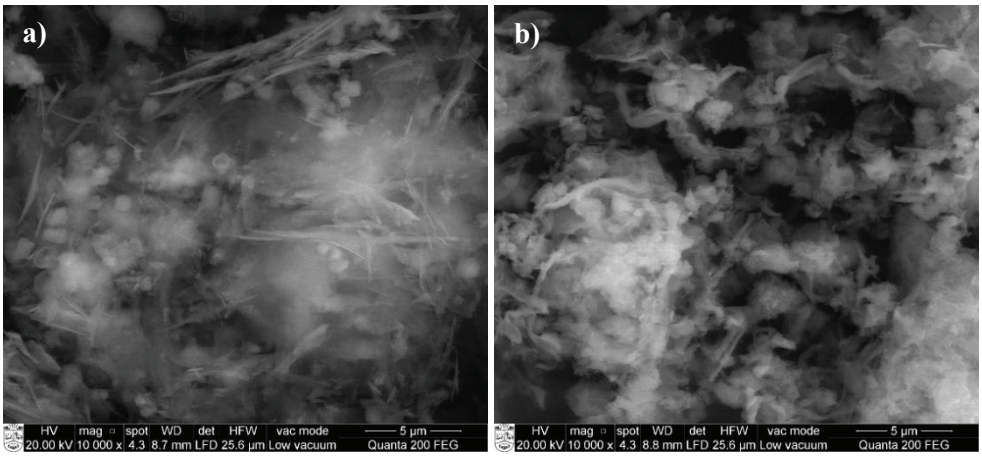


Fig. 3.23. SEM images of samples of CaO-silica gel waste-H_2O system: a – hydrothermally obtained (200°C, 12 h); and b – after calcination at 900°C for 1 h

By summarising the obtained results of hydrothermal synthesis and calcination, the formation of wollastonite and the intermediate phases in the CaO-silica gel waste mixture can be presented in the following order:

$$\text{CaO+silica gel waste+}H_2O \xrightarrow{\text{Synthesis at 200°C for 4-48 h}} \begin{bmatrix}\text{C-S-H(I)}\\ \text{tobermorite}\\ \text{cuspidine}\\ \text{katoite}\end{bmatrix} \xrightarrow{\text{Calcination at 900°C for 1 h}} \xrightarrow{\text{Calcination at 900°C for 1 h}} \begin{bmatrix}\text{wollastonite}\\ \text{cuspidine}\\ \text{fluormayenite}\end{bmatrix} \xrightarrow{\text{Calcination at 1000-1100°C for 1 h}} \begin{bmatrix}\text{wollastonite}\\ \text{cuspidine}\\ \text{gehlenite}\end{bmatrix}.$$

When the precursor was synthesised at 200°C for 12 h under stirring, it consisted of tobermorite, cuspidine, katoite and C-S-H(I) (precursor XS). Furthermore, the obtained material was mesoporous, and its specific surface area was 67.92 m^2/g. After calcination, it recrystallised into wollastonite and fluormayenite, while cuspidine remained stable. However, the specific surface area decreased to 16.09 m^2/g, but the material remained mesoporous nevertheless (sample WS).

It can be summarised that the chemical composition of the starting mixture has a crucial effect on the mineralogical compositions of the hydrothermal synthesis and calcination products. In the mixture of pure amorphous silica and calcium oxide, only one crystalline phase – wollastonite – was formed after the two-step synthesis. Meanwhile, in the mixture of silica gel waste and calcium oxide, wollastonite, cuspidine and fluormayenite were identified after the calcination of the hydrothermal synthesis products at a temperature of 900°C. Silica gel waste consists mainly of amorphous silicon dioxide and crystalline aluminium fluoride trihydrate;

therefore, in order to fully understand the influence of silica gel waste on the formation of wollastonite during the two-step synthesis, hydrothermal synthesis experiments in the mixture of calcium oxide, reagent grade amorphous silicon dioxide, and aluminium fluoride were prepared. It is to be noted that, in the latter mixture, the concentration of fluoride ions was equal to 4.32 mass%, i.e., the same as in the mixture of silica gel waste and calcium oxide; however, the amount of Al^{3+} ions was equal to 2.05% instead of 2.65%.

Acknowledgements:

Reprinted/Adapted by permission from *Elsevier Ltd*.: Ceramics International / Synthesis and characterisation of wollastonite with aluminium and fluoride ions / A. Gineika, T. Dambrauskas, K. Baltakys, 47(16):22900-22910. 2021 https://doi.org/10.1016/J.CERAMINT.2021.05.003

3.3. Two-step Synthesis of Wollastonite in the $CaO\text{-}SiO_2 \cdot nH_2O\text{-}AlF_3\text{-}H_2O$ System

The admixture of aluminium fluoride, which is present in the silica gel waste, has been determined to exert a significant influence on the mineral composition of the products of hydrothermal synthesis. 1.13 nm tobermorite and cuspidine were the dominant compounds in the synthesis products under all experimental conditions (Fig. 3.22. a). In addition, traces of calcium fluoride CaF_2 were also identified. The formation of the latter compound can proceed according to the reaction between two poorly soluble compounds (3.1):

$$3Ca(OH)_2 + 2AlF_3 \rightarrow 3CaF_2 + 2Al(OH)_3. \quad (3.1)$$

To investigate the influence of the AlF_3 additive on the formation of wollastonite, two AlF_3 sources were used: the saturated leftover AlF_3 solution, and the dry $CaO\text{-}SiO_2 \cdot nH_2O\text{-}AlF_3\text{-}H_2O$ system. The latter system contained 4.32 wt% F^- ions – which is the same amount as in the system with silica gel waste. The purpose of this composition was to imitate the silica gel waste.

3.3.1. Application of saturated AlF_3 solution for synthesis of calcium silicate hydrate

Silica gel waste is only one of the by-products of AlF_3 manufacturing. In addition, the process generates a substantial amount of AlF_3 saturated solution. Thus, it was investigated whether it was possible to use the liquid to synthesise calcium silicate precursors of wollastonite.

Influence of dilution on the synthesis products

For the investigation application of the saturated AlF_3 solution for the calcium silicate hydrate synthesis, the original solution (100 vol%), the dilutions of 1, 5, 10, 15, 20, 25, 50, 75, 90, 95 vol%, and distilled water (0 vol%) were used. The obtained liquids were mixed with $CaO/SiO_2 \cdot nH_2O$ (CaO/SiO_2 = 1) mixture (water-to-solid ratio 10). The incorporation was carried out under stirring by using a magnetic stirrer at room temperature for 30 min (Fig. 3.24. a). It was determined that, after the primary interaction (neutralisation), when the concentration was increased from 0 to 25 vol%, the pH value reached 12.4. When the concentration

was 50 vol%, the pH value was around 11, while, for 75 vol%, we obtained pH ≈ 8.5. The pH value of the most concentrated solutions (90–100 vol%) reached 7–7.5. It was also noticed that, after the incorporation of powders into the solutions of 0–25 vol%, the obtained suspensions were well dispersed; meanwhile, the particles in the more concentrated (50–100 vol%) solutions tended to agglomerate.

After the neutralisation, the obtained suspensions were hydrothermally treated without stirring for 12 h at 200°C. It was determined (Fig. 3.24. b) that, in distilled water (0 vol%), the main products were calcium silicate hydrates: gyrolite, 1.13 nm tobermorite, and xonotlite. In the suspensions which were obtained from diluted solutions (1–25 vol%), only one calcium silicate hydrate – 1.13 nm tobermorite – was obtained. The intensity of its peaks did not differ much in the above mentioned dilution range. In addition to tobermorite, katoite and fluorite were also identified. When the concentration was increased to 50 vol%, while only traces of semi-crystalline C-S-H(I) and katoite were identified, fluorite dominated in the product. The latter compound was the only one identified in the suspensions of the more concentrated (75–95 vol%) solutions. After the neutralisation of the original solution (100 vol%), fluorite was the main new compound. In addition, the formation of prosopite $CaAl_2(OH)_4F_4$ (PDF No. 11-13-10) and halloysite $Al_2Si_2O_5(OH)_4$ (PDF No. 29-1487) traces was identified.

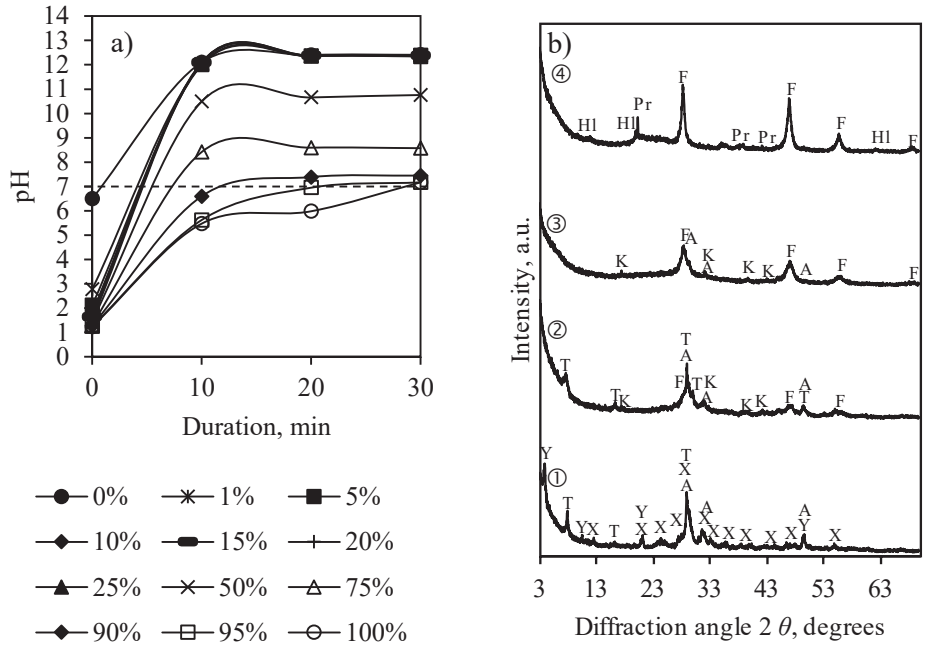


Fig. 3.24. Neutralisation of saturated AlF_3 solution: a – pH values after neutralisation by $CaO/SiO_2 \cdot nH_2O$ mixture; b – XRD patterns of the products from obtained suspensions after hydrothermal curing at 200°C for 12 h without stirring: 1 – 0 vol% AlF_3 solution; 2 – 25 vol%; 3 – 50 vol%; and 4 – 100 vol%
Indices: Y – gyrolite; T – 1.13 nm tobermorite; X – xonotlite; A – C-S-H(I); K – katoite; F – fluorite; Pr – prosopite; Hl – halloysite

Two-stage reaction

The first reaction was the neutralisation of saturated AlF_3 solution by reagent grade calcium carbonate and $CaCO_3$-bearing rocks – opoka and limestone (Fig. 3.25). The neutralisation was carried out in suspensions with water-to-solid ratio 20, under stirring.

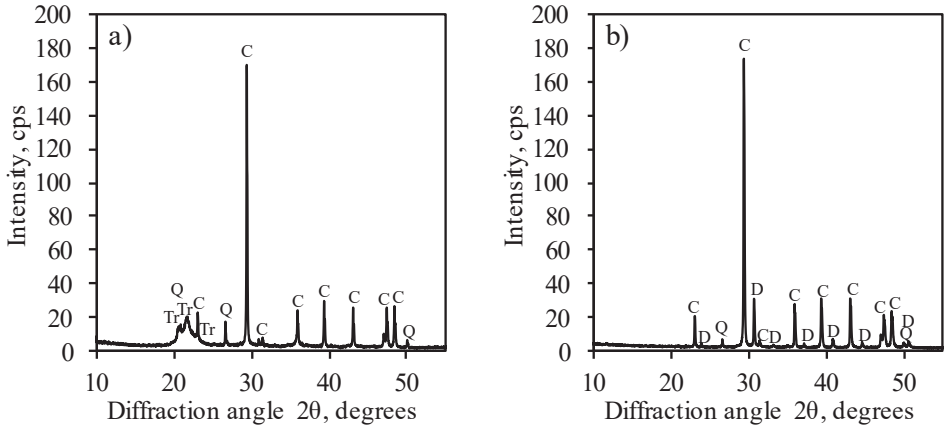


Fig. 3.25. XRD patterns of natural $CaCO_3$-bearing rocks: a – opoka; b – limestone
Indices: C – calcite ; D – dolomite ; Q – quartz ; Tr – tridymite

It was determined that, after 30 min of the reaction, the lowest pH value was reached at ~3.5. It should be noted that opoka contains less calcium carbonate than limestone (~96 mass%) as it is both SiO_2 (54.6 mass%) and $CaCO_3$ (39.5 mass%) bearing rock , thus it raised the pH value only to ~1.8 (Fig. 3.26. a). The XRD patterns of the residue (Fig. 3.27. a) showed that a part of calcium carbonate remained, even though the pH value did not reach 7. Thus, it can be stated that insoluble calcium carbonate cannot participate in the neutralisation past pH ≈3.5.

For the second stage of neutralisation, the obtained suspensions were additionally neutralised by $CaO/SiO_2 \cdot nH_2O$ ($CaO/SiO_2 = 1$) mixture (water-to-solid ratio 10). Similarly to the dilution experiment, the maximum pH value of 8.5–9 was reached within 30 min (Fig. 3.26. b). The neutralised suspensions were hydrothermally treated at 200°C for 12 h without stirring. It was determined that the main product of the neutralisation was fluorite (Fig. 3.27 b). However, no calcium silicate hydrates were identified, but the peak intensity of calcium carbonate and, in the case of opoka, the peak intensity of quartz and tridymite decreased. The appearance of the fluorite peaks and the decrease of the calcite/dolomite peaks indicated that the interaction between the acidic solution and the insoluble carbonates can occur only under hydrothermal conditions. The lower peak intensity of SiO_2 phases could be caused by their interaction with F^- ions which were abundant in the solution. In addition, even though limestone contained Mg-bearing dolomite, no sellaite MgF_2 was identified in the XRD patterns.

To sum up, the application of industrial leftover saturated AlF_3 saturated solution for the synthesis of calcium silicate hydrate, it can be stated that the use of the solution for the synthesis of calcium silicate hydrates is limited.

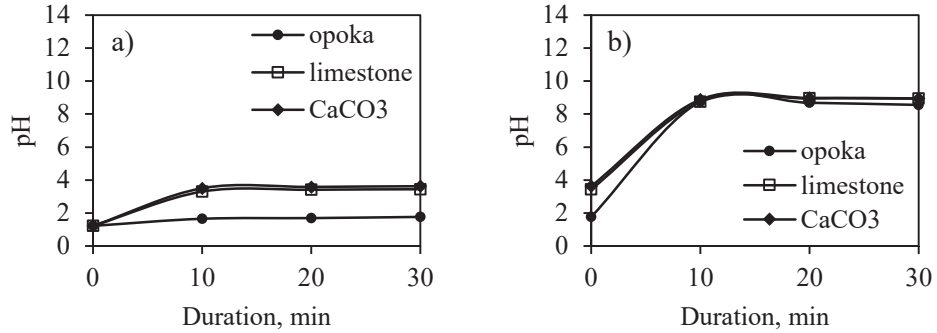


Fig. 3.26. Neutralisation curves of saturated AlF_3 solution with additives: a – only carbonaceous additives; b – after neutralisation by carbonaceous additives and further addition of $CaO/SiO_2 \cdot nH_2O$

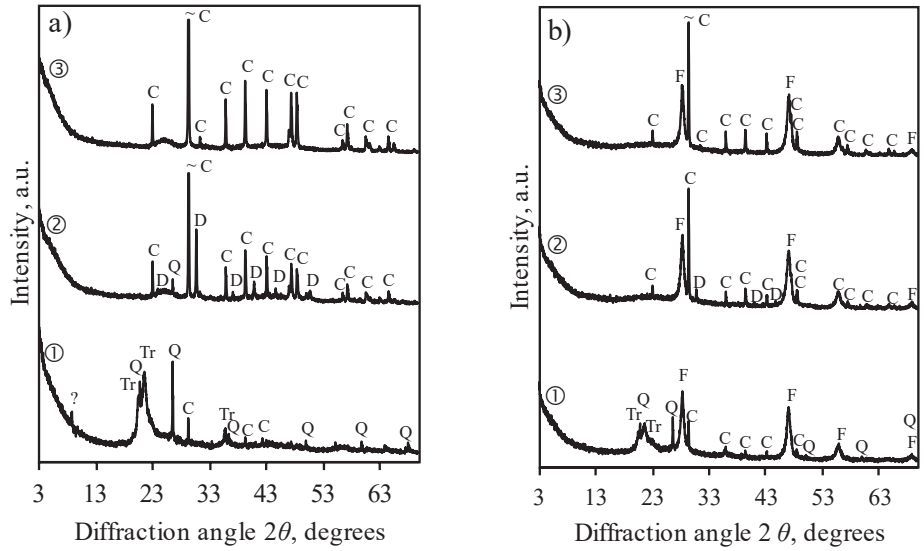


Fig. 3.27. XRD patterns of residue that formed after the neutralisation of saturated AlF_3 solution with additives: a – only carbonaceous additives; b – after neutralisation by carbonaceous additives (1 – opoka; 2 – limestone; and 3 – $CaCO_3$) and further addition of $CaO/SiO_2 \cdot nH_2O$ mixture and hydrothermal treatment at 200°C for 12 h without stirring
Indices: C – calcite; Q – quartz; Tr – tridymite; Cr – cristobalite; D – dolomite; F – fluorite; ? – unknown phase

To conclude the investigation of the application of the saturated AlF_3 solution, it can be stated that its application is limited. The pH of the liquid and its concentration had a negative influence on the formation of the phases of calcium silicate hydrate. It was observed that the pH value of the medium had to be ~12 for

the crystalline calcium silicate hydrate phases to form. Lower values blocked their formation. In addition, the calcium carbonate additive could not provide the required pH of the solution.

3.3.2. Direct (single-step) synthesis of wollastonite by using the dry initial mixture

Wollastonite residues (97 cps, Table 3.7) were identified in the sintered products as early as at 900°C in the $CaO\text{-}SiO_2 \cdot nH_2O\text{-}AlF_3$ system (Fig. 3.28). Similarly to the previously described mixtures, the increase in the temperature had a positive impact on the formation of the target compound, as its main peak increased twice at 1000° C (211 cps) and four times at 1100°C (390 cps). Yet, differently from the other systems with CaO, in this case, it had reacted completely already at 900°C. However, in addition to wollastonite and calcium oxide, the 900°C temperature product contained the same admixtures as the CaO-silica gel waste system: larnite, fluormayenite, kumtyubeite, and cuspidine. The intensity of the larnite peaks tended to decrease with the increasing temperature. The molar CaO/SiO_2 ratio of the latter compound was two times higher than the mixture, thus larnite should further react with SiO_2 to form wollastonite. On the other hand, the intensity of the wollastonite peaks increased with the increasing temperature, which could indicate the increased crystal order and amount. The intensity of the peaks of the latter compound increased significantly with the increase of the temperature: 96 cps at 900°C, 964 at 1000°C, and 1643 at 1100°C due to the increased crystal order. Fluorite, a mineral which formed during the $CaO\text{-}AlF_3$ interaction, was identified in the sintered products at 900 and 1000°C, but it had reacted completely at 1100°C.

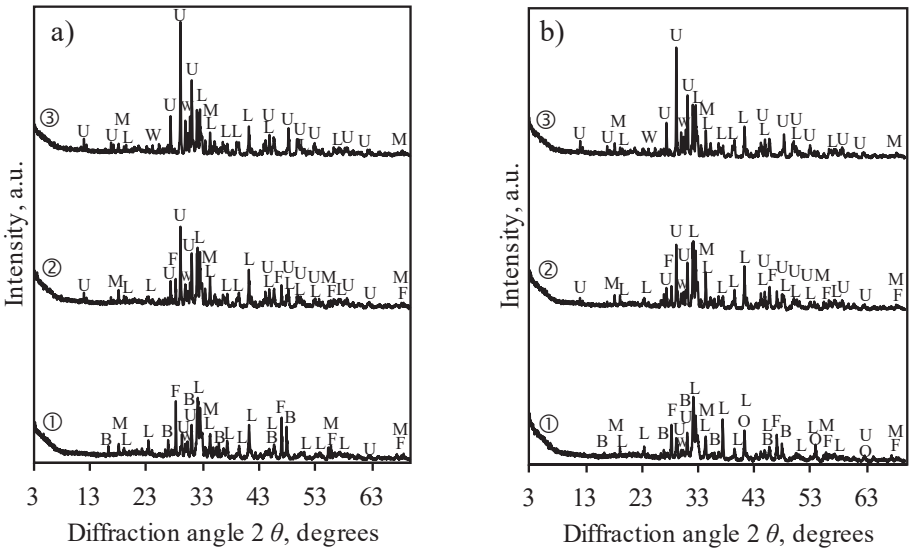


Fig. 3.28. XRD patterns of direct synthesis products: a – $CaO\text{-}SiO_2 \cdot nH_2O\text{-}AlF_3$ system; b – $CaCO_3$- $SiO_2 \cdot nH_2O\text{-}AlF_3$ system
Indices: F – fluorite; L – larnite; B – kumtyubeite; M – fluormayenite; U – cuspidine; W – wollastonite

The replacement of CaO with $CaCO_3$ in the initial mixture was observed to hardly improve the wollastonite formation during the direct synthesis in the $CaCO_3$-$SiO_2 \cdot nH_2O$-AlF_3 system (Fig. 3.28, Table 3.7). In addition, a part of lime did not react completely at 900°C. Similarly to the system with CaO, the increment of the temperature was determined to have a positive impact mainly on the formation of cuspidine, as the intensity of its main peak increased seven times. Overall, the mineral composition of the sintered products in the aforementioned system followed the same trend as in the previous case with CaO, where larnite and cuspidine were the dominant compounds.

Table 3.7. Intensity of the main peaks of lime, larnite, wollastonite, cuspidine and fluorite in the products of direct synthesis in CaO-$SiO_2 \cdot nH_2O$-AlF_3 system

System	Temperature, °C	Intensity, cps				
		Lime	Larnite	Wollastonite	Cuspidine	Fluorite
		0.2406 nm	0.2747 nm	0.2976 nm	0.3066 nm	0.3149 nm
CaO-$SiO_2 \cdot nH_2O$-AlF_3	900	0	592	97	96	672
	1000	0	618	211	964	300
	1100	0	496	390	1643	0
$CaCO_3$-$SiO_2 \cdot nH_2O$-AlF_3	900	493	515	79.7	179	395
	1000	0	690	154	755	243
	1100	0	595	271	1324	0

The summarised reactions of direct synthesis in the CaO-$SiO_2 \cdot nH_2O$-AlF_3 and $CaCO_3$-$SiO_2 \cdot nH_2O$-AlF_3 systems in the temperature range of 900–1100°C are given in the schemes below:

$$CaO + SiO_2 \cdot nH_2O + AlF_3 \xrightarrow{\text{sintering 900°C, 1 h}} \begin{bmatrix} \text{fluorite} \\ \text{larnite} \\ \text{kumtyubeite} \\ \text{fluormayenite} \end{bmatrix} \xrightarrow{\text{1000°C, 1 h}} \begin{bmatrix} \text{larnite} \\ \text{fluorite} \\ \text{cuspidine} \\ \text{fluormayenire} \end{bmatrix} \xrightarrow{\text{1100°C, 1 h}} \begin{bmatrix} \text{cuspidine} \\ \text{larnite} \\ \text{wollastonite} \\ \text{fluormayenite} \end{bmatrix}$$

$$CaCO_3 + SiO_2 \cdot nH_2O + AlF_3 \xrightarrow{\text{sintering 900°C 1 h}} \begin{bmatrix} \text{larnite} \\ \text{fluorite} \\ \text{fluormayenite} \\ \text{kumtyubeite} \end{bmatrix} \xrightarrow{\text{sintering 1000°C 1 h}} \begin{bmatrix} \text{cuspidine} \\ \text{larnite} \\ \text{fluorite} \\ \text{fluormayenite} \end{bmatrix} \xrightarrow{\text{sintering 1100°C, 1 h}} \begin{bmatrix} \text{cuspidine} \\ \text{larnite} \\ \text{fluormayenite} \end{bmatrix}$$

To summarise on the investigation of the direct synthesis of wollastonite in the $CaO\text{-}SiO_2 \cdot nH_2O\text{-}AlF_3$ and $CaCO_3\text{-}SiO_2 \cdot nH_2O\text{-}AlF_3$ systems, it can be stated that the additive promotes the interaction of lime with the other initial materials. However, AlF_3 does not work as a fluxing agent, and thus it does not lower the temperature of wollastonite formation because the products mainly contain minerals exhibiting a higher CaO/SiO_2 ratio than the initial mixture (CaO/SiO_2 = 1). Furthermore, summarising on the direct (single-step) synthesis of wollastonite in three systems, it can be stated that the method is ineffective because the target compound did not dominate in the products, and in some cases it hardly even formed at all.

3.3.3. Hydrothermal synthesis of the precursors of wollastonite in stirred suspensions and calcination

The XRD analysis results (Fig. 3.29. a) showed that, after 4 h of hydrothermal synthesis at a temperature of 200°C, the initial compounds (including AlF_3) had reacted completely. The products contained 1.13 nm tobermorite $Ca_5Si_6O_{16}(OH)_2 \cdot 4H_2O$, cuspidine $Ca_4Si_2O_7F_2$, C-S-H(I), and fluorite CaF_2. Katoite $Ca_3Al_2(SiO_2)_{0.5}(OH)_{10}$ was not identified. By prolonging the duration of the synthesis to 24 h and 48 h, the composition of the synthesis products remained unchanged, despite being characterised by an increase in the intensity of the main diffraction peaks of tobermorite. The main differences from the system with silica gel waste are the formation of fluorite and the lack of katoite.

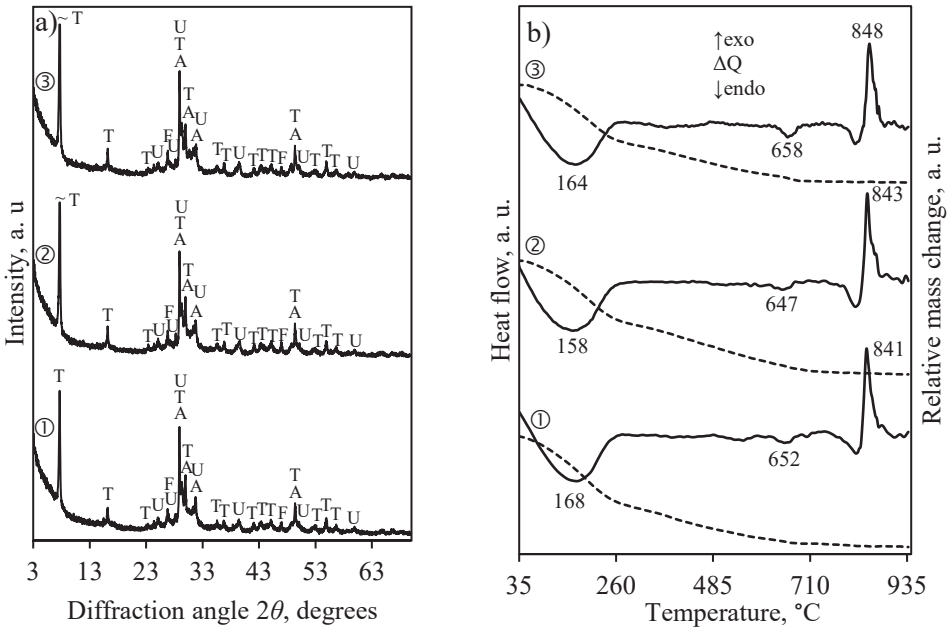


Fig. 3.29. XRD patterns (a) and STA (b) curves (solid line – DSC; dashed line – TG) of the hydrothermal synthesis products obtained in $CaO\text{-}SiO_2 \cdot nH_2O\text{-}AlF_3$ system: 1 – after 4 h; 2 – 12 h; 3 – 48 h

Indices: T – 1.13 nm tobermorite; F – fluorite; U – cuspidine; A – C-S-H(I)/(II)

The shape of the STA curve (Fig. 3.29. b) and the enthalpy of the reaction (Table 3.8) of the synthesis products are in good agreement with the XRD data and are similar to the previously obtained results (Fig. 3.4. b, Fig. 3.18. b, Table 3.2, and Table 3.5). In the DSC curve: the first endothermic effect (35–250°C) can be assigned to the adsorbed water and the partial dehydration of tobermorite; meanwhile, the second endothermic effect (~650°C) can be assigned to the decomposition of calcium carbonate, whereas the exothermic effect (at 841–848°C) corresponds to the formation of wollastonite from semi-crystalline C-S-H phases. It should be noted that heat values of the thermal effect (enthalpy) are similar to those obtained in the DSC curve of the synthesis product obtained in the mixture of silica gel and calcium oxide.

Table 3.8. Thermal characteristics of the synthesis products formed at different durations of hydrothermal synthesis in mixtures of amorphous silicon dioxide, calcium oxide, and aluminium fluoride

Synthesis duration, h	The main characteristics of thermal effects		
	Temperature, °C	Enthalpy, J/g	Mass change, %
4 h	35–250	-306.96	-7.27
12 h		-342.01	-8.26
48 h		-289.22	-7.21
4 h	610–710	-14.50	-0.52
12 h		-11.74	-0.74
48 h		-19.2	-0.65
4 h	840–880	90.57	~0
12 h		77.23	~0
48 h		89.31	~0

FT-IR analysis (Fig. 3.30) provided additional information and confirmed the results of XRD and STA. A broad adsorption band in the range of 3100–3800 cm^{-1} and a peak at ~1640 cm^{-1} are common to the vibration and deformation of the H–OH bond which indicates the presence of water or the hydration of synthetic samples. Small peaks in the range of 1450–1510 cm^{-1} are common to the bending vibration of C–O bonds in the CO_3^{2-} anions, which indicates carbonation and the presence of $CaCO_3$. A peak at ~1205 cm^{-1} is common to Si–O–Si symmetric stretching [168]. An intense peak at ~975 cm^{-1} is common to the asymmetric stretching vibration of O–Si–O bonds. A set of small peaks in the range of 670–450 cm^{-1} is common to the symmetrical vibration of Si–O–Si bonds and the deformational vibrations of O–Si–O bonds [169,170].

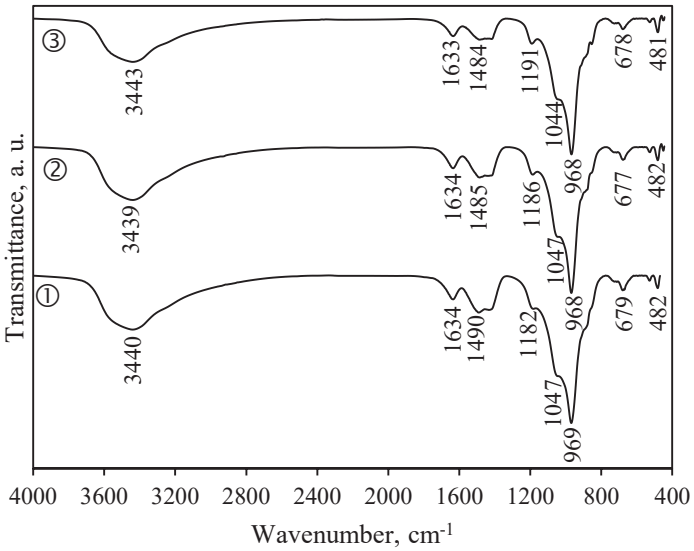


Fig. 3.30. FT-IR spectra of synthetic samples in $CaO\text{-}SiO_2 \cdot nH_2O\text{-}AlF_3\text{-}H_2O$ system: 1 – 4 h; 2– 12 h; and 3 – 48 h

The results of dilatometric analysis of the samples obtained in amorphous silica, calcium oxide and aluminium fluoride showed prominently different results (Fig. 3.31 a, Table 3.9) compared to the previous cases (Table 3.3 and Table 3.6). The shrinkage associated with the recrystallisation of calcium silicate hydrates to wollastonite (845–850°C) was similar to that obtained in the mixture of silica gel waste and calcium oxide. However, in a higher temperature range (> 900°C), an intense two-step shrinkage (with the inflection points at temperatures of 990°C and 1083°C) occurred, with a relative length of decrease of ~11–23% (Table 3.9). The final shrinkage step may be related to some chemical reactions between calcium fluoride and calcium silicates. The total dimension change of the synthesis products was measured to be 34–38%, thereby making them most susceptible to shrinkage (Table 3.9).

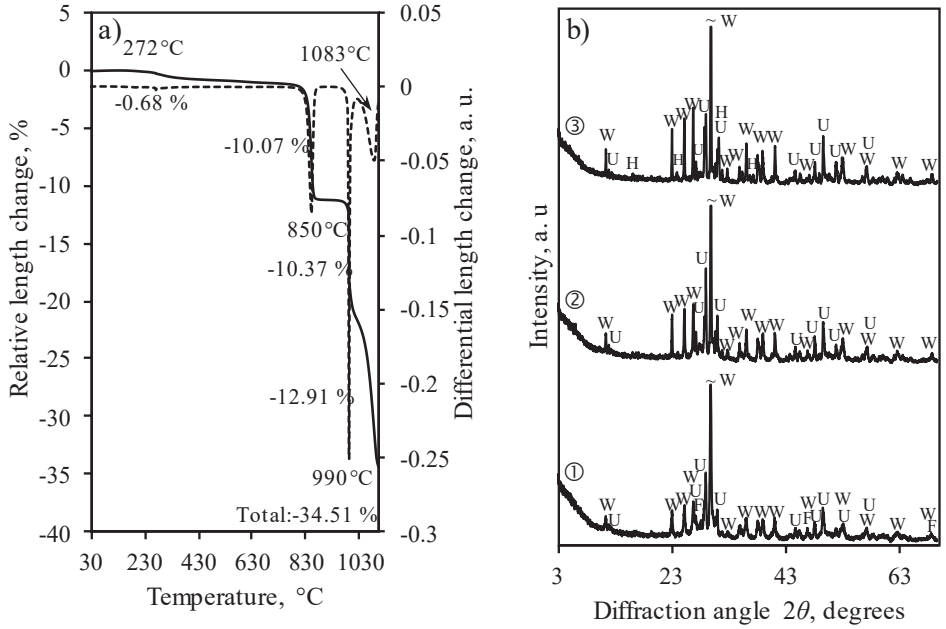


Fig. 3.31. Dilatometry curves (a, solid line – relative length change; dashed line – differential length change) of the synthesis products obtained after 12 h of hydrothermal synthesis; b – XRD patterns of the calcined synthesis product (12 h) at different temperatures (1 – 900°C; 2 – 1000°C; 3 – 1100°C) for 1 h

Indices: W – wollastonite; U – cuspidine; M – fluormayenite; H – gehlenite; F – fluorite

Table 3.9. Dilatometry data of synthesis products formed at different durations of hydrothermal synthesis in $CaO\text{-}SiO_2 \cdot nH_2O\text{-}AlF_3$ system

Synthesis duration, h	Temperature range, °C	Inflection point, °C	Relative length change, %
4 h	174–422	320	-1.14
	754–898	844	-21.04
	933–1025	995	-4.84
	1025–(1100)	1078	-6.44
	Total:		-34.47
12 h	181–382	272	-0.68
	754–883	850	-10.07
	940–1019	990	-10.37
	1019–(1100)	1083	-12.91
	Total:		-34.51
48 h	182–338	286	-0.39
	765–885	851	-13.48
	946–1007	977	-8.26
	1007–(1100)	1084	-15.90
	Total:		-38.17

As in the previous cases of calcination (Fig. 3.6. b and Fig. 3.20. b), the hydrothermal synthesis products obtained after 12 h of synthesis were chosen. It was determined that, during calcination at a temperature of 900°C, calcium fluoride and cuspidine remained stable, while calcium silicate hydrates recrystallised to wollastonite (Fig. 3.31b). Meanwhile, after calcination at a higher temperature (1000°C), calcium fluoride became metastable and reacted with other compounds to form cuspidine. It is notable that, during this reaction, the shrinkage of the synthesis products was equal to 10.37% (Table 3.9). Nevertheless, aluminium did not form any separate phase either during the hydrothermal synthesis, or during calcination up to 1000°C, such as katoite and fluormayenite; it was only at 1100°C that traces of gehlenite were identified. The latter compound could form due to the increased crystal order of the other components of the calcination products.

To summarise on the obtained results of hydrothermal synthesis and calcination, the formation of wollastonite and intermediate phases in the CaO-$SiO_2 \cdot nH_2O$-AlF_3 mixture can be presented in the following order:

$$CaO+SiO_2 \cdot nH_2O+ +AlF_3+H_2O \xrightarrow{\text{Synthesis at 200°C for 4-48 h}} \left[\begin{array}{c}\text{C-S-H(I)}\\ \text{tobermorite}\\ \text{cuspidine}\\ \text{fluorite}\end{array}\right. \xrightarrow{\text{Calcination at 900°C for 1 h}}$$

$$\xrightarrow{\text{Calcination at 900°C for 1 h}} \left[\begin{array}{c}\text{wollastonite}\\ \text{cuspidine}\\ \text{fluorite}\end{array}\right. \xrightarrow{\text{Calcination at 1000°C for 1 h}} \left[\begin{array}{c}\text{wollastonite}\\ \text{cuspidine}\end{array}\right. \xrightarrow{\text{Calcination at 1100°C for 1 h}}$$

$$\xrightarrow{\text{Calcination at 1100°C for 1 h}} \left[\begin{array}{c}\text{wollastonite}\\ \text{cuspidine}\\ \text{gehlenite}\end{array}\right. .$$

Acknowledgements:

Reprinted/Adapted by permission from *Elsevier Ltd.*: Ceramics International / Synthesis and characterisation of wollastonite with aluminium and fluoride ions / A. Gineika, T. Dambrauskas, K. Baltakys, 47(16):22900-22910. 2021 https://doi.org/10.1016/J.CERAMINT.2021.05.003

3.4. The Influence of Temperature on the Formation of Wollastonite via Two-step Synthesis

After obtaining positive results of wollastonite synthesis via two-step synthesis in the CaO-silica gel waste-H_2O system, when the hydrothermal synthesis was carried out at 200°C under stirring, the temperature of the synthesis of the precursors was lowered to 95–130°C.

According to the XRD data, it was determined that, during isothermal curing at 95°C, some amount of portlandite $Ca(OH)_2$ (PDF No. 04-0733; d = 0.2628; 0.4900; 0.1927 nm) remained unreacted after 0–48 h (Fig. 3.32).

The new crystalline compounds were katoite $Ca_3Al_2(SiO_2)_{0.5}(OH)_{10}$, and gibbsite $Al(OH)_3$ which formed due to the presence of Al^{3+} ions in the silica gel waste, calcite $CaCO_3$, and calcium carboaluminate hydrate $Ca_4Al_4O_9(CO_3) \cdot 11H_2O$

(PDF Nr. 54-0848, d = 0.94100; 0.2507; 0.3800; 0.2700; 0.2152 nm) which formed because of the adsorption of atmospheric CO_2. As portlandite was not completely bound during hydrothermal synthesis at 95°C, this temperature was considered not high enough, and the same experiment was carried out at an increased temperature.

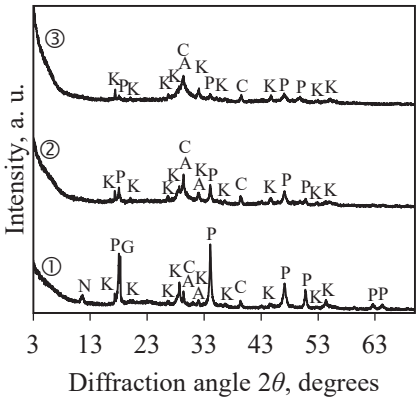


Fig. 3.32. XRD patterns of hydrothermal synthesis at 95°C; products after: 1 – 0 h; 2 – 4 h; 3 – 48 h
Indices: P – portlandite; K – katoite; G – gibbsite; C – calcite; N – calcium carboaluminate hydrate; and A – C-S-H(I)/(II)

The reaction at 130°C between CaO and SiO_2 was much faster: even though portlandite was identified in the XRD pattern after 4 h (Fig. 3.33, curve 1), it was bound completely within 8 h (Fig. 3.33, curve 2). The new compounds after 4 h were the same as the ones at 95°C: katoite and calcite, but the intensity of their peaks increased. After 8 h, cuspidine $Ca_4Si_2O_7F_2$ was identified (Fig. 3.33, curve 3). It was determined that, after 24 h (Fig. 3.33, curve 3), 1.13 nm tobermorite $Ca_5Si_6O_{16}(OH)_2 \cdot 4H_2O$ started to crystallise. The main crystalline compounds of hydrothermal synthesis products remained the same after 48 h of synthesis, but the crystal order of 1.13 nm tobermorite increased (Fig. 3.33, curve 4).

Since all portlandite was completely bound during the synthesis at 130°C within 8 h and 1.13 nm tobermorite started to crystallise after 24 h, it was expected that this temperature would be more favourable rather than 95°C for the hydrothermal synthesis of the precursors for wollastonite. In addition, the admixtures in the silica gel waste, i.e. aluminium fluoride and hydroxide, were bound into katoite and cuspidine.

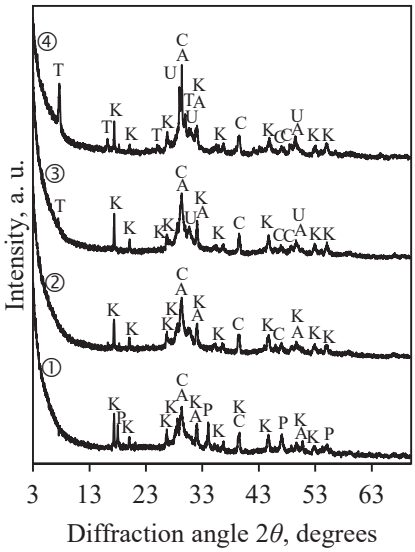


Fig. 3.33. XRD patterns of hydrothermal synthesis at 130°C products after: 1 – 4 h; 2 – 8 h; 3 – 24 h; 4 – 48 h
Indices: P – portlandite; K – katoite; C – calcite; A – C-S-H(I)/(II); U – cuspidine; and T – 1.13 nm tobermorite

STA results (Fig. 3.34) supplemented and confirmed the XRD data: after 0 h at 130°C (Fig. 3.34. a, curve 1), the first endothermal effect in the DSC curve (100–130°C) can be assigned to the loss of crystallisation water from calcium silicate hydrates, the second endothermal effect (320–325°C) is typical of the decomposition of katoite, whereas the third endothermal effect (444–446°C) is common to the dehydration of portlandite. The exothermal effect (832–868°C) is typical of the recrystallisation of semi-crystalline C-S-H(I)/(II) into wollastonite. The endothermal effect (662–697°C) belongs to the decarbonation of calcite. Both STA and XRD showed that portlandite was bound within 8 h (Fig. 3.34 a, curve 3) because there was no endothermal effect at ~445°C, and no peak was observed at 0.2627 nm in the XRD patterns.

Important differences of the exothermal effect (830–870°C) between the precursors of 130°C were observed in the DSC curves. With a longer duration of isothermal treatment, the effect migrates from the higher (850–870°C after 0–12 h (Fig. 3.34 a, curves 1–3, Fig. 3 b, curve 1)) to the lower (840–832°C after 24–48 h (Fig. 3.34 b, curves 2 and 3)) temperatures, and its enthalpy increases from ~20 to 86 J/g. This can be explained by the different types of semi-crystalline C-S-H in the synthesis products: a small and ‘blunt’ effect in samples of 0–12 h is common to C-S-H(II) [159], while a tall and ‘sharp’ one in the samples of 24–48 h belongs to C-S-H(I) [159,183] which is denoted by lower basicity and is closer to the stoichiometric composition of the primary mixture. As Al^{3+} ions formed a separate compound, katoite, the previously observed shift of the peak temperature of wollastonite formation from C-S-H was negligible.

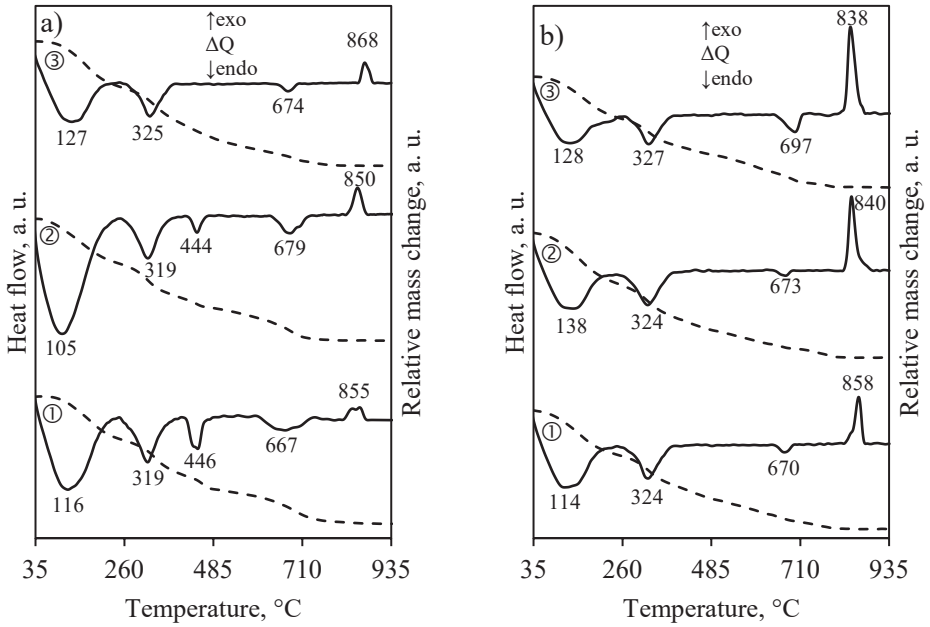


Fig. 3.34. STA curves (solid – DSC, dashed – TG) of the hydrothermal synthesis at 130°C products after: a) 1 – 0 h; 2 – 4 h; and 3 – 8 h; b) 1 – 12 h; 2 – 24 h; and 3 – 48 h

The FT-IR spectra of the synthesis products at both 95 and 130°C (Fig. 3.35) were in good agreement with the results of XRD and STA. A broad adsorption band in the range of 3100–3800 cm^{-1} and a peak at ~1635–1660 cm^{-1} are common to the vibration and deformation of the H–OH bond, which indicates the presence of water or the hydration of a material. The peaks in the range of 1400–1490 cm^{-1} and 870–875 cm^{-1} are common to the bending vibration of C–O bonds in CO_3^{2-} anions, which indicates carbonation and the presence of $CaCO_3$. An intense peak in the range of 965–1105 cm^{-1} is common to the asymmetric stretching vibration of O–Si–O bonds, while a small peak at ~675 cm^{-1} is common to the symmetrical vibration of Si–O–Si bonds. A medium intensity peak at 450–475 cm^{-1} is common to the deformational vibrations of O–Si–O bonds [169,170]. A distinct peak at ~3645 cm^{-1} is common to the asymmetric vibrations of the H–O bond of portlandite [184]. The decrement of the peak corresponds with the decrement of the amount of portlandite with the prolonged curing and an increased temperature. It was observed that the aforementioned intense broad peak in the range of 965–1105 cm^{-1} shifts its position from higher to lower wavenumbers according to the same trend as portlandite. The shift may be related to the consumption of amorphous silica, which yields the peak maximum at ~1100 cm^{-1} [185], while ~960–970 cm^{-1} is more common to calcium silicate hydrates [186,187].

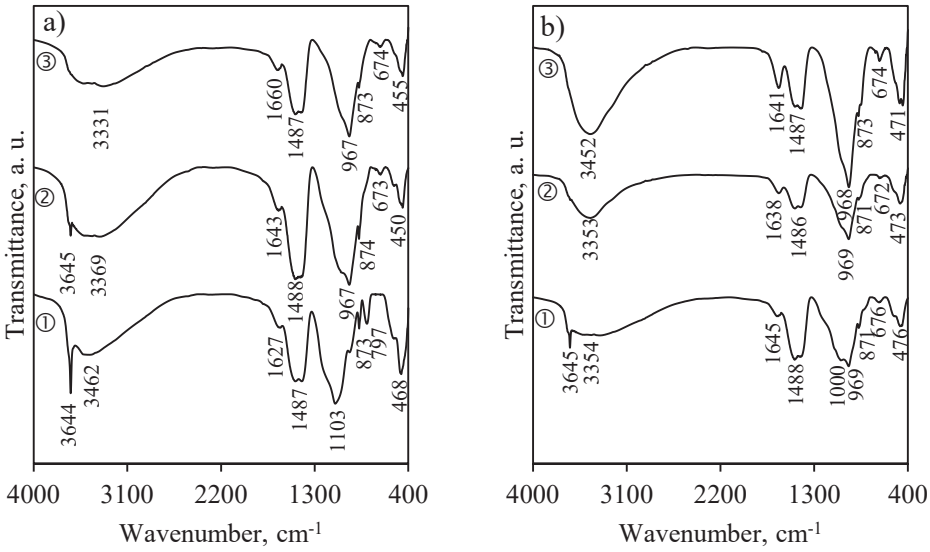
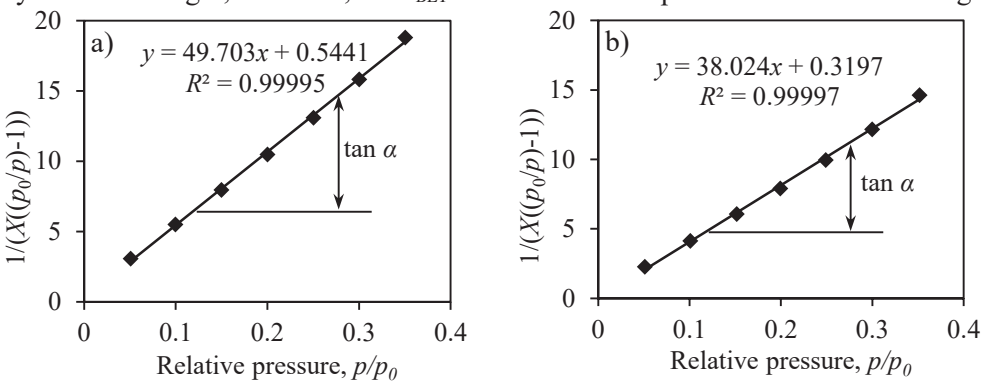


Fig. 3.35. FT-IR spectra of hydrothermally synthesised products at: a – 95°C within 1 – 0 h; 2 – 4 h; and 3 – 48 h; b – 130°C within 1 – 0 h; 2 – 8 h; and 3 – 48 h

The samples of hydrothermal synthesis at 130°C (8, 24, and 48 h) were characterised by the BET method (Table 3.10). It was determined that the surface area depends on the chemical/mineral composition of the compounds formed during hydrothermal synthesis. As mentioned above, after 8–48 h of synthesis, semi-crystalline C-S-H(II) and 1.13 nm tobermorite (Fig. 3.33, curve 4) were identified. For this reason, S_{BET} values increased from 69.3 (8 h) to 90.8 m^2/g (24 h). During 48 h of synthesis, more 1.13 nm tobermorite (Fig. 3.33, curve 5) formed, and its crystals were larger, therefore, the S_{BET} values of the sample decreased to 82.7 m^2/g.



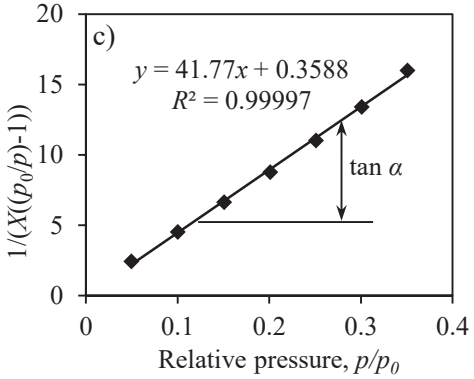


Fig. 3.36. Adsorption isotherms of N_2 in BET plots of synthetic samples after a – 8 h; b – 24 h; and c – 48 h of isothermal curing at 130°C under stirring

To determine the influence of isothermal curing on the synthetic products and to compare the obtained data with the previous results, the synthetic samples which were cured for 8, 24 and 48 h at 130°C were used for nitrogen gas adsorption experiments. As in the previous cases (cf. Fig. 3.8 and Fig. 3.22), the nitrogen adsorption–desorption isotherms of both samples do not exhibit a final saturation plateau, but are rather characterised by a narrow hysteresis loop [174] (Fig. 3.37). The hysteresis loop of the synthetic samples can be classified as type H1, which indicates the formation of pores between cylindrical-shaped pores and spherical particles.

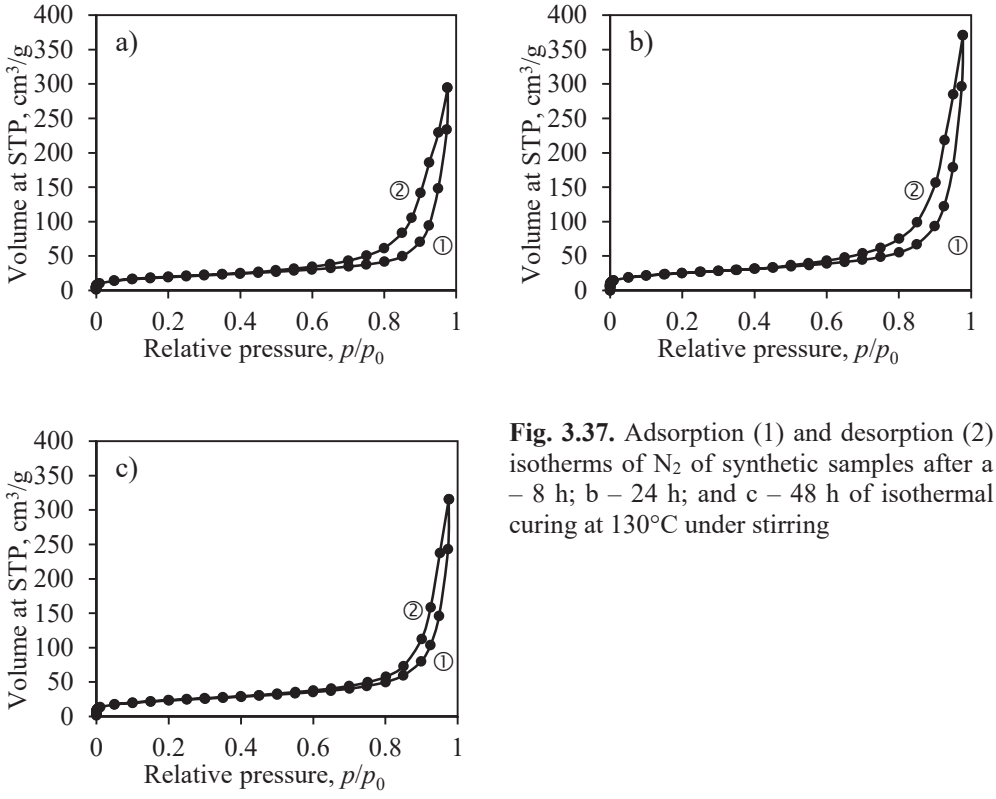


Fig. 3.37. Adsorption (1) and desorption (2) isotherms of N_2 of synthetic samples after a – 8 h; b – 24 h; and c – 48 h of isothermal curing at 130°C under stirring

Table 3.10. Calculated parameters of the samples of hydrothermal synthesis at 130°C under stirring in CaO-silica gel waste-H_2O system; determined by BET analysis

Duration of hydrothermal synthesis, h	BET equation constants		Capacity of monolayer X_m, g	C_{BET} constant	S_{BET}, m^2/g	R^2
	Slope S	Intercept I				
8	49.703	0.5441	0.0197	92.356	69.308	0.99995
24	38.024	0.3197	0.0256	119.937	90.824	0.99997
48	41.77	0.3588	0.0234	117.429	82.664	0.99997

The products of hydrothermal synthesis were calcined in the temperature range of 850–1050°C for 1 h to investigate the formation of wollastonite and the changes of its crystallinity.

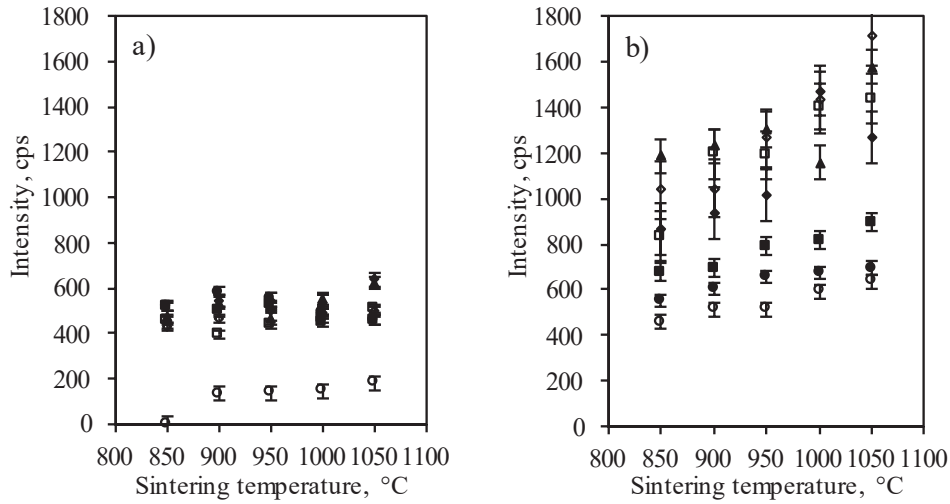


Fig. 3.38. Intensity of the main peak of wollastonite (d = 0.2980 nm) in XRD patterns of calcined products. Hydrothermal synthesis temperature: a – 95°C; b – 130°C. Duration indices: ○ – 0 h; ● – 4 h; ■ – 8 h; ♦ – 12 h; □ – 24 h; ◊ – 36 h; ▲ – 48 h

Even though the amount of portlandite in the products of hydrothermal synthesis at 95°C decreased from 23.31% (0 h) to 4.73% (48 h), the intensity of the wollastonite main peak (d = 0.2980 nm) in the XRD patterns of calcined products (Fig. 3.38. a) was in the range of 0–600 cps, and it depended neither on the hydrothermal synthesis duration (from 0 to 48 h), nor on the calcination temperature (from 850 to 1050°C). The amount of wollastonite in the calcined products of the hydrothermal synthesis at 130°C (Fig. 3.38 b) was much larger: the intensity range of the main peak of wollastonite was from 450 to 1750 cps. The products that contained portlandite (0–4 h) showed a similar intensity (450–600 cps) of the

wollastonite main peak to those of 95°C synthesis (Fig. 3.39, curve 1). The products without portlandite had more intense peaks (600–1750 cps) of wollastonite and depended on both the synthesis duration and the calcination temperature. The latter dependence is more evident for the products of 12 h and longer synthesis (Fig. 3.39, curves 2 and 3). According to the intensity of the main peak of wollastonite in the XRD patterns, it can be concluded that portlandite had to react completely during the synthesis. As a result, after calcination, the products without portlandite contained more wollastonite, while the products with portlandite yielded a lower amount of this mineral and contained more larnite – a compound where the CaO/SiO_2 molar ratio is two times higher than that of the primary mixture.

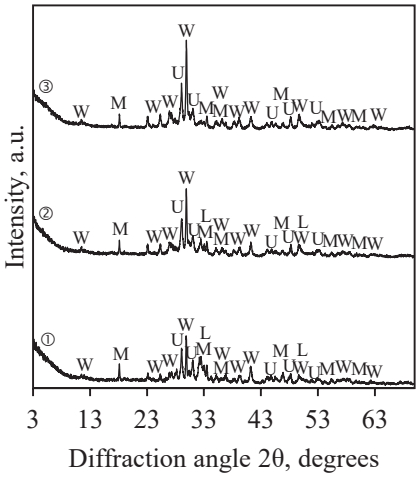


Fig. 3.39. XRD patterns of calcined (900°C 1 h) hydrothermal synthesis (130°C, under stirring, CaO-silica gel waste-H_2O system) products after: 1 – 4 h; 2 – 12 h; and 3 – 48 h
Indices: W – wollastonite; U – cuspidine; L – larnite; M – fluormayenite

According to the XRD data of the calcined samples, in addition to wollastonite and larnite, cuspidine and fluormayenite $Ca_{12}Al_{14}O_{32}F_2$ were identified. The latter crystalline compounds are non-toxic chemically, and thermally they are stable up to 1000°C.

According to the XRD and DSC data, the mineralogical composition variation of the products during the hydrothermal synthesis at 130°C and calcination at 850–1050°C can be presented in the following order:

$$\text{CaO + silica gel waste + } H_2O \xrightarrow[0\text{ h}]{\text{synthesis at 130°C}} \begin{bmatrix}\text{portlandite}\\ \text{C-S-H(I)/(II)}\\ \text{katoite}\\ \text{fluorite}\end{bmatrix} \xrightarrow[8\text{ h}]{\text{synthesis at 130°C}}$$

$$\begin{bmatrix}\text{C-S-H(I)/(II)}\\ \text{katoite}\\ \text{cuspidine}\end{bmatrix} \xrightarrow[48\text{ h}]{\text{synthesis at 130°C}} \begin{bmatrix}\text{tobermorite}\\ \text{C-S-H(I)}\\ \text{katoite}\\ \text{cuspidine}\end{bmatrix} \xrightarrow[850\text{-}1050°C]{\text{calcination at}} \begin{bmatrix}\text{wollastonite}\\ \text{cuspidine}\\ \text{fluormayenite}\\ \text{larnite}\end{bmatrix}$$

To summarise on the results of the two-step synthesis of wollastonite in the CaO-silica gel waste-H_2O system, when hydrothermal synthesis was carried out at 95–130°C, it can be stated that the presently discussed temperature range is not high enough to produce a suitable precursor. The products of hydrothermal synthesis at 95°C contained portlandite, yet no crystalline calcium silicate hydrate phases were observed. After calcination, the dominant phase was larnite. The increment of temperature to 130°C improved the interaction of portlandite, but crystalline calcium silicate hydrate phases (tobermorite) started to form only after 12 h of isothermal curing. After the calcination of the latter precursors, the peaks of wollastonite dominated over the peaks of larnite.

Acknowledgements:

Reprinted/Adapted by permission from *Springer Nature*: Scientific Reports / Synthesis of wollastonite from AlF_3-rich silica gel and its hardening in the CO_2 atmosphere / A. Gineika, R. Siauciunas, K. Baltakys, 9(1):18063-18072. 2019 https://doi.org/ 10.1038/s41598-019-54219-6

3.5. The Application of Wollastonite Samples

3.5.1. Carbonation curing of wollastonite

Two types of wollastonite samples were chosen for the investigation of curing in carbon dioxide atmosphere. The product of hydrothermal synthesis at 130°C for 8 h (Fig. 3.33, curve 3) and calcining at 900°C for 1 h (type 1, Fig. 3.41 a, curve 1) was used for the production of wollastonite-based mortar samples, and their potential for hardening in the CO_2 environment was determined. These synthesis conditions were chosen from the economic point of view because 8 h was the shortest period of time for hydrothermal synthesis to bind portlandite completely, whereas calcination at 900°C for 1 h is sufficient to produce wollastonite.

The product of hydrothermal synthesis at 200°C for 12 h (Fig. 3.33, curve 3) and calcining at 900°C for 1 h (type 2, Fig. 3.41. a, curve 1) was investigated.

The visual appearance of the prepared cylindrical (h = d = 36 mm) binder-sand samples is shown in Fig. 3.40.

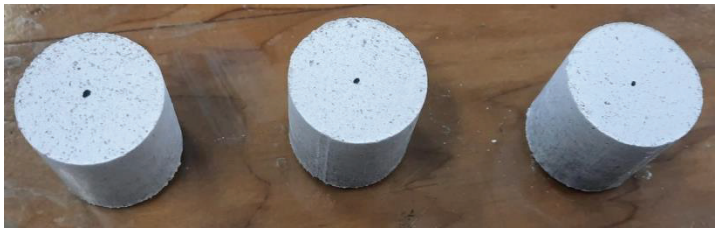


Fig. 3.40. Visual image of the prepared binder-sand samples

Carbonation curing of wollastonite Type 1

It was determined that the main compounds in the binding material before curing (Fig. 3.41. a, curve 1) were wollastonite, cuspidine, and fluormayenite with

some traces of larnite. After curing for 24 h at 45°C and 15 bar CO_2 (Fig. 3.41 a, curve 2), the main components were two polymorphs of calcium carbonate $CaCO_3$: calcite (PDF No. 07-8659, d = 0.3035; 0.1875; 0.2284; 0.1912; 0.2094 nm) and vaterite (PDF No. 67-0200, d = 0.2721; 0.3292; 0.1820; 0.4229; 0.3574 nm) with small amounts of fluormayenite and fluorite CaF_2. Wollastonite, larnite and cuspidine had reacted completely. According to Ashraf *et al*. [60], during the carbonation reaction of wollastonite, XRD-amorphous SiO_2 is released.

According to the STA data (Fig. 3.41. c), the first endothermal effect in the DSC curve (107°C) is typical of the loss of adsorbed water, whereas the second double endothermal effect (640–760°C) is typical of the decomposition of carbonates: the first one (645°C) refers to the decarbonisation of vaterite, while the second one (at 756°C) relates to calcite. This suggests that a very low onset temperature (~500°C) may be related to the decomposition of amorphous calcium carbonate; hence, these results are directly in line with the previous findings [188,189]. The exothermal effect at 872°C belongs to the formation of wollastonite from calcium oxide, a product of the calcination of $CaCO_3$, and amorphous SiO_2, which was released during the carbonation process [6,190].

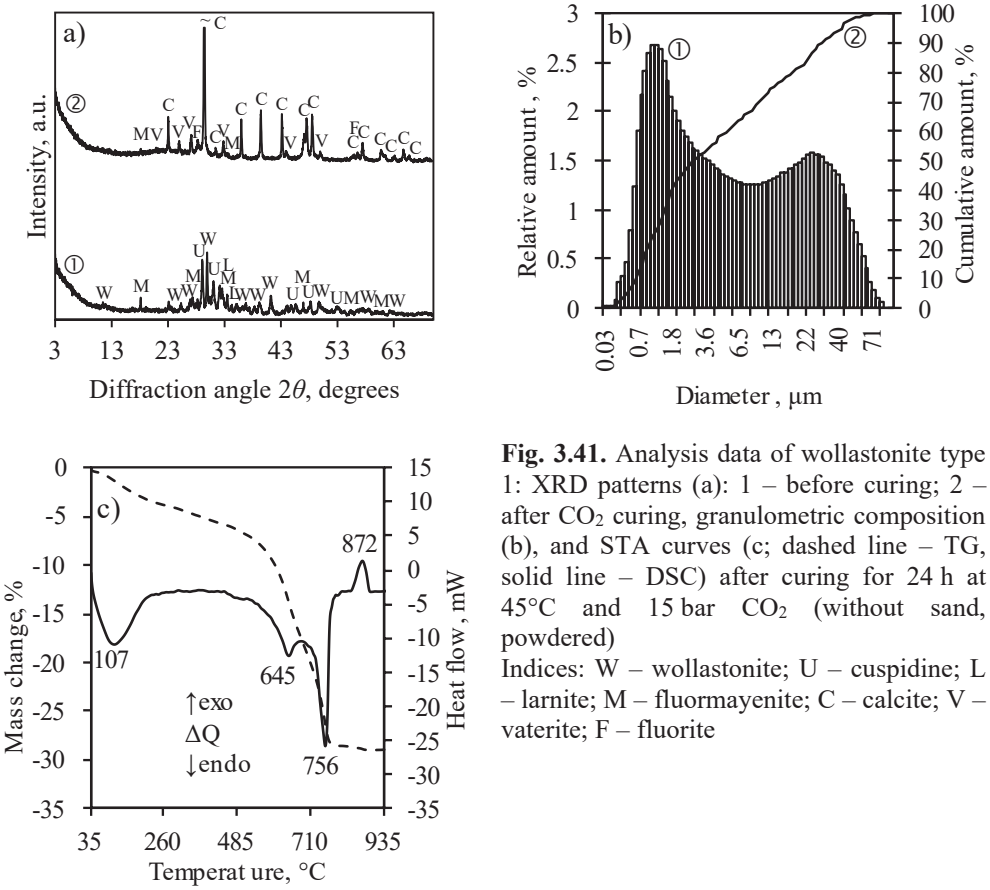


Fig. 3.41. Analysis data of wollastonite type 1: XRD patterns (a): 1 – before curing; 2 – after CO_2 curing, granulometric composition (b), and STA curves (c; dashed line – TG, solid line – DSC) after curing for 24 h at 45°C and 15 bar CO_2 (without sand, powdered)
Indices: W – wollastonite; U – cuspidine; L – larnite; M – fluormayenite; C – calcite; V – vaterite; F – fluorite

It was determined that the compressive strength depends mostly on the amount of the binding material in the samples. By increasing the binding material from 20 to 35 mass%, the strength was boosted more than twice: from 7.34 to 15.68 MPa (Fig. 3.42. a). With the increment of the compaction pressure, when the binder/sand ratio was 1:3 (the amount of binder equals to 25 mass%), the compressive strength goes up by a third: from 9.51 (10 kN) to 12.15 (15 kN) MPa (Fig. 3.42. b). The curing duration had a low impact on the compressive strength as the increase of the compressive strength was only 14%: from 10.64 (4 h) to 12.13 (24 h) MPa (Fig. 3.42. c).

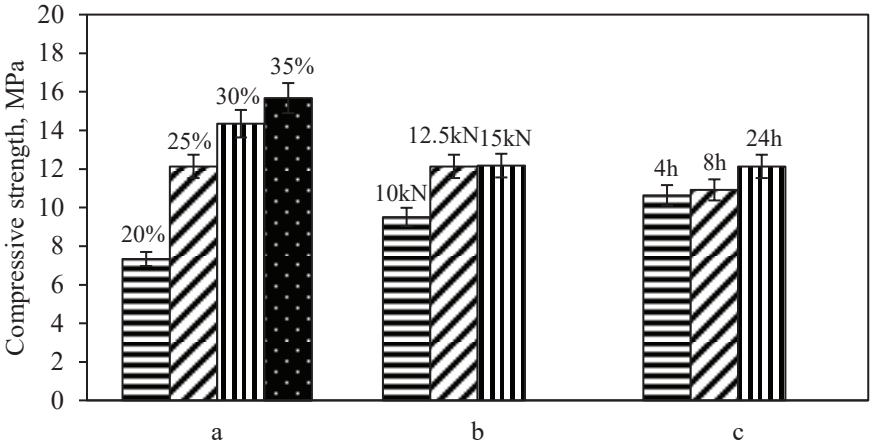


Fig. 3.42. Compressive strength of cured sand-binder (wollastonite type 1) samples dependency on: a – amount of binding material; b – compaction pressure; c – curing duration (a and b – cured for 24 h; b and c – 25 mass% of binding material; a and c – compaction pressure: 12.5 kN)

The degree of carbonation was calculated from the TG data of the samples without sand (water-to-binder ratio = 0.35, compaction pressure 12.5 kN, curing duration: 4, 8, and 24 h), and it was determined that there was ~23 mass% CO_2 in all the samples without sand. The maximum amount of CO_2 that can be stored in the binding material can be calculated by using the Steinour Formula (3.2) [191,192]:

$$CO_2\ (\%max) = 0.785(CaO - 0.7SO_3) + 1.091MgO + 1.420Na_2O + 0.935K_2O \qquad (3.2)$$

here: CaO, SO_3, MgO, Na_2O, and K_2O are the mass percentages of the relevant constituent oxides. In this case, in the initial mixture, there is only CaO = 48.31 mass%. It follows that:

$$CO_2\ (\%max) = 0.785 \cdot 48.31\ \% = 37.92\%.$$

To calculate the degree of carbonation, Formula (3.3) [60] was used:

$$\text{Degree of carbonation, \%} = \frac{\text{Amount of } CO_2 \text{ (mass\%)}}{\text{Maximum amount of } CO_2 \text{ (mass\%)}} \times 100\ \%; \qquad (3.3)$$

$$\text{Degree of carbonation, \%} = \frac{23\%}{37.92\%} \times 100\% = 60.65\%.$$

Acknowledgements:

Reprinted/Adapted by permission from *Springer Nature*: Scientific Reports / Synthesis of wollastonite from AlF_3-rich silica gel and its hardening in the CO_2 atmosphere / A. Gineika, R. Siauciunas, K. Baltakys, 9(1):18063-18072. 2019 https://doi.org/ 10.1038/s41598-019-54219-6

Carbonation curing of wollastonite Type 2

The particles with a diameter of 0.05–60 μm were determined to be present in the synthetic wollastonite Type 2 sample which was prepared for curing in CO_2 atmosphere (Fig. 3.43). The particles with a diameter of up to 30 μm were dominant (>90%). It was calculated that the value of the external surface area was about 250 m^2/kg. The density of the sample was measured to be around 3500 kg/m^3.

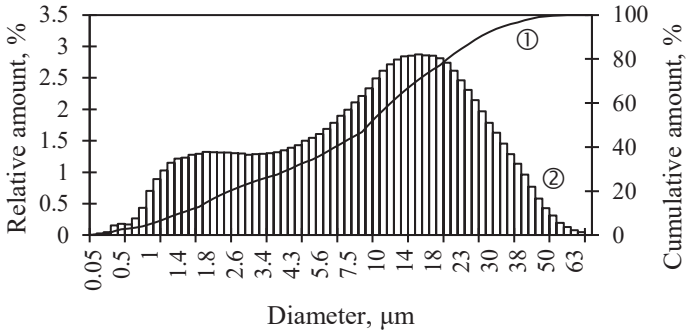


Fig. 3.43. Particle size distribution of synthetic wollastonite Type 2 which was used for CO_2-curing

It was determined that the compressive strength of CO_2-cured synthetic wollastonite-sand samples ranged between from ~14 MPa after 2 hours of curing to ~18 MPa after 8–24 h of curing (Fig. 3.44 a). The maximum value was 1.5 times higher than in the earlier investigation, where synthetic wollastonite, which was obtained after hydrothermal synthesis at 130°C for 8 h, was used. In addition, as in the previous experiment, the strength gain depended on the curing duration in the current case as well. However, the values of compressive strength were by about 2.5–3 times lower than rankinite or calcio-olivine which contain 1.5–2 times more CaO [57,193,194].

The degree of carbonation of wollastonite Type 2 was calculated by using Steinour Formula (Eq. 3.3) and presented in Fig. 3.44 b. It was observed that the values ranged from 42 to 57% and, similarly to the compressive strength, they were dependent on the curing duration. In addition, it was noticed that the values were slightly lower than in the previous investigation where the degree of carbonation was around 60%. Compared to the previous investigation of wollastonite, rankinite and calcio-olivine, a trend can be observed that, with an increment of compressive strength, the degree of carbonation decreases due to the different chemical properties of the binder.

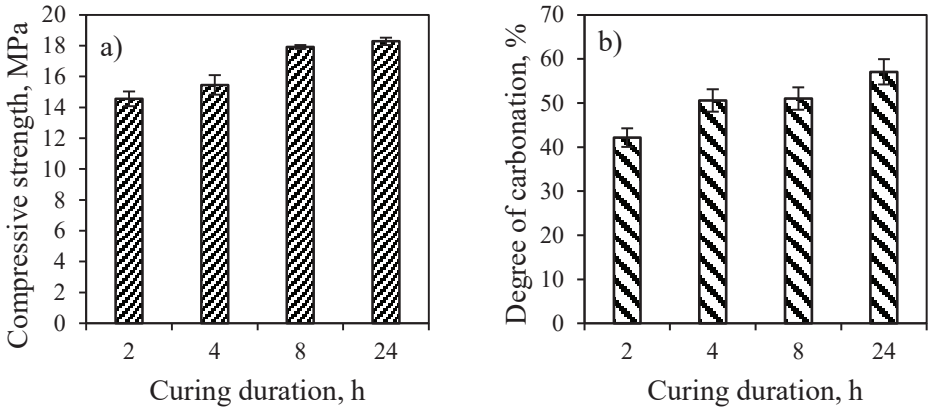


Fig. 3.44. Compressive strength (a) and degree of carbonation (b) of binder-sand (1:3 ratio by mass, wollastonite type 2) samples

The XRD patterns of the carbonated samples (Fig. 3.45. a) were in line with the results of the compressive strength and the degree of carbonation, but were different from the previous investigation. Firstly, the main phase in all the cured samples was calcite, and the intensity of its main peak (*d*-spacing 0.3030 nm) increased from 3170 cps (2 h) to 3980 cps (24 h). Furthermore, unlike in the previous investigation, part of wollastonite remained unreacted, and its traces were still identified in the sample which was cured for 24 h. The intensity of the main peak of wollastonite decreased from 590 cps (2 h) to 190 cps (24 h). The second polymorph of calcium carbonate – vaterite – was identified only in the 24 h sample. In addition, fluormayenite was no longer identified in the carbonated samples. Finally, similarly to the previous findings, fluorite also crystallised after carbonation.

The STA (Fig. 3.45. b) results were in line with the previously conducted analyses. At first, the mass loss in the temperature range of 500–800°C increased from 16% (2 h) to 21.6% (24 h). The mass loss in this range was used to calculate the degree of carbonation. The DSC curves of the cured samples are similar to the previously obtained ones. Here, the main difference is the profile of the endothermal effect of the decomposition of calcium carbonate phases. The earlier samples contained vaterite from the shortest curing durations, thus generating a well-expressed endothermal effect at 645°C (Fig. 3.41. b). However, in this case, an endothermal effect of the 'shoulder' type was observed at ~630°C in the 2–8 h samples which did not contain vaterite (Fig. 3.45 b, curves 1), correspond to the decomposition of amorphous and semi-amorphous calcium carbonate. A modestly expressed endothermal effect at 637°C was observed in the DSC curve of the 24 h sample (Fig. 3.45. b, curves 2), thus indicating the presence of vaterite in the carbonation products. Similarly to the previous case, the exothermal effect at ~855°C belongs to the formation of wollastonite from calcium oxide and amorphous SiO_2 which was released during the carbonation process.

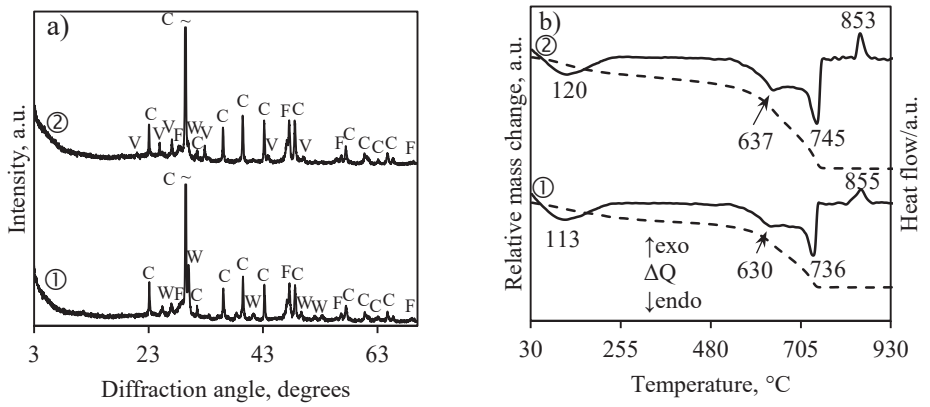


Fig. 3.45. XRD patterns (a) and STA curves (b; dashed – TG; solid – DSC) of wollastonite Type 2 after curing for 1 – 2 h; 2 – 24 h at 45°C and 15 bar CO_2 (without sand, powdered)
Indices: C – calcite; W – wollastonite; V – vaterite; F – fluorite

To conclude on the investigation of CO_2-curing of synthetic wollastonite which was obtained from a higher temperature precursor, it can be stated that the better interaction of raw materials during hydrothermal synthesis ensures that the produced binder will form a denser and stronger structure after curing in CO_2 atmosphere. The compressive strength of Type 2 wollastonite was 1.5 times bigger than that of Type 1; however, the degree of carbonation decreased by 10–15%.

3.5.2. Silane coupling and polymer composites

Most resins in polymer composites are petroleum-derived and non-biodegradable (meth)acrylates, which has a negative impact on the environment [195]. Acrylated epoxydised soybean oil (AESO) is a commercially available biobased material that can be photocross-linked by free radical polymerisation, thus producing a solid, biodegradable polymer [196]. The aim of this experiment was to investigate the application of synthetic wollastonite-based fillers W and WS in order to produce novel AESO-based composites. To improve the performance of the fillers, they were additionally functionalised with acryloxypropyltrimethoxysilane (APTMS) – a silane coupling agent which introduced acrylic groups to the fillers. The presence of the functional groups allowed the fillers to participate in the photocross-linking of the resin. The obtained functionalised fillers were named accordingly: W-C and WS-C.

The FT-IR spectrum of acryloxypropyltrimethoxysilane (APTMS) (Fig. 3.46, curve 1) shows a distinctive peak at 1724 cm^{-1} which refers to the stretching vibrations of the C=O bond in the acrylate fragment of APTMS. Other important peaks were the following: symmetric and antisymmetric stretching of the C–H bond in the methylene CH_2 groups at 2945 cm^{-1} and methyl CH_3 groups at 2842 cm^{-1}, as well as scissors-type stretching at 1466, 1408, 1185 and 775 cm^{-1}, the axial deformation of the C=C bond at 1636 cm^{-1}, the stretching and bending of the Si–O–C bond at 1076 and 810 cm^{-1} [197, 198]. The FT-IR spectra of all the functionalised fillers W-C (Fig. 3.46, curve 2) and WS-C (Fig. 3.46, curve 3 contain a peak at 1724 cm^{-1} which indicates the presence of acrylate fragments (acrylic C=O bond);

therefore, it could be stated that APTMS had reacted with the synthetic wollastonite fillers successfully.

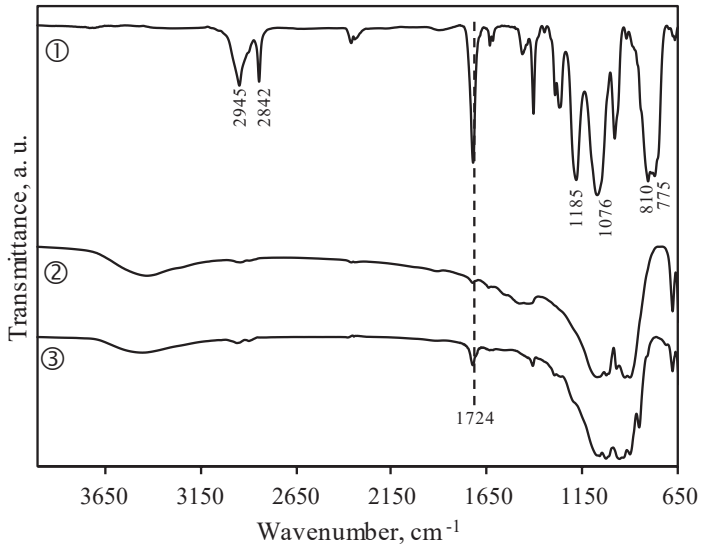


Fig. 3.46. FT-IR curves of: 1 – acryloxypropyltrimethoxysinane, and the modified fillers: 2 – W-C and 3 – WS-C

The DSC data of the functionalised fillers W-C (Fig. 3.47 a) and WS-C (Fig. 3.47 b) showed an exothermal peak in the range of ~340–640°C, which refers to the oxidation and decomposition of the carbon chains of the silane molecules. The mass loss of W-C and WS-C fillers was 3.23 mass% and 3.65 mass%, respectively.

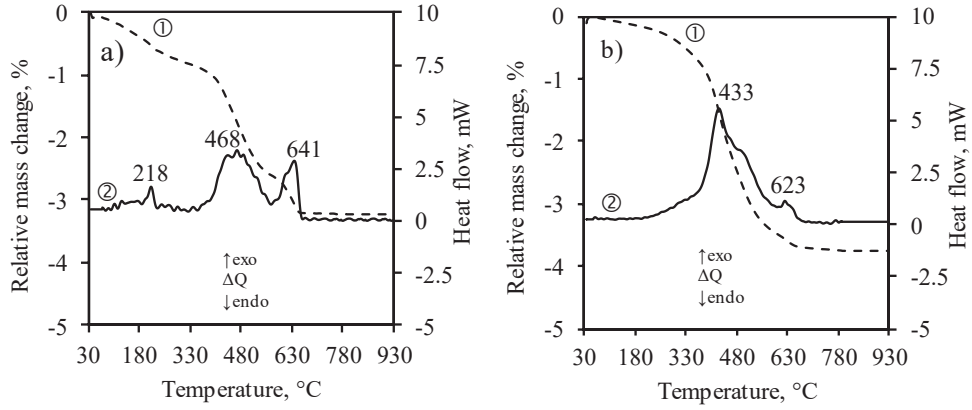


Fig. 3.47. STA curves (1 – TG; 2 – DSC) of the modified fillers: a – W-C; and b – WS-C

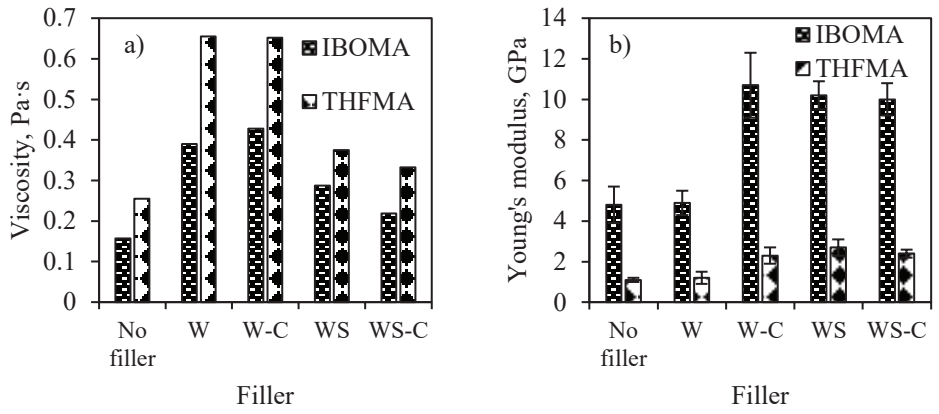
The viscosity values of the AESO-IBOMA mixture (40 mass%:60 mass%, AI resin), and the AESO-THFMA mixture (60 mass%:40 mass%, AT resin) without any filler were 157.4 and 255 mPa·s, respectively (Fig. 3.48 a). The addition of 5 mass% of the fillers W/W-C to the AI and AT resins increased the viscosity by ~2.6 times. It should be noted that the coupling of filler W had no positive effect on the

viscosity of the resins. On the other hand, a positive effect of the coupling of filler WS on the viscosity of the resins was observed. The addition of 5 mass% of fillers WS/WS-C increased the values of the viscosity of AI and AT resins by ~1.6 and ~1.4 times, respectively. The viscosity of the mixtures with the coupled fillers was 24% lower for the AI resin and 11% lower for the AT resin. These results go in line with the general tendency that hydrophobic coating should improve the performance of hydrophilic fillers in resins [199].

It was observed that the addition of filler W hardly changed the Young's modulus of the composite as the values for both AI and AT resins did not differ much from the initial 4.8 and 1.1 MPa, respectively (Fig. 3.48 b). The addition of every other filler increased the Young's modulus by about 2.2 times for both resins.

The dependency of the tensile strength on the filler was observed to be different for each resin (Fig. 3.48 c). Initially, the sample of the filler-free AI resin showed the tensile strength of 69.6 MPa. The addition of uncoupled fillers W and WS improved the strength by 35% and 17%, respectively; however, the addition of the same amount of coupled fillers W-C and WS-C decreased the strength by 28% and 16%, respectively. The effect of fillers on the tensile strength of the AT resin composites was similar to the effect on the Young's modulus. It was observed that the addition of filler W only slightly increased the value: from the initial 65.1 to 69.6 MPa. Yet, the addition of every other filler improved the tensile strength to ~93 MPa, or by ~43%.

The elongation at break was observed to be negatively impacted by the addition of fillers. The initial value of the AI resin sample was 1.4%. Only the addition of filler W improved the value by 50%, while the other fillers reduced it by 45–60%. The initial elongation at break of the AT resin samples was 18.5%. The addition of the filler reduced the value by 12.7%, W-C by 27.6%, WS by 21%, and WS-C by 12.2%. These results correspond to the changes of the Young's modulus because all the samples which became stiffer due to addition of a filler had their elongation at break value decreased.



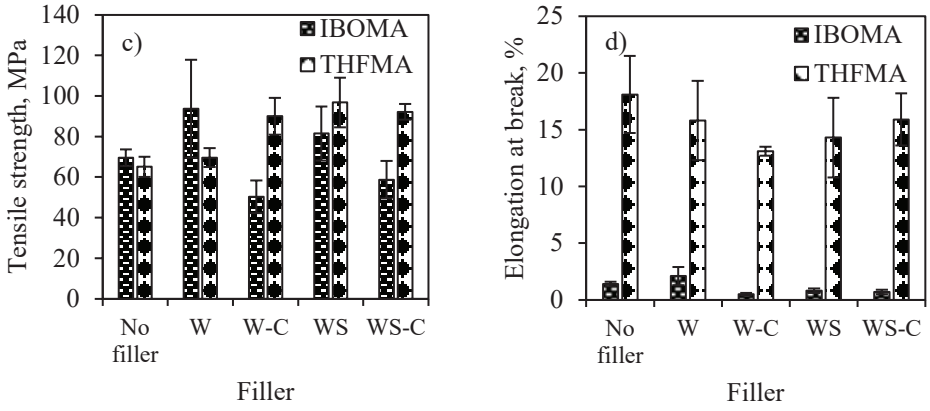


Fig. 3.48. The mechanical properties of wollastonite-polymer composite samples: a – viscosity of uncured resin; b – Young's (elastic) modulus; c – tensile strength; and d – elongation at break

In general, it can be summed up that the addition of wollastonite-based fillers, either coupled with acryloxypropylsilane or uncoupled, produced harder samples than the filler-free resin samples. The developed calcium silicate and soybean derived resin composites have a great potential to be a competitive alternative to the conventional petroleum-derived ones and can reduce the negative impact on the nature.

3.5.3. Optically 3D printed silicate-polymer scaffolds

Optical 3D printing technologies, such as digital light processing (DLP), in which liquid resins are layer-by-layer photocross-linked under ultraviolet (UV) irradiation, are renowned for their high printing accuracy which can reach micro- and nanoscale as well as a high printing-curing speed in the range of s or min. The thermal 3D printing, however, is a cheaper technology, yet it is limited to the micro-, macroscale and larger objects, and by a finite range of usable thermoplastics. Although the materials for the optical printing are more expensive, but, on the other hand, the composition of the resins is unlimited. In addition, optical 3D printing is a more environmentally friendly technology because the process takes place at room temperature, and no volatile substances are released. Glycerol dimethacrylate is a biobased monomer which originates from natural oils after their conversion into biodiesel, and the application of the material contributes to the valorisation of glycerol.

The results of thermogravimetric analysis show that all three green bodies decomposed in a similar way (Fig. 3.49). The first mass loss of ~7% (Table 3.11) occurred at RT-220°C, which can be attributed to the decomposition of insoluble oligomers which did not adhere well to the main polymer matrix. Meanwhile, the main decomposition of the green bodies starts at ~220–235°C. This stage consists of two coupled reactions because two inflection points can be identified at ~300 and 360°C, and the separation temperature between the processes is ~340°C. The sum mass loss of the coupled reaction is ~70%, but the mass loss from the start to the

intersection is the double value of that of the second process. The literature does not cover the decomposition of the polymer sufficiently [200,201]: the first reaction may be attributed to the release and decomposition of methacrylate, whereas the second reaction can be attributed to the same processes of glycerol. The mass loss ratio (2:1) of the processes corresponds to the molar mass ratio of methacrylate and glycerol in the glycerol dimethacrylate monomer. The third stage of decomposition may be attributed to the breakdown of the polymer which was absorbed by the filler particles which could delay the exposure to air. With the exception of WS, the decomposition temperatures T_{d5} and T_{d10} of the remaining green bodies were ~160 and 240–270°C. The $T_{d5\%}$ and $T_{d10\%}$ temperatures of the WS green body were 260 and 362°C, respectively. The temperature change is related to the lower mass loss during the first stage compared to the other green bodies. This may show that the presently mentioned green body could reach the highest degree of cross-linking. The residual mass of the green bodies was lower than the theoretical value (12.5% for W, 20% for others), thus indicating sedimentation of the filler particles, and it could also be possible for the volatile decomposition compounds to carry away a part of loosely attached filler fragments.

Table 3.11. Results of thermogravimetric analysis of green bodies

Sample	1st stage	2nd stage	3rd stage	4th stage	5% and 10% mass loss	Residue, mass%
W	RT-235°C	235–343°C	343–426°C	462–549°C	158 and 270°C	9.12
	–8.8 mass%	–50.87 mass%	–21.98 mass%	–8.54 mass%		
WS	RT-235°C	235–335°C	335–421°C	421–540°C	260 and 279°C	18.79
	–4.08 mass %	–43.65 mass%	–24.54 mass%	–8.51 mass%		
WD	RT-253°C	254–354°C	354–427°C	427–571°C	161 and 237°C	13.70
	–10.88 mass%	–51.99 mass%	–15.08 mass%	–8.02 mass%		

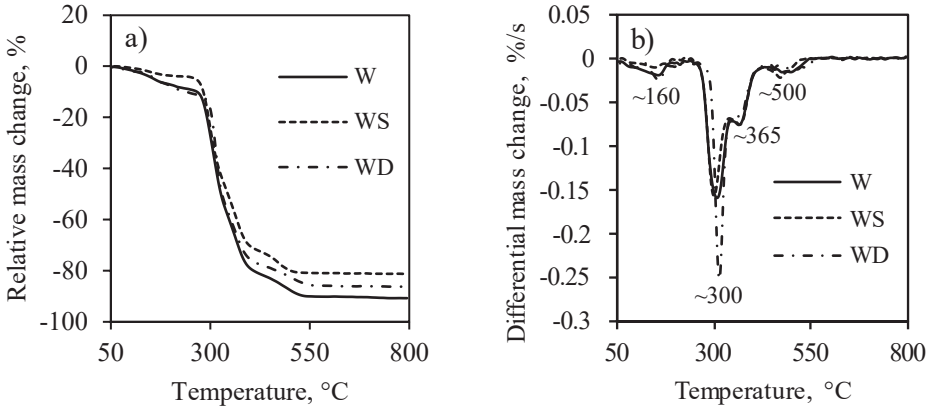
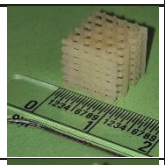
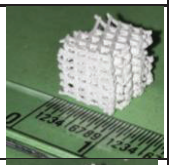
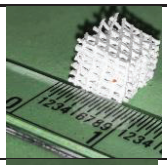
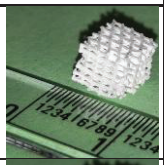
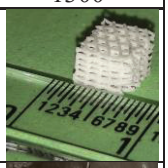
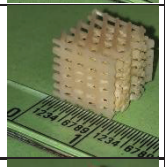
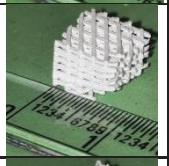
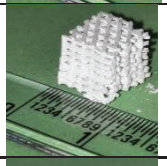
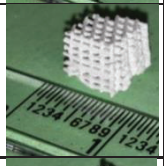
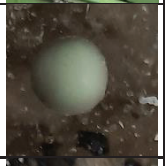
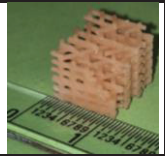
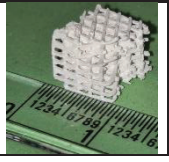
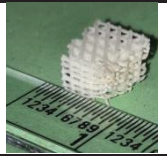
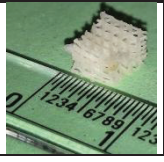


Fig. 3.49. Thermal analysis results of the green bodies: a – TG; and b – DTG

During the sintering process (Table 3.12), the weakly attached outer parts were observed to wrinkle slightly. In addition, the green bodies were well distinguishable by their colour, however, the sintered samples were almost completely white with the exception of the WD samples. The green body scaffold of the latter precursor appeared pinkish in colour, and slight shading remained after sintering at 1100°C. At 1200–1300°C, only the WD scaffold appeared to be slightly fused and translucent. However, at 1300°C, only the W scaffold remained intact, while the WS scaffold melted down, and WD underwent heavy deformation and adhered strongly to the platinum plate. Both deformation and fusion were caused by the presence of F^- ions which lowered the melting temperature of silicate materials [202]. However, it is possible that cuspidine, which was abundant in the WS scaffold, did not promote fusion and vitrification, meanwhile, fluorite, which was present in the WD, might have done that [203].

Table 3.12. Visual appearance of scaffolds before and after sintering

		Temperature, °C				
		25	1100	1200	1250	1300
Precursor	W					
	WS					
	WD					

The shrinkage of the scaffolds was observed to be strongly dependent on the sintering temperature (Fig. 3.50. a). After sintering at 1100°C, W and WD scaffolds shrank by about 40%, and the WS scaffold shrank by ~60%. The subsequent temperature increase showed that the latter scaffold was less prone to shrinkage. After sintering at 1300°C, both W and WD scaffolds shrank by 90–95%.

The compressive strength (Fig. 3.50. b) of the green bodies was measured to be around ~2 MPa. The sintering at 1100°C only removed the polymer matrix, but it did not fuse the filler particles, and all the scaffolds were thus extremely brittle and were measured to have almost zero compressive strength. At least 1200°C was required for the particles to fuse and for the scaffolds to gain strength: W and WS showed ~0.1 MPa, meanwhile the WD scaffold, which started vitrifying, showed 0.35 MPa. The same trend was also observed at 1250°C: W and WS reached about 0.2 MPa, and the WD scaffold reached about 0.85 MPa. However, at 1300°C, the

WD sample became unsuitable for the compressive strength test due to deformations and adhesion; this is not to mention the WS sample which had molten down. The W scaffold, which was the only one to remain intact at 1300°C, reached only 0.36 MPa. In summary, F^- ions from CaF_2 may help to improve the mechanical properties of scaffolds, while fluoride ions from cuspidine $Ca_4Si_2O_7F_2$ do not achieve that. Other works have also observed that 3D-printed scaffolds from pure wollastonite often exhibit poor mechanical properties and must be mixed with additives [101].

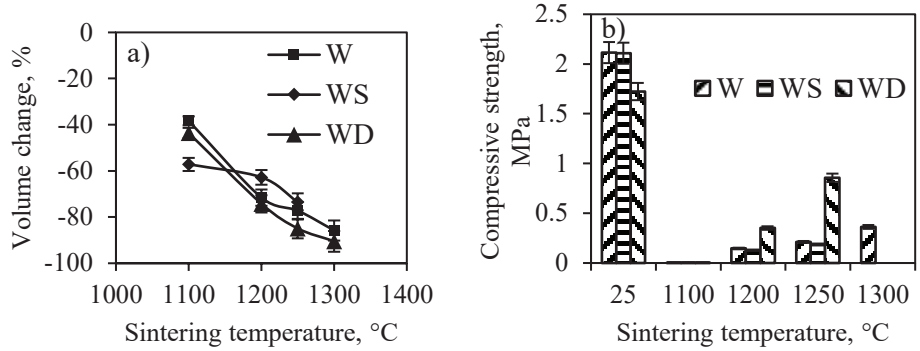


Fig. 3.50. Influence of the sintering temperature on the properties of printed scaffolds: a – volume change; b – compressive strength

To sum up on the application of synthetic wollastonite samples for 3D printed scaffolds, it can be stated that the particles of the synthetic materials (especially sample W synthesised by using amorphous hydrated silica) alone do not fuse well enough to produce strong structures. Furthermore, the amount of F^- ions in the WS sample (synthesised by using raw silica gel waste) makes the sintering temperature harder to control. On the other hand, the WD sample (synthesised by using defluorinated silica gel waste) contained less F^- ions and showed better results.

3.6. Formation of Cuspidine in the $CaO\text{-}SiO_2\cdot nH_2O\text{-}CaF_2\text{-}H_2O$ System

In previous parts of this work, cuspidine was observed to form together with calcium silicates or calcium silicate hydrates if the system contained F^- ions (CaO-silica gel waste-H_2O or $CaO\text{-}SiO_2\cdot nH_2O\text{-}AlF_3\text{-}H_2O$ systems). However, there is no scientific literature on its formation and the influence on the common properties of cement hardened in CO_2 atmosphere. Thus, the main objective of this part of the work was to investigate the influence of the temperature, duration, and the source of SiO_2 in the initial mixture with the molar $CaO/SiO_2/CaF_2$ ratio (3:2:1) on the cuspidine formation via two-step synthesis, and to investigate the behaviour of synthetic cuspidine samples during hydration and CO_2-curing.

The results of X-ray diffraction (Fig. 3.51 a) showed that, within 4 h at 95–130°C, the reaction proceeded with difficulty because only traces of C-S-H(I) were identified together with the initial compounds – portlandite $Ca(OH)_2$ and fluorite CaF_2. Calcite $CaCO_3$ formed during drying due to the interaction of the sample with atmospheric CO_2. Portlandite and fluorite were still unreacted after 4 h of isothermal curing at 150°C. After increasing the temperature up to 170–200°C, cuspidine dominated in the products, and portlandite was no longer identified; however,

fluorite was still observed in the mixture. When isothermal curing was prolonged to 12 h (Fig. 3.51. b), cuspidine was identified in the products obtained as early as at 130°C, and the mineral composition of the sample was similar to the one obtained at 150°C within 4 h. In the temperature range of 150–200°C, cuspidine and fluorite with traces of calcite were identified in the synthesis products. The XRD peak area was determined from the main diffraction peak of a compound: fluorite – *d*-spacing 0.3157 nm and cuspidine – *d*-spacing 0.3051 nm.

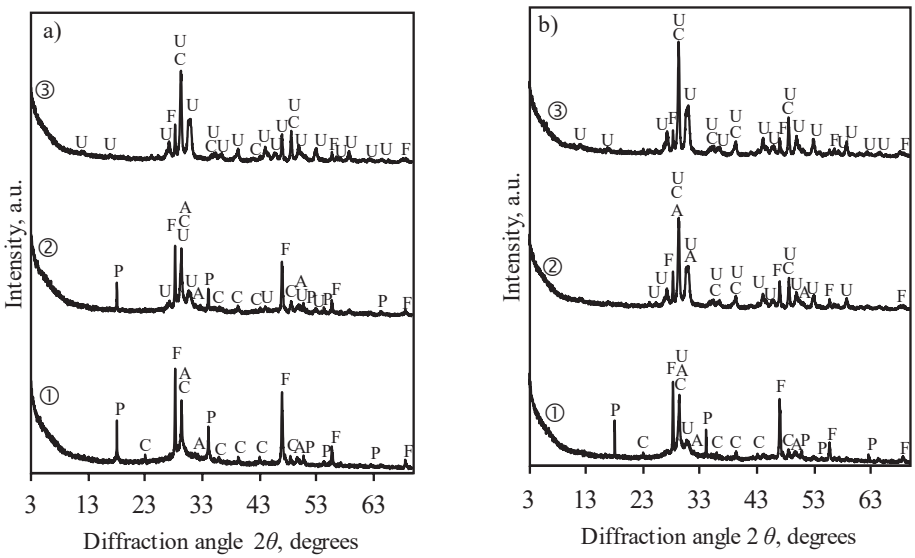


Fig. 3.51. XRD patterns of synthetic cuspidine samples synthesised for: a – 4 h (1 – 95°C; 2 – 150°C; 3 – 170°C); and b – 12 h (1 – 130°C; 2 – 150°C; 3 – 200°C) in $CaO\text{-}SiO_2 \cdot nH_2O\text{-}CaF_2\text{-}H_2O$ system

Indices: P – portlandite; F – fluorite; C – calcite; A – C-S-H(I); U – cuspidine

In the XRD patterns, it was observed that fluorite reacted slowly at 95 and 130°C (Fig. 3.52 a) because the area of the main peak of the compound (*d*-spacing 0.3157 nm) decreased from 4.735 a.u. to 4.379–3.943 a.u. Furthermore, in the temperature range of 150–170°C, the decrement of the relative area was more significant: it decreased to 2.029–0.9911 a.u., respectively. In addition, in the above mentioned temperature range, a considerable difference was observed between the values of the 4 and 12 h samples, which could indicate its increased activity at the afore-stated temperatures. Finally, at 200°C, the relative area of the main peak of fluorite decreased to 25% of the initial value – 1.229 a.u. – after 4 h, and to 20% – 0.9537 a.u. – after 12 h.

Simultaneously, while the area of the main peak of fluorite decreased, the area of the main peak of cuspidine (*d*-spacing = 0.3051 nm) increased and reached the peak value of 11.48 a.u. at 200°C after 12 h of synthesis. It was observed that the temperature of 95°C was insufficient for cuspidine to form, and this correlated with the activity of fluorite. At an increased temperature (130–170°C), there was a significant increase in the area of the main peak of cuspidine: 5.746 a.u. at 130°C,

9.745 a.u. at 150°C, and 11.28 a.u. at 170°C. Similarly to fluorite, a difference was observed between the peak area values in 4 h and 12 h samples at 130–170°C, which indicated the formation of cuspidine. The difference between the values at 200°C was negligible, which suggests that the maximum amount of cuspidine under the given conditions could have formed within 4 h.

The results of simultaneous thermal analysis (Fig. 3.52. b) are well consistent with the XRD results. The endothermal effect in the range of 30–250°C is common to the dehydration of semi-crystalline calcium silicate hydrates, such as C-S-H(I) and C-S-H(II), as well as adsorbed moisture [159]. The endothermal effect at ~445°C is common to the decomposition of portlandite (Fig. 3.52. b, curve 1) [204], and the endothermal effect at ~690°C indicates the decomposition of calcium carbonate. The exothermal effect at ~850°C is common to the recrystallisation of semi-crystalline calcium silicate hydrate phases into wollastonite (Fig. 3.52. b, curves 1 and 2) [159,204]. The latter effect was not present in the sample obtained at 200°C (12 h) (Fig. 3.52. b, curve 3), which suggests that the amount of semi-crystalline phases was negligible, and the evaporation of adsorbed moisture was taking place instead. In addition, the mass loss in the aforementioned sample (up to 930°C) was ~3.6 mass% (~1 mass% was lost during the decomposition of calcium carbonate), while the mass loss in the samples obtained at lower temperatures were: 95°C – ~20 mass%, 130°C – ~15 mass%, 150°C – ~6 mass%, 170°C – ~4 mass%. In the samples obtained up to 150°C, a part of portlandite was still present. The results of the thermal analysis indicated that, at 200°C, under hydrothermal treatment, within 12 h, nearly anhydrous cuspidine was obtained.

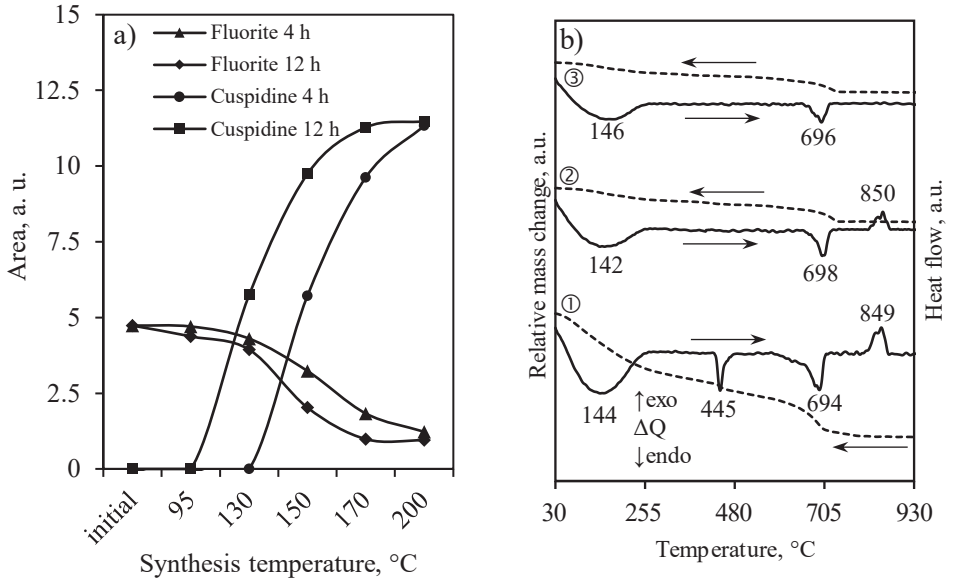


Fig. 3.52. Area (a) of the main peak of fluorite (*d*-spacing 0.3157 nm) and cuspidine (*d*-spacing 0.3051 nm) in XRD patterns and STA (b, DSC – solid line; TG – dashed line) curves of synthetic cuspidine samples in $CaO\text{-}SiO_2 \cdot nH_2O\text{-}CaF_2\text{-}H_2O$ system: 1 – 130°C 12 h; 2 – 170°C 12 h; and 3 – 200°C 12h

The hydrothermally synthesised samples were also investigated by using FT-IR analysis (Fig. 3.53 a). The main absorption peaks in the spectra were those which indicated the silicate structure: a broad peak in the range of 400–600 cm^{-1} is common to the deformation or bending of the O–Si–O bond, whereas the absorption peak at ~660 cm^{-1} is common to the vibration of the bending of the Si–O–Si bonds. Another broad absorption band is in the range of 780–1100 cm^{-1}, which is characteristic of the bending and stretching vibrations of Si–O bonds in the [SiO_4] tetrahedra. Hydration of the obtained products was confirmed by a broad absorption band in the range of 3200–3650 cm^{-1}, which is common to OH^- groups, while an absorption peak at ~1640 cm^{-1} corresponds to the deformational vibrations of water molecules. FT-IR analysis also confirmed the presence of carbonates as the absorption peaks at ~1420 and 874 cm^{-1}, which are common to the C–O bonds in the CO_3^{2-} anion, were identified. It should be noted that the intensity of the silicate-related absorption bands increased with the increasing synthesis temperature, thus indicating the formation of more ordered silicate compounds [141,205,206].

The SEM image of a sample obtained at 200°C within 12 h under hydrothermal treatment (Fig. 3.53 b) shows that a hydrothermally synthesised cuspidine sample exhibits a scaffold-like nanostructure and is more similar to low-basic semi-crystalline calcium silicate hydrates rather than to dense calcium silicates of high basicity, such as larnite (belite) or hatrurite (alite) [207].

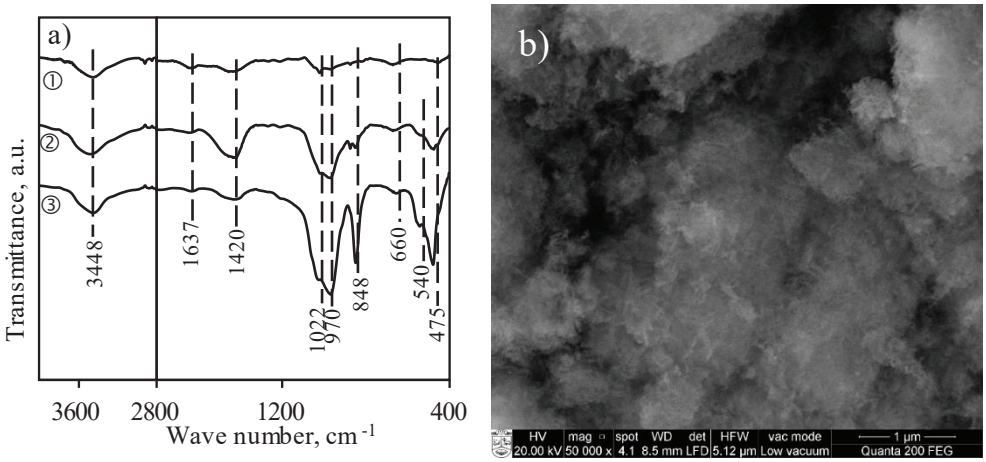


Fig. 3.53. FT-IR curves (a) of hydrothermally synthesised samples at 1 – 95°C; 2 – 130°C; 3 – 200°C for 12 h from $CaO\text{-}SiO_2 \cdot nH_2O\text{-}CaF_2$ mixture; and SEM image (b) of the hydrothermally synthesised sample at 200°C for 12 h from the presently mentioned mixture

In order to investigate the texture and porosity of hydrothermally synthesised cuspidine, nitrogen gas adsorption porosimetry was performed, and the Brunauer-Emmett-Teller (BET) Equation was employed for calculations. According to IUPAC, when the C_{BET} constant is in the range of 50–100, and the isotherm is not nearly horizontal at the maximum p/p_0 values, the N_2 sorption-desorption isotherm (Fig. 3.54. a) can be classified as Type II, which is common to non-porous or macroporous materials. Furthermore, the narrow vertical hysteresis loop at the maximum p/p_0 values of the isotherm suggests that cylindrical pores were dominant

in the sample. On the other hand, the rapid increase in the adsorbed volume can also indicate the formation of a multilayer of nitrogen molecules [174,208].

As the BET model can describe the obtained Type II adsorption-desorption isotherm, the N_2 adsorption isotherm was also plotted in the BET coordinates (Fig. 3.54. b). The graph obtained with the BET equation shows a linear profile in the range of relative pressure (p/p_0) of 0.05–0.35 with the correlation coefficient R^2 equal to 0.9997. According to the literature, the most reliable results of S_{BET} calculations are obtained when the value of the C_{BET} constant is in the range of 50–250 [172,174]. The value of the C_{BET} constant of the sample was determined to be 60.53; therefore, the calculated specific surface area that is equal to 56.90 m^2/g can be considered correct.

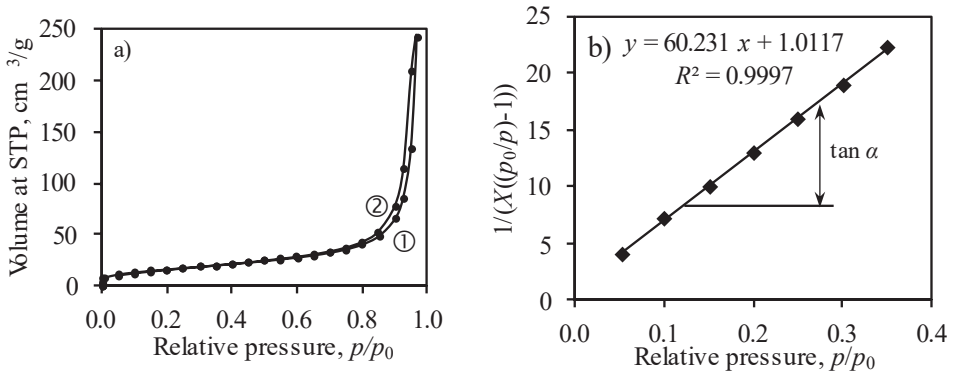


Fig. 3.54. BET analysis results of hydrothermally synthesised sample (200°C, 12 h): a – adsorption (1) and desorption (2) isotherms of N_2; b) – adsorption isotherm of N_2 in BET plots

To summarise on the hydrothermal synthesis in the $CaO\text{-}SiO_2 \cdot nH_2O\text{-}CaF_2\text{-}H_2O$ system (Table 3.13), it can be stated that cuspidine starts to form at 130°C; however, at this temperature, it requires a prolonged duration of isothermal curing (more than 4 h). At a higher temperature (150–200°C), the mineral started to form within 4 h. Since the CaO/SiO_2 molar ratio of the initial mixture is 1.5, the synthesis requires 170–200°C for portlandite to react completely. However, the temperature range of 95–200°C was not sufficient for fluorite to get bound completely.

Table 3.13. Products of hydrothermal synthesis in $CaO\text{-}SiO_2 \cdot nH_2O\text{-}CaF_2\text{-}H_2O$ system

<table>
<tr><th></th><th>95°C</th><th>130°C</th><th>150°C</th><th>170°C</th><th>200°C</th></tr>
<tr><td>4 h</td><td rowspan="2">portlandite, fluorite, C-S-H(I), (calcite)</td><td></td><td>portlandite, fluorite, cuspidine, (calcite)</td><td rowspan="2">cuspidine, fluorite, (calcite)</td><td></td></tr>
<tr><td>12 h</td><td>portlandite, fluorite, cuspidine, (calcite)</td><td></td><td></td><td></td></tr>
</table>

In addition (Table 3.13), no crystalline intermediate phases were identified as a high amount of fluoride ions blocked the formation of possible crystalline calcium silicate hydrates which could match the CaO/SiO_2 molar ratio of the mixture, such as afwillite or jennite (CaO/SiO_2 = 1.5), or killalaite (CaO/SiO_2 = 1.6). Instead, cuspidine $Ca_4Si_2O_7F_2$ formed from semi-crystalline calcium silicate hydrates, as only C-S-H(I) was identified in the temperature range of 95–130°C when cuspidine was not yet identified.

Acknowledgements:

Reprinted/Adapted by permission from *Springer Nature*: Springer Nature; Journal of Thermal Analysis and Calorimetry / The effect of hydrothermal treatment conditions and silica source on the formation of cuspidine / A. Gineika, K. Baltakys, 148:3965–3974. 2023 https://doi.org/10.1007/s10973-023-12022-6; License No. 5574040260515.

3.7. The Formation of Cuspidine in the CaO-silica Gel Waste-CaF_2-H_2O System

For the investigation of the formation of cuspidine in the CaO-silica gel waste-CaF_2-H_2O system, reagent grade amorphous silica $SiO_2 \cdot nH_2O$ was replaced with silica gel waste. In this case, the synthesis was carried out at 200°C for 4–48 h under stirring.

The XRD patterns of the obtained samples (Fig. 3.55. a) showed a similar trend of cuspidine formation compared to amorphous hydrated silica. In addition, some fluorite was also identified. A new compound in the system was katoite $Ca_3Al_2(SiO_2)_{0.5}(OH)_{10}$ which formed due to the presence of Al^{3+} ions in the silica gel waste. No significant differences were observed between the XRD patterns of the samples obtained in 12 and 48 h. Therefore, it can be stated that the reaction reached equilibrium in 12 h, and the products remained stable up to 48 h.

Simultaneous thermal analysis (Fig. 3.55. b) confirmed the results obtained by XRD: the endothermal effect at ~394°C is common to the decomposition of katoite [209]. However, the analysis showed an increase in the mass loss and endothermal effect in the range of 50–260°C, which is related to the increased hydration of the sample compared to the samples obtained by using hydrated silica. Furthermore, an endothermal effect was observed at ~645°C, which is common to the decomposition of calcium carbonate. The mass loss of the obtained samples was: 9.67 mass% for the sample obtained within 4 h, 7.70 mass% within 12 h, 7.90 mass% within 24 h, and 7.35 mass% within 48 h. The average mass loss of ~7.65 mass% for the samples obtained within 12–48 h also confirmed the XRD results, which indicates that the reaction reached equilibrium within 12 h.

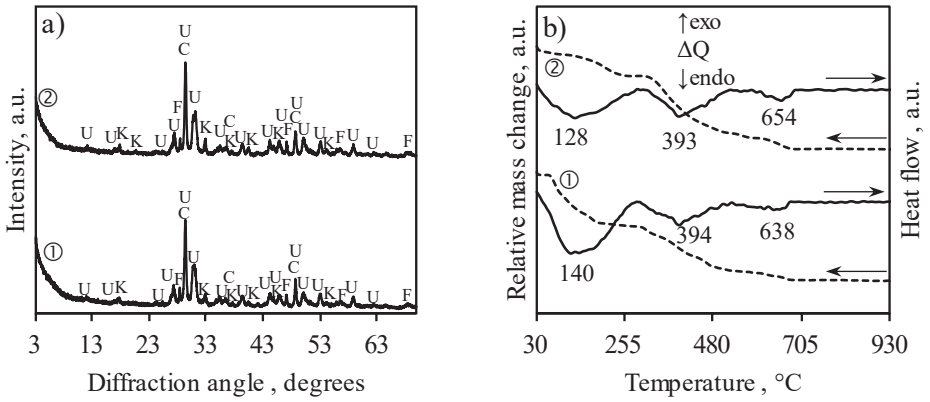


Fig. 3.55. XRD (a) and STA (b, DSC – solid line; TG – dashed line) curves of hydrothermally synthesised samples at 200°C for 1 – 12 h; 2 – 48 h from CaO-silica gel waste-CaF_2-H_2O system
Indices in XRD patterns: U – cuspidine; F – fluorite; K – katoite; C – calcite

In the XRD patterns, it was observed that the area of the main peak of fluorite (*d*-spacing 0.3157 nm, Fig. 3.56) decreased to 22% of the initial value – specifically, from 3.64 to 0.79 a.u. – within 4 h, and it did not undergo any further significant changes up to 48 h. On the contrary, the relative area of the main peaks of cuspidine (*d*-spacing 0.3051 nm) in the synthesis products was already 9.6 a.u. and reached 10.3 a.u. within 48 h. Therefore, it can be stated that, at 200°C, the consumption of fluorite and the formation of cuspidine proceeded in a similar way both in the system of hydrated amorphous silica and in silica gel waste.

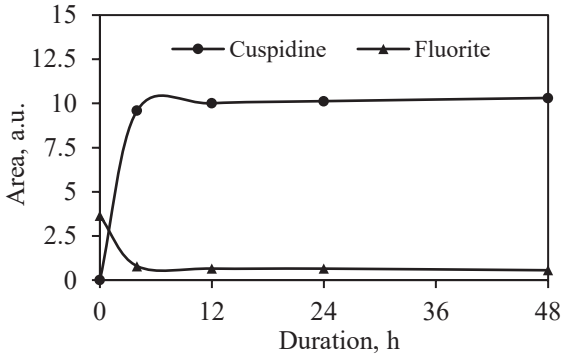


Fig. 3.56. Area of the main peak of fluorite (*d*-spacing 0.3157 nm) and cuspidine (*d*-spacing 0.3051 nm) in XRD patterns (CaO-silica gel waste-CaF_2-H_2O system)

The FT-IR analysis results (Fig. 3.57. a) showed that the aluminium ions that were in the silica gel waste increased the intensity of the adsorption bands of the silicate structure, and now they were similar to the patterns of the samples with amorphous hydrated silica obtained at 95°C. However, the position of the bands remained the same: a broad band in the range of 400–600 cm^{-1} of the O–Si–O

bonds, 660 cm^{-1} of the Si–O–Si bonds, and a broad band in the range of 770–1100 cm^{-1} of the [SiO_4] tetrahedra. The adsorption bands which indicate hydration (3200–3650 and 1640 cm^{-1}) were more intense compared to the previous case as well. The FT-IR analysis, similarly to STA and XRD, also proved that the presence of carbonate anions in the samples as adsorption bands in the range of 1420–1500 cm^{-1} was identified.

The SEM image of a sample obtained after synthesis for 12 h (Fig. 3.57. b) showed that the structure of cuspidine synthesised by using silica gel was similar to cuspidine synthesised by using reagent grade amorphous hydrated silica.

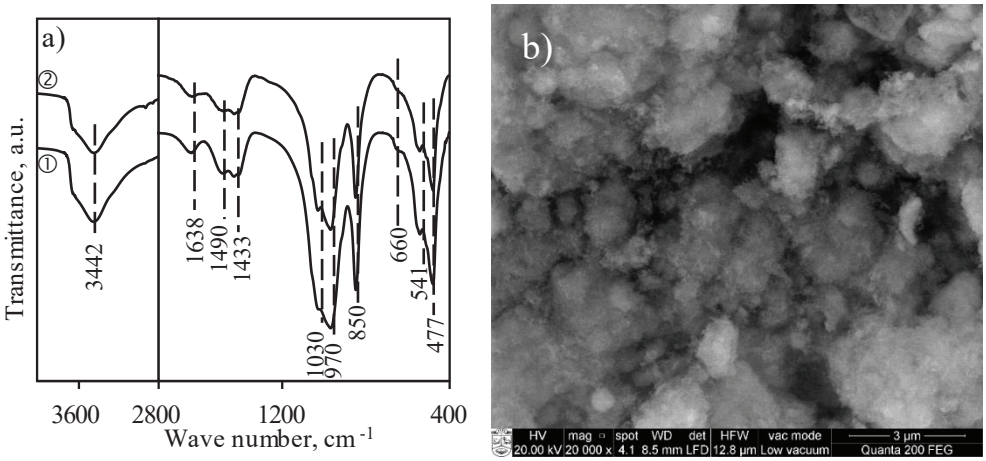


Fig. 3.57. FT-IR curves (a) of hydrothermally synthesised samples at 200°C for 1 – 12 h; 2 – 48 h from CaO-silica gel waste-CaF_2-H_2O system; and SEM image (b) of the hydrothermally synthesised sample at 200°C for 12 h from the afore-mentioned mixture

To conclude on the hydrothermal synthesis experiment in the CaO-silica gel waste-CaF_2-H_2O system, it can be stated that, at 200°C, the reaction was complete within 4–12 h, and the main product was cuspidine with admixture of katoite. However, similarly to the system with amorphous hydrated silica, part of fluorite remained unreacted:

$$\text{CaO+Silica gel waste+}CaF_2\text{+}H_2O \xrightarrow[\text{at 200°C for 4-48 h}]{\text{Hydrothermal synthesis}} \begin{bmatrix}\text{cuspidine}\\ \text{katoite}\\ \text{fluorite}\end{bmatrix}$$

Acknowledgements:

Reprinted/Adapted by permission from *Springer Nature*: Springer Nature; Journal of Thermal Analysis and Calorimetry / The effect of hydrothermal treatment conditions and silica source on the formation of cuspidine / A. Gineika, K. Baltakys, 148:3965–3974. 2023 https://doi.org/10.1007/s10973-023-12022-6; License No. 5574040260515

3.8. Direct Synthesis and Calcination of Hydrothermally Synthesised Precursors of Cuspidine

3.8.1. Direct synthesis of cuspidine

$CaO\text{-}SiO_2 \cdot nH_2O\text{-}CaF_2$ and CaO-silica gel waste-CaF_2 systems

In both systems (Fig. 3.58 a and b), the interaction between the initial materials at 900°C was determined to be weak, and only traces of new compounds kumtyubeite $Ca_5Si_2O_9F_2$ (PDF No. 29-0324) and larnite β-Ca_2SiO_4 (PDF No. 33-0302) were identified, while calcium oxide CaO and fluorite CaF_2 dominated in the samples. Fluormayenite $Ca_{12}Al_{14}O_{32}F_2$ was present in the system with silica gel waste as it contained aluminium ions. A similar trend was visible after calcination at 1000°C with larnite being the main product. Cuspidine $Ca_4Si_2O_7F_2$ formed only at 1100°C in both systems, thus leaving no unreacted calcium oxide; however, some calcium fluoride still remained in the products, especially in the sample with amorphous silica. This sample also contained calcio-olivine γ-Ca_2SiO_4 (PDF No. 49-1672). When silica gel waste was used for the sintering at 1100°C, only traces of larnite remained. It was observed that the peak profile of fluormayenite did not depend on the calcination temperature.

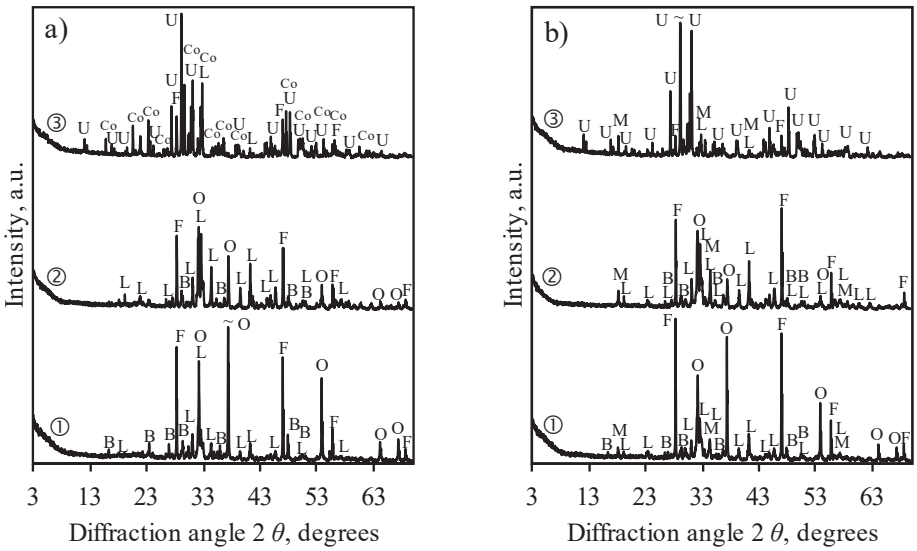


Fig. 3.58. XRD patterns of calcined mixtures for 1 h in: a) $CaO\text{-}SiO_2 \cdot nH_2O\text{-}CaF_2$; b) CaO-silica gel waste-CaF_2 systems at 1 – 900°C; 2 – 1000°C; and 3 – 1100°C
Indices: B – kumtyubeite; F – fluorite; O – lime; L – larnite; U – cuspidine; M – fluormayenite; Co – calcio-olivine

SEM images (Fig. 3.59) of the samples were taken which were obtained after sintering at 1100°C because cuspidine dominated only at this temperature. The images showed that the silica source strongly influenced the formation and texture of cuspidine. Amorphous hydrated silica (Fig. 3.59. a) promoted the formation of

roundish smooth and densely packed/fused particles, while silica gel waste (Fig. 3.59. b) led to the formation of a more porous scaffold-like structure without distinguishable separate fragments.

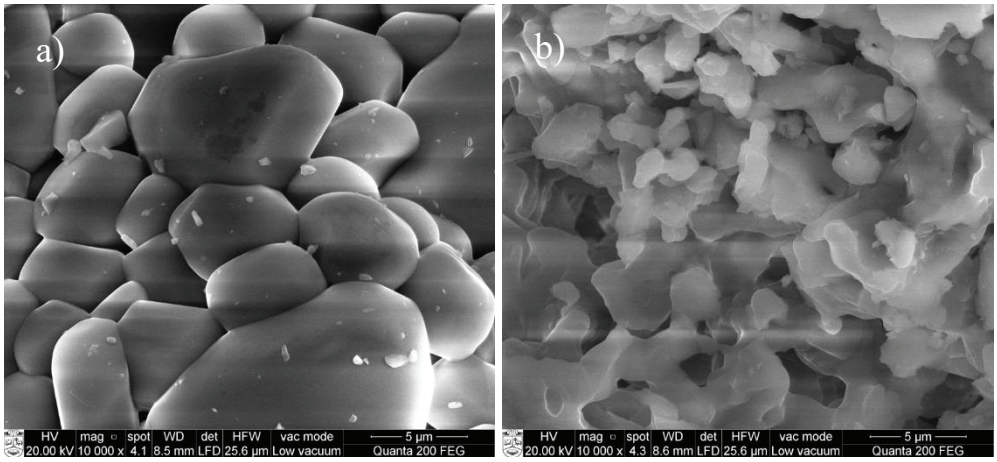


Fig. 3.59. SEM images of products obtained after direct synthesis at 1100°C for 1 h of mixtures: a) CaO-$SiO_2 \cdot nH_2O$-CaF_2, b) CaO-silica gel waste-CaF_2

To conclude on the direct synthesis experiment in the CaO-$SiO_2 \cdot nH_2O$-CaF_2-H_2O and CaO-silica gel waste-CaF_2-H_2O system, it can be stated that the synthesis method was ineffective to bind the initial materials, and that it produced many by-products. Furthermore, cuspidine started to form only at 1100°C:

$$CaO+SiO_2 \cdot nH_2O+CaF_2 \xrightarrow{\text{Direct synthesis at 900-1000°C for 1 h}} \begin{bmatrix} \text{lime} \\ \text{fluorite} \\ \text{kumtyubeite} \\ \text{larnite} \end{bmatrix} \xrightarrow{\text{Direct synthesis at 1100°C for 1 h}} \begin{bmatrix} \text{cuspidine} \\ \text{calcio-olivine} \\ \text{fluorite} \\ \text{larnite} \end{bmatrix},$$

$$CaO+\text{Silica gel waste}+CaF_2 \xrightarrow{\text{Direct synthesis at 900-1000°C for 1 h}} \begin{bmatrix} \text{lime} \\ \text{fluorite} \\ \text{kumtyubeite} \\ \text{larnite} \\ \text{fluormayenite} \end{bmatrix} \xrightarrow{\text{Direct synthesis at 1100°C for 1 h}} \begin{bmatrix} \text{cuspidine} \\ \text{larnite} \\ \text{fluorite} \\ \text{fluormayenite} \end{bmatrix}.$$

$CaCO_3$-$SiO_2 \cdot nH_2O$-CaF_2 and $CaCO_3$-silica gel waste-CaF_2 systems

For the next part of the investigation of the formation of cuspidine via direct synthesis, calcium oxide was replaced with an equivalent amount of calcium carbonate. The products after calcination at 900°C (Fig. 3.60) were similar to those with CaO (Fig. 3.58): kumtyubeite, larnite and fluormayenite (a silica gel waste system). However, in the mixture with waste material, no calcium oxide was present. In addition, unlike in the previous mixtures, here, cuspidine started to form at 1000°C, and kumtyubeite was still present at this temperature. After calcination at 1100°C, both mixtures consisted mostly of similarly crystalline cuspidine with traces of larnite. However, calcium fluoride reacted completely only when amorphous silica was used.

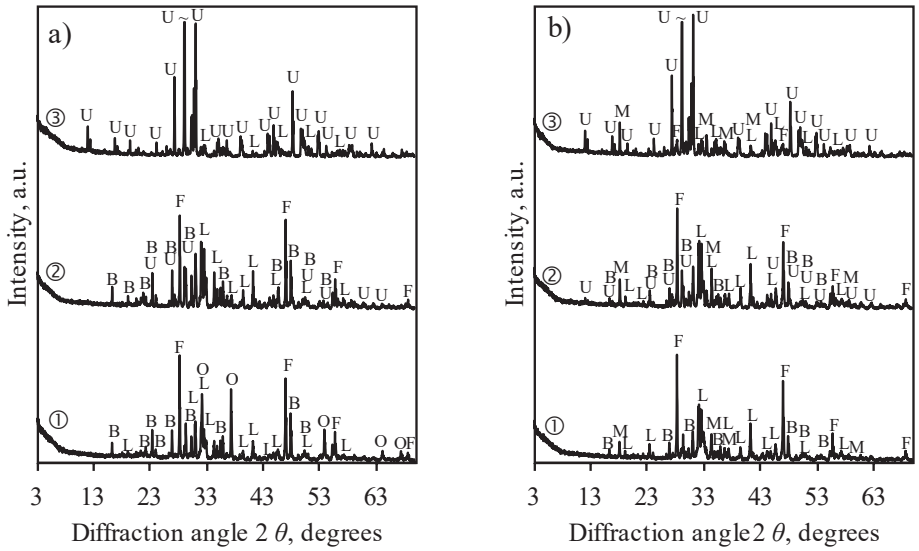


Fig. 3.60. XRD patterns of calcined mixtures for 1 h: a) $CaCO_3$-$SiO_2 \cdot nH_2O$-CaF_2; b) $CaCO_3$-silica gel waste-CaF_2 systems at 1 – 900°C; 2 – 1000°C; and 3 – 1100°C
Indices: B – kumtyubeite; F – fluorite; O – lime; L – larnite; U – cuspidine; M – fluormayenite

The SEM images of the samples obtained after sintering at 1100°C when calcium carbonate was being used (Fig. 3.61) showed that the change of CaO source did not have any significant influence on the formation of cuspidine when the SiO_2 source was amorphous hydrated silica (Fig. 3.61. a). $CaCO_3$-silica gel waste-CaF_2 interaction produced a much denser 'mass' with a rugged surface which differed completely from the products in the CaO-silica gel waste-CaF_2 system (Fig. 3.61. b).

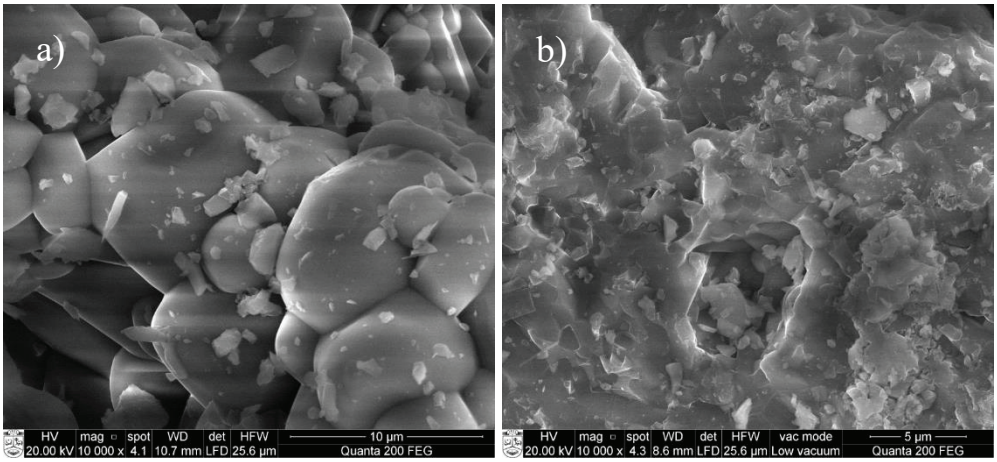


Fig. 3.61. SEM images of products obtained after direct synthesis at 1100°C for 1 h of mixtures: a) $CaCO_3$-$SiO_2 \cdot nH_2O$-CaF_2; b) $CaCO_3$-silica gel waste-CaF_2

The compounds which form in the $CaCO_3$-$SiO_2 \cdot nH_2O$-CaF_2-H_2O and $CaCO_3$-silica gel waste-CaF_2-H_2O systems during the direct synthesis in the temperature range of 900–1100°C can be listed in the following sequences:

$$CaCO_3+SiO_2 \cdot nH_2O+CaF_2 \xrightarrow{\text{Direct synthesis at 900°C for 1 h}} \begin{bmatrix} \text{lime} \\ \text{fluorite} \\ \text{kumtyubeite} \\ \text{larnite} \end{bmatrix} \xrightarrow{\text{Direct synthesis at 1000°C for 1 h}} \begin{bmatrix} \text{cuspidine} \\ \text{kumtyubeite} \\ \text{fluorite} \\ \text{larnite} \end{bmatrix}$$

$$\xrightarrow{\text{Direct synthesis at 110°C for 1 h}} \begin{bmatrix} \text{cupidine} \\ \text{larnite} \end{bmatrix},$$

$$CaCO_3+\text{Silica gel waste}+CaF_2 \xrightarrow{\text{Direct synthesis at 900°C for 1 h}} \begin{bmatrix} \text{fluorite} \\ \text{larnite} \\ \text{kumtyubeite} \\ \text{fluormayenite} \end{bmatrix} \xrightarrow{\text{Direct synthesis at 1000°C for 1 h}} \begin{bmatrix} \text{fluorite} \\ \text{larnite} \\ \text{cuspidine} \\ \text{kumtyubeite} \\ \text{fluormayenite} \end{bmatrix}$$

$$\xrightarrow{\text{Direct synthesis at 1100°C for 1 h}} \begin{bmatrix} \text{cuspidine} \\ \text{fluormayenite} \\ \text{fluorite} \\ \text{larnite} \end{bmatrix}.$$

To sum up on the investigation of the direct synthesis of cuspidine, it can be stated that silica gel waste is more active than amorphous hydrated silica at 900–1000°C; however, relatively pure cuspidine forms only at 1100°C. $SiO_2 \cdot nH_2O$ promotes the formation of smooth densely packed particles, while silica gel waste yields different structures: scaffold-like with CaO, and a rough pore-less one-piece lump with $CaCO_3$.

3.8.2. Calcination of the synthetic precursors

CaO-$SiO_2 \cdot nH_2O$-CaF_2 system

According to the XRD data, in the samples where cuspidine did not form or its formation was minor (95 and 130°C) under hydrothermal treatment (Fig. 3.62. a, curves 1 and 2), the further formation was also incomplete at 900°C, and their mineral composition was similar to the samples obtained after direct synthesis (Fig. 3.59. a and Fig. 3.60. a). The samples contained a relatively high amount of fluorite and kumtyubeite.. In addition, larnite was identified in the samples, which confirmed that there were fluoride-free calcium silicate hydrates before calcination. In the sample which was obtained at 200°C under hydrothermal treatment within 12 h, all portlandite had been consumed, and cuspidine was already the main compound. Only traces of fluorite and larnite were identified after calcination at 900°C (Fig. 3.62. a, curve 3).

After calcination at 1100°C, kumtyubeite was no longer identified in the samples independently from the temperature of hydrothermal synthesis. However, the lower is the temperature of the first step of the synthesis, the more intense are the peaks of fluorite and larnite in the calcined samples. Fluorite reacted completely in the calcined samples obtained within 12 h of hydrothermal curing at 150–200°C. The smallest traces of larnite were identified when the hydrothermal synthesis temperature was 200°C (Fig. 3.62. a, curve 4).

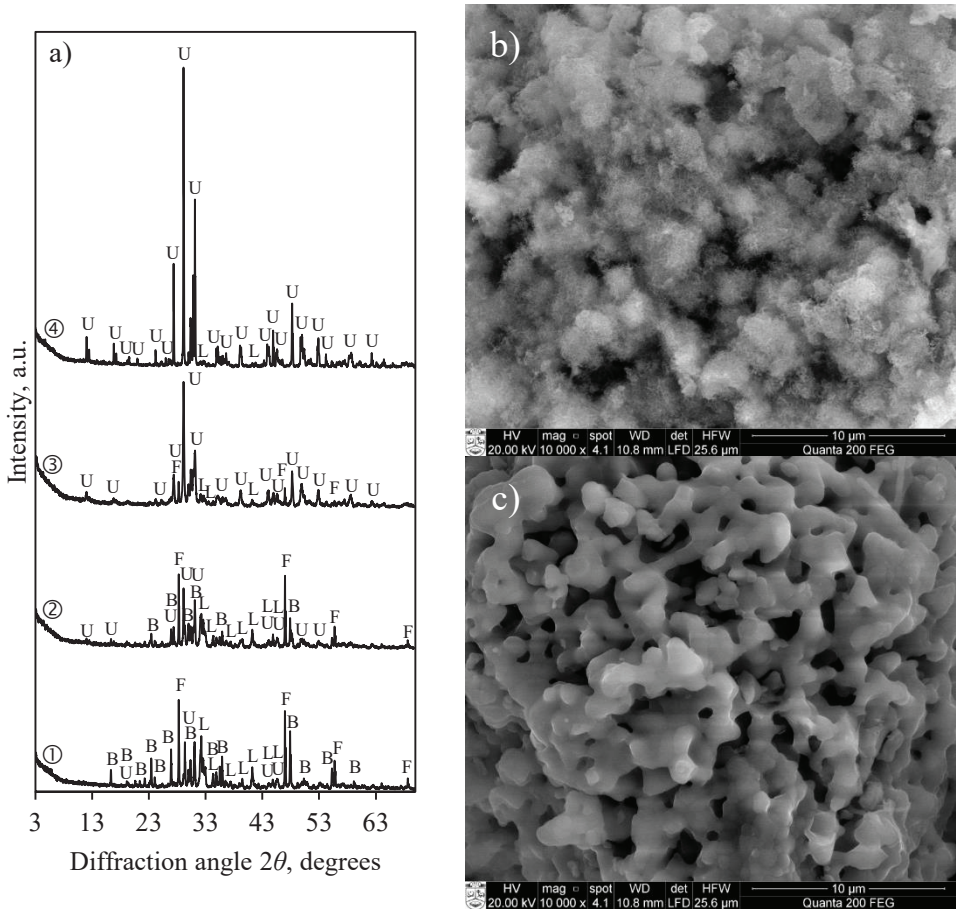


Fig. 3.62. XRD patterns (a) of: 1 – hydrothermally synthesised at 95°C for 12 h and calcined at 900°C for 1 h; 2 – 130°C – 12 h and 900°C – 1 h; 3 – 200°C – 12 h and 900°C – 1 h; 4 – 200°C – 12 h and 1100°C – 1 h; b – SEM image of 200°C – 12 h and 900°C – 1 h; c – 200°C – 12 h and 1100°C – 1 h when using $CaO\text{-}SiO_2 \cdot nH_2O\text{-}CaF_2$ system
Indices: B – kumtyubeite; U – cuspidine; F – fluorite; L – larnite

The SEM image of the sample which was obtained within 12 h of hydrothermal treatment at 200°C and calcined at 900°C (Fig. 3.62. b) showed that the structure of cuspidine remained unchanged and exhibited a spherical scaffold-like texture. The similarity of the texture corresponds to the similarity of the XRD patterns of calcined and uncalcined samples. After calcination of the same sample at 1100°C, cuspidine appears to be fused (Fig. 3.62. c), and the scaffold structure seems to be partially lost. This appearance is similar to the one obtained when using the calcium oxide, silica gel waste and calcium fluoride system and direct synthesis (Fig. 3.59 b).

It was observed that the main peak of cuspidine (*d*-spacing 0.3051 nm) strongly depended both on the composition of the precursor and the calcination temperature (Fig. 3.63). The formation of cuspidine in the hydrothermally prepared samples, where the area was already the lowest (95, 130°C 4–12 h, 150°C 4 h), was

similar to the formation of cuspidine during direct synthesis. The area in these samples after the calcination at 900°C was less than 1 a.u., and a more significant increment was observed after the calcination at 1000°C when the values reached 3–6 a.u. Cuspidine started dominating only at 1100°C in the presently discussed samples, and the area reached 8–11 a.u. The area in the remaining samples, where cuspidine was already dominating after the hydrothermal synthesis (150°C 12, 170–200°C 4–12 h), was already 8–10 after the calcination at 900°C. The impact of the further increment of the calcination temperature on the area was less significant as the maximum value of ~13 a.u. was determined for the samples of 200°C. The area of the latter samples was already about ~11.5 a.u., and the further increment only by 10% could indicate that the most sizable amount of cuspidine could form under hydrothermal conditions.

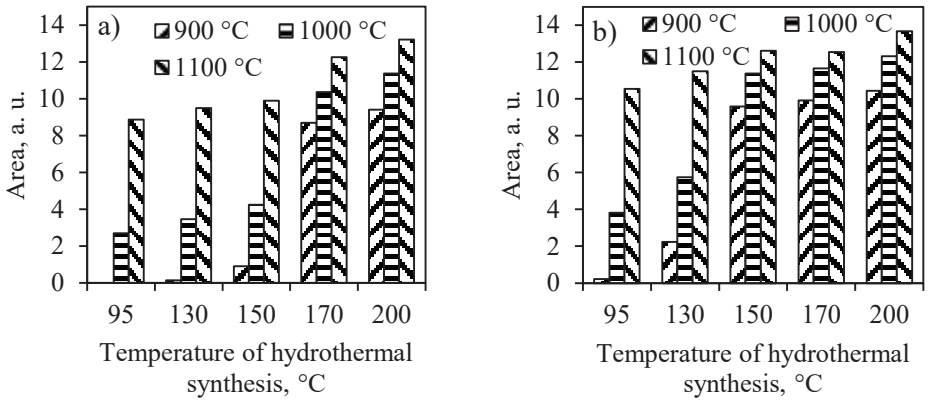


Fig. 3.63. Area of the main peak of cuspidine (*d*-spacing 0.3051 nm) in $CaO\text{-}SiO_2 \cdot nH_2O\text{-}CaF_2$ system: a – hydrothermal synthesis for 4 h; b – 12 h

CaO-silica gel waste-CaF_2 system

When silica gel waste was used for the hydrothermal synthesis of cuspidine, the aluminium ions promoted the formation of katoite; however, no other impact on the formation of cuspidine was observed. Similarly, after the calcination of hydrothermally obtained samples containing Al^{3+} ions, in addition to cuspidine and the traces of fluorite and larnite, fluormayenite and gehlenite $Ca_2Al_2SiO_7$ were observed (Fig. 3.64 a). According to the XRD patterns, in the samples, obtained within 48 h at 200°C under hydrothermal conditions and additionally calcined at 900°C for 1 h (Fig. 3.64 a, curves 1 and 2), some fluorite remained unreacted, and traces of larnite did actually form. Katoite, which formed during the first step of the synthesis, recrystallised into fluormayenite. Later on, when the samples were calcined at 1100°C, the intensity of the cuspidine peaks doubled. In addition, fluorite was no longer present, yet, some traces of larnite remained. It is also noteworthy that in the samples which were hydrothermally synthesised within 12 h, gehlenite formed

together with fluormayenite. However, in the samples that were hydrothermally obtained within 48 h of isothermal curing, gehlenite was no longer identified.

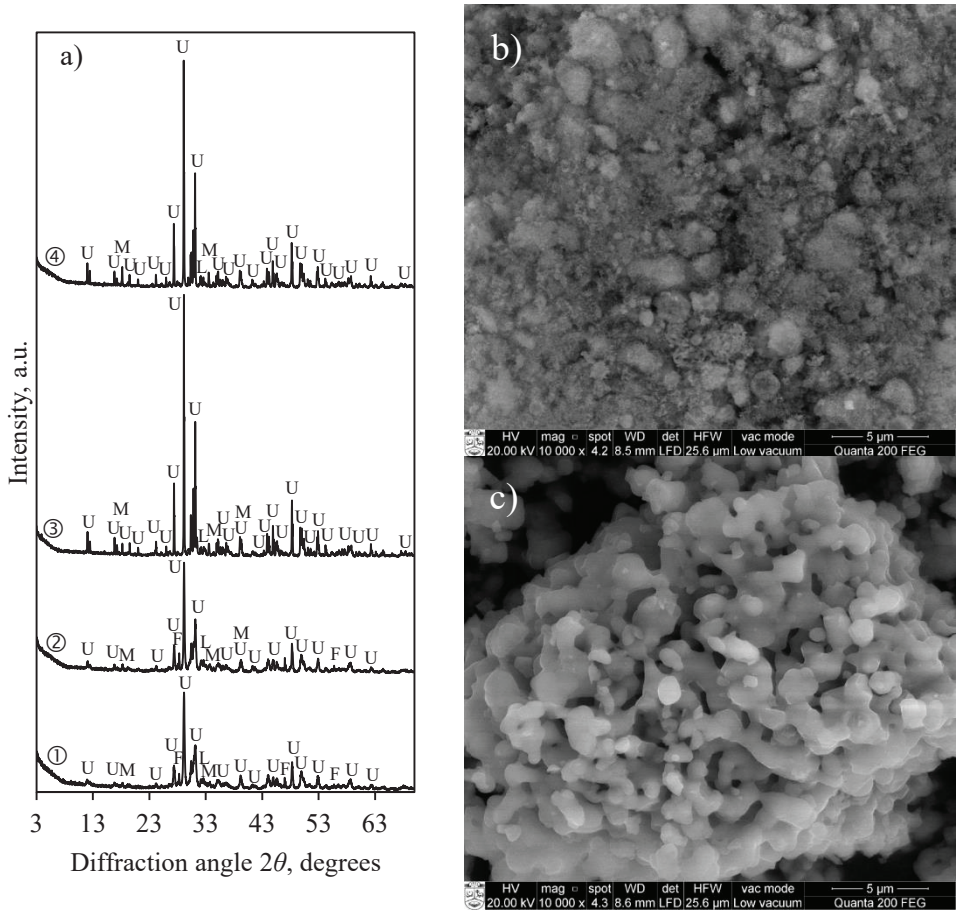


Fig. 3.64. a – XRD patterns of hydrothermally synthesised at 200°C for: 12 h and calcined at 900°C for 1 h; 2 – 48 h and 900°C 1 h; 3 – 12 h and calcined at 1100°C for 1 h; 4 – 48 h and 1100°C 1 h; b – SEM image of 200°C 12 h and 900°C 1 h; c – 200°C 12 h and 1100°C 1 h; when using CaO-silica gel waste-CaF_2 system
Indices: U – cuspidine; F – fluorite; L – larnite; M – fluormayenite

The SEM image of the sample, which was hydrothermally synthesised at 200°C for 12 h and calcined at 900°C for 1 h by using CaO-silica gel waste-CaF_2 system (Fig. 3.64 b), showed that the structure of the obtained cuspidine sample was similar, but denser compared to the mineral obtained when amorphous hydrated silica was used. After the calcination of the sample at 1100°C for 1 h (Fig. 3.64. c), a glass-like texture similar to the system with amorphous hydrated silica was obtained, but as well as after calcination at 900°C, the structure was more fused, and it contained fewer hollows.

The area of the main peak of cuspidine (*d*-spacing 0.3051 nm) was already ~10 a.u. after the hydrothermal synthesis at 200°C, and thus calcination at 900°C had a

negligible impact on the values (Fig. 3.65). As in the previous findings, a more significant (by 1–1.5 a.u.) increment was observed after calcination at 1000°C. A further calcination at 1100°C increased the area only slightly (by 0.5 a.u.). Similarly to the previous findings in the $CaO\text{-}SiO_2 \cdot nH_2O\text{-}CaF_2$ system, the most amount of cuspidine could have formed during the hydrothermal synthesis. Nevertheless, the complete consumption of fluorite at 1100°C indicated that part of cuspidine still formed during the calcination.

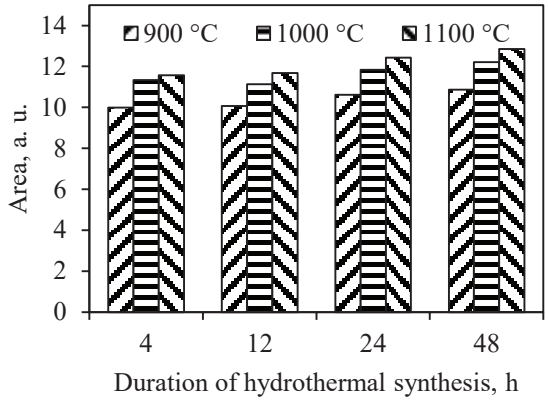


Fig. 3.65. Area of the main peak of cuspidine (*d*-spacing 0.3051 nm) in CaO-silica gel waste-CaF_2 system

To sum up on the calcination of hydrothermally synthesised precursors, it can be stated that calcination up to 1000°C slightly increased the crystal order of cuspidine and retained its scaffold-like structure. However, this temperature was not sufficient for fluorite to react completely. This was reached after the calcination at 1100°C. In addition, the crystal order of cuspidine increased greatly, but the structure fused, and it was thus similar to fused spheres or plates rather than scaffolds.

3.9. Investigation of the Binding Properties of Synthetic Cuspidine Samples

3.9.1. Hydration of synthetic cuspidine samples

The microcalorimetric curves of the synthetic cuspidine samples are very different compared to belite-based cement [210,211] or OPC [212,213]. The microcalorimetric curves of OPC or belite-based cement consist of five periods: 1) the initial (wetting) period; 2) the induction period (the period of slow reaction); 3) the acceleratory period; 4) the deceleratory period; 5) the period of slow continuous reaction. In the case of cuspidine samples, microcalorimetric curves showed the initial period and the period of slow continuous reaction (a negligible continuous heat release after 0.5 h of hydration). Other stages of hydration did not occur. The data of the heat flow (mW/g) and the cumulative heat of hydration (J/g) are presented in Fig. 3.66. a and b.

The CSF-r-900 sample was observed to immediately produce heat at the beginning of hydration (Fig. 3.66. a, curve 1). The initial period lasted for 13.2 min, while the peak (~7.5 mW/g) was observed after 3 min. After the initial reaction, a stage of inhibition followed for the next 6.5 h (no heat was released from the sample). Later on, the sample continuously released heat, and, after 72 h of hydration, the amount of the released heat was ~35 J/g (Fig. 3.66. b, curve 1).

A similar trend was observed during the hydration of the CSF-w-900 sample (Fig. 3.66. a, curve 2). The CSF-w-900 sample immediately reacted with water and reached the peak (8 mW/g) of the initial reaction after 3 min. The initial reaction lasted for 37.8 min. After this period, the heat flow continuously decreased. In total, within 72 h of hydration, the sample released ~40 J/g of heat (Fig. 3.66. b, curve 2). The maximum heat flow rate of the initial reaction was reached at the same time as in the case of CSF-r-900; however, the initial stage lasted ~3 times longer in the case of CSF-w-900. Probably, this difference appeared due to the presence of fluormayenite in the CSF-w-900 sample.

The hydration process of the CSF-r-1100 sample was observed to be hardly occurring because only a negligible initial period was observed (Fig. 3.66. a, curve 3) and, after 72 h of hydration, the amount of the released heat was only 5 mW/g (Fig. 3.66. b, curve 3).

The CSF-w-1100 sample intensively reacted with water at the beginning of hydration (~12 h) (Fig. 3.66. a, curve 4). The initial reaction was slightly delayed, and the heat flow reached a peak value of ~3 mW/g within ~15 min. Later on, the rate of the released heat continuously decreased, and, after 12 h of hydration, the sample did not release heat anymore (Fig. 3.66. b, curve 4). It was determined that, after 12 h of hydration, the sample released ~25 J/g of heat.

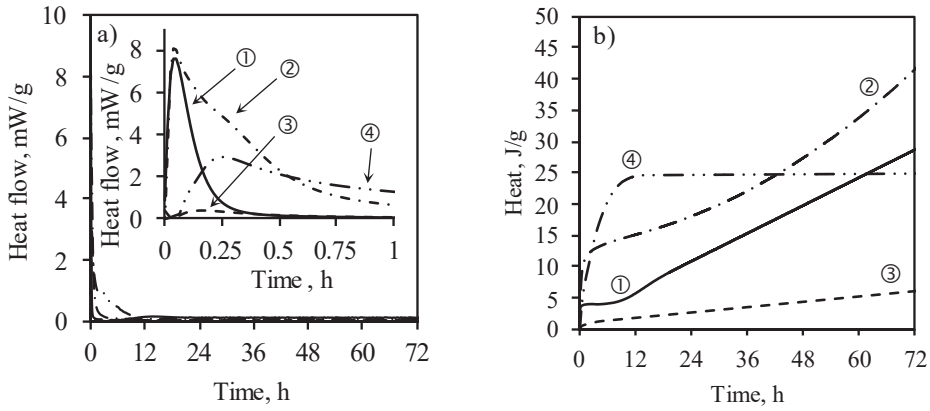


Fig. 3.66. Heat evolution rate (a) and cumulative heat (b) of calcined synthetic cuspidine samples. Curve 1 – CSF-r-900; 2 – CSF-w-900; 3 – CSF-r-1100; and 4 – CSF-w-1100

The XRD patterns of the hydrated samples showed that the changes in the mineralogical composition of the hydrated synthetic cuspidine samples were negligible (Fig. 3.67):

- the intensity of the characteristic diffraction peaks of larnite decreased;
- no significant changes were observed in the XRD patterns of hydrated CSF-r-900 and CSF-r-1100 samples (Fig. 3.67. 5 a);
- fluormayenite, which was present in the CSF-w-900 and CSF-w-1100 samples, completely reacted (Fig. 3.67 b). However, there is no evidence for the formation of new crystalline phases in the XRD patterns. Fluormayenite probably recrystallised into a new amorphous phase which was not detected in the XRD patterns.

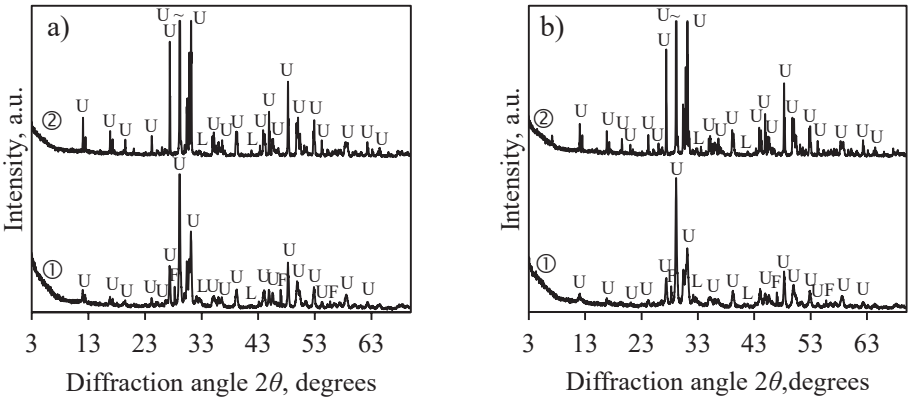
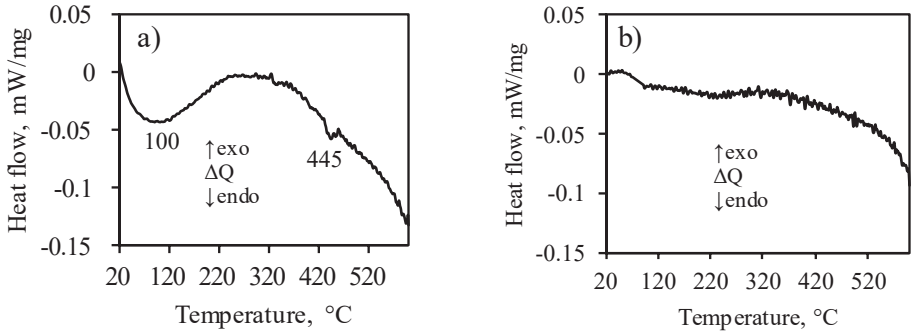


Fig. 3.67. XRD patterns of hydrated (72 h) cuspidine samples: a – $CaO\text{-}SiO_2\cdot nH_2O\text{-}CaF_2$ mixture: 1 – CSF-r-900 and 2 – CSF-r-1100; b – CaO-silica gel waste-CaF_2 mixture: 1 – CSF-w-900 and 2 – CSF-w-1100.
Indices: U – cuspidine; F – fluorite; L – larnite

The results of the DSC analysis (Fig. 3.68) were in good agreement with the XRD data and provided additional data about the hydration process. It was determined that two endothermal effects occurred in the DSC curve of the hydrated CSF-r-900 sample (Fig. 3.68. a). The first broad endothermal effect at 100°C can be assigned to the removal of adsorbed water or the dehydration of amorphous calcium silicate hydrates formed due to the hydration of larnite. The second effect (445°C) can be assigned to the decomposition of portlandite which probably forms during the hydration of larnite. However, portlandite was not identified on the XRD pattern because only a small amount of it was formed. As expected, in the DSC curve of the hydrated CSF-r-1100 sample, a new thermal effect did not appear (Fig. 3.67 b), which shows the absence of portlandite in the hydration products. The discussed results of the DSC analysis are in good agreement with the data of microcalorimetric analysis (Fig. 3.66). Since portlandite did not form during the hydration of the CSF-r-1100 sample, the released heat was only ~5 J/g after 72 h of the experiment (Fig.

3.66. b). Meanwhile, portlandite and some amorphous calcium silicate hydrates were formed during the hydration of the CSF-r-900 sample; thus, the amount of the released heat (~25 J/g) was five times higher compared to the CSF-r-1100 sample.

The samples synthesised by using silica gel waste showed different results compared to the CSF-r-900 and CSF-r-1100 samples (Fig. 3.68). In the DSC curve of the CSF-w-900 sample, two sharp endothermal effects were observed (Fig. 3.68. c). As in the case of the CSF-w-900 sample, the first endothermal effect at 130°C indicates the removal of the adsorbed water and the dehydration of amorphous calcium silicate hydrates. Meanwhile, the effect at higher temperature (233°C) can be attributed to the decomposition of calcium aluminate hydrates. These compounds formed during the hydration of fluormayenite. It should be noted that an endothermic effect characteristic of portlandite was not observed in the DSC curve. It is likely that only amorphous calcium silicate hydrates were formed during the hydration of larnite. Also, it is possible that amorphous aluminium hydroxide and/or calcium aluminates (which formed during fluormayenite hydration) reacted with portlandite (whose small amount was formed during larnite hydration); thus, the latter compound was not detected in the DSC curve. A similar DSC curve was obtained during the investigation of the CSF-w-1100 sample (Fig. 3.68. d). The main difference between the DSC curves of the CSF-w-900 and CSF-w-1100 samples is an intense endothermal effect at 289°C. According to the literature [214], the latter effect can be attributed to the dehydration of amorphous aluminium hydroxide. It is likely that, after calcination at 1100°C, a higher amount of fluormayenite was formed in the CSF-w-1100 sample because the intensity of the diffraction peaks characteristic of this compound was significantly higher compared to the CSF-w-900 sample. Thus, during hydration of the CSF-w-1100 sample, a higher amount of amorphous aluminium hydroxide was formed.



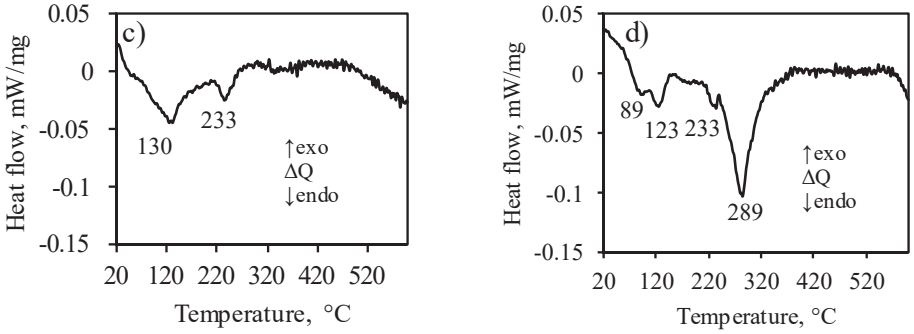


Fig. 3.68. DSC curves of hydrated samples for 72 h: a – CSF-r-900; b – CSF-r-1100; c – CSF-w-900; and d – CSF-w-1100

To sum up on the microcalorimetric test for hydraulic properties of the synthetic cuspidine samples, it can be stated that synthetic cuspidine samples showed weak interaction with water similarly to non-hydraulic calcium silicates, such as wollastonite and rankinite [215]. Therefore, it should be underlined that the use of silica gel waste is limited for the production of low lime binders, such as belite or α-C_2SH, because the formation and presence of cuspidine in the binder would delay its hardening and reduce the mechanical properties.

3.9.2. CO_2-curing of synthetic cuspidine sample

To determine the compressive strength of carbonated cuspidine, the sample synthesised by using silica gel waste and calcined at 900°C (CSF-w-900 sample) was used for the CO_2-curing experiments. The particle size can be a crucial factor for the hydration and carbonisation rate [62]. Usually, smaller particles have a higher external surface area and react more intensely. Particles of a diameter of 0.05–60 μm were determined to be present in the CSF-w-900 sample (Fig. 3.69). Particles of a diameter lower than 20 μm were dominant (>90%). It was calculated that the value of the external surface area was 397 m^2/kg, which is close to rankinite (~400 m^2/kg [216]) and OPC (~350 m^2/kg [217]).

A helium gas pycnometer was used to determine the density of the synthetic cuspidine sample. The density of the CSF-w-900 sample (3350 kg/m^3) was determined to be slightly higher compared to rankinite (3036 kg/m^3) and OPC (3150 kg/m^3). Thus, the physical properties of the cuspidine sample are similar to those of OPC and rankinite.

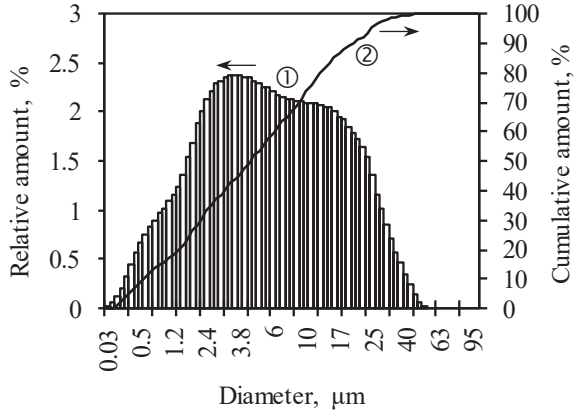


Fig. 3.69. Particle size distribution of synthetic cuspidine sample (CSF-w-900)

It was determined, that the compressive strength of the carbonated CSF-w-900-sand samples insignificantly depended on the curing duration because all the samples were characterised by a similar value of compressive strength (13–14 MPa) (Fig. 3.70. a). It is evident that the compressive strength slightly decreased by increasing the duration of curing, which can be explained by the recrystallisation of calcium carbonate polymorphs. The XRD data (Fig. 3.70. b) are in good agreement with the results of compressive strength. It is worth noting that the samples free of sand were used for the XRD analysis. The main reason is that the diffraction peaks of quartz are very intensive, and they overlap with the carbonisation products; thus, in order to identify the mineralogical composition, it is more precise to use samples free of sand. It was obtained that the main products of carbonisation were two polymorphs of $CaCO_3$: calcite and vaterite. In addition, similarly to the previous findings (cf. Fig. 3.41 and Fig. 3.45), fluorite also crystallised during the carbonisation experiments. It should be highlighted that amorphous silica is forming during carbonisation [218]; however, due to its amorphous state, it cannot be identified in the XRD patterns. The synthetic CSF-w-900 sample contained fluormayenite; however, in the XRD pattern, products containing aluminium were not detected after carbonisation. Probably, only a negligible amount of compounds containing aluminium ions was formed. A further analysis of XRD patterns showed that the mineralogical composition and the peak parameters did not change by prolonging the duration of carbonisation.

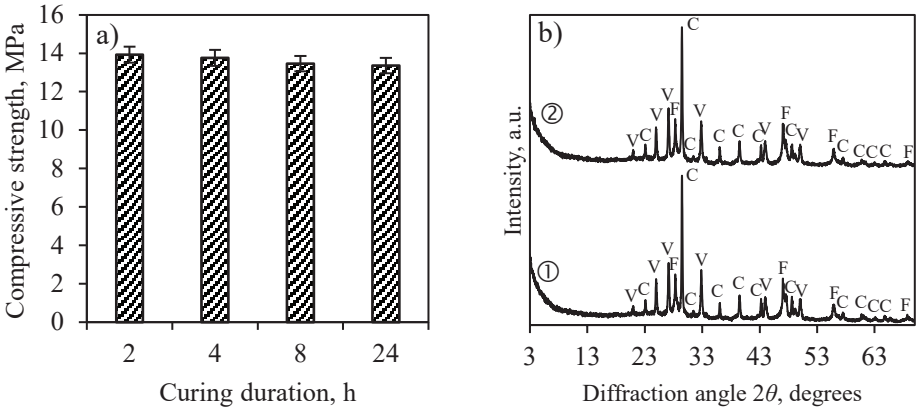


Fig. 3.70. Compressive strength (a) of CO_2-cured cuspidine samples (with sand, at ratio 1:3, powdered); and XRD patterns (b) of the synthetic cuspidine after curing for 1 – 2 h; 2 – 24 h at 15 bar CO_2 and 45°C (without sand, powdered)
Indices: V – vaterite; C – calcite; F – fluorite

The STA data (Fig. 3.71) were in line with the previously discussed results: the endothermal effect in the temperature range of 30–250°C corresponds to the dehydration of the hydrated silica which formed during the carbonation process. Also, within this temperature range, the removal of the adsorbed water can proceed. A second intensive endothermal effect (400–700°C) corresponds to the decomposition of the main carbonisation product calcium carbonate. It was determined that the mass loss during the presently discussed process was equal to 21.73% and 22.28% after 2 h and 24 h of hydration, respectively.

The concentration of CaO was 50.18 mass% in the initial mixture. For this reason, the theoretical amount of CO_2 which can be bound by a sample is equal to (Eq. 3.4):

$$CO_2\ (\%max) = 0.785 \cdot 50.18\% = 39.39\% \quad (3.4)$$

It was calculated that, after 2 h of curing, the degree of carbonisation was 55.17%. This value slightly increased by extending the duration of the experiment to 24 h, i.e. degree of carbonisation was 56.56%. These results are in good agreement with the literature data, where a similar degree of the carbonisation of calcium silicates was determined [215,219,220].

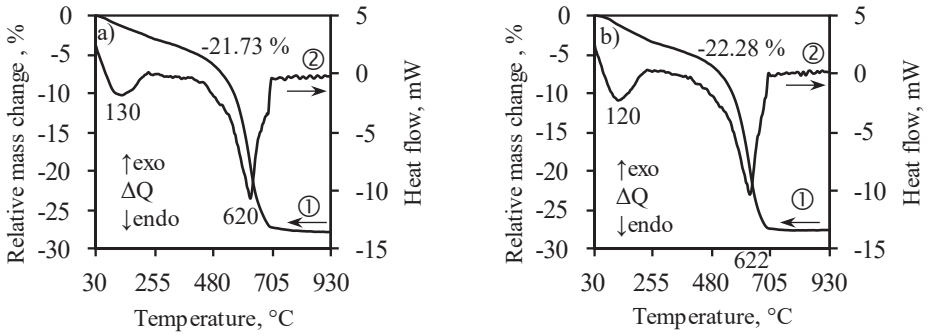


Fig. 3.71. STA curves (1 – TG; 2 – DSC) of CO_2-cured cuspidine samples (without sand, powdered) after curing for: a – 2 h; b – 24 h at 15 bar CO_2 and 45°C

To sum up on CO_2-curing of synthetic cuspidine, it can be stated that the material *did* gain strength during the accelerated carbonation. However, compared to rankinite, a fluoride-free calcium silicate, which shares the same CaO/SiO_2 = 1.5 ratio, the compressive strength of carbonated synthetic cuspidine samples was 3–7 times lower [193]. On the other hand, the formation and presence of cuspidine in CO_2-curable binders would not have a strong impact on the mechanical properties of the final products because cuspidine-based binders gain strength. In addition, after the carbonation, the F^- ions remain immobilised in an insoluble compound, fluorite CaF_2.

Acknowledgements:

Reprinted/Adapted by permission from Springer Nature: Springer Nature; Journal of Thermal Analysis and Calorimetry / Hydration properties and CO2-curing of synthetic cuspidine samples / A. Gineika, K. Baltakys, T. Dambrauskas, R. Siauciunas, 148:1511-1521. 2022 https://doi.org/ 10.1007/S10973-022-11843-1; License No. 5574040484311

4. CONCLUSIONS

1. It was determined that, during the direct synthesis of wollastonite, $SiO_2 \cdot nH_2O$ was less active with other components than the silica gel waste in the temperature range of 900–1100°C for 1 h because a part of calcium oxide remained unreacted. Nevertheless, larnite – which exhibits a two times higher CaO/SiO_2 ratio than wollastonite – also formed in the reaction products.
2. It was estimated that, during the two-step synthesis in the $CaO\text{-}SiO_2 \cdot nH_2O\text{-}H_2O$ system, the hydrothermally synthesised precursor (200°C, 12 h,), which contained xonotlite, 1.13 nm tobermorite and C-S-H(I)/(II), completely recrystallised into wollastonite within 1 h at 900°C. The obtained wollastonite sample exhibited S_{BET} = 33.42 m^2/g and a macroporous needle-like structure.
3. It was determined that, in the CaO-silica gel waste-H_2O and $CaO\text{-}SiO_2 \cdot nH_2O\text{-}AlF_3\text{-}H_2O$ systems, tobermorite and cuspidine were dominant in the synthesis products after hydrothermal synthesis at 200°C for 4–48 h. In addition, depending on the mixture (silica gel waste or AlF_3 additive), traces of katoite or calcium fluoride formed, respectively. It was demonstrated that, during calcination, tobermorite and traces of C-S-H(I) recrystallised into wollastonite, while cuspidine remained stable under all experimental conditions.
4. Wollastonite-based binder and sand (mass ratio 1:3) samples gain relatively high compressive strength (10–18 MPa). It was determined that, with an increment of the amount of the wollastonite-based binding material from 20 to 35 mass%, the compressive strength increased 2 times up to 16 MPa; meanwhile, the compaction force (10–15 kN), as well as the exposure duration in the CO_2 environment (2–24 h) improved the compressive strength only by 1.2 times.
5. It was observed that the addition of wollastonite filler hardly changed the Young's modulus of the AESO-IBOMA and AESO-THFMA resin and wollastonite-based filler composites as the values did not differ much from the initial 4.8 and 1.1 MPa, respectively. After the sintering of the optically 3D-printed polymer-wollastonite scaffolds, it was observed that the particles of the synthetic materials alone did not fuse well enough to produce strong structures.
6. It was determined that two-step synthesis (hydrothermal synthesis at 200°C for 12 h and calcination at 900–1100°C for 1 h) is efficient to produce synthetic cuspidine in the $CaO\text{-}SiO_2\text{-}CaF_2$ and CaO-silica gel waste-CaF_2 systems. Together with cuspidine, traces of larnite were present under all calcination conditions. Since silica gel waste contains Al^{3+} ions, katoite was formed during hydrothermal synthesis. Under all experimental conditions (up

to 1100°C), this calcium aluminate recrystallised to fluormayenite during calcination and remained stable.

7. It was observed that the amount of the evolved heat from the synthetic cuspidine samples depends on the calcination temperature of the latter compound: the samples calcined at 900°C released 15–30 J/g more heat after 72 h of hydration compared to the samples calcined at 1100°C. Additionally, due to the interaction of fluormayenite with water, an increase in the amount of the evolved heat in the wetting stage was observed in the samples synthesised in the CaO-silica gel waste-CaF_2 system.
8. Synthetic cuspidine samples act as an active component in the capture and storage of CO_2 because their degree of carbonation was more than 55%. Meanwhile, the synthetic cuspidine-sand samples gained 13–14 MPa compressive strength during accelerated curing in CO_2 atmosphere.

5. Santrauka

5.1. Įvadas

Volastonitas – tai kalcio silikatas $CaSiO_3$, kurio galima tiek rasti gamtoje, tiek pagaminti pramoniniu būdu. Volastonitas plačiai pritaikomas plastikų gamyboje, specializuotoms dangoms, taip pat keramikos, rišamųjų medžiagų, dažų, popieriaus bei medicinos srityse dėl mažo matmenų pokyčio kintant temperatūrai ir didelio terminio stabilumo, baltumo, mechaninio stiprio ir specifiškos adatėlių formos kristalų struktūros. Žinomi keli kalcio silikato gamybos būdai, tačiau iš jų plačiausiai taikomi šie: 1) aukštatemperatūris – šiuo atveju kaip pradinės žaliavos paprastai naudojamos karbonatinės kalcio uolienos, tokios kaip klintis, o kaip silicio dioksido šaltinis naudojamas kvarcinis smėlis. Šių medžiagų mišinys išdegamas 1200–1400 °C temperatūroje, kurioje kietafazės reakcijos metu susidaro volastonitas; 2) antruoju atveju pradinės medžiagos kalcio oksidas ir silicio dioksidas sumaišomos su vandeniu ir gauta suspensija hidrotermiškai apdorojama 130-220 °C temperatūroje, kad susidarytų kalcio hidrosilikatai, tokie kaip ksonotlitas, 1,13 nm tobermoritas ir kiti. Šiai sintezei taip pat galima naudoti tirpias kalcio ir silikato druskas, tokias kaip kalcio nitratas ar chloridas, natrio ar kalio silikatai. Gautas prekursorius vėliau išdegamas 800-900 °C temperatūroje, kad persikristalizuotų į volastonitą.

Į aplinką išskiriamo anglies dioksido sumažinimas yra vienas didžiausių rišamųjų medžiagų pramonės iššūkių, nes gaminant portlandcementį išmetama ~5 % viso dėl žmogaus veiklos išmetamo anglies dioksido. Kaip alternatyva portlandcemenčiui galėtų būti volastonitas $CaSiO_3$ ar rankinitas $Ca_3Si_2O_7$. Nors jie nekietėja vandeninėje terpėje, tačiau jie įgauna stiprumines savybes anglies dioksido aplinkoje esant drėgmei. Volastonito privalumai šiuo atveju yra didesnis jo tirpumas vandenyje, dėl kurio jo reakcija su CO_2 yra greitesnė, ir mažesnio jo gamybai reikalingo CaO kiekio. Po tokio kietinimo susidariusi $CaCO_3$ ir $SiO_2 \cdot nH_2O$ struktūra pasižymi panašiomis stipruminėmis savybėmis, kaip ir sukietėjusio portlandcemenčio. Pagrindiniai volastonito privalumai, palyginti su portlandcemenčiu, yra tai, kad, nors juos abu galima gaminti iš praktiškai tų pačių žaliavų, tačiau volastonitui susidaryti reikia 250-500 °C mažesnės temperatūros. Vietoje kvarcinio smėlio naudojant amorfinį silicio dioksidą, volastonitas susidaro greičiau, tačiau tokia silicio dioksido atmaina gamtoje reta, todėl ieškoma alternatyvų. Viena iš jų – aliuminio fluorido gamybos atlieka silikagelis. Galimybė panaudoti šią medžiagą alternatyvių rišamųjų medžiagų sintezei taip pat padėtų spręsti pramoninių atliekų problemą.

Darbo tikslas – ištirti volastonito ir kuspidino susidarymą skirtingais sintezės metodais naudojant aliuminio fluorido gamybos atlieką – silikagelį arba SiO_2-nH_2O, nustatyti gautų produktų hidratacijos ir karbonizacijos ypatumus bei pasiūlyti racionalius jų panaudojimo būdus.

Darbo uždaviniai:

1. Ištirti $SiO_2 \cdot nH_2O$ ir užteršto silikagelio įtaką volastonito kristalizacijai taikant vienos ar dviejų stadijų sintezės metodus.
2. Ištirti sintetinio volastonito bandinių mikrostruktūrą, fizikines ir chemines savybes bei jų taikymą rišamųjų medžiagų, polimerinių kompozitų ar 3D karkasų spausdinimo gamyboje.
3. Susintetinti kuspidiną kietafazės ar dviejų stadijų sintezės metodais $CaO\text{-}SiO_2\text{-}CaF_2$ sistemoje.
4. Ištirti sintetinio kuspidino bandinių kietėjimą skirtingose aplinkose.

Disertacijos ginamieji teiginiai:

1. Volastonito susidarymą 900 °C temperatūroje lemia sintetinio prekursoriaus mineralinė sudėtis ir savybės.
2. Sintetinio kuspidino bandiniai aktyviai dalyvauja CO_2 šalinimo ir izoliavimo procesuose.

Mokslinio darbo naujumas:

1. Sintezės metodas turi lemiamą įtaką volastonito ir kuspidino susidarymui, struktūrai ir tekstūrai.
2. Nustatyta, kad volastonito ar kuspidino prekursoriaus sudėtyje neturi būti kalcio hidroksido, nes degimo produktuose susidaro didesnio molinio CaO/SiO_2 santykio junginiai – larnitas arba kumtiubeitas.
3. Įrodyta, kad dviejų stadijų (hidroterminė sintezė 200 °C temperatūroje 12 h ir degimas 900–1100 °C temperatūroje) sintezė yra efektyvi sintetinant kuspidiną.

Praktinė vertė:

Nustatyta, kad aliuminio fluorido gamybos atlieka silikagelis gali būti naudojamas / utilizuojamas alternatyvių rišamųjų medžiagų sintezėje: pagaminti volastonito-smėlio bandiniai kietėdami CO_2 atmosferoje įgauna 18 MPa gniuždomąjį stiprį. O greitosios karbonizacijos metu kuspidino-smėlio bandiniai pasiekė 13–14 MPa gniuždomąjį stiprį.

Nustatyta, kad tiek funkcionalizuoti, tiek nefunkcionalizuoti akriloksipropilsilanu užpildai, pagaminti iš sintetinio volastonito, suteikia didesnį kietumą kompozitams, palyginti su dervų bandiniais be užpildų. Be to, sukurti volastonito ir sojų aliejaus dervų kompozitai turi didelį potencialą tapti konkurencinga alternatyva įprastinėms iš naftos gaunamoms dervoms ir gali sumažinti neigiamą poveikį gamtai.

Susintetinti kalcio silikatų ir / ar hidrosilikatų, kietėjančių CO_2 aplinkoje, prototipų bandiniai panaudoti baltojo betono plokščių pramoninėje gamyboje.

Darbo aprobavimas ir publikavimas

Disertacinio darbo tema paskelbtos 4 mokslinės publikacijos: 4 straipsniai recenzuojamuose mokslo leidiniuose *Web of Science* duomenų bazėje, indeksuotuose leidiniuose su cituojamumo rodikliu (JCR SCIE). Darbo rezultatai pristatyti 6 tarptautinėse mokslinėse konferencijose.

Darbo apimtis

Disertaciją sudaro įvadas, literatūrinių duomenų analizė, eksperimentinė dalis, tyrimų rezultatai bei jų aptarimas, išvados, 221 literatūros šaltinio sąrašas, mokslinių publikacijų sąrašas. Pagrindinė medžiaga išdėstyta 194 puslapiuose, įskaitant 13 lentelių ir 75 paveikslus.

Autoriaus ir bendraautorių mokslinis indėlis

Tyrimų planą ir tiriamas medžiagas parinko Andrius Gineika ir prof. dr. Kęstutis Baltakys. Autorius ištyrė ir aprašė volastonito ir kuspidino sintezę; autorius taip pat išnagrinėjo jų karbonatinio kietėjimo procesą ir sintetinio volastonito bandinių taikymą. Kęstutis Baltakys konsultavo dėl eksperimento eigos ir rankraščių rengimo. Tadas Dambrauskas konsultavo dėl BET analizės, Raimundas Šiaučiūnas – dėl sintezės metodų, Jolita Ostrauskaitė – dėl volastonito ir polimerų kompozitų tyrimų. Kompozitinės medžiagos pagamintos Polimerų chemijos ir technologijos katedroje, o 3D karkasai atspausdinti Vilniaus universitete.

5.2. Eksperimentinė dalis

5.2.1. Naudotos medžiagos

Aliuminio fluorido gamybos atlieka – **silikagelis** (AB „Lifosa“): džiovintas 25 °C temperatūroje 24 h, maltas 2,5 min, 950 aps./min greičiu planetariniu-vibraciniu diskiniu malūnu „Fritsch Pulverisette 9“ (Vokietija); tankis $\rho = 2350$ kg/m^3; savitasis paviršiaus plotas $S_{sav} = 1540$ m^2/kg. Pagrindiniai elementai: 39,86 % Si (85,41 % SiO_2), 5,37 % Al (10,14 % Al_2O_3), 8,76 % F. Dalelių dydis nuo 0,05 iki ~20 μm.

Kalcio oksidas CaO, gautas iš $Ca(OH)_2$ („Honeywell“, Vokietija; $Ca(OH)_2 \geq 96$ %), jį išdegus 1 h 550 °C krosnyje „Snol 8,2/1100“ ir per 30 s sumalus 950 aps./min greičiu planetariniame-vibraciniame diskiniame malūne. Laisvo CaO kiekis (aktyvumas) – 94,22 %; tankis: $\rho = 2837$ kg/m^3; savitasis paviršiaus plotas $S_{sav} = 2076$ m^2/kg. Dalelių dydis nuo 0,05 iki ~50 μm.

Amorfinis silicio dioksidas $SiO_2 \cdot nH_2O$ („Reaktiv“, Rusija); maltas 2,5 min 950 aps./min greičiu planetariniu-vibraciniu diskiniu malūnu; tankis $\rho = 2389$ kg/m^3; savitasis paviršiaus plotas $S_{sav} = 1425$ m^2/kg; kaitmenys – 11,79 %. Dalelių dydis nuo 0,05 iki ~50 μm.

Aliuminio fluoridas AlF_3 (≥96 % „Lifosa“, Lietuva) maltas 2,5 min 950 aps./min greičiu planetariniu-vibraciniu diskiniu malūnu; tankis $\rho = 3065$ kg/m^3; savitasis paviršiaus plotas $S_{sav} = 2970$ m^2/kg. Dalelių dydis nuo 0,05 iki ~80 μm.

Kalcio fluoridas CaF_2 (99 %, „Reaktiv“, Rusija); maltas 2,5 min 950 aps./min greičiu planetariniu-vibraciniu diskiniu malūnu; tankis $\rho = 3155$ kg/m^3; savitasis paviršiaus plotas $S_{sav} = 2060$ m^2/kg. Dalelių dydis nuo 0,05 iki ~80 μm.

Standartinis smėlis „Cen-Normsand“ („Normensand“, Vokietija, atitinka standartus EN 196-1 ir ISO 679).

3-akriloksipropiltrimetoksisilanas APTMS (94%, stab. su 100ppm BHT, „Alfa Aesar“, Vokietija);

Akrilintas epoksidintas sojų pupelių aliejus AESO („Merck“, Vokietija);

Izobornilmetakrilatas IBOMA („Evonik Industries“, Vokietija);

Tetrahidrofurfurilmetakrilatas THFMA („Evonik Industries“, Vokietija);

Glicerolio dimetakrilatas, izomerų mišinys (90 %, „Alfa Chemistry“, JAV);.

Kiti reagentai:

Druskos rūgštis HCl („Reachem Slovakia“, Slovakija), tirpalas: 1 mol/l; natrio fluoridas NaF („Reachem Slovakia“, Slovakija), tirpalai: 1000 ppm (2,2105 g/l), 100 ppm (0,22105 g/l), 10 ppm (0,022105 g/l); natrio hidroksidas NaOH (99 %, „Reachem Slovakia“, Slovakija); kalio hidroksidas KOH (85 %, „Reachem Slovakia“, Slovakija); amonio karbonatas $(NH_4)_2CO_3$ (99 %, „Riedel-de Haën“, Vokietija); acto rūgštis CH_3COOH(r. gr., „Reachem Slovakia“, Slovakija); acetonas („Reachem Slovakia“, Slovakija); izopropanolis („Reachem Slovakia“, Slovakija); etil(2,4,6- trimetilbenzoil) fenilfosfinatas TPOL („Fluorochem“, Jungtinė Karalystė); Aerosil R972 („Evonik“, Vokietija), akrilinis plastifikatorius betonui „Dynamon XTend“ („Mapei“, Norvegija).

5.2.2. Metodai

Sintezė

Volastonito sintezei su skirtingomis pradinėmis medžiagomis paruošti trys mišiniai:

1) Amorfinio silicio dioksido ir kalcio oksido mišinys, kurio molinis CaO/SiO_2 santykis lygus 1; (48,28 % CaO; 51,72 % SiO_2);
2) Silikagelio ir kalcio oksido mišinys, kurio molinis $CaO/(Al_2O_3+SiO_2+F^-)$ santykis lygus 1; (48,49 % CaO; 42,18 % SiO_2; 5,01 % Al_2O_3; 4,32 % F^-);
3) Amorfinio silicio dioksido, kalcio oksido ir aliuminio fluorido mišinys, kurio molinis $CaO/(Al_2O_3+SiO_2+F^-)$ santykis lygus 1; (48,71 % CaO; 43,10 % SiO_2; 3,87 % Al_2O_3; 4,32 % F^-).

Kuspidino sintezei su skirtingos kilmės SiO_2 paruošti du mišiniai:

1) Amorfinio silicio dioksido, kalcio oksido ir kalcio fluorido mišinys, kurio molinis $CaO:SiO_2:CaF_2$ santykis lygus 3:2:1 (45,90 % CaO; 32,79 % SiO_2; 21,31 % CaF_2).
2) Užteršto silikagelio, kalcio oksido ir kalcio fluorido mišinys, kurio molinis $CaO:(SiO_2 + Al_2O_3):(CaF_2+F^-)$santykis lygus 3:2:1 (50,18 % CaO; 30,71 % SiO_2; 2,69 % Al_2O_3; 3.37 % F^-; 13.04 % CaF_2).

Vienos stadijos (tiesioginės) sintezės tyrimui buvo paruošti analogiški mišiniai kalcio oksidą pakeičiant kalcio karbonatu.

Hidroterminės sintezės atlikimas

Ruošiant kalcio oksido ir silikagelio mišinį hidroterminei sintezei, pasverti reikiami komponentų kiekiai supilti į sandarų plastikinį indą ir į jį įdėti 3 porcelianiniai malimo kūnai (homogenizavimo kokybei užtikrinti). Mišinys homogenizuotas 1 h (49 aps/min greičiu) įrenginiu „Turbula Type T2F“ (Šveicarija). Paruoštas mišinys užpiltas distiliuotu vandeniu, kad suspensijoje vandens ir kietųjų medžiagų santykis V/K būtų lygus 20, o bendras tūris – 300 cm^3. Sintezė vykdyta suspensiją maišant 100 aps/min greičiu 600 cm^3 talpos autoklave „Parr Instruments“ (Vokietija), kai izoterminio išlaikymo temperatūra 95–200 °C, o trukmė – 4–48 h. Sintezės produktai buvo nufiltruoti vakuuminiu filtru ir praplauti acetonu (reakcijai sustabdyti ir sintezės produktų karbonizacijai sumažinti), išdžiovinti 80/105 ±0,3 °C temperatūroje „Snol 30/200“ (Lietuva) džiovykloje per 24 h ir persijoti per sietą, kurio akučių dydis 100 μm.

Aukštatemperatūrės sintezės atlikimas

Visi hidroterminės sintezės produktai buvo išdegti 900–1100 °C temperatūroje vamzdinėje „Nabertherm B 180“ (Vokietija) krosnyje, oro aplinkoje porcelianiniuose tigliuose. Temperatūros didinimo greitis: 10 °C/min, išlaikymas: 1 h.

Kietinimo atlikimas ir stiprio nustatymas

Buvo paruošti sintetinio volastonito ir smėlio mišiniai, kuriuose buvo 20, 25, 30 ir 35 % dviejų stadijų sintezės produkto, ir homogenizuoti 1 h (49 aps/min greičiu) įrenginiu „Turbula Type T2F“ (Šveicarija). Į gautus mišinius įpilta vandens santykiu vandens/rišamosios medžiagos = 0,35 ir išmaišyta iki tolygios tekstūros. 36 × 36 mm cilindro formos bandiniams formuoti imta 65–80 g drėgno mišinio ir supresuoti 10, 12,5 ir 15 kN jėga 1,0 kN/s greičiu ir išlaikant 20 s presu „Form Test MEGA 10-400-50“ (Vokietija). Suformuoti bandiniai kietinti autoklave „Parr instruments“ (Vokietija), 2–24 h 45 °C temperatūroje 15 bar slėgyje CO_2 aplinkoje. Bandiniai po kietinimo buvo gniuždomi presu „Form Test MEGA 10-400-50“ 1,5 kN/s greičiu.

Kompozitų gamyba

Kompozitams gaminti naudoti du sintetiniai užpildai:

- W – $CaO\text{-}SiO_2 \cdot nH_2O\text{-}H_2O$ sistema ($CaO/SiO_2 = 1$); sintetintas 200 °C temperatūroje 12 h maišant ir išdegtas 900 °C temperatūroje 1 h;
- WS – CaO-užterštо silikagelio -H_2O sistema ($CaO/(Al_2O_3+SiO_2+F^-) = 1$); sintetintas 200 °C temperatūroje 12 h maišant ir išdegtas 900 °C temperatūroje 1 h.

Kompozitams gaminti taip pat paruošti funkcionalizuoti užpildai:

- W-C – užpildas W, funkcionalizuotas APTMS;

- WS-C – užpildas WS, funkcionalizuotas APTMS.

Funkcionalizavimas atliktas naudojant funkcionalizavimo (kopuliavimo) agentą akriloksipropiltrimetoksisilaną APTMS, kurio naudota 10 % nuo užpildo masės. Tam, kad susihidrolizuotų, APTMS buvo supiltas į acto rūgštimi (0,1 mol/l) parūgštintą iki pH = 3–4 ir pašildytą iki 70 °C distiliuotą vandenį 30 min maišant. Po to, įmaišius užpildą, gauta suspensija, kurios vandens ir sausos medžiagos masių santykis buvo 10. Funkcionalizavimas atliktas 70 °C temperatūroje 5 h suspensiją maišant. Po reakcijos funkcionalizuoti užpildai išdžiovinti 70 °C temperatūroje iki pastovios masės. Sausi mišiniai dar perplauti izopropanoliu, kad išsiplautų silpnai prisijungusios silano molekulės ir silano homokondensatai – silikonai. Po plovimo užpildai vėl džiovinti 70 °C temperatūroje iki pastovios masės.

Kompozitams gaminti naudota dviejų sudėčių derva: pirmoji buvo sudaryta iš monomero AESO ir reaktyviojo tirpiklio IBOMA masių santykiu 2:3, o antroji – iš AESO ir reaktyviojo tirpiklio THFMA masių santykiu 3:2. Į abi dervas taip įdėta po 3 mol% nuo abiejų monomerų fotoiniciatoriaus TPOL. Į dervas įmaišyta 5 % užpildo nuo masės. Gautos suspensijos homogenizuotos „Ika T25 Digital Ultra Turrax“ (Vokietija) dispergatoriumi 15000 aps./min greičiu 2 min kambario temperatūroje.

Dervų-silikatų kompozitai ((70 × 10 × 1) ± 0,08 mm dydžio plokštelės) suformuoti PTFE formose ir sutinklinti po „Helios Italquartz GR.E 500 W“ (Italija) UV lempa. Intensyvumas 310 mW/cm^2, atstumas nuo bandinio – 15 cm, trukmė, kol sukietės bandinys, – 5 min.

Karkasų gamyba

Karkasų gamybai naudoti volastonito bandiniai W, WS, ir WD:

- W – CaO-SiO_2·nH_2O-H_2O sistema (CaO/SiO_2 = 1); sintetintas 200 °C temperatūroje 12 h maišant ir išdegtas 900 °C temperatūroje 1 h;
- WS – CaO-užteršto silikagelio -H_2O sistema (CaO/(Al_2O_3+SiO_2+F^-) = 1); sintetintas 200 °C temperatūroje 12 h maišant ir išdegtas 900 °C temperatūroje 1 h.
- WD – CaO-plauto užteršto silikagelio-H_2O sistema (CaO/(Al_2O_3+SiO_2+F^-) = 1); sintetintas 200 °C temperatūroje 12 h nemaišant ir išdegtas 900 °C temperatūroje 1 h.

Dervų paruošimas susidėjo iš dviejų pagrindinių dalių. Pirmiausia GDMA sumaišytas su 0,1 masės% Aerosil R972, naudotu kaip suspensijos stabilizatorius. Maišyta 30 s iki homogeniškos masės. Po to įdėta užpildo ir fotoiniciatoriaus ir vėl maišyta 30 s. Gautų dervų karkasų gamybai sudėtis pateikta 5.1 lentelėje.

5.1 lentelė. Karkasų 3D spausdinimui naudotų suspensijų sudėtis

Užpildas	Užpildo masės dalis	Fotoiniciatoriaus kiekis, masės% nuo monomero masės	Stabilizatoriaus kiekis, masės% nuo bendros užpildo ir monomero masės
-	-	0,415	-
W	0,125		0,1
WS	0,2		
WD			

Karkasų gamybai naudotas „Asiga PICO2 39 UV“ (Australija) optinis 3D spausdintuvas. Vieno karkaso sluoksnio storis 100 μm, o 405 nm UV spinduliuotės trukmė vienam sluoksniui – 1 s. Pirmo sluoksnio storis – 220 μm, kuris švitintas 6 s. Spausdinimui parinktas „malkų rietuvės“ (ang. *woodpile*) modelis. Vienos „malkos“ (angl. *log*) plotis ir aukštis – 0,4 mm, o tarpas tarp jų – 1,6 mm. Šios struktūros periodas – 2 mm. Spausdinant naują sluoksnį, „malkos“ pasukamos 60 laipsnių kampu, taip sudarant šešiakampį tinklą. Išoriniai karkasų matmenys – 9,89 × 10,8 × 10 mm. Aštuonios tokios struktūros atspausdintos ant 0,5 mm storio pagrindo.

Atspausdinti karkasai buvo išdegti 1100, 1200, 1250 ir 1300 °C temperatūrose krosnyje „Snol 30/1300“ (Lietuva) ant platinos lėkštelių oro aplinkoje. Temperatūros didinimo greitis – 100 °C/h (1⅔ °C/min), bandiniai izotermiškai išlaikyti pasiektoje temperatūroje 3 h. Po degimo karkasai ataušinti savaime [101, 151].

F^- jonų nustatymas silikagelyje

Remiantis šaltinyje [176] aprašyta metodika, iš užteršto silikagelio paruoštas tirpalas, kuriame esantis F^- kiekis nustatytas potenciometriniu titratoriumi „Mettler Toledo T 70“ naudojant selektyvų F^- jonams elektrodą.

Aktyvaus CaO nustatymas

Aktyvaus CaO kiekis nustatytas pagal standartą ASTM C25-11 [221] ir apskaičiuotas pagal 5.1 formulę:

$$x = \frac{V \cdot n \cdot 2{,}804}{m}\,\%; \qquad (5.1)$$

čia x – CaO aktyvumas, %, V – titravimui sunaudoto HCl kiekis, cm^3, n – HCl koncentracija (1 mol/dm^3), m – tyrimui paimto kalcio oksido masė, g.

Rentgeno spinduliuotės fluorescencinė analizė RSFA

Bandinių elementinė analizė atlikta rentgeno spinduliuotės fluorescenciniu spektrometru „Bruker X-ray S8 Tiger WD“ (Vokietija). Naudotas rodžio (Rh) vamzdelis, antodinė įtampa U_a iki 60 kV, srovės stipris I iki 130 mA. Presuoti bandiniai buvo matuoti helio atmosferoje. Matavimai atlikti naudojant SPECTRA Plus QUANT EXPRESS metodą.

Rentgeno spinduliuotės difrakcinė analizė RSDA

Rentgeno spinduliuotės difrakcinė analizė atlikta difraktometru „Bruker AXS D8 Advance“ (Vokietija). Naudota: spinduliuotė – CuK_{α}, filtras – Ni, detektoriaus judėjimo žingsnis 0,02°, intensyvumo matavimo trukmė žingsnyje – 0,5 s, antodinė įtampa $U_a = 40$ kV, srovės stipris $I = 40$ mA. Rentgeno difrakcinės analizės matavimų tikslumas $2\,\theta = 0{,}01°$.

Vienalaikė terminė analizė VTA

VTA atlikta „LINSEIS STA PT-1000“ (Vokietija) terminiu analizatoriumi. DSK–TGA parametrai: temperatūros didinimo greitis – 10 °C/min, temperatūros intervalas – 25–945 °C, etalonas – tuščias platinos tiglis, atmosfera krosnyje – azotas N_2, bandinio masė – 10 mg. Matavimų tikslumas ± 3 °C.

Diferencinė skenuojamoji kalorimetrija (DSK)

Diferencinė skenuojamoji kalorimetrija (DSK) ir savitosios šiluminės talpos matavimas atlikti naudojant „Netzsch DSC 214 Polyma“ (Vokietija). Temperatūros didinimo greitis – 5 °C/min, o intervalas – 10–50 °C. Atmosfera krosnyje – azotas N_2, kurio srautas – 20 mL/min, naudoti keraminiai bandinių laikikliai ir aliumininiai tigliai.

Dilatometrija (DIL)

Šiluminio terminio matmenų pokyčio matavimai atlikti naudijant „Linseis 75PT 1600“ dilatometrą (Vokietija) su korundo Al_2O_3 bandinio laikikliu. Temperatūros intervalas – KT-1100 °C, temperatūros didinimo greitis – 10 °C/min, azoto N_2 srautas – 20 mL/min. Miltelių pavidalo bandiniai buvo įdėti į korundinį vamzdelį.

Dalelių dydžio nustatymas

Pradinių medžiagų dalelių dydis ir granuliometrija nustatyta lazeriniu granuliometru CILAS 1090 LD (CILAS, Prancūzija) 0,05–500 μm intervale. Dispersinė fazė – suspaustas oras (2,5 bar), kietų dalelių pasiskirstymas oro sraute 12–15 %, matavimo trukmė 15 s. Iš gautų matavimo duomenų buvo apskaičiuotas savitasis paviršiaus plotas S_A.

FT-IR spektrinė analizė

Infraraudonųjų spindulių spektrinė analizė atlikta spektrometru „Perkin Elmer FT-IR System“ (JAV). Analizei naudota vakuuminėje presformoje supresuota tabletė (1 mg medžiagos sumaišytas su 200 mg KBr). Tirta infraraudonojo spektro pagrindiniame diapazone nuo 4000 iki 400 cm^{-1}.

Tankio nustatymas

Bandinių piltinis tankis nustatytas automatiniu tankio matuokliu „Ultrapyc 1200e.“ („Quantachrome instruments“, JAV). Analizei naudotos helio dujos. Bandinio tankis ir tūris pateikiami kaip trijų matavimų aritmetinis vidurkis. Tankio matavimo nuokrypis yra lygus ±0,003 %.

Skenuojamoji elektroninė mikroskopija (SEM)

Analizė atlikta naudojant „Quanta 200 FEG“ („Fei“, Nyderlandai) mikroskopą, kurio darbinė įtampa – 10 kV, o darbinis atstumas – 6,8 mm.

Savitojo paviršiaus ploto S_{BET} analizė

Matavimai atlikti prietaisu „Autosorb iQ Station 1“ („Quantachrome Instruments“, JAV), panaudojant azoto adsorbcijos izotermę 77 K temperatūroje. Savitojo paviršiaus plotas apskaičiuotas pagal BET lygtį, naudojant N_2 adsorbcijos izotermės duomenis $0,05 < p/p_0 < 0,35$ intervale:

$$\frac{1}{X\left(\frac{p_0}{p}-1\right)}=\frac{C-1}{X_m \cdot C}\cdot\frac{p}{p_0}+\frac{1}{X_m \cdot C}; \quad (5.2)$$

čia X_M – N_2 masė viensluoksnyje, g; C – konstanta, susieta su viensluoksnio adsorbcijos aktyvacijos energija; p – N_2 dalinis dujų mišinio N_2 – He slėgis, esant 77 K; p_0 – N_2 sočiųjų garų slėgis eksperimento sąlygomis.

BET lygtis gerai tinka, kai $0,05 < p/p_o < 0,3$. Kai $p/p_s < 0,05$, iškraipymai gaunami dėl paviršiaus nevienalytiškumo, o kai $p/p_o > 0,3$ – dėl pasireiškiančios tarp adsorbuotų molekulių sąveikos. Nepaisant visų apribojimų, polimolekulinės adsorbcijos teorija šiuo metu geriausia ir plačiausiai taikoma fizikinės adsorbcijos teorija.

Dervų klampos nustatymas

Dervų klampa nustatyta rotaciniu viskozimetru „Fungilab SMART L“ (Ispanija), kuriame naudota L2 tipo antgalis. Maišymo greitis – 20 aps./min, temperatūra – 25 °C.

Mechaninės kompozitų savybių nustatymas

Dinaminė termomechaninė analizė (DMTA) buvo atlikta prietaisu „TA Instruments RSA-G2“ (JAV), kuriame sumontuotas trijų taškų lenkimo bandinio laikilis. Analizei naudotas 1 Hz dažnis, apkrova – 0,01 %, o jėga – 0,1 N. Temperatūros intervalas – 25–200 °C, temperatūros didinimo greitis – 3 °C min. Mechaninės sintetinių polimerinių kompozitų savybės nustatytos pagal standartą ISO 527–3 ir šaltinyje [153] nurodytą atlikimo tvarką.

5.3. Rezultatai ir aptarimas

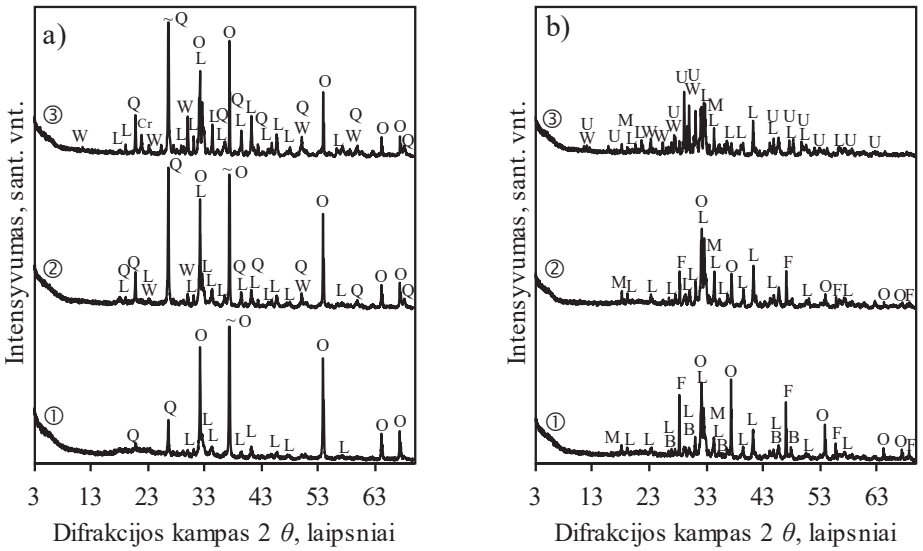
5.3.1. Vienos ir dviejų stadijų volastonito sintezė

Vienos stadijos (tiesioginė) $CaO\text{-}SiO_2 \cdot nH_2O\text{-}H_2O$ sistemoje

Nustatyta, kad vienos stadijos sintezės 900 °C temperatūroje per 1 h $CaO\text{-}SiO_2 \cdot nH_2O$ sistemoje (žr. 5.1 pav., a) susidarė tik larnito Ca_2SiO_4, kuriam būdingas dvigubai didesnis CaO/SiO_2 molinis santykis nei volastonitui $CaSiO_3$, užuomazgos. Tikslinio junginio susidarymas identifikuotas 1000 °C temperatūroje, kai pagrindinės smailės (0,2976 nm) intensyvumas buvo 117 sm. sk./s. Didinant temperatūrą iki 1100 °C, jo pagrindinės smailės intensyvumas padidėjo iki 467 sm. sk./s. Be to, pastebėta, kad kalcio oksidas nevisiškai sureagavo visame 900–1100 °C temperatūrų intervale. Taip pat nustatyta, kad amorfinio silicio dioksidas

persikristalizavo į kvarcą: pagrindinės smailės intensyvumas (0,3346 nm) padidėjo nuo 428 sm. sk./s 900 °C temperatūroje iki 2201 sm. sk./s 1100 °C temperatūroje.

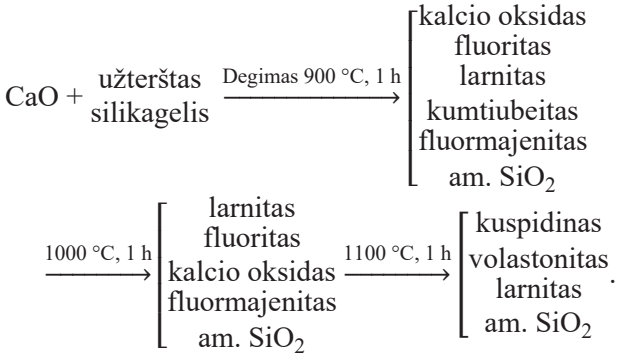
Nustatyta, kad komponentų sąveika pradiniame CaO ir užteršto silikagelio sistemoje (žr. 5.1 pav., b), esant 900 °C temperatūrai, buvo nežymi: pagrindinis naujas junginys, susidaręs dėl $CaO\text{-}F^-$ reakcijos, – fluoritas CaF_2; identifikuotos intensyvios CaO smailės (975 sm. sk./s); susidarė kelios silikatinės fazės, kurių CaO/SiO_2 santykis yra 2: larnitas ir kumtiubeitas $Ca_5Si_2O_8F_2$. Šioje sistemoje aliuminio jonai skatino fluormajenito $Ca_{12}Al_{14}O_{32}F_2$ susidarymą. Padidinus temperatūrą iki 1000 °C, pagrindinės CaO smailės intensyvumas sumažėjo daugiau kaip du kartus (403 sm. sk./s), o larnito smailių intensyvumas padidėjo. Be to, šioje temperatūroje kumtiubeitas nebuvo identifikuotas. Padidinus temperatūrą iki 1100 °C, sintezės produktuose identifikuotas volastonitas, sureagavo visas fluoritas ir susidarė kuspidinas $Ca_4Si_2O_7F_2$ – junginys, artimas kumtiubeitui, tačiau jo molinis CaO/SiO_2 santykis mažesnis (1,5).



5.1 pav. Vienos stadijos sintezės (1 h) produktų RSDA kreivės: a – $CaO\text{-}SiO_2{\cdot}nH_2O$ sistema, b – CaO-užteršto silikagelio sistema. Kreivės: 1 –900 °C, 2 – 1000 °C, ir 3 – 1100 °C. Čia: O – kalcio oksidas, Q – kvarcas, Cr – kristobalitas, L – larnitas, W – volastonitas

Apibendrintas junginių susidarymas $CaO\text{-}SiO_2{\cdot}nH_2O$ ir CaO-užteršto silikagelio sistemose vienos stadijos sintezės 900–1100 °C temperatūroje metu (1 h), pateiktas schemose:

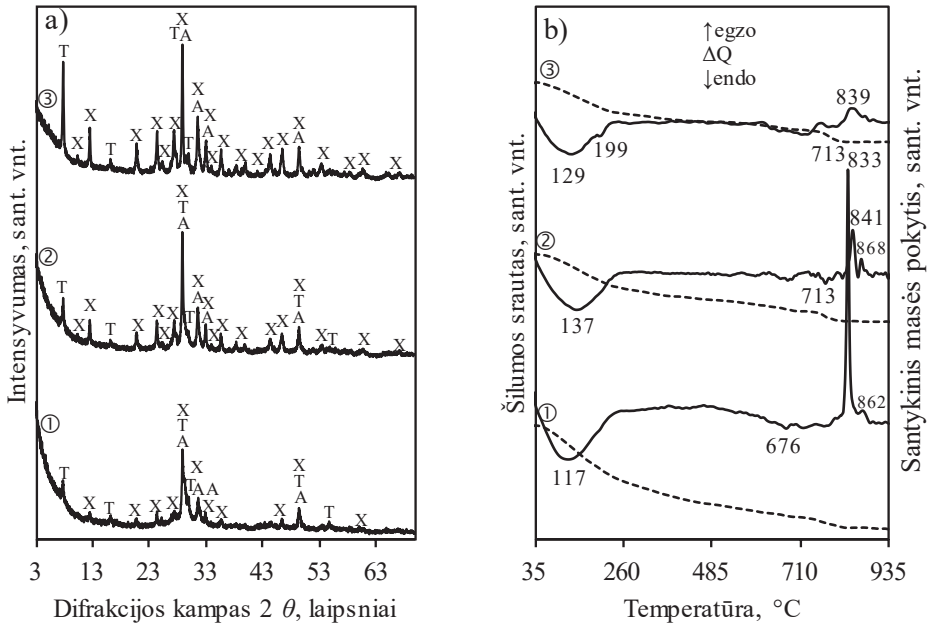
$$CaO + SiO_2{\cdot}nH_2O \xrightarrow{\text{Degimas 900 °C, 1 h}} \begin{bmatrix}\text{kalcio oksidas}\\ \text{larnitas}\\ \text{kvarcas}\\ \text{am. } SiO_2\end{bmatrix} \xrightarrow{\text{1000-1100 °C, 1 h}} \begin{bmatrix}\text{kalcio oksidas}\\ \text{larnitas}\\ \text{kvarcas}\\ \text{am. } SiO_2\\ \text{volastonitas}\end{bmatrix};$$



Apibendrinant galima teigti, kad, naudojant kalcio oksido ir silicio dioksido / užteršto silikagelio sistemas vienos stadijos sintezei, volastonitas susidaro ~1100 °C temperatūroje, tačiau produktuose identifikuojama tiek pradinių, tiek tarpinių junginių. Tačiau užterštame silikagelyje esančios priemaišos pagerino kalcio oksido ir kitų junginių sąveiką. Tačiau dauguma susidariusių kristalinių fazių pasižymėjo didesniu CaO/SiO_2 moliniu santykiu nei tikslinis junginys.

Dviejų stadijų sintezė $CaO\text{-}SiO_2{\cdot}nH_2O\text{-}H_2O$ sistemoje

Nustatyta, kad po 4 h izoterminio išlaikymo 200 °C temperatūroje susiformavo C-S-H(I)/(II), 1,13 nm tobermoritas ir ksonotlitas (žr. 5.2 pav., a). Nustatyta, kad, hidroterminės sintezės trukmei pailgėjus iki 12–48 h, susintetintų produktų mineralinė sudėtis nepakito. Pagrindinis skirtumas tarp sintetintų produktų RSDA kreivių, gautų po 4 ir 48 h, yra difrakcijos smailių intensyvumas. Literatūros duomenimis [155–157], tobermoritas ir C-S-H(I)/(II) yra nestabilūs mišiniuose, kuriuose molinis CaO/SiO_2 santykis lygus 1,0, ir po ilgos sintezės trukmės (> 72 h) turėtų persikristalizuoti į termodinamiškai stabilų junginį – ksonotlitą.



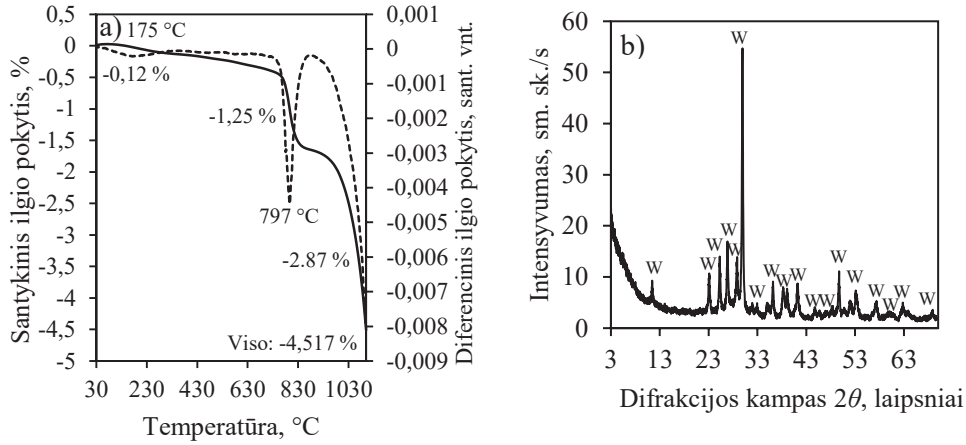
5.2 pav. Hidroterminės sintezės CaO-SiO_2·nH_2O-H_2O sistemoje produktų (200 °C, maišant) produktų RSDA (a) ir VTA (b, vientisa linija – DSK, punktyrinė linija – TG) kreivės: 1 – po 4 h, 2 – 12 h, 3 – 48 h.
Čia T – 1.13 nm tobermoritas, X – ksonotlitas, A – C-S-H(I)/(II)

RSDA rezultatus patvirtino VTA duomenys. Pirmąjį endoterminį efektą 35–250 °C temperatūros intervale galima priskirti adsorbcinio vandens pašalinimui ir dalinei kalcio hidrosilikatų dehidratacijai (žr. 5.2 pav., b). Nustatyta, kad šio efekto šilumos ir masės nuostoliai gerokai sumažėjo ilginant hidroterminės sintezės trukmę, o tai rodo, kad sumažėjo hidratuotų junginių kiekis. Antrasis nedidelis šiluminis efektas 610–710 °C temperatūrų intervale yra būdingas kalcio karbonato skilimui. Pastarajame intervale masės nuostoliai sudaro 0,6–0,8 %, o tai atitinka ~1,5 % kalcio karbonato masės bandinyje. Dėl mažo kalcio karbonato kiekio šis junginys nebuvo aptiktas RSDA kreivėse. Sintetinių produktų, gautų po 4 h izoterminio išlaikymo, DSK kreivėje nustatytas intensyvu egzoterminis efektas 833 °C temperatūroje. Literatūros duomenimis [142, 145-148], ksonotlitas ir tobermoritas persikristalizavo į volastonitą neišskirdami šilumos (be egzoterminio efekto). Šio šiluminio efekto buvimas rodo, kad sintezės produktuose yra pusiau kristalinio kalcio hidrosilikato (C-S-H(I)). Verta paminėti, kad dėl mažo minėto junginio kristališkumo, kai produkte yra kitų kalcio hidrosilikatų, RSDA kreivėse C-S-H(I)/(II) sunku identifikuoti [149, 150]. Pailginus sintezės trukmę nuo 4 iki 48 h, C-S-H(I)/(II) tapo metastabilus ir, sprendžiant pagal egzoterminio efekto šilumos sumažėjimą nuo 109 iki 35 J/g, persikristalizavo į kitus sintezės produktus – 1,13 nm tobermoritą ir ksonotlitą.

Siekiant išsamiai apibūdinti sintetinių bandinių terminį stabilumą, buvo atlikta dilatometrinė analizė. Bandinio, gauto po 12 h sintezės, dilatometrinės kreivės

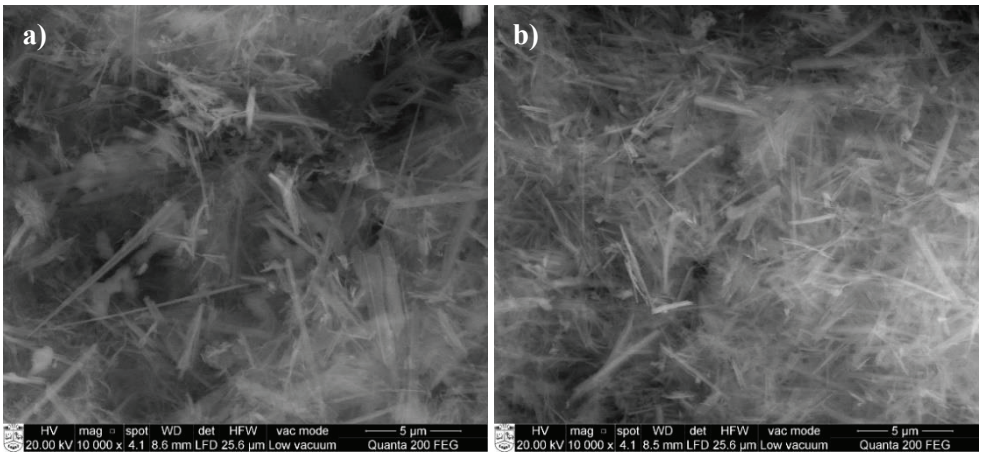
pateiktos 5.3 pav., a. Nustatyta, kad visų bandinių susitraukimas 35–650 °C temperatūrų intervale buvo nedidelis, tačiau aukštesnėse temperatūrose susitraukimas priklauso nuo bandinių hidroterminės sintezės trukmės. Bandinių, gautų po 4 h sintezės, bendrojo susitraukimo vertė buvo didžiausia (10,28 %), ji sumažėjo iki 4,52 % ir 1,2 % didinant hidroterminės sintezės trukmę atitinkamai iki 12 ir 48 h. Reikšmingą susitraukimo sumažėjimą galima paaiškinti C-S-H(I)/(II) kiekio sintezės produktuose sumažėjimu.

Nustatyta, kad nei hidroterminės sintezės trukmė, nei degimo temperatūra neturėjo didelės įtakos volastonito susidarymui degant hidroterminės sintezės produktus 900–1100 °C temperatūrų intervale. Volastonito, išdegto 900 °C temperatūroje, RSDA kreivė pateikta 5.3 pav. RSDA rezultatai parodė, kad pagrindinis skirtumas tarp išdegtų produktų buvo volastonito difrakcinių smailių intensyvumas.



5.3 pav. Hidroterminės sintezės $CaO\text{-}SiO_2 \cdot nH_2O\text{-}H_2O$ sistemoje produktų (200 °C, 12 h, maišant) dilatometrijos kreivės (a, vientisa linija – santykinis ilgio pokytis, punktyrinė linija – diferencinis ilgio pokytis), išdegto 900 °C temperatūroje 1 h bandinio RSDA kreivė (b). Čia: W – volastonitas

Kai volastonito prekursorius buvo sintetinamas 12 h maišant 200 °C temperatūroje, jį sudarė ksonotlitas, tobermoritas ir C-S-H(I) (žr. 5.4 pav., a). Be to, gauta medžiaga buvo makroporinė, o jos savitasis paviršiaus plotas buvo 40,18 m^2/g. Išdegus prekursorių, jis visiškai persikristalizavo į volastonitą, kurio savitasis paviršiaus plotas buvo 33,42 m^2/g ir išlaikė plokštelių arba pluošto struktūrą (W bandinys, 5.4 pav., b).



5.4 pav. SEM nuotraukos: a – bandinio po hidroterminės sintezės ($CaO\text{-}SiO_2\cdot nH_2O\text{-}H_2O$ sistema, 200 °C, 12 h, maišant), b – bandinį išdegus 900 °C temperatūroje 1 h

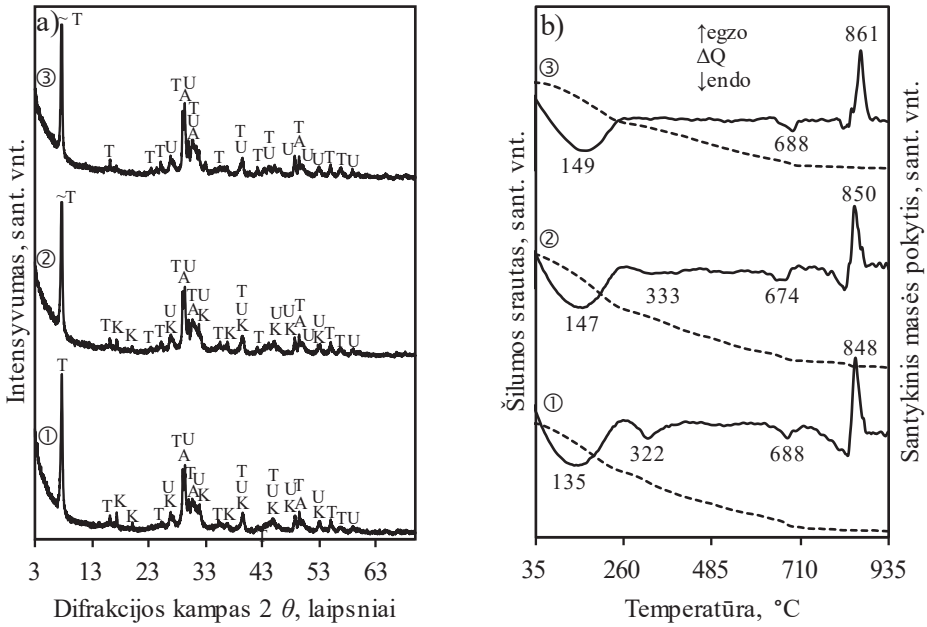
Apibendrinant volastonito dviejų stadijų sintezės (hidroterminės sintezės ir degimo) $CaO\text{-}SiO_2\cdot nH_2O\text{-}nH_2O$ sistemoje rezultatus, junginių susidarymą galima pavaizduoti taip:

$$CaO+SiO_2\cdot nH_2O+H_2O \xrightarrow{\text{Hidroterminė sintezė 200 °C, 4–48 h}} \left[\begin{array}{l}\text{C–S–H(I)/(II)}\\ \text{ksonotlitas}\\ \text{tobermoritas}\end{array}\right. \xrightarrow{\text{Degimas 900–1100 °C, 1 h}} [\text{volastonitas}.$$

Dviejų stadijų sintezė CaO-užteršto silikagelio-H_2O sistemoje

Nustatyta, kad pirminio mišinio cheminė sudėtis turi didelę įtaką kalcio hidrosilikatų susidarymui hidroterminėmis sąlygomis 200 °C temperatūroje. RSDA rezultatai rodo, kad po 4 h hidroterminės sintezės 200 °C temperatūroje visi pradiniai junginiai, portlanditas $Ca(OH)_2$, rosenbergitas $AlF_3\cdot 3H_2O$ ir gibsitas $Al(OH)_3$), reaguodami sudarė tris kristalinius junginius: 1,13 nm tobermoritą, kuspidiną $Ca_4Si_2O_7F_2$ ir katoitą $Ca_3Al_2(SiO_2)_{0,5}(OH)_{10}$ (žr. 5.5 pav., a). Pailginus izoterminio išlaikymo trukmę iki 24 h, sintezės produktų sudėtis išliko nepakitusi, tačiau tobermorito pagrindinių difrakcinių smailių intensyvumas padidėjo, o katoito – sumažėjo. 48 h sintezės produktuose katoitas nebuvo identifikuotas. Taigi galima teigti, kad, pailginus sintezės trukmę, pastarasis junginys tampa metastabilus ir pradeda persikristalizuoti į kitus junginius ir aliuminio jonai įsiterpia į kitų junginių struktūrą.

Sintezės produktų VTA kreivės (žr. 5.5 pav., b) ir reakcijų šiluminiai efektai atitinka RSDA duomenis. DSK kreivėje pirmasis endoterminis efektas (35–250 °C) yra būdingas adosrbcinio vandens pasišalinimui ir dalinei tobermorito dehidratacijai; antrasis endoterminis efektas (~650 °C) būdingas kalcio karbonato skilimui, o trečiasis endoterminis efektas (~816 °C) būdingas pusiau kristalinių kalcio hidrosilikatų dehidratacijai. Egzoterminis efektas (841–848 °C) būdingas volastonito susidarymui iš pusiau kristalinio C-S-H(I).

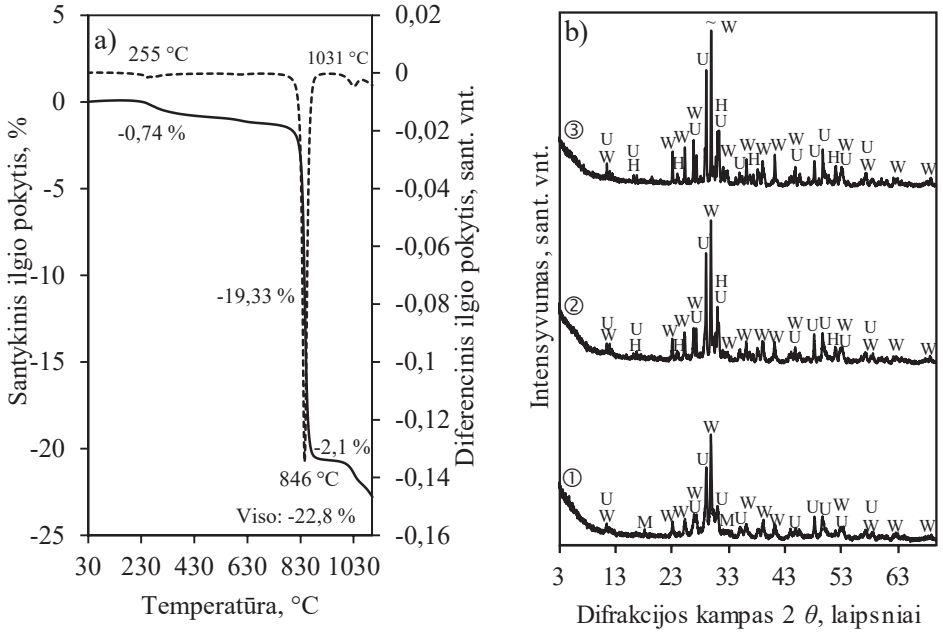


5.5 pav. Hidroterminės sintezės CaO-užteršto silikagelio-H_2O sistemoje produktų (200 °C, maišant) produktų RSDA (a) ir VTA (b, vientisa linija – DSK, punktyrinė linija – TG) kreivės: 1 – po 4 h, 2 – 12 h, 3 – 48 h.
Čia: T – 1,13 nm tobermoritas, U – kuspidinas, K – katoitas, A – C-S-H(I)

Siekiant nustatyti degimo temperatūros įtaką bandinių matmenims (susitraukimui), buvo atlikta dilatometrinė analizė. Bandinio, gauto po 12 h sintezės, dilatometrinės kreivės pateiktos 5.6 pav., a. Gautiems rezultatams būdingos keturios susitraukimo stadijos 35–1100 °C temperatūrų intervale, jos gerai sutampa su VTA rezultatais (žr. 5.5 pav., b). Pirmasis bandinių matmenų pokyčių etapas buvo nustatytas tame pačiame temperatūrų intervale, kaip ir adsorbuoto vandens pašalinimas ir dalinė sintezės produktų dehidratacija (100–450 °C). Šio proceso metu visų bandinių santykiniai ilgio pokyčiai buvo nedideli (~–1 %). Antrąjį susitraukimo intervalą lėmė kalcio karbonato skilimas. Dėl mažo kalcio karbonato kiekio gaminiuose (< 3 masės %) susitraukimas buvo nereikšmingas. Trečiojo susitraukimo etapo temperatūros intervalas atitinka galutinius endoterminį ir egzoterminį efektus (žr. 5.5 pav., b). Remiantis literatūros duomenimis, gryno 1,13 nm tobermorito matmenų pokytis iki 1000 °C yra nedidelis, o ryškus susitraukimas būdingas kalcio hidrosilikatams su įsiterpusiais aliuminio jonais [164]. Gauti duomenys parodė, kad per galutinį tobermorito skilimo / persikristalizavimo etapą (840–900 °C) visų bandinių santykinis ilgis sumažėjo 16–19 %. Gauti duomenys gerai sutampa su literatūros duomenimis. Galutinis susitraukimo etapas gali būti susijęs su tam tikrais mineralinės sudėties pokyčiais. Remiantis skaičiavimais, hidroterminės sintezės trukmė neturi įtakos bendram bandinių susitraukimui, nes visi bandiniai rodo panašias vertes. O sintezės produktų mineralinė sudėtis turi lemiamą įtaką minėtam parametrui, nes sintezės produktų, gautų iš amorfinio silicio dioksido

ir kalcio oksido, bendras susitraukimas yra lygus atitinkamai 4,52 % (po 12 h sintezės) ir 1,2 % (po 48 h sintezės), o bandinių, gautų iš mišinių su užterštu silikageliu, vertės yra didesnės atitinkamai 5 ir 18 kartų.

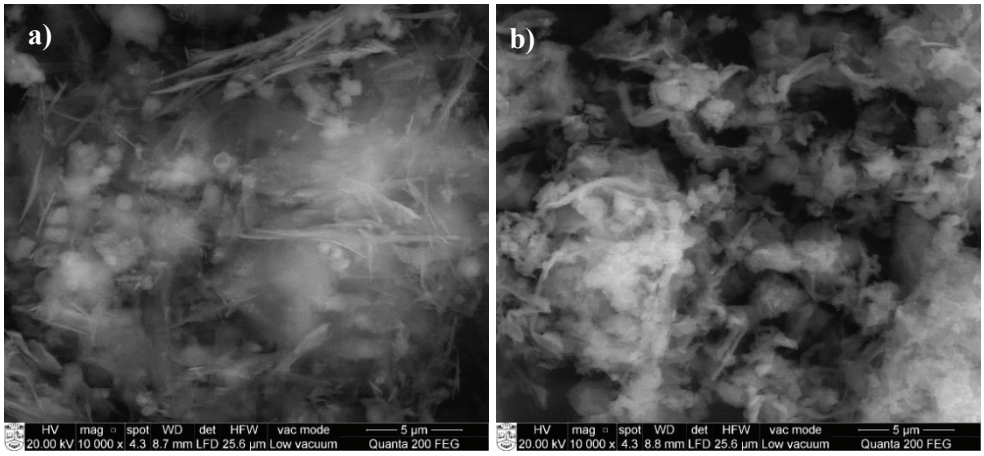
Kadangi pradiniai junginiai sureagavo per 12 h sintezės (žr. 5.5 pav., a), o hidroterminio apdorojimo trukmė neturėjo didelės įtakos sintezės produktų terminėms savybėms, po 12 h sintezės gauti sintezės produktai 1 h buvo degami skirtingose temperatūrose. Gauti rezultatai parodė, kad, degant 900 °C temperatūroje, hidroterminės sintezės produktuose esantys kalcio hidrosilikatai persikristalizavo į volastonitą, o kuspidinas išliko stabilus (žr. 5.6 pav., b). Katoitas persikristalizavo į fluormajenitą $Ca_{12}Al_{14}O_{32}F_2$. Šis junginys susidarė dėl katoito / majenito ir sistemoje esančių fluorido jonų sąveikos. Aukštesnėse temperatūrose (1000 °C ir 1100 °C) fluormajenitas reagavo su kitais junginiais, todėl identifikuotas gelenitas $Ca_2Al_2SiO_7$, kurio struktūroje nėra fluorido jonų. Dėl šios priežasties sintezės produkto nerekomenduojama degti aukštesnėje nei 1000 °C temperatūroje. Be to, galutinis susitraukimo etapas esant > 950 °C temperatūrai gali būti susijęs su rekristalizacijos procesu iš fluormajenito į gelenitą.



5.6 pav. Hidroterminės sintezės CaO-užteršto silikagelio-H_2O sistemoje produktų (200 °C, 12 h, maišant) dilatometrijos kreivės (a, vientisa linija – santykinis ilgio pokytis, punktyrinė linija – diferencinis ilgio pokytis), išdegto 900 °C temperatūroje 1 h bandinio RSDA kreivė (b, 1 – 900 °C, 2 – 1000 °C, 3 – 1100 °C).
Čia: W – volastonitas, U – kuspidinas, M – fluormajenitas, H – gelenitas

Kai volastonito prekursorius CaO-užteršto silikagelio-H_2O sistemoje buvo sintetinamas 12 h maišant 200 °C temperatūroje, jį sudarė tobermoritas, kuspidinas, katoitas ir C-S-H(I) (žr. 5.7 pav., a). Be to, gauta medžiaga buvo mezoporinė, o jos

savitasis paviršiaus plotas buvo 67,92 m^2/g. Po degimo jis persikristalizavo į volastonitą ir fluormajenitą, o kuspidinas išliko stabilus. Nors medžiaga išliko mezoporinė, tačiau savitasis paviršiaus plotas sumažėjo iki 16,09 m^2/g (bandinys WS, 5.7 pav., b).



5.7 pav. SEM nuotraukos: a – bandinio po hidroterminės sintezės (CaO-užteršto silikagelio-H_2O sistema, 200 °C, 12 h, maišant), b – bandinį išdegus 900 °C temperatūroje 1 h

Apibendrinant hidroterminės sintezės ir degimo rezultatus CaO-užteršto silikagelio-nH_2O sistemoje, junginių susidarymą galima pateikti tokia tvarka:

$$\text{CaO+užterštas silikagelis+}H_2O \xrightarrow{\text{Hidroterminė sintezė 200 °C, 4–48 h}} \begin{bmatrix}\text{C-S-H(I)}\\ \text{tobermoritas}\\ \text{kuspidinas}\\ \text{katoitas}\end{bmatrix} \xrightarrow{\text{Degimas 900°C, 1 h}} \begin{bmatrix}\text{volastonitas}\\ \text{kuspidinas}\\ \text{fluormajenitas}\end{bmatrix} \xrightarrow{\text{Degimas 1000–1100°C, 1 h}} \begin{bmatrix}\text{volastonitas}\\ \text{kuspidinas}\\ \text{gelenitas}\end{bmatrix}.$$

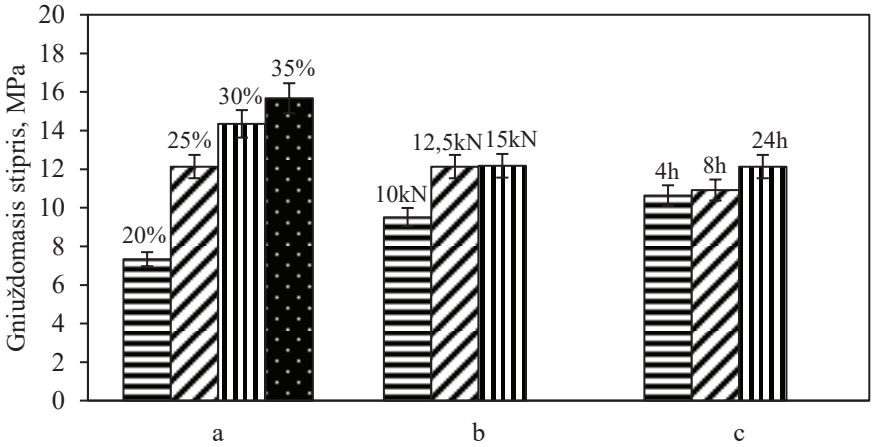
5.3.2. Sintetinio volastonito panaudojimas

Kietinimas CO_2 aplinkoje

Kietinimui anglies dioksido aplinkoje tirti buvo pasirinkti du sintetinio volastonito bandiniai. Pirmasis – hidrotermiškai susintetintas (130 °C, 8 h, suspensiją maišant, CaO-užteršto silikagelio-nH_2O sistema) ir išdegtas 900 °C temperatūroje 1 h volastonito bandinys – V1. Antrasis – hidroterminės sintezės produktas, gautas 12 h veikiant 200 °C temperatūrai ir 1 h kalcinuojant 900 °C temperatūroje – bandinys V2.

Tiriant volastonito V1-smėlio bandinių kietinimą CO_2 aplinkoje, nustatyta, kad gniuždomasis stipris labiausiai priklauso nuo rišamosios medžiagos kiekio mišinyje. Padidinus rišamosios medžiagos kiekį nuo 20 iki 35 % masės, stipris padidėjo daugiau kaip du kartus: nuo 7,34 iki 15,68 MPa (žr. 5.8 pav., a). Didėjant presavimo jėgai bandinių formavimo metu, kai rišamosios medžiagos ir smėlio santykis buvo

1:3 (rišamosios medžiagos kiekis – 25 masės %), gniuždomasis stipris padidėjo trečdaliu: nuo 9,51 (10 kN) iki 12,15 (15 kN) MPa (žr. 5.8 pav. b). Kietinimo trukmė gniuždymo stipriui turėjo mažą įtaką, nes gniuždomasis stipris padidėjo tik 14 %: nuo 10,64 (4 h) iki 12,13 (24 h) MPa (žr. 5.8 pav., c).



5.8 pav. V1-smėlio bandinių stiprumo gniuždant priklausomybė nuo: a – rišamosios medžiagos kiekio, b – presavimo jėgos, c – kietinimo trukmės. (a ir b – kietinti 24 h, b ir c – 25 % rišamosios medžiagos, a ir c – 12,5 kN presavimo jėga)

Karbonizacijos laipsnis apskaičiuotas pagal bandinių be smėlio TG duomenis (vandens ir rišamosios medžiagos santykis = 0,35, formavimo jėga – 12,5 kN, kietėjimo trukmė: 4, 8 ir 24 h) ir nustatyta, kad visuose bandiniuose be smėlio buvo ~23 % masės CO_2. Didžiausią CO_2 kiekį, kuris gali būti surištas rišamojoje medžiagoje, galima apskaičiuoti pagal Steinour'o formulę (5.3):

$$CO_2\ (\%max) = 0{,}785(CaO - 0{,}7SO_3) + 1{,}091MgO + 1{,}420Na_2O + 0{,}935K_2O;\ (5.3)$$

čia: CaO, SO_3, MgO, Na_2O ir K_2O yra atitinkamų sudedamųjų oksidų masės procentinės dalys. Šiuo atveju pradiniame mišinyje yra tik CaO = 48,31 % masės. Taigi:

$$CO_2\ (\%max) = 0{,}785 \cdot 48{,}31\ \% = 37{,}92\ \%.$$

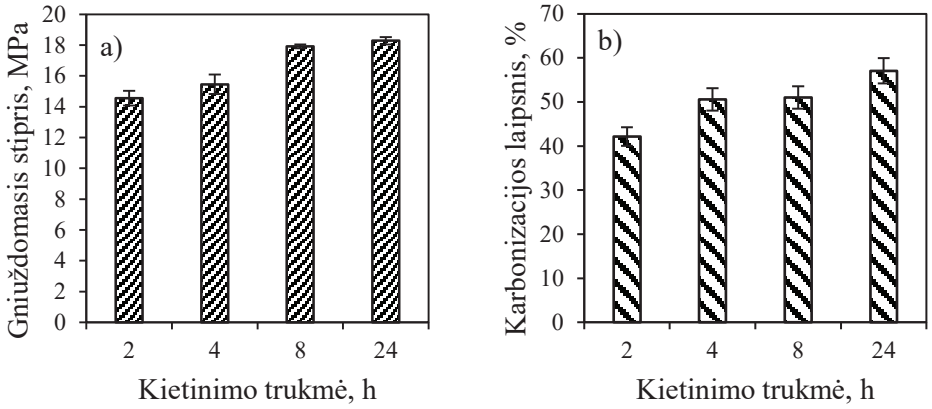
Norint apskaičiuoti karbonizacijos laipsnį, naudota formulė (5.4):

$$\text{Karbonizacijos laipsnis, \%} = \frac{CO_2 \text{ kiekis (masės\%)}}{\text{Maksimalus } CO_2 \text{ kiekis (masės\%)}} \cdot 100\ \%;\ (5.4)$$

$$\text{Karbonizacijos laipsnis, \%} = \frac{23\ \%}{37{,}92\ \%} \cdot 100\ \% = 60{,}64\ \%.$$

Nustatyta, kad CO_2 aplinkoje sukietintų sintetinio volastonito V2 ir smėlio bandinių gniuždomasis stipris svyravo nuo ~14 MPa po 2 h kietinimo iki ~18 MPa po 8–24 h (žr. 5.9 pav., a). Didžiausia reikšmė buvo 1,5 karto didesnė nei ankstesniame tyrime, kuriame naudotas sintetinis volastonitas V1. Vis dėlto sintetinio volastonito-smėlio bandinių gniuždomojo stiprio vertės buvo apie 2,5–3 kartus mažesnės nei rankinito ar kalcio olivino, kuriuose CaO yra 1,5–2 kartus daugiau.

Volastonito karbonizacijos laipsnis apskaičiuotas pagal Steinouro formulę (5.3 lygtis) ir pateiktas 5.9 pav., b. Apskaičiuota, kad vertės kito nuo 42 iki 57 % ir, kaip ir gniuždomasis stipris, priklausė nuo kietėjimo trukmės. Be to, V2 karbonizacijos laipsnio vertės buvo šiek tiek mažesnės nei ankstesniame tyrime, kuriame karbonizacijos laipsnis siekė apie 60 %. Palyginti su ankstesniais volastonito, rankinito ir kalcio olivino tyrimais, galima pastebėti tendenciją, kad, didėjant gniuždomajam stipriui, karbonizacijos laipsnis mažėja dėl skirtingų cheminių rišamosios medžiagos savybių.

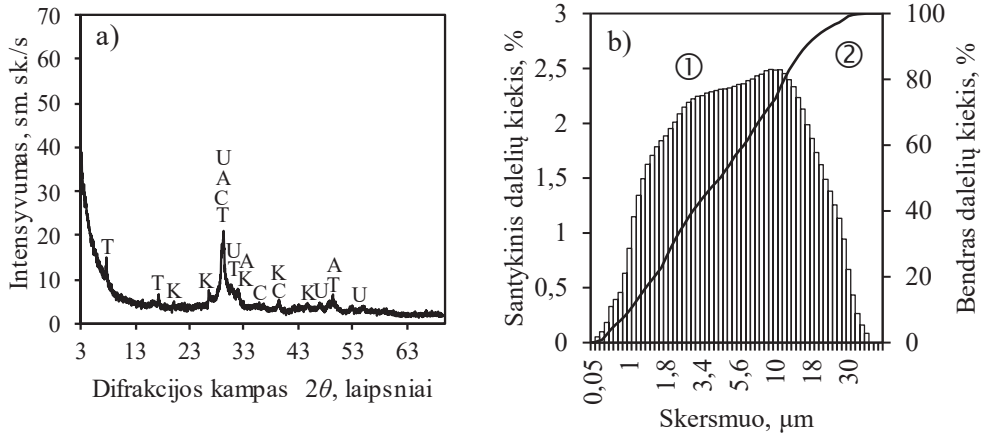


5.9 pav. V2-smėlio (santykis 1:3) bandinių gniuždomasis stipris (a) ir karbonizacijos laipsnis (b)

Sintetinių kalcio (hidro)silikatų panaudojimas baltojo betono gamybai

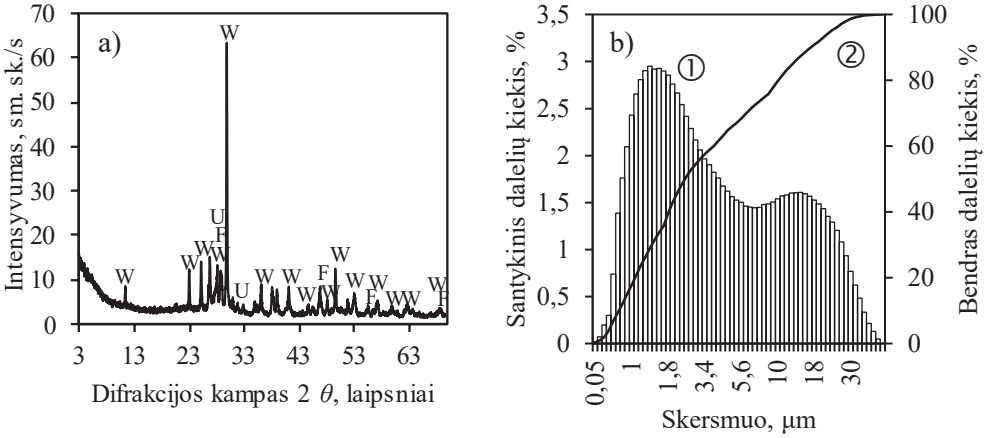
Aliuminio fluorido gamybos atliekoje silikagelyje paprastai būna 8–10 % fluorido jonų, o tai labai susiaurina atliekų panaudojimo galimybes. Todėl, siekiant sumažinti fluorintų junginių, tokių kaip kuspidinas ir fluormajenitas, susidarymą, reikia atlikti papildomą eksperimentą – sumažinti F^- jonų kiekį užterštame silikagelyje ir panaudoti jį volastonitui sintetinti dviejų stadijų sintezės būdu. Fluorido jonų kiekis silikagelyje buvo sumažintas iki mažiau nei 1 % taikant dinaminį plovimo metodą [177].

Rentgeno difrakcinės analizės metodu nustatyta, kad pirmosios stadijos produkto – sintetinio kalcio hidrosilikatų pagrindu paruošto priedo (prototipas XD) – mineralinė sudėtis buvo: tobermoritas $Ca_5Si_6O_{17}\cdot 5{,}5H_2O$, katoitas $Ca_3Al_2(OH)_{12}$, kuspidinas $Ca_4Si_2O_7F_2$ ir C-S-H(I) (žr. 5.10 pav., a). Išmatavus priedo granuliometrinę sudėtį, nustatyta, kad dalelių skersmuo kito nuo 0,05 iki 50 μm (žr. 5.10 pav., b).



5.10 pav. Kalcio hidrosilikatų pagrindu paruošto priedo (priedas (prototipas) XD) sudėtis: a – mineralinė, b – granuliometrinė (1 – santykinis kiekis, 2 – absoliutusis kiekis).
Čia: T – tobermoritas, K – katoitas, A – C-S-H(I), U – kuspidinas, C – kalcitas

Rentgeno difrakcinės analizės metodu nustatyta, kad išdegto produkto – sintetinio kalcio silikatų pagrindu paruošto priedo (prototipas WD) – mineralinė sudėtis buvo: volastonitas $CaSiO_3$, kuspidinas $Ca_4Si_2O_7F_2$ ir fluoritas CaF_2 (žr. 5.11 pav., a). Išmatavus priedo granuliometrinę sudėtį, nustatyta, kad dalelių skersmuo kito nuo 0,05 iki 50 μm (žr. 5.11 pav., b).



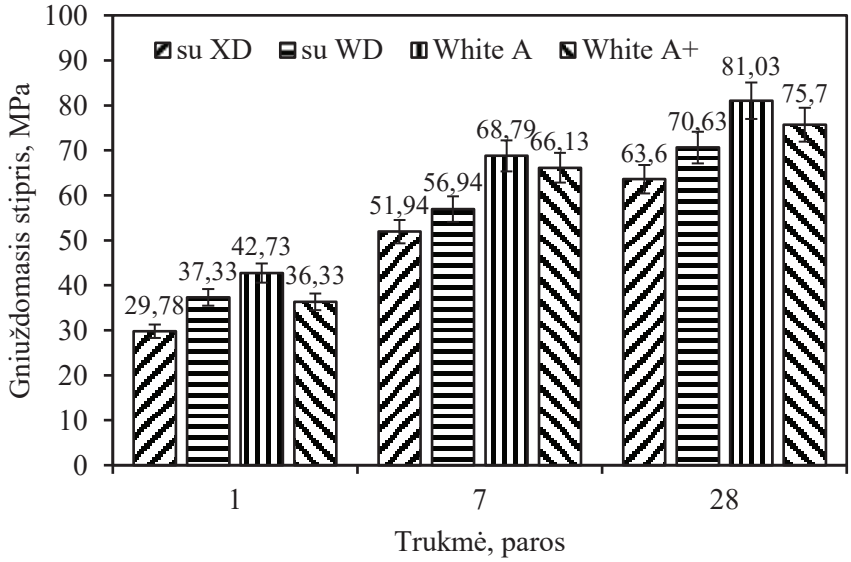
5.11 pav. Kalcio silikatų (volastonito) pagrindu paruošto priedo (priedas (prototipas) WD) sudėtis: a – mineralinė, b – granuliometrinė (1 – santykinis kiekis, 2 – absoliutusis kiekis).
Čia: W – volastonitas, F – fluoritas, U – kuspidinas

Baltojo betono plokščių gamybinio bandymo metu su UAB „Inhus Prefab“ (žr. 1 priedas) pagal standartinę įmonės receptūrą pagamintos plokštės 1 – White A ir 2 – White A+, o mišiniuose mikroužpildą keičiant priedais (prototipais) XD ir WD pagamintos plokštės: 3 – su priedu XD, 4 – su priedu WD (žr. 5.12 pav.).



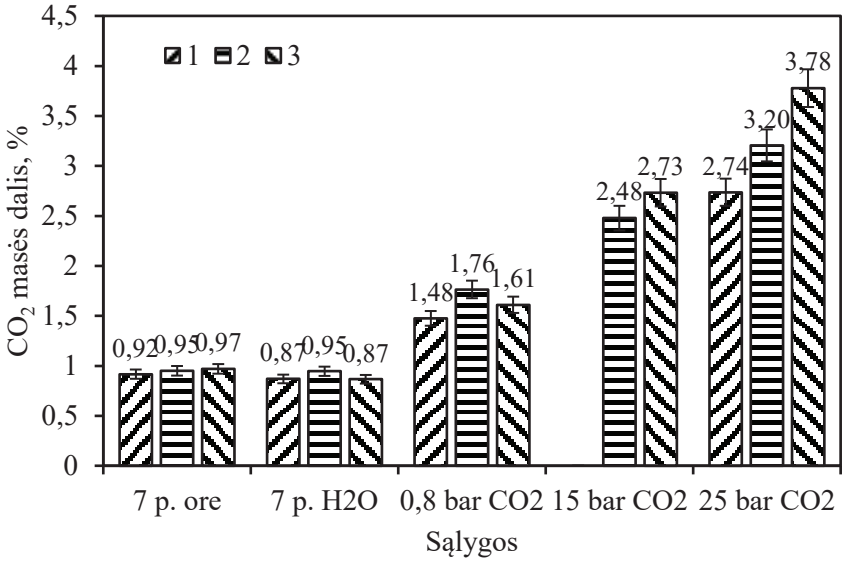
5.12 pav. Gamybinio bandymo metu pagamintos plokštės (su 8 masės % priedo): 1 – White A, 2 – White A+, 3 – su priedu XD, 4 – su priedu WD

Gamybinio bandymo metu nustatyta, kad po 28 kietėjimo parų plokštės White A pasižymėjo didžiausiu gniuždomuoju stipriu – ~81 MPa. Kitų plokščių vertės buvo: su priedu XD – ~21,5 %, su priedu WD – ~17 %, o White A+ – ~10 % mažesnės (žr. 5.13 pav.).



5.13 pav. Skirtingos sudėties baltojo betono plokščių gniuždomojo stiprio priklausomybė nuo kietėjimo trukmės

Nustatyta, kad mažiausiai CO_2 buvo sugerta bandinius kietinant po vandeniu – 0,87–0,95 %, nedaug didesni rezultatai gauti kietinant ore – 0,92–0,97 %. Kietinant 0,8 bar CO_2 slėgyje, sugerto anglies dioksido kiekis padidėjo iki ~1,6 %. Šiomis sąlygomis aiškių skirtumų tarp bandinių nenustatyta, nes verčių skirtumai buvo iki paklaidos ribų. Po kietinimo 25 bar CO_2 slėgyje nustatyta, kad bandinyje su 10 % WD priedo buvo ~3,8 % anglies dioksido, t. y. 38 % daugiau nei baltojo betono bandinyje be priedo ir plastifikatoriaus arba 18 % daugiau nei baltojo betono bandinyje be priedo, bet su plastifikatoriumi (žr. 5.14 pav.).



5.14 pav. Skirtingomis kietinimo sąlygomis sugerto anglies dioksido masės dalis bandiniuose: 1 – baltasis cementas, smėlis ir vanduo, 2 – baltasis cementas, smėlis ir vanduo su plastifikatoriumi (1 %), 3 – baltasis cementas su 10 % WD priedu, smėlis ir vanduo su plastifikatoriumi (1 %)

Sintetinio volastonito funkcionalizavimas ir polimeriniai kompozitai

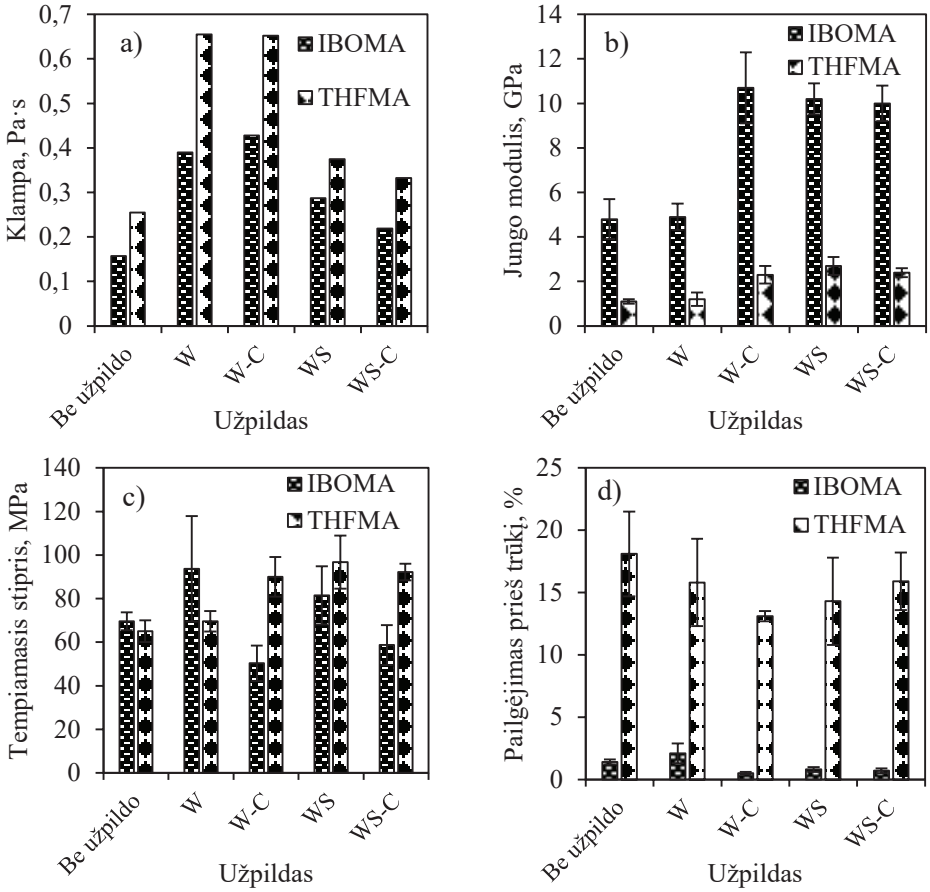
AESO-IBOMA mišinio (40 % masės: 60 % masės, AI derva) ir AESO-THFMA mišinio (60 % masės: 40 % masės, AT derva) be jokių užpildų klampos vertės buvo atitinkamai 157,4 ir 255 mPa·s (žr. 5.15 pav., a). Į AI ir AT dervas pridėjus 5 % masės W/W-C užpildų, klampa padidėjo ~2,6 karto. Reikia pažymėti, kad užpildo W funkcionalizavimas neturėjo teigiamos įtakos dervų klampai. Kita vertus, nustatytas teigiamas užpildo WS funkcionalizavimo poveikis dervų klampai. Pridėjus 5 % masės užpildų WS/WS-C, AI ir AT dervų klampos vertės padidėjo atitinkamai ~1,6 ir ~1,4 karto. Mišinių su funkcionalizuotais užpildais klampa buvo 24 % mažesnė negu grynos AI dervos ir 11 % mažesnė nei AT dervos. Šie rezultatai atitinka bendrą tendenciją, kad hidrofobinis padengimas turėtų pagerinti hidrofilinių užpildų savybes dervose.

Nustatyta, kad, pridėjus užpildo W beveik nepasikeitė kompozitų Jungo modulis, nes tiek AI, tiek AT dervų su priedu vertės nedaug skyrėsi nuo pradinių, atitinkamai 4,8 ir 1,1 MPa (žr. 5.15 pav., b). Pridėjus kiekvieno kito užpildo, abiejų dervų Jungo modulis padidėjo apie 2,2 karto.

Nustatyta, kad tempiamojo stiprio priklausomybė nuo užpildo kiekvienos dervos buvo skirtinga (žr. 5.15 pav., c). Grynos AI dervos bandinio tempiamasis stipris buvo 69,6 MPa. Pridėjus nefunkcionalizuotų užpildų W ir WS, stipris padidėjo atitinkamai 35 % ir 17 %, tačiau, pridėjus tiek pat funkcionalizuotų užpildų W-C ir WS-C, stipris sumažėjo atitinkamai 28 % ir 16 %. Užpildų poveikis AT dervų kompozitų tempimo stipriui buvo panašus į Jungo modulio poveikį. Nustatyta, kad, pridėjus užpildo W, ši vertė padidėjo nedaug: nuo pradinės 65,1 iki 69,6 MPa.

Tačiau, pridėjus visų kitų užpildų, tempiamasis stipris padidėjo iki ~93 MPa, t. y. ~43 %.

Nustatyta, kad užpildai turėjo neigiamos įtakos pailgėjimui nutrūkimo momentu (žr. 5.15 pav., d). Pradinė AI dervos bandinio vertė buvo 1,4 %. Pridėjus užpildo W, ši vertė padidėjo 50 %, o dėl kitų užpildų ji sumažėjo 45–60 %. Pradinis AT dervos bandinių pailgėjimas nutrūkimo momentu buvo 18,5 %. Pridėjus užpildo W, ši vertė sumažėjo 12,7 %, W-C – 27,6 %, WS – 21 %, o WS-C – 12,2 %. Šie rezultatai atitinka Jungo modulio pokyčius, nes visų bandinių, kurie dėl užpildo tapo standesni, pailgėjimo nutrūkstant vertė sumažėjo.



5.15 pav. Mechaninės volastonito-polimerų kompozitų savybės: a – nesutinklintos dervos klampa, b – Jungo (tampros) modulis, c – tempiamasis stipris, d – pailgėjimas nutrūkstant

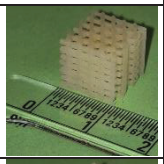
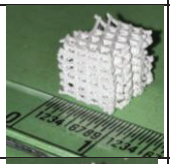
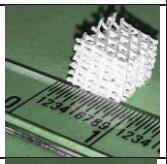
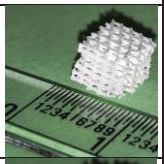
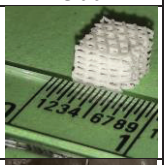
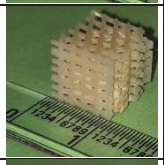
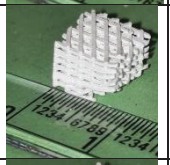
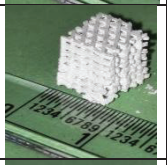
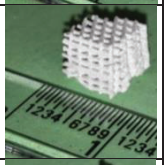
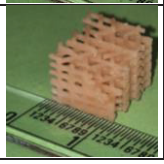
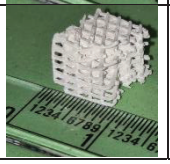
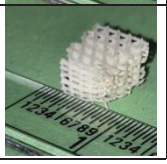
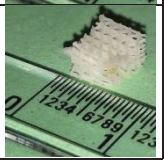
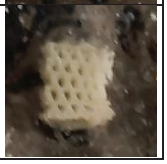
Optiškai 3D spausdinti volastonito-polimero karkasai

Išdegus pradinius polimero-sintetninio volastonito karkasus (prekursorius, 5.2 lentelė), pastebėta, kad silpnai pritvirtintos išorinės dalys atlipo ir deformavosi. Be to, pradinius karkasus buvo galima gerai atskirti pagal jų spalvas, tačiau išdegti jie buvo beveik visiškai balti, išskyrus karkasą su užpildu WD. Pastarasis prieš išdegant atrodė rausvos spalvos, o po sukepinimo 1100–1300 °C temperatūroje išliko

nedidelis atspalvis. Išdegus gaminius 1300 °C temperatūroje, tik W karkasas liko nedeformuotas, WS karkasas išsilydė, o WD smarkiai deformavosi ir stipriai prilipo prie platinos lėkštelės. Pastebėtina, kad 1200–1300 °C temperatūroje tik WD karkasas atrodė šiek tiek sukepęs ir skaidrus. Tiek deformaciją, tiek lydymąsi lėmė F^- jonų, kurie mažina silikatinių medžiagų lydymosi temperatūrą, buvimas. Tikėtina, kad kuspidinas, kurio buvo gausu WS karkase, neskatino sukepimo ir vitrifikacijos, o fluoritas, kurio buvo WD, skatino.

Išmatuota, kad prieš išdegant karkasų gniuždomasis stipris buvo apie ~2 MPa. 1100 °C temperatūroje išdegė polimerinė matrica, o užpildo dalelės nesukepė, todėl visi karkasai buvo labai trapūs ir neturėjo gniuždomojo stiprio. Norint, kad dalelės susilietų ir karkasai įgytų tvirtumo, reikėjo išdegti mažiausiai 1200 °C temperatūroje: W ir WS vertės buvo ~0,1 MPa, o pradėjusio stiklėti WD karkaso – 0,35 MPa. Tokia pati tendencija pastebėta ir esant 1250 °C temperatūrai: W ir WS pasiekė apie 0,2 MPa, o WD – apie 0,85 MPa. Tačiau 1300 °C temperatūroje WS ir WD bandiniai tapo netinkami gniuždomojo stiprio bandymui dėl deformacijų ir prilipimo prie platinos lėkštelės. W bandinys, kuris vienintelis išliko tinkamos būklės 1300 °C temperatūroje, pasiekė tik 0,36 MPa. Kituose darbuose taip pat pastebėta, kad iš gryno volastonito atspausdinti 3D karkasai dažnai pasižymi prastomis mechaninėmis savybėmis ir turi būti maišomi su priedais [101].

5.2 lentelė. Karkasų išvaizda prieš ir po degimo 1100–1300 °C temperatūroje

		Temperatūra, °C				
		25	1100	1200	1250	1300
Užpildas	W					
	WS					
	WD					

Apibendrinant sintetinių volastonito bandinių taikymą 3D spausdintuvu atspausdintiems karkasams, galima teigti, kad vien tik sintetinio volastonito dalelės (ypač W bandinys, susintetintas naudojant $SiO_2 \cdot nH_2O$) nepakankamai gerai sukepa, kad susidarytų tvirtos struktūros. Be to, dėl F^- jonų kiekio WS bandinyje (susintetintame naudojant neapdorotą užterštą silikagelį) sunkiau kontroliuoti sukepimo temperatūrą. Kita vertus, WD bandinyje (susintetintame naudojant plautą užterštą silikagelį) buvo mažiau F^- jonų ir rezultatai buvo geresni.

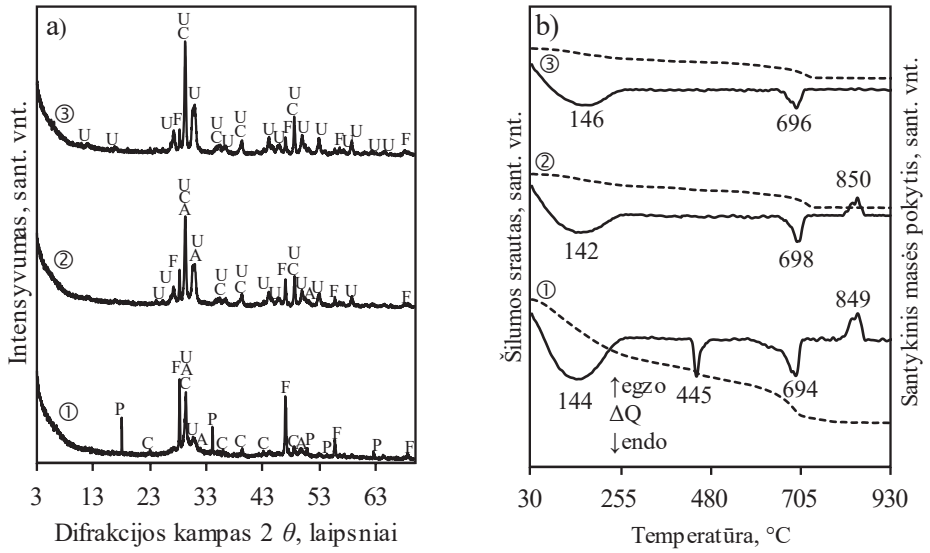
5.3.3. Dviejų stadijų kuspidino sintezė

Ankstesnėse darbo dalyse buvo pastebėta, kad kuspidinas susidaro kartu su kalcio silikatais arba hidrosilikatais, jei sistemoje yra F^- jonų (CaO-užteršto silikagelio-H_2O sistema). Tačiau mokslinės literatūros duomenys apie jo susidarymą ir įtaką bendrosioms cemento rišimosi ir kietėjimo CO_2 aplinkoje savybėms yra riboti ir nesistemingi. Taigi pagrindinis šios darbo dalies tikslas buvo ištirti temperatūros, trukmės ir skirtingos kilmės SiO_2 pradiniame mišinyje su moliniu $CaO/SiO_2/CaF_2$ santykiu 3:2:1 įtaką kuspidino susidarymui dviejų stadijų sintezės būdu ir ištirti sintetinio kuspidino bandinių elgseną hidratacijos ir kietėjimo CO_2 aplinkoje metu.

Hidroterminė sintezė CaO-$SiO_2 \cdot nH_2O$-CaF_2-H_2O sistemoje

Remiantis RSDA rezultatais, (žr. 5.16 pav., a) nustatyta, kad kuspidinas $Ca_4Si_2O_7F_2$ susidaro per 12 h jau 130 °C temperatūroje. Tačiau produktuose buvo ir nesureagavusių portlandito ir fluorito bei C-S-H(I). Sintezės 150–200 °C temperatūroje produktuose dominavo kuspidinas ir fluoritas su kalcito pėdsakais.

Vienalaikės terminus analizės rezultatai (žr. 5.16 pav., b) gerai atitinka RSDA būdu gautais duomenis. Endoterminis efektas 30–250 °C intervale būdingas pusiau kristalinių kalcio hidrosilikatų, C-S-H(I) ir C-S-H(II), dehidratacijai bei adsorbuoto vandens pasišalinimui. Endoterminis efektas ~445 °C temperatūroje būdingas portlandito skilimui, kuris buvo identifikuojamas bandiniuose, gautuose iki 150 °C. Endoterminis efektas ~690 °C temperatūroje rodo kalcio karbonato skilimą. Egzoterminis efektas esant ~850 °C temperatūrai būdingas pusiau kristalinių kalcio hidrosilikatų persikristalizavimui į volastonitą. Pastarojo efekto nebuvo bandinyje, gautame 200 °C temperatūroje (12 h), vyko tik adsorbuotos drėgmės pasišalinimas. Be to, masės nuostoliai minėtame bandinyje (iki 930 °C) sudarė ~3,6 % (~1 % masės sumažėjo skylant kalcio karbonatui), o bandiniuose, gautuose žemesnėje temperatūroje, masės nuostoliai buvo 95 °C – ~20 %, 130 °C – ~15 %, 150 °C – ~6 %, 170 °C – ~4 %. Terminės analizės rezultatai parodė, kad hidroterminės sintezės 200 °C temperatūroje metu per 12 h buvo gautas beveik bevandenis kuspidinas.

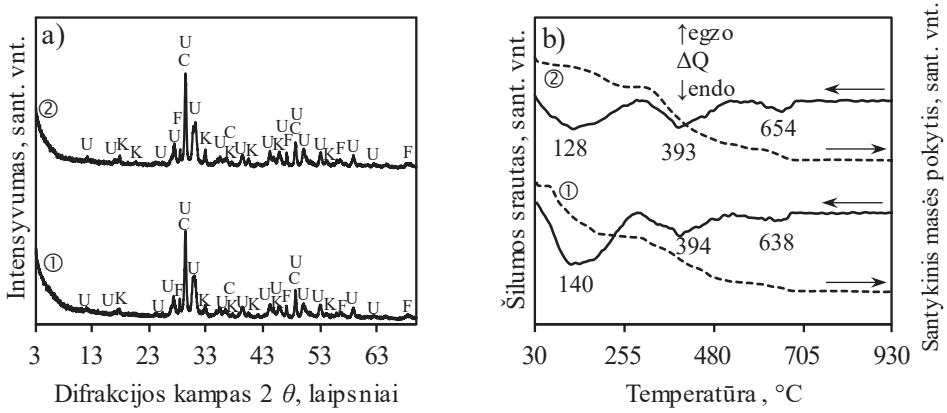


5.16 pav. Hidroterminės sintezės CaO-SiO_2·nH_2O-CaF_2-H_2O sistemoje produktų (12 h, maišant) RSDA (a) ir VTA (b, vientisa linija – DSK, punktyrinė linija – TG) kreivės: 1 – 130 °C, 2 – 150 °C, 3 – 200 °C.
Čia: U – kuspidinas, P – portlanditas, A – C-S-H(I), F – fluoritas, C – kalcitas

Hidroterminė sintezė CaO-užteršto silikagelio-CaF_2-H_2O sistemoje

Gautų bandinių RSDA kreivės (žr. 5.17 pav., a) parodė panašią kuspidino susidarymo tendenciją CaO-užteršto silikagelio-CaF_2-H_2O sistemoje, kaip ir su SiO_2·nH_2O. Be to, produktuose nustatyta ir šiek tiek nesureagavusio fluorito. Naujas junginys šioje sistemoje buvo katoitas $Ca_3Al_2(SiO_2)_{0.5}(OH)_{10}$, kuris susidarė dėl užterštame silikagelyje esančių Al^{3+} jonų. Nustatyta, kad reakcija tarp pradinių medžiagų CaO-užteršto silikagelio-CaF_2-H_2O sistemoje pasiekė pusiausvyrą per 12 h ir produktai išliko stabilūs iki 48 h.

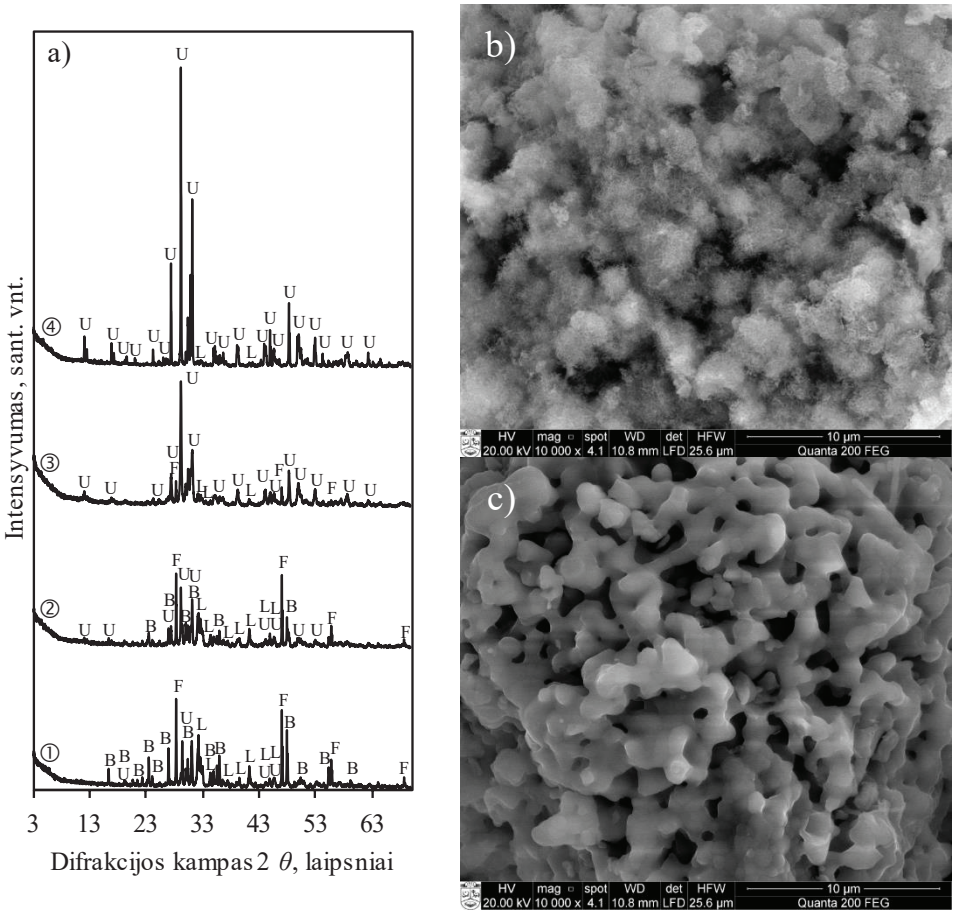
VTA rezultatai (žr. 5.17 pav., b) patvirtino RSDA duomenis: endoterminis efektas ~394 °C temperatūroje būdingas katoito skilimui. Tačiau analizė parodė, kad 50–260 °C intervale padidėjo masės nuostoliai ir endoterminis efekto šiluminė vertė, o tai susiję su padidėjusia produktų hidratacija, palyginti su gautaisiais naudojant SiO_2·nH_2O. Be to, nustatytas endoterminis efektas esant ~645 °C temperatūrai, kuris būdingas kalcio karbonato skilimui. Gautų bandinių masės nuostoliai atitinkamai buvo lygūs: per 4 h gauto bandinio masės nuostoliai – 9,67 %, per 12 h – 7,70 %, per 24 h – 7,90 %, o per 48 h – 7,35 %. 12–48 h gautų mėginių vidutiniai masės nuostoliai ~7,65 %.



5.17 pav. Hidroterminės sintezės CaO-užteršto silikagelio-CaF_2-H_2O sistemoje produktų (200 °C, maišant) RSDA (a) ir VTA (b, vientisa linija – DSK, punktyrinė linija – TG) kreivės: 1 – po 4 h, 2 – 12 h.
Čia: U – kuspidinas, K – katoitas, F – fluoritas, C – kalcitas

Hidroterminės sintezės produktų degimas

Remiantis RSDA duomenimis, nustatyta, kad bandiniuose, kuriuose hidrotermiškai apdorojant kuspidinas nesusidarė arba jo susidarė tik pėdsakai (95 ir 130 °C), 900 °C temperatūroje per 1 h jis taip pat formavosi sunkiai (žr. 5.18 pav., a). Gautuose bandiniuose buvo palyginti daug fluorito, o kartu su tiksliniu junginiu susidarė kumtiubeitas. Be to, bandiniuose nustatytas larnitas, susidaręs iš kalcio hidrosilikatų be fluorido jonų. Išdegus prekursorių (200 °C, 12 h, suspensiją maišant) visas portlanditas buvo sureagavęs, ir pagrindinis junginys jau buvo kuspidinas, išdegus 900 °C temperatūroje fluorito ir larnito nustatyti tik pėdsakai. Išdegus 1100 °C temperatūroje, nepriklausomai nuo hidroterminės sintezės temperatūros, bandiniuose kumtiubeito nebuvo identifikuota. Pažymėtina, kad, kuo žemesnė prekursoriaus sintezės temperatūra buvo naudojama, tuo intensyvesnės buvo fluorito ir larnito smailės gautuose bandiniuose išdegus. Fluoritas visiškai sureagavo išdegtuose bandiniuose, gautuose hidroterminės sintezės būdu 150–200 °C temperatūroje per 12 h. Mažiausi larnito pėdsakai nustatyti, kai hidroterminės sintezės temperatūra buvo 200 °C.



5.18 pav. Bandinių, gautų po hidroterminės sintezės (12 h) ir išdegtų (1 h) $CaO\text{-}SiO_2 \cdot nH_2O\text{-}CaF_2$ sistemoje RSDA kreivės (a): 1 – 95 °C ir 900 °C, 2 – 130 °C ir 900 °C, 3 – 200 °C ir 900 °C, 4 – 200 °C ir 1100 °C; b – 200 °C ir 900 °C bandinio SEM nuotrauka, c – 200 °C ir 1100 °C bandinio SEM nuotrauka.
Čia: B – kumtiubeitas, U – kuspidinas, F – fluoritas, L – larnitas

Prekursoriaus, gauto po 12 h hidroterminio apdorojimo 200 °C temperatūroje ir išdegto 900 °C temperatūroje 1 h (žr. 5.18 pav., b), SEM nuotraukoje buvo matyti, kad kuspidino struktūra buvo panaši į iš adatėlių sudarytų sferinių karkasų sankaupą. Išdegus tą patį bandinį 1100 °C temperatūroje, atrodo, kad kuspidino adatėlės susilydo (žr. 5.18 pav., c) ir iš dalies praranda karkasinę struktūrą. Analogiški rezultatai gauti ir išdegus CaO-užteršto silikagelio-CaF_2 sistemoje hidroterminės sintezės būdu gautus bandinius.

5.3.4. Kuspidino rišamosios savybės

Rišamųjų savybių tyrimui naudoti dviejų stadijų sintezės metodu gauti kuspidino bandiniai:

- CSF-r-900 ir CSF-r-1100 – $CaO\text{-}SiO_2 \cdot nH_2O\text{-}CaF_2\text{-}H_2O$ sistema, hidroterminė sintezė 200 °C, 12 h, išdegta atitinkamai 900 ir 1100 °C temperatūroje 1 h;
- CSF-w-900 ir CSF-w-1100 – CaO-užteršto silikagelio-$CaF_2\text{-}H_2O$ sistema, hidroterminė sintezė 200 °C, 12 h, išdegta atitinkamai 900 ir 1100 °C temperatūroje 1 h.

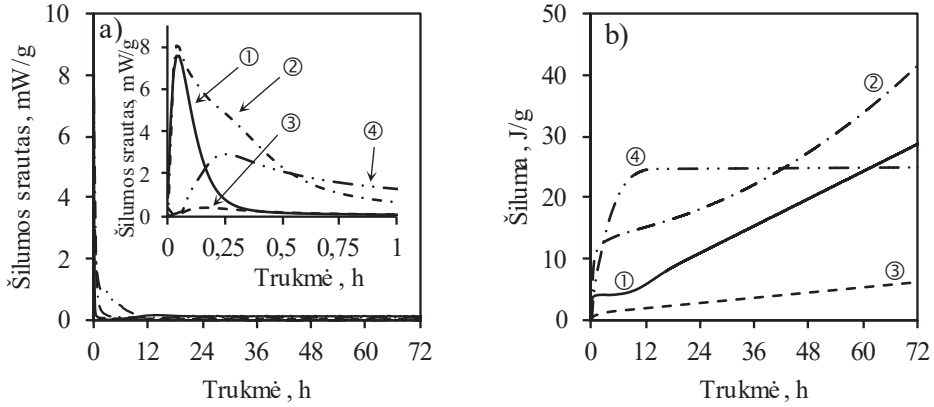
Hidratacija

Nustatyta, kad sintetinio kuspidino bandinys CSF-r-900 hidratacijos pradžioje intensyviai išskiria šilumą (žr. 5.19 pav., a, 1 kreivė). Pradinis periodas truko 13,2 min, o maksimumas (~7,5 mW/g) nustatytas po 3 min. Po pradinės reakcijos sekė sulėtėjimo etapas, trukęs 6,5 h (sumažėjo išsiskiriančios šilumos srautas). Nustatyta, kad po 72 h hidratacijos išsiskyrusios šilumos kiekis buvo ~35 J/g (žr. 5.19 pav., b, 1 kreivė).

Panaši tendencija buvo ir hidratuojantis CSF-w-900 bandiniui (žr. 5.19 pav., a, 2 kreivė). Šis bandinys iš karto reagavo su vandeniu ir po 3 min pasiekė pradinės reakcijos maksimumą (8 mW/g). Pradinė reakcija truko 37,8 min – ~3 kartus ilgiau nei CSF-r-900 atveju. Tikėtina, kad tai nulėmė CSF-w-900 bandinyje buvęs fluormajenitas. Po šio laikotarpio šilumos srautas nuolat mažėjo. Iš viso per 72 h hidratacijos mėginys išskyrė ~40 J/g šilumos (žr. 5.19 pav., b, 2 kreivė).

Nustatyta, kad CSF-r-1100 bandinyje hidratacijos procesas beveik nevyko, nes nustatytas tik nedidelis šilumos srautas (~0,5 mW/g) pradiniu sąveikos su vandeniu etapu (žr. 5.19 pav., a, 3 kreivė), o po 72 h hidratacijos išsiskyrusios šilumos kiekis buvo tik 5 J/g (žr. 5.19 pav., b, 3 kreivė).

CSF-w-1100 mėginys reagavo su vandeniu tik hidratacijos pradžioje (~12 h) (žr. 5.19 pav., a, 4 kreivė). Maksimali šilumos srauto vertė ~3 mW/g pasiekta praėjus 15 min nuo pradinė reakcijos pradžios. Vėliau išsiskiriančios šilumos srautas nuolat mažėjo, o po 12 h hidratacijos bandinys šilumos nebeišskyrė (žr. 5.19 pav., b, 4 kreivė). Nustatyta, kad per 12 h hidratacijos bandinys išskyrė ~25 J/g šilumos.

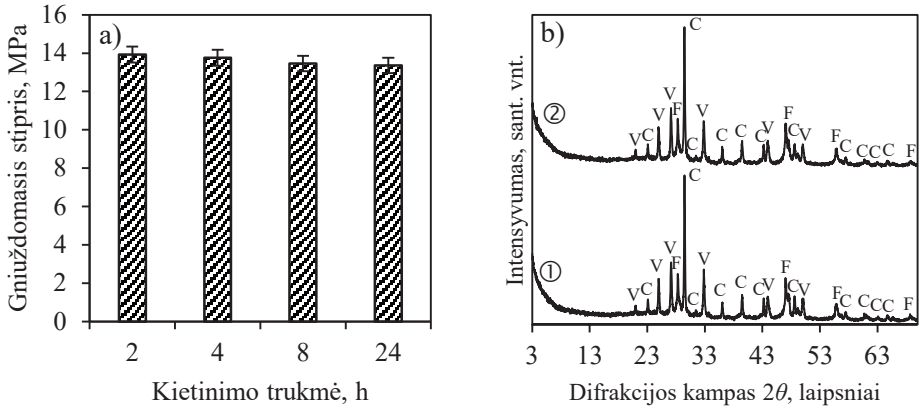


5.19 pav. Sintetinių kuspidino bandinių hidratacijos metu išsiskyrusios šilumos srautas (a) ir bendras šilumos kiekis (b): 1 – CSF-r-900, 2 – CSF-w-900, 3 – CSF-r-1100 ir 4 – CSF-w-1100

Apibendrinant mikrokalorimetrinį sintetinių kuspidino bandinių hidratacijos tyrimą, galima teigti, kad sintetinės medžiagos silpnai sąveikauja su vandeniu, panašiai kaip ir kalcio silikatai, tokie kaip volastonitas, rankinitas ir kalcio olivinas (γ-C_2S). Taip pat pastebėta, kad hidratacijos metu nė vienas kuspidino bandinys nesukietėjo, o mineraloginė sudėtis pakito mažai. Todėl yra prielaida, kad užteršto silikagelio naudojimas gaminant mažabazes rišamąsias medžiagas, tokias kaip belitas ar α-C_2SH, yra ribotas, nes susidaręs ir rišamojoje medžiagoje esantis kuspidinas sulėtintų jos kietėjimą ir pablogintų gaminių mechanines savybes.

Kietinimas CO_2 aplinkoje

Nustatyta, kad karbonizuotų sintetinio kuspidino-smėlio bandinių (kuspidino bandinys CSF-w-900, 15 bar CO_2, 45 °C) gniuždomasis stipris nedaug priklausė nuo kietėjimo trukmės, nes visų bandinių gniuždomasis stipris buvo panašus (13–14 MPa) (žr. 5.20 pav., a). Matyti, kad gniuždymo stipris šiek tiek mažėjo ilgėjant kietėjimo trukmei, o tai galima paaiškinti kristalografinių kalcio karbonato atmainų rekristalizacija. RSDA rezultatai (žr. 5.20 pav., b) atitiko išmatuotų gniuždomojo stiprio verčių tendenciją. Verta paminėti, kad analizei buvo naudojami bandiniai be smėlio. Nustatyta, kad pagrindiniai karbonizacijos produktai yra dvi kristalografinės $CaCO_3$ atmainos: kalcitas ir vateritas. Be to, panašiai kaip ir anksčiau, karbonizacijos eksperimentų metu išsiskyrė fluoritas. Verta paminėti, kad karbonizacijos metu susidaro amorfinis silicio dioksidas, kurio dėl amorfinės būsenos jo negalima identifikuoti RSDA kreivėse. Sintetiniame CSF-w-900 bandinyje buvo fluormajenito, tačiau po karbonizacijos aliuminio turinčių produktų neidentifikuota. Tolesnė analizė parodė, kad karbonizacijos produktų mineraloginė sudėtis ir smailių parametrai nesikeitė ilgėjant karbonizacijos trukmei.



5.20 pav. CO_2 aplinkoje sukietintų kuspidino-smėlio (santykiu 1:3) bandinių gniuždomasis stipris (a) ir RSDA kreivės (b): 1 – kuspidinas prieš kietinimą, 2 – po kietinimo. Čia: V – vateritas, C – kalcitas, F – fluoritas

Apibendrinant sintetinio kuspidino kietinimą CO_2 aplinkoje, galima teigti, kad pagreitinto kietinimo metu medžiaga įgavo tvirtumo (13–14 MPa). Tačiau, palyginti su rankinitu, kalcio silikatu be fluoro, kuriam būdingas toks pat molinis CaO/SiO_2 = 1,5 santykis, karbonizuotų sintetinio kuspidino bandinių gniuždomasis stipris buvo 3–7 kartus mažesnis. Kita vertus, kuspidino susidarymas ir buvimas CO_2 aplinkoje kietėjančiose rišamosiose medžiagose neturėtų didelės įtakos galutinėms gaminių mechaninėms savybėms. Be to, po karbonizacijos F^- jonai lieka surišti netirpiame junginyje – fluorite CaF_2.

5.4. Išvados

1. Nustatyta, kad volastonito vienos stadijos sintezės metu (900–1100 °C, 1 h) amorfinis silicio dioksidas blogiau sąveikauja su kitais komponentais negu užterštas silikagelis, nes sintezės produktuose lieka dalis nesureagavusio kalcio oksido. Be to, sintezės produktuose susidaro larnitas, kuriam būdingas dvigubai didesnis molinis CaO/SiO_2 santykis nei volastonito.
2. Nustatyta, kad, taikant dviejų stadijų sintezės metodą $CaO\text{-}SiO_2\cdot nH_2O\text{-}H_2O$ sistemoje, hidroterminės sintezės metu susintetintas (200 °C, 12 h) prekursorius, sudarytas iš ksonotlito, 1,13 nm tobermorito ir C-S-H(I)/(II), visiškai persikristalizuoja į volastonitą per 1 h 900 °C temperatūroje, kuriam būdingas S_{BET} = 33,42 m^2/g ir makroporinių adatėlių struktūra.
3. Nustatyta, kad CaO-užteršto silikagelio-H_2O ir $CaO\text{-}SiO_2\cdot nH_2O\text{-}AlF_3\text{-}H_2O$ sistemose po hidroterminės sintezės (200 °C, 4-48 h) susidarė tobermoritas ir kuspidinas. Be to, priklausomai nuo pradinio mišinio sudėties (užterštas silikagelis ar AlF_3 priedas), sintezės produktuose susidarė katoitas arba fluoritas.

Degimo (900-1100 °C) metu tobermoritas ir C-S-H(I) persikristalizavo į volastonitą, o kuspidinas liko stabilus visomis eksperimentinėmis slygomis.

4. Volastonitinių rišamųjų medžiagų-smėlio (masės santykis 1:3) bandiniai pasižymi 10–18 MPa gniuždomuoju stipriu. Nustatyta, kad, didinant volastonitinės rišamosios medžiagos kiekį nuo 20 iki 30 masės %, gniuždomasis stipris padidėjo 2 kartus. Didinant bandinio formavimo jėgą (10–15 kN), taip pat ir išlaikymo CO_2 aplinkoje trukmę (2–24 h), gniuždomasis stipris padidėjo tik 1,2 karto.
5. Nustatyta, kad volastonito užpildo priedas šiek tiek pakeitė AESO-IBOMA ir AESO-THFMA dervų ir volastonitinio užpildo kompozitų Jungo modulį ir gautos vertės nedaug skyrėsi nuo pradinių, atitinkamai 4,8 ir 1,1 MPa verčių. Išdegus (1100–1300 °C) iš polimero-volastonito optiniu 3D būdu atspausdintus karkasus, pastebėta, kad užpildo dalelės nepakankamai sukepė ir gauti karkasai nepasižymėjo gniuždomuoju stipriu.
6. Nustatyta, kad dviejų stadijų sintezės metodas (hidroterminė sintezė 200 °C temperatūroje 12 h ir degimas 1 h 900–1100 °C) yra tinkamas susintetinti kuspidinui CaO-SiO_2-CaF_2-H_2O ir CaO-užteršto silikagelio-CaF_2-H_2O sistemose. Kartu su tiksliniu junginiu visomis eksperimentinėmis sąlygomis liko larnito pėdsakų. Dėl užterštame silikagelyje esančių Al^{3+} jonų hidroterminės sintezės metu susidarė katoitas, kuris, išdegus bandinius, visomis tirtomis sąlygomis (iki 1100 °C) persikristalizavo į patvarų fluormajenito junginį.
7. Nustatyta, kad sintetinio kuspidino bandinių hidratacijos metu išsiskiriančios šilumos kiekis priklauso nuo jų degimo temperatūros. Bandiniai, išdegti 900 °C temperatūroje, per 72 h išskyrė 15–30 J/g daugiau šilumos nei bandiniai, išdegti 1100 °C temperatūroje. Be to, dėl fluormajenito sąveikos su vandeniu drėkinimo stadijoje buvo pastebėtas didesnis išskyrusios šilumos kiekis iš CaO-užteršto silikagelio-CaF_2-H_2O sistemos bandinių.
8. Sintetinio kuspidino bandiniai aktyviai dalyvauja CO_2 adsorbcijos ir izoliavimo procesuose, nes nustatytas jiems būdingas karbonizacijos laipsnis yra didesnis nei 55 %. Taip pat sintetinio kuspidino-smėlio bandiniai pagreitintos karbonizacijos metu pasiekė 13–14 MPa gniuždomąjį stiprį.

References

1. LUDWIG, Horst-Michael and ZHANG, Wensheng. Research review of cement clinker chemistry. *Cement and Concrete Research*. December 2015. Vol. 78, p. 24–37. DOI 10.1016/j.cemconres.2015.05.018.
2. KNOCHE, R., ANGEL, R. J., SEIFERT, F. and FLIERVOET, T. F. Complete substitution of Si for Ti in titanite Ca(Ti(1-x)Si(x))(VI)Si(IV)O5. *American Mineralogist*. 1998. Vol. 83, no. 11-12 PART 1, p. 1168–1175. DOI 10.2138/am-1998-11-1204.
3. GALUSKIN, Evgeny V., GFELLER, Frank, SAVELYEVA, Valentina B., ARMBRUSTER, Thomas, LAZIC, Biljana, GALUSKINA, Irina O., TOBBENS, D. M., ZADOV, Aleksandr E., DZIERZANOWSKI, Piotr, PERTSEV, Nikolai N. and GAZEEV, Viktor M. Pavlovskyite Ca8(SiO4)2(Si3O10): A new mineral of altered silicate-carbonate xenoliths from the two Russian type localities, Birkhin massif, Baikal Lake area and Upper Chegem caldera, North Caucasus. *American Mineralogist*. 1 April 2012. Vol. 97, no. 4, p. 503–512. DOI 10.2138/am.2012.3970.
4. DAMBRAUSKAS, T., BALTAKYS, K., EISINAS, A. and SIAUCIUNAS, R. A study on the thermal stability of kilchoanite synthesized under hydrothermal conditions. *Journal of Thermal Analysis and Calorimetry*. 1 January 2017. Vol. 127, no. 1, p. 229–238. DOI 10.1007/s10973-016-5424-8.
5. KOUMPOURI, D. and ANGELOPOULOS, G. N. Effect of boron waste and boric acid addition on the production of low energy belite cement. *Cement and Concrete Composites*. 1 April 2016. Vol. 68, p. 1–8. DOI 10.1016/j.cemconcomp.2015.12.009.
6. NOUR, W.M.N., MOSTAFA, A.A. and IBRAHIM, D.M. Recycled wastes as precursor for synthesizing wollastonite. *Ceramics International*. January 2008. Vol. 34, no. 1, p. 101–105. DOI 10.1016/j.ceramint.2006.08.019.
7. ABD RASHID, Rashita, SHAMSUDIN, Roslinda, ABDUL HAMID, Muhammad Azmi and JALAR, Azman. Low temperature production of wollastonite from limestone and silica sand through solid-state reaction. *Journal of Asian Ceramic Societies*. 2014. Vol. 2, no. 1, p. 77–81. DOI 10.1016/j.jascer.2014.01.010.
8. KANZAKI, Masami, STEBBINS, Jonathan F. and XUE, Xianyu. Characterization of quenched high pressure phases in CaSiO 3 system by XRD and 29 Si NMR. *Geophysical Research Letters*. 1 March 1991. Vol. 18, no. 3, p. 463–466. DOI 10.1029/91GL00463.
9. BRAITHWAITE, James and STIXRUDE, Lars. Melting of CaSiO3 Perovskite at High Pressure. *Geophysical Research Letters*. 28 February 2019. Vol. 46, no. 4, p. 2037–2044. DOI 10.1029/2018GL081805.
10. MILANI, Sula, COMBONI, Davide, LOTTI, Paolo, FUMAGALLI, Patrizia, ZIBERNA, Luca, MAURICE, Juliette, HANFLAND, Michael and MERLINI, Marco. Crystal Structure Evolution of CaSiO3 Polymorphs at Earth's Mantle Pressures. *Minerals*. 2021. Vol. 11, no. 6, p. 1–14. DOI https://doi.org/10.3390/min11060652.
11. ANGEL, R. J., ROSS, N. L., SEIFERT, F. and FLIERVOET, T. F. *Structural characterization of pentacoordinate silicon in a calcium silicate*. 1996.
12. SABURI, Shinsuke, KUSACHI, Isao, HENMI, Chiyoko, KAWAHARA,

Akira, HENMI, Kitinosuke and KAWADA, Isao. Refinement of the structure of rankinite. *Mineralogical Journal*. 1976. Vol. 8, no. 4, p. 240–246. DOI 10.2465/minerj.8.240.
13. AGRELL, S. O. and GAY, P. Kilchoanite, a polymorph of rankinite. *Nature*. 1961. Vol. 189, no. 4766, p. 743. DOI 10.1038/189743a0.
14. CUESTA, Ana, ARANDA, Miguel A.G., SANZ, Jesús, DE LA TORRE, Ángeles G. and LOSILLA, Enrique R. Mechanism of stabilization of dicalcium silicate solid solution with aluminium. *Dalton Transactions*. 7 February 2014. Vol. 43, no. 5, p. 2176–2182. DOI 10.1039/c3dt52194j.
15. AÏTCIN, Pierre Claude. Portland cement. In : *Science and Technology of Concrete Admixtures*. Online. Elsevier Ltd, 2016. p. 27–51. ISBN 9780081006962.
16. SKINNER, L. B., BENMORE, C. J., WEBER, J. K.R., TUMBER, S., LAZAREVA, L., NEUEFEIND, J., SANTODONATO, L., DU, J. and PARISE, J. B. Structure of molten CaSiO3: Neutron diffraction isotope substitution with aerodynamic levitation and molecular dynamics study. *Journal of Physical Chemistry B*. 15 November 2012. Vol. 116, no. 45, p. 13439–13447. DOI 10.1021/jp3066019.
17. YAZDANI, Arash, REZAIE, Hamid Reza, GHASSAI, Hossein and MAHMOUDIAN, Masoud. The effect of processing parameters on the hydrothermal synthesis of wollastonite at low pressure. *Journal of Ceramic Processing Research*. 2013. Vol. 14, no. 1, p. 12–16.
18. SERYOTKIN, Yurii V., SOKOL, Ella V. and KOKH, Svetlana N. Natural pseudowollastonite: Crystal structure, associated minerals, and geological context. *Lithos*. 1 March 2012. Vol. 134–135, p. 75–90. DOI 10.1016/j.lithos.2011.12.010.
19. YANG, Hexiong and PREWITT, Charles T. On the crystal structure of pseudowollastonite (CaSiO3). *American Mineralogist*. 1999. Vol. 84, no. 5–6, p. 929–932. DOI 10.2138/am-1999-5-628.
20. MAZZUCATO, E. and GUALTIERI, A. F. Wollastonite polytypes in the CaO-SiO2 system. Part I. Crystallisation kinetics. *Physics and Chemistry of Minerals*. 2000. Vol. 27, no. 8, p. 565–574. DOI 10.1007/s002690000095.
21. ZHU, L.Z., SOHN, H.Y. and BRONSON, T.M. Flux growth of 2M-wollastonite crystals for the preparation of high aspect ratio particles. *Ceramics International*. May 2014. Vol. 40, no. 4, p. 5973–5982. DOI 10.1016/j.ceramint.2013.11.045.
22. EDREES, Shaker J., SHUKUR, Majid M. and OBEID, Mohammed M. First-principle analysis of the structural, mechanical, optical and electronic properties of wollastonite monoclinic polymorph. *Computational Condensed Matter*. 2018. Vol. 14, no. December, p. 20–26. DOI 10.1016/j.cocom.2017.12.004.
23. HENMI, Chiyoko, KAWAHARA, Akira, HENMI, Kitinosuke, KUSACHI, Iseo and TAKEUCHI, Yoshio. The 3T, 4T and 5T polytypes of wollastonite from Kushiro, Hiroshima Prefecture, Japan. *American Mineralogist*. 1983. Vol. 68, p. 156–163.
24. HENMI, C., KUSACHI, I., KAWAHARA, A. and HENMI, K. 7T wollastonite from Fuka, Okayama Prefecture. *Mineralogical Journal (Japan)*. 1978. Vol. 9, p. 169–181. DOI 10.2465/minerj.9.169.

25. OHASHI, Yoshikazu. Polysynthetically-twinned structures of enstatite and wollastonite. *Physics and Chemistry of Minerals*. April 1984. Vol. 10, no. 5, p. 217–229. DOI 10.1007/BF00309314.
26. HESSE, K. F. Refinement of the crystal structure of wollastonite-2M (parawollastonite). *Zeitschrift fur Kristallographie - New Crystal Structures*. 1984. Vol. 168, no. 1–4, p. 93–98. DOI 10.1524/zkri.1984.168.1-4.93.
27. HEDVALL, J. Arvid, GARPING, E., LINDEKRANTZ, N. and NELSON, L. Über die Rolle der Ionen und kristallographischer Umwandlungen bei Reaktionen im festen Zustande. *Zeitschrift für anorganische und allgemeine Chemie*. 1931. Vol. 197, no. 1, p. 399–421. DOI 10.1002/zaac.19311970143.
28. JANDER, Wilhelm. Der Verlauf von Reaktionen im festen Zustande. *Angewandte Chemie*. 21 April 1934. Vol. 47, no. 16, p. 235–238. DOI 10.1002/ange.19340471602.
29. KURCZYK, HG and WUHRER, J. Synthetic wollastonite and its use in ceramic bodies. *Interceram*. 1971.
30. KURCZYK, H. G. Synthetic Raw Materials for Ceramic Products. *Berichte der Deutschen Keramischen Gesellschaft*. 1978. Vol. 55, p. 212–215.
31. LEITE, F. H.G., ALMEIDA, T. F., FARIA, R. T. and HOLANDA, J. N.F. Synthesis and characterization of calcium silicate insulating material using avian eggshell waste. *Ceramics International*. 2017. Vol. 43, no. 5, p. 4674–4679. DOI 10.1016/j.ceramint.2016.12.146.
32. LIN, Kaili, CHANG, Jiang and LU, Jianxi. Synthesis of wollastonite nanowires via hydrothermal microemulsion methods. *Materials Letters*. October 2006. Vol. 60, no. 24, p. 3007–3010. DOI 10.1016/j.matlet.2006.02.034.
33. XU, Lin, SUN, Panpan, CHEN, Xiuping, LI, Jie, ZHAI, Peiyan, ZHANG, Heng, ZHANG, Zhaoshun and ZHU, Wancheng. High aspect ratio Ca6Si6O17(OH)2 nanowires: Green hydrothermal synthesis, formation mechanism, optical and photoluminescence properties. *Powder Technology*. 15 July 2018. Vol. 335, p. 360–370. DOI 10.1016/j.powtec.2018.05.010.
34. LIN, Kaili, CHANG, Jiang and LU, Jianxi. Synthesis of wollastonite nanowires via hydrothermal microemulsion methods. *Materials Letters*. 2006. Vol. 60, no. 24, p. 3007–3010. DOI 10.1016/j.matlet.2006.02.034.
35. LIN, Kaili, CHANG, Jiang, CHEN, Guofeng, RUAN, Meiling and NING, Congqin. A simple method to synthesize single-crystalline β-wollastonite nanowires. *Journal of Crystal Growth*. 15 March 2007. Vol. 300, no. 2, p. 267–271. DOI 10.1016/j.jcrysgro.2006.11.215.
36. RIBAS, Renata Guimarães, CAMPOS, Tiago Moreira Bastos, SCHATKOSKI, Vanessa Modelski, DE MENEZES, Beatriz Rossi Canuto, MONTANHEIRO, Thaís Larissa do Amaral and THIM, Gilmar Patrocínio. α-wollastonite crystallization at low temperature. *Ceramics International*. 1 April 2020. Vol. 46, no. 5, p. 6575–6580. DOI 10.1016/j.ceramint.2019.11.143.
37. ISMAIL, Hamisah, SHAMSUDIN, Roslinda and ABDUL HAMID, Muhammad Azmi. Effect of autoclaving and sintering on the formation of β-wollastonite. *Materials Science and Engineering C*. 2016. Vol. 58, p. 1077–1081. DOI 10.1016/j.msec.2015.09.030.

38. PEI, L. Z., YANG, L. J., YANG, Y., FAN, C. G., YIN, W. Y., CHEN, J. and ZHANG, Q. F. A green and facile route to synthesize calcium silicate nanowires. *Materials Characterization*. 2010. Vol. 61, no. 11, p. 1281–1285. DOI 10.1016/j.matchar.2010.07.002.
39. LI, H. C., WANG, D. G. and CHEN, C. Z. Effect of zinc oxide and zirconia on structure, degradability and in vitro bioactivity of wollastonite. *Ceramics International*. 2015. Vol. 41, no. 8, p. 10160–10169. DOI 10.1016/j.ceramint.2015.04.117.
40. ROS-TÁRRAGA, Patricia, MURCIANO, Ángel, MAZÓN, Patricia, GEHRKE, Sergio A. and DE AZA, Piedad N. In vitro behaviour of sol-gel interconnected porous scaffolds of doped wollastonite. *Ceramics International*. 2017. Vol. 43, no. 14, p. 11034–11038. DOI 10.1016/j.ceramint.2017.05.146.
41. OBRADOVIĆ, Nina, FILIPOVIĆ, Suzana, MARKOVIĆ, Smilja, MITRIĆ, Miodrag, RUSMIROVIĆ, Jelena, MARINKOVIĆ, Aleksandar, ANTIĆ, Vesna and PAVLOVIĆ, Vladimir. Influence of different pore-forming agents on wollastonite microstructures and adsorption capacities. *Ceramics International*. 2017. Vol. 43, no. 10, p. 7461–7468. DOI 10.1016/j.ceramint.2017.03.021.
42. BERNARDO, Enrico, COLOMBO, Paolo, CACCIOTTI, Ilaria, BIANCO, Alessandra, BEDINI, Rossella, PECCI, Raffaella, PARDUN, Karoline, TRECCANI, Laura and REZWAN, Kurosch. Porous wollastonite-hydroxyapatite bioceramics from a preceramic polymer and micro- or nano-sized fillers. *Journal of the European Ceramic Society*. 2012. Vol. 32, no. 2, p. 399–408. DOI 10.1016/j.jeurceramsoc.2011.08.010. Nespausdinti karkasai
43. LIU, Shen, JIN, Fangchun, LIN, Kaili, LU, Jianxi, SUN, Jiao, CHANG, Jiang, DAI, Kerong and FAN, Cunyi. The effect of calcium silicate on in vitro physiochemical properties and in vivo osteogenesis, degradability and bioactivity of porous β-tricalcium phosphate bioceramics. *Biomedical Materials (Bristol)*. 2013. Vol. 8, no. 2. DOI 10.1088/1748-6041/8/2/025008.
44. KUNJALUKKAL PADMANABHAN, Sanosh, GERVASO, Francesca, CARROZZO, Marina, SCALERA, Francesca, SANNINO, Alessandro and LICCIULLI, Antonio. Wollastonite/hydroxyapatite scaffolds with improved mechanical, bioactive and biodegradable properties for bone tissue engineering. *Ceramics International*. 2013. Vol. 39, no. 1, p. 619–627. DOI 10.1016/j.ceramint.2012.06.073. Nespausdinti karkasai
45. XIE, Jiajun, YANG, Xianyan, SHAO, Huifeng, YE, Juan, HE, Yong, FU, Jianzhong, GAO, Changyou and GOU, Zhongru. Simultaneous mechanical property and biodegradation improvement of wollastonite bioceramic through magnesium dilute doping. *Journal of the Mechanical Behavior of Biomedical Materials*. 1 February 2016. Vol. 54, p. 60–71. DOI 10.1016/J.JMBBM.2015.09.012. Nespausdintas karkasas
46. ILJINA, Aliona, BALTAKYS, Kestutis, BANKAUSKAITE, Agne, EISINAS, Anatolijus and KITRYS, Saulius. The stability of formed CaF2 and its influence on the thermal behavior of C–S–H in CaO–silica gel waste-H2O system. *Journal of Thermal Analysis and Calorimetry*. 6 January 2017. Vol. 127, no. 1, p. 221–228. DOI 10.1007/s10973-016-5412-z.

47. ABDEL WAHAB, Mona, ABDEL LATIF, Ibrahim, KOHAIL, Mohamed and ALMASRY, Amira. The use of Wollastonite to enhance the mechanical properties of mortar mixes. *Construction and Building Materials*. 15 October 2017. Vol. 152, p. 304–309. DOI 10.1016/j.conbuildmat.2017.07.005.
48. ZAREEI, Seyed Alireza, AMERI, Farshad, SHOAEI, Parham and BAHRAMI, Nasrollah. Recycled ceramic waste high strength concrete containing wollastonite particles and micro-silica: A comprehensive experimental study. *Construction and Building Materials*. 20 March 2019. Vol. 201, p. 11–32. DOI 10.1016/J.CONBUILDMAT.2018.12.161.
49. RANSINCHUNG R. N., G. D. and KUMAR, Brind. Investigations on Pastes and Mortars of Ordinary Portland Cement Admixed with Wollastonite and Microsilica. *Journal of Materials in Civil Engineering*. 19 April 2010. Vol. 22, no. 4, p. 305–313. DOI 10.1061/(asce)mt.1943-5533.0000019.
50. SOLIMAN, A. M. and NEHDI, M. L. Effects of shrinkage reducing admixture and wollastonite microfiber on early-age behavior of ultra-high performance concrete. *Cement and Concrete Composites*. 1 February 2014. Vol. 46, p. 81–89. DOI 10.1016/j.cemconcomp.2013.11.008.
51. KALLA, Pawan, MISRA, Anurag, GUPTA, Ramesh Chandra, CSETENYI, Laszlo, GAHLOT, Vimal and ARORA, Amarnath. Mechanical and durability studies on concrete containing wollastonite-fly ash combination. *Construction and Building Materials*. 1 March 2013. Vol. 40, p. 1142–1150. DOI 10.1016/j.conbuildmat.2012.09.102.
52. MATHUR, Renu, MISRA, A K and GOEL, Pankaj. Influence of wollastonite on mechanical properties of concrete. *Journal of Scientific & Industrial Research*. 2007. Vol. 66, p. 1029–1034.
53. HAMEDANIMOJARRAD, Pedram. *Development of High Performance Shrinkage Resistant Concrete, Using Novel Shrinkage Compensating Admixtures*. . Sydney University of Technology, 2012.
54. GALEA, N. L., HAMEDANIMOJARRAD, P., VESSALAS, K. and THOMAS, P. S. Assessment of wollastonite microfibre on drying shrinkage behaviour of cement-based composites. In : *From Materials to Structures: Advancement Through Innovation - Proceedings of the 22nd Australasian Conference on the Mechanics of Structures and Materials, ACMSM 2012*. 2013. p. 499–504. ISBN 9780415633185. DOI 10.1201/b15320-87.
55. SIAUCIUNAS, Raimundas, HILBIG, Harald, PRICHOCKIENE, Edita, SMIGELSKYTE, Agne and TAKULINSKAS, Zilvinas. Accelerated carbonation of C2SH based dense concrete. *Ceramics International*. 15 December 2020. Vol. 46, no. 18, p. 29436–29442. DOI 10.1016/j.ceramint.2020.05.027.
56. ASHRAF, Warda, OLEK, Jan and JAIN, Jitendra. Microscopic features of non-hydraulic calcium silicate cement paste and mortar. *Cement and Concrete Research*. 2017. Vol. 100, p. 361–372. DOI 10.1016/j.cemconres.2017.07.001.
57. SMIGELSKYTE, Agne, SIAUCIUNAS, Raimundas, HILBIG, Harald, DECKER, Marco, URBONAS, Liudvikas and SKRIPKIUNAS, Gintautas. Carbonated rankinite binder: effect of curing parameters on microstructure, strength development and durability performance. *Scientific Reports*. 1 December 2020.

Vol. 10, no. 1. DOI 10.1038/s41598-020-71270-w.
58. ASHRAF, Warda. Carbonation of cement-based materials: Challenges and opportunities. *Construction and Building Materials*. 2016. Vol. 120, p. 558–570. DOI 10.1016/j.conbuildmat.2016.05.080.
59. DAVAL, Damien, MARTINEZ, Isabelle, CORVISIER, Jérôme, FINDLING, Nathaniel, GOFFÉ, Bruno and GUYOT, François. Carbonation of Ca-bearing silicates, the case of wollastonite: Experimental investigations and kinetic modeling. *Chemical Geology*. 15 July 2009. Vol. 265, no. 1–2, p. 63–78. DOI 10.1016/J.CHEMGEO.2009.01.022.
60. ASHRAF, Warda, OLEK, Jan and TIAN, Nannan. Multiscale characterization of carbonated wollastonite paste and application of homogenization schemes to predict its effective elastic modulus. *Cement and Concrete Composites*. 1 September 2016. Vol. 72, p. 284–298. DOI 10.1016/j.cemconcomp.2016.05.023.
61. BUKOWSKI, J. M. and BERGER, R. L. Reactivity and strength development of CO2 activated non-hydraulic calcium silicates. *Cement and Concrete Research*. 1979. Vol. 9, no. 1, p. 57–68. DOI 10.1016/0008-8846(79)90095-4.
62. WANG, Xiaoli, GUO, Ming-Zhi and LING, Tung-Chai. Review on CO2 curing of non-hydraulic calcium silicates cements: Mechanism, carbonation and performance. *Cement and Concrete Composites*. 1 October 2022. Vol. 133, p. 104641. DOI 10.1016/j.cemconcomp.2022.104641.
63. Carbon Dioxide | Vital Signs – Climate Change: Vital Signs of the Planet. Online. [Accessed 8 September 2022]. Available from: https://climate.nasa.gov/vital-signs/carbon-dioxide/
64. LIDE, David R. *CRC Handbook of Chemistry and Physics*. Online. American Chemical Society, 2003. ISBN 073540111X.
65. HUIJGEN, Wouter J.J., WITKAMP, Geert Jan and COMANS, Rob N.J. Mechanisms of aqueous wollastonite carbonation as a possible CO2 sequestration process. *Chemical Engineering Science*. 1 July 2006. Vol. 61, no. 13, p. 4242–4251. DOI 10.1016/J.CES.2006.01.048.
66. ZHANG, Duo, GHOULEH, Zaid and SHAO, Yixin. Review on carbonation curing of cement-based materials. *Journal of CO2 Utilization*. 1 October 2017. Vol. 21, p. 119–131. DOI 10.1016/j.jcou.2017.07.003.
67. LAGERBLAD, Björn. Carbon dioxide uptake during concrete life cycle - State of the art. *Carbon dioxide uptake during concrete life cycle - State of the art*. Online. 2005. [Accessed 10 January 2021]. Available from: https://www.researchgate.net/publication/285309293_Carbon_dioxide_uptake_during_concrete_life_cycle_-_State_of_the_art
68. RIMAN, Richard E., GUPTA, Surojit, ATAKAN, Vahit and LI, Qinghua. Patent Publication No.: US 2013/0344194A1. US 2013/0122267 A1. 2013. United States of America.
69. LIU, Songhui, ZHANG, Li, XUAN, Dongxing, SHEN, Peiliang, ZHU, Jianping, GUAN, Xuemao and SHI, Caijun. Enhanced carbonation reactivity of wollastonite by rapid cooling process: Towards an ultra-low calcium CO2 sequestration binder. *Construction and Building Materials*. 13 September 2021. Vol. 299, p. 124336. DOI 10.1016/J.CONBUILDMAT.2021.124336.

70. KHAN, Rakibul I., ASHRAF, Warda and OLEK, Jan. Amino acids as performance-controlling additives in carbonation-activated cementitious materials. *Cement and Concrete Research*. 1 September 2021. Vol. 147, p. 106501. DOI 10.1016/J.CEMCONRES.2021.106501.
71. KHAN, Rakibul I., SIDDIQUE, Salman and ASHRAF, Warda. Effects of magnesia in semi-hydraulic and non-hydraulic calcium silicate binders during carbonation curing. *Construction and Building Materials*. 4 July 2022. Vol. 338, p. 127628. DOI 10.1016/J.CONBUILDMAT.2022.127628.
72. FATT, Wong Joon, XIN, Chan Jia, HASSAN, Azman bin, MOHAMAD, Zurina binti and OTHMAN, Norhayani binti. Thermal and flammability properties of wollastonite-filled thermoplastic composites: a review. *Journal of Materials Science*. 2020. Vol. 56, p. 8911–8950. DOI 10.1007/s10853-020-05255-5.
73. DASARI, A. and MISRA, R. D.K. The role of micrometric wollastonite particles on stress whitening behavior of polypropylene composites. *Acta Materialia*. 2004. Vol. 52, no. 6, p. 1683–1697. DOI 10.1016/j.actamat.2003.12.013.
74. MISRA, R. D.K., HADAL, R. and DUNCAN, S. J. Surface damage behavior during scratch deformation of mineral reinforced polymer composites. *Acta Materialia*. 16 August 2004. Vol. 52, no. 14, p. 4363–4376. DOI 10.1016/j.actamat.2004.06.003.
75. A DASARI, S Sarang, RDK Misra. Strain rate sensitivity of homopolymer polypropylenes and micrometric wollastonite-filled polypropylene composites. *Mater Sci Eng A*. 2004. Vol. 368, p. 191–204.
76. ŠVAB, Iztok, MUSIL, Vojko, JURKIN, Tanja and ŠMIT, Ivan. Phase structure and morphology of wollastonite-reinforced polypropylene composites modified with SEBS and SEBS-g-MA elastomers. *Polymer Engineering & Science*. 1 December 2007. Vol. 47, no. 12, p. 2145–2154. DOI 10.1002/pen.20899.
77. FARHADINEJAD, Z, EHSANI, M, KHOSRAVIAN, B and EBRAHIMI, G. Study of thermal properties of wood plastic composite reinforced with cellulose micro fibril and nano inorganic fiber filler. *Eur J Wood Wood Prod*. 2012. Vol. 70, no. 6, p. 823–828. DOI 10.1007/s00107-012-0630-y.
78. TROTIGNON, JP, DEMDOUM, L and VERDU, J. Effect of mineral fillers in low concentration on the mechanical properties of polymeric materials. Part 1: static and fatigue fracture of polypropylene, qualitative aspects. *Composites*. 1992. Vol. 23, no. 5, p. 313–318.
79. HADAL, RS, DASARI, A, ROHRMANN, J and MISRA, RDK. Effect of wollastonite and talc on the micromechanisms of tensile deformation in polypropylene composites. *Mater Sci Eng A*. 2004. Vol. 372, p. 296–315.
80. HADAL, RS, DASARI, A, ROHRMANN, J and MISRA, RDK. Susceptibility to scratch surface damage of wollastonite- and talc-containing polypropylene micrometric composites. *Mater Sci Eng A*. 2004. Vol. 380, p. 326–339. DOI 10.1016/j.msea.2004.03.058.
81. HADAL, RS and MISRA, RDK. The influence of loading rate and concurrent microstructural evolution in micrometric talc- and wollastonite-reinforced high isotactic polypropylene composites. *Mater Sci Eng A*. 2004. Vol. 374, p. 374–389. DOI 10.1016/j.msea.2004.03.035.

82. TIGGEMANN, Hugo M., TOMACHESKI, Daiane, CELSO, Fabrício, RIBEIRO, Vanda F. and NACHTIGALL, Sônia M.B. Use of wollastonite in a thermoplastic elastomer composition. *Polymer Testing*. 2013. Vol. 32, no. 8, p. 1373–1378. DOI 10.1016/j.polymertesting.2013.08.017.
83. ZHOU, Rimin, LAI, Xuejun, LI, Hongqiang, TANG, Shuang and ZENG, Xingrong. Enhancement of wollastonite on flame retardancy and mechanical properties of PP/IFR composite. *Polymer Composites*. Online. January 2014. Vol. 35, no. 1, p. 158–166. [Accessed 3 December 2020]. DOI 10.1002/pc.22645.
84. LIANG, J. Z., LI, B. and RUAN, J. Q. Crystallization properties and thermal stability of polypropylene composites filled with wollastonite. *Polymer Testing*. 2015. Vol. 42, p. 185–191. DOI 10.1016/j.polymertesting.2015.01.017.
85. LUYT, A. S., DRAMIĆANIN, M. D., ANTIĆ, Ž and DJOKOVIĆ, V. Morphology, mechanical and thermal properties of composites of polypropylene and nanostructured wollastonite filler. *Polymer Testing*. 2009. Vol. 28, no. 3, p. 348–356. DOI 10.1016/j.polymertesting.2009.01.010.
86. S CHUAYJULJIT, T Karnjanamayul. Ultrafine wollastonite reinforced polypropylene/ethylene propylene diene rubber thermoplastic elastomers. *Adv Mater Res*. 2012. Vol. 488–489, p. 945–949.
87. DING, Qian, ZHANG, Zishou, WANG, Chunguang, JIANG, Juan, LI, Gu and MAI, Kancheng. Crystallization behavior and melting characteristics of wollastonite filled β-isotactic polypropylene composites. *Thermochimica Acta*. 2012. Vol. 536, p. 47–54. DOI 10.1016/j.tca.2012.02.023.
88. LI, L and DOU, Q. Effects of malonic acid treatment on crystal structure, melting behavior, morphology, and mechanical properties of isotactic poly(propylene)/wollastonite composites. *Polym Compos*. 2010. Vol. 31, no. 6, p. 966–973.
89. BALKAN, O, EZDESIR, A and DEMIRER, H. Microstructural characteristics of glass bead- and wollastonite-filled isotactic-polypropylene composites modified with thermoplastic elastomers. *Polym Compos*. 2010. Vol. 31, p. 1265–1284.
90. LIU, J, WEI, X and GUO, Q. The β-Crystalline Form of Wollastonite-Filled Polypropylene. *J Appl Polym Sci*. 1990. Vol. 41, p. 2829–2835.
91. FU, Z, DAI, W, YU, H, ZOU, X and CHEN, B. Effect of composition on fracture behavior of polypropylene–wollastonite–polyolefin elastomer system. *J Mater Sci*. 2011. Vol. 46, p. 1272–1280.
92. CHEN, M, WAN, C, SHOU, W, ZHANG, Y, ZHANG, Y and ZHANG, J. Effects of interfacial adhesion on properties of polypropylene/wollastonite composites. *J Appl Polym Sci*. 2008. Vol. 107, p. 1718–1723.
93. MENG, MR and DOU, Q. Effect of pimelic acid on the crystallization, morphology and mechanical properties of polypropylene/wollastonite composites. *Mater Sci Eng A*. 2008. Vol. 492, p. 177–184.
94. DING, Q, ZHANG, Z, WANG, C, JIANG, J, DAI, X and MAI, K. Preparation and characterization of wollastonite with a β-nucleating surface and its filled isotactic polypropylene composites. *J Mater Sci*. 2013. Vol. 48, no. 15, p. 5225–5235.
95. YANG, R, LIU, Y, YU, J and WANG, K. Thermal oxidation products and

kinetics of polyethylene composites. *Polym Degrad Stab*. 2006. Vol. 91, p. 1651–1657.
96. LAPČÍK, Lubomír, MAŇAS, David, LAPČÍKOVÁ, Barbora, VAŠINA, Martin, STANĚK, Michal, ČÉPE, Klára, VLČEK, Jakub, WATERS, Kristian E., GREENWOOD, Richard W. and ROWSON, Neil A. Effect of filler particle shape on plastic-elastic mechanical behavior of high density poly(ethylene)/mica and poly(ethylene)/wollastonite composites. *Composites Part B: Engineering*. 2018. Vol. 141, no. July 2017, p. 92–99. DOI 10.1016/j.compositesb.2017.12.035.
97. TONG, Jin, MA, Yunhai, ARNELL, R. D. and REN, Luquan. Free abrasive wear behavior of UHMWPE composites filled with wollastonite fibers. *Composites Part A: Applied Science and Manufacturing*. 1 January 2006. Vol. 37, no. 1, p. 38–45. DOI 10.1016/j.compositesa.2005.05.023.
98. PANIN, Sergey V., HUANG, Qitao, ALEXENKO, Vladislav O., BUSLOVICH, Dmitry G., KORNIENKO, Lyudmila A., BERTO, Filippo, BOCHKAREVA, Svetlana A., PANOV, Iliya L. and RYABOVA, Natalya V. Design of wear-resistant UHMWPE-based composites loaded with wollastonite microfibers treated with various silane coupling agents. *Applied Sciences (Switzerland)*. 1 July 2020. Vol. 10, no. 13. DOI 10.3390/app10134511.
99. MA, Gang, YUE, Xigui, ZHANG, Shuling, RONG, Changru, WANG, Lifeng, WANG, Guibin and WANG, Hongliang. Effect of the addition of silane coupling agents on the properties of wollastonite-reinforced poly(ether ether ketone) composites. *Polymer Engineering & Science*. 1 June 2011. Vol. 51, no. 6, p. 1051–1058. DOI 10.1002/pen.21925.
100. MA, Gang, YUE, Xigui, ZHANG, Shuling, RONG, Changru and WANG, Guibin. Preparation and properties of poly(ether ether ketone) composites reinforced by modified wollastonite grafting with different oligomers. *High Performance Polymers*. 22 March 2011. Vol. 23, no. 2, p. 160–169. DOI 10.1177/0954008310395416.
101. ZHANG, Hanxu, JIAO, Chen, LIU, Zibo, HE, Zhijing, MENGXING GE, ZONGJUN TIAN, WANG, Changjiang, WEI, Zhen, SHEN, Lida and LIANG, Huixin. 3D-printed composite, calcium silicate ceramic doped with CaSO4·2H2O: Degradation performance and biocompatibility. *Journal of the Mechanical Behavior of Biomedical Materials*. 1 September 2021. Vol. 121, p. 104642. DOI 10.1016/J.JMBBM.2021.104642.
102. WU, Chengtie, FAN, Wei, ZHOU, Yinghong, LUO, Yongxiang, GELINSKY, Michael, CHANG, Jiang and XIAO, Yin. 3D-printing of highly uniform CaSiO3 ceramic scaffolds: preparation, characterization and in vivo osteogenesis. *Journal of Materials Chemistry*. 29 May 2012. Vol. 22, no. 24, p. 12288–12295. DOI 10.1039/C2JM30566F.
103. SHAO, Huifeng, HE, Yong, FU, Jianzhong, HE, Dongshuang, YANG, Xianyan, XIE, Jiajun, YAO, Chunlei, YE, Juan, XU, Sanzhong and GOU, Zhongru. 3D printing magnesium-doped wollastonite/β-TCP bioceramics scaffolds with high strength and adjustable degradation. *Journal of the European Ceramic Society*. 1 May 2016. Vol. 36, no. 6, p. 1495–1503. DOI 10.1016/J.JEURCERAMSOC.2016.01.010.

104. TCACENCU, Ion, RODRIGUES, Natacha, ALHARBI, Naif, BENNING, Matthew, TOUMPANIARI, Sotiria, MANCUSO, Elena, MARSHALL, Martyn, BRETCANU, Oana, BIRCH, Mark, MCCASKIE, Andrew and DALGARNO, Kenneth. Osseointegration of porous apatite-wollastonite and poly(lactic acid) composite structures created using 3D printing techniques. *Materials Science and Engineering: C*. 1 September 2018. Vol. 90, p. 1–7. DOI 10.1016/J.MSEC.2018.04.022.
105. ELSAYED, Hamada, SCHMIDT, Johanna, BERNARDO, Enrico and COLOMBO, Paolo. Comparative Analysis of Wollastonite-Diopside Glass-Ceramic Structures Fabricated via Stereo-Lithography. *Advanced Engineering Materials*. 2019. Vol. 21, no. 6, p. 1–8. DOI 10.1002/adem.201801160.
106. KAMBOJ, Nikhil, AGHAYAN, Marina, RODRIGO-VAZQUEZ, C. Sara, RODRÍGUEZ, Miguel A. and HUSSAINOVA, Irina. Novel silicon-wollastonite based scaffolds for bone tissue engineering produced by selective laser melting. *Ceramics International*. 15 December 2019. Vol. 45, no. 18, p. 24691–24701. DOI 10.1016/J.CERAMINT.2019.08.208.
107. KAMBOJ, Nikhil, KAZANTSEVA, Jekaterina, RAHMANI, Ramin, RODRÍGUEZ, Miguel A. and HUSSAINOVA, Irina. Selective laser sintered bio-inspired silicon-wollastonite scaffolds for bone tissue engineering. *Materials Science and Engineering: C*. 1 November 2020. Vol. 116, p. 111223. DOI 10.1016/J.MSEC.2020.111223.
108. XU, Chuchu, WU, Fanghui, YANG, Jun, WANG, Hui, JIANG, Jimin, BAO, Zhaonan, YANG, Xianyan, YANG, Guojing, GOU, Zhongru and HE, Fuming. 3D printed long-term structurally stable bioceramic dome scaffolds with controllable biodegradation favorable for guided bone regeneration. *Chemical Engineering Journal*. 15 December 2022. Vol. 450, p. 138003. DOI 10.1016/J.CEJ.2022.138003.
109. PLUEDDEMANN, Edwin P. Silane Coupling Agents. *Silane Coupling Agents*. 1991. DOI 10.1007/978-1-4899-2070-6.
110. XANTHOS, Marino. *Functional Fillers for Plastics*. . Second. WILEY-VCH Verlag GmbH & Co. KGaA, 2010. ISBN 978-3-527-32361-6.
111. PAPE, Peter G. Adhesion Promoters: Silane Coupling Agents. In : *Applied Plastics Engineering Handbook: Processing, Materials, and Applications: Second Edition*. Elsevier Inc., 2017. p. 555–572. ISBN 9780323390408.
112. HERMANSON, Greg T. Silane Coupling Agents. In : *Bioconjugate Techniques*. Elsevier, 2013. p. 535–548.
113. KHABIBULLIN, Amir, BHANGAONKAR, Karan, MAHONEY, Clare, LU, Zhao, SCHMITT, Michael, SEKIZKARDES, Ali Kemal, BOCKSTALLER, Michael R. and MATYJASZEWSKI, Krzysztof. Grafting PMMA Brushes from α-Alumina Nanoparticles via SI-ATRP. *ACS Applied Materials and Interfaces*. 2 March 2016. Vol. 8, no. 8, p. 5458–5465. DOI 10.1021/acsami.5b12311.
114. MATINLINNA, Jukka Pekka, LUNG, Christie Ying Kei and TSOI, James Kit Hon. Silane adhesion mechanism in dental applications and surface treatments: A review. *Dental Materials*. 1 January 2018. Vol. 34, no. 1, p. 13–28. DOI 10.1016/j.dental.2017.09.002.
115. SIMMLER, Walter. Silicon Compounds, Inorganic. *Ullmann's Encyclopedia*

of Industrial Chemistry. 2000.
116. YEVCHUK, Iryna, DEMCHYNA, Oksana, KOPYLETS, Volodymyr, KOVAL, Zenoviya and ROMANIUK, Hanna. Kinetic regularities of the early stages of sol-gel process in tetraethoxysilane-based systems. *Chemistry and Chemical Technology*. 2014. Vol. 8, no. 2, p. 147–155. DOI 10.23939/chcht08.02.147.
117. RÖSCH, Lutz, JOHN, Peter and REITMEIER, Rudolf. Silicon Compounds, Organic. *Compounds of Groups 15 (As, Sb, Bi) and Silicon Compounds*. 2002.
118. ISSA, Ahmed A. and LUYT, Adriaan S. Kinetics of alkoxysilanes and organoalkoxysilanes polymerization: A review. *Polymers*. 2019. Vol. 11, no. 3. DOI 10.3390/polym11030537.
119. OKUMOTO, Satoshi, FUJITA, Naokatsu and YAMABE, Shinichi. Theoretical study of hydrolysis and condensation of silicon alkoxides. *Journal of Physical Chemistry A*. 28 May 1998. Vol. 102, no. 22, p. 3991–3998. DOI 10.1021/jp980705b.
120. MCINTOSH, Grant J. Theoretical investigations into the nucleation of silica growth in basic solution part I-ab Initio studies of the formation of trimers and tetramers. *Physical Chemistry Chemical Physics*. 7 March 2013. Vol. 15, no. 9, p. 3155–3172. DOI 10.1039/c3cp43399d.
121. MCINTOSH, Grant J. Theoretical investigations into the nucleation of silica growth in basic solution part II-derivation and benchmarking of a first principles kinetic model of solution chemistry. *Physical Chemistry Chemical Physics*. 28 October 2013. Vol. 15, no. 40, p. 17496–17509. DOI 10.1039/c3cp53223b.
122. AMIDON, G L, YALKOWSKY, S H and LEUNG, S. Solubility of Nonelectrolytes in Polar Solvents II: Solubility of Aliphatic Alcohols in Water. *Journal of Pharmaceutical Sciences*. 1974. Vol. 63, p. 1858–1866. DOI 10.1002/jps.2600631207.
123. CHAMBERS, R. Carlisle, JONES, Wayne E., HARUVY, Yair, WEBBER, Stephen E. and FOX, Marye Anne. Influence of Steric Effects on the Kinetics of Ethyltrimethoxysilane Hydrolysis in a Fast Sol-Gel System. *Chemistry of Materials*. Online. 1993. Vol. 5, no. 10, p. 1481–1486. [Accessed 29 November 2020]. DOI 10.1021/cm00034a018.
124. ALTMANN, Stefan and PFEIFFER, Jürgen. The Hydrolysis/Condensation Behaviour of Methacryloyloxyalkylfunctional Alkoxysilanes: Structure-Reactivity Relations. *Monatshefte fur Chemie*. August 2003. Vol. 134, no. 8, p. 1081–1092. DOI 10.1007/s00706-003-0615-y.
125. BROCHIER SALON, Marie Christine, BAYLE, Pierre Alain, ABDELMOULEH, Makki, BOUFI, Sami and BELGACEM, Mohamed Naceur. Kinetics of hydrolysis and self condensation reactions of silanes by NMR spectroscopy. *Colloids and Surfaces A: Physicochemical and Engineering Aspects*. 15 January 2008. Vol. 312, no. 2–3, p. 83–91. DOI 10.1016/j.colsurfa.2007.06.028.
126. KANNAN, Balamurali, HIGGINS, Daniel A. and COLLINSON, Maryanne M. Aminoalkoxysilane reactivity in surface amine gradients prepared by controlled-rate infusion. *Langmuir*. 20 November 2012. Vol. 28, no. 46, p. 16091–16098. DOI 10.1021/la303580c.
127. CHEN, Sheng Li, DONG, Peng, YANG, Guang Hua and YANG, Jiu Jin.

Kinetics of Formation of Monodisperse Colloidal Silica Particles through the Hydrolysis and Condensation of Tetraethylorthosilicate. *Industrial and Engineering Chemistry Research*. 1996. Vol. 35, no. 12, p. 4487–4493. DOI 10.1021/ie9602217.
128. ISSA, Ahmed A., ELAZAZY, Marwa S. and LUYT, Adriaan S. Polymerization of 3-cyanopropyl (triethoxy) silane: A kinetic study using gas chromatography. *International Journal of Chemical Kinetics*. Online. 1 December 2018. Vol. 50, no. 12, p. 846–855. [Accessed 29 November 2020]. DOI 10.1002/kin.21219.
129. ŠEFČÍK, J. and MCCORMICK, A. V. Kinetic and thermodynamic issues in the early stages of sol-gel processes using silicon alkoxides. *Catalysis Today*. 28 March 1997. Vol. 35, no. 3, p. 205–223. DOI 10.1016/S0920-5861(96)00158-7.
130. ABE, Yoshimoto and GUNJI, Takahiro. Oligo- and polysiloxanes. *Progress in Polymer Science (Oxford)*. 1 March 2004. Vol. 29, no. 3, p. 149–182. DOI 10.1016/j.progpolymsci.2003.08.003.
131. HUBER, Michael Peter, KELCH, Steffen and BERKE, Heinz. FTIR investigations on hydrolysis and condensation reactions of alkoxysilane terminated polymers for use in adhesives and sealants. *International Journal of Adhesion and Adhesives*. 1 January 2016. Vol. 64, p. 153–162. DOI 10.1016/j.ijadhadh.2015.10.014.
132. BOROVIN, Evgeny, CALLONE, Emanuela, RIBOT, Francois and DIRÉ, Sandra. Mechanism and Kinetics of Oligosilsesquioxane Growth in the In Situ Water Production Sol-Gel Route: Dependence on Water Availability. *European Journal of Inorganic Chemistry*. 1 May 2016. Vol. 2016, no. 13–14, p. 2166–2174. DOI 10.1002/ejic.201501220.
133. WATANABE, Takashi, FUKUYAMA, Hiroyuki and NAGATA, Kazuhiro. Stability of Cuspidine (3CaO 2SiO2 CaF2) and Phase Relations in the CaO-SiO2-CaF2 System. *ISIJ International*. Online. 15 May 2002. Vol. 42, no. 5, p. 489–497. [Accessed 23 December 2021]. DOI 10.2355/isijinternational.42.489.
134. GALUSKINA, Irina O., LAZIC, Biljana, ARMBRUSTER, Thomas, GALUSKIN, Evgeny V., GAZEEV, Viktor M., ZADOV, Aleksander E., PERTSEV, Nikolai N., JEZAK, Lidia, WRZALIK, Roman and GURBANOV, Anatoly G. Kumtyubeite Ca5(SiO4)2F2—A new calcium mineral of the humite group from Northern Caucasus, Kabardino-Balkaria, Russia. *American Mineralogist*. 1 October 2009. Vol. 94, no. 10, p. 1361–1370. DOI 10.2138/AM.2009.3256.
135. SMIRNOVA, R. F., RUMANOVA, I. M. and BELOV, N. V. Crystal structure of cuspidine. *Zapiski Vsesoyuznogo Mineralogicheskogo Obshchestva*. 1955. Vol. 84, p. 159–169.
136. SABURI, S., KAWAHARA, A., HENMI, C., KUSACHI, I. and KIHARA, K. The refinement of the crystal structure of cuspidine. *Mineralogical Journal*. 1977. Vol. 8, no. 5, p. 286–298. DOI 10.2465/minerj.8.286.
137. MERLINO, S and PERCHIAZZI, N. Modular mineralogy in the cuspidine group of minerals. *The Canadian Mineralogist*. Online. 1988. Vol. 26, p. 933–943. Available from: http://canmin.geoscienceworld.org/content/26/4/933.short
138. OGORODOVA, L P, VIGASINA, M F, KONONOV, O V,

KOSHLYAKOVA, N N, KSENOFONTOV, D A, KHANIN, D A, SHCHERBAKOV, V D and MEL'CHAKOVA, L. V. Thermodynamic Properties of Natural Cuspidine. *Geochemistry International*. Online. 3 August 2018. Vol. 56, no. 8, p. 865–869. DOI 10.1134/S0016702918080098.
139. TILLEY, C. E. Cuspidine from dolomite contact skarns, Broadford, Skye. *Mineralogical Magazine and Journal of the Mineralogical Society*. Online. 14 June 1947. Vol. 28, no. 197, p. 90–95. DOI 10.1180/minmag.1947.028.197.03.
140. SEO, Myung Duk, SHI, Cheng Bin, WANG, Hui, CHO, Jung Wook and KIM, Seon Hyo. Non-isothermal melt crystallization of cuspidine in CaO-SiO2-CaF2 based glasses. *Journal of Non-Crystalline Solids*. 15 March 2015. Vol. 412, p. 58–65. DOI 10.1016/j.jnoncrysol.2015.01.008.
141. CRUZ-RAMÍREZ, Alejandro, ROMO-CASTAÑEDA, Julio, HERNÁNDEZ-PÉREZ, María De Los Ángeles, VARGAS-RAMÍREZ, Marissa, ROMERO-SERRANO, Antonio and HALLEN-LÓPEZ, Manuel. An application of infrared analysis to determine the mineralogical phases formation in fluxes for thin slab casting of steel. *Journal of Fluorine Chemistry*. 1 May 2011. Vol. 132, no. 5, p. 323–326. DOI 10.1016/j.jfluchem.2011.02.019.
142. JIA, Yongchao, QIAO, Hui, GUO, Ning, ZHENG, Yuhua, YANG, Mei, HUANG, Yeju and YOU, Hongpeng. Electronic structure and photoluminescence properties of Eu2+-activated Ca4Si2O7F2. *Optical Materials*. 1 September 2011. Vol. 33, no. 11, p. 1803–1807. DOI 10.1016/J.OPTMAT.2011.06.012.
143. LÜ, Wei, LUO, Yongshi, HAO, Zhendong, ZHANG, Xia, WANG, Xiaojun and ZHANG, Jiahua. A new dual-emission phosphor Ca4Si2O7F2:Ce3 +, Mn2 + with energy transfer for near-UV LEDs. *Materials Letters*. 15 June 2012. Vol. 77, p. 45–47. DOI 10.1016/J.MATLET.2012.02.095.
144. XIE, Mubiao, ZHU, Guoxian, LI, Dongyu, PAN, Rongkai, ZHOU, Xiaoping and XIE, Wei. Synthesis and photoluminescence properties of tunable emission phosphors Ca4Si2O7F2:Ce3+. *Solid State Sciences*. 1 October 2015. Vol. 48, p. 193–196. DOI 10.1016/J.SOLIDSTATESCIENCES.2015.08.009.
145. TALEWAR, Rupesh A., MAHAMUDA, Sk, VYAS, Arpita, RAO, A. S. and MOHARIL, S. V. Enhancement of 1.54 μm emission in Ce3+-Er3+ codoped Ca4Si2O7F2 phosphor. *Journal of Alloys and Compounds*. 15 February 2019. Vol. 775, p. 810–817. DOI 10.1016/J.JALLCOM.2018.10.198.
146. XU, Zefeng, ZHU, Yuhan, FAN, Pu, LUO, Qi, HE, Zongjie, LIU, Xiaoguang and LI, Ling. A dual-excited emission phosphor Eu3+/Eu2+ co-doped Ca4Si2O7F2: Lattice occupancy and luminescence characterization. *Journal of Luminescence*. 1 October 2020. Vol. 226, p. 117480. DOI 10.1016/J.JLUMIN.2020.117480.
147. SPEAKMAN, K., TAYLOR, H. F. W., BENNETT, J. M. and GARD, J. A. Hydrothermal Reactions of γ-Dicalcium Silicate. *Journal of the Chemical Society A: Inorganic, Physical, Theoretical*. 1967. Vol. 2, no. 2, p. 1052–1060. DOI https://doi.org/10.1039/J19670001052.
148. MITSUDA, Takeshi and FUKUO, Ken'ichi. Synthesis of Kilchoanite. *Mineralogical Journal*. 1969. Vol. 6, no. 1–2, p. 17–35. DOI https://doi.org/10.2465/minerj1953.6.17.
149. RASHAD, Mohammed and BALASUBRAMANIAN, M. Characteristics of

porous mullite developed from clay and AlF3·3H2O. *Journal of the European Ceramic Society*. 2018. Vol. 38, no. 10, p. 3673–3680. DOI 10.1016/j.jeurceramsoc.2018.03.002.
150. VASILE, Bogdan Stefan, DOBRA, Gheorghe, ILIEV, Sorin, COTET, Lucian, NEACSU, Ionela Andreea, SURDU, Vasile Adrian, NICOARA, Adrian Ionut, BOIANGIU, Alina and FILIPESCU, Laurențiu. Thermally Activated Al(OH)3 Part II—Effect of Different Thermal Treatments. *Ceramics*. 11 October 2021. Vol. 4, no. 4, p. 564–575. DOI 10.3390/ceramics4040040.
151. GONZALEZ-HERNANDEZ, Diana, VARAPNICKAS, Simonas, MERKININKAITĖ, Greta, ČIBURYS, Arūnas, GAILEVIČIUS, Darius, ŠAKIRZANOVAS, Simas, JUODKAZIS, Saulius and MALINAUSKAS, Mangirdas. Laser 3D Printing of Inorganic Free-Form Micro-Optics. *Photonics*. Online. 14 December 2021. Vol. 8, no. 12, p. 577. [Accessed 30 June 2022]. DOI 10.3390/photonics8120577.
152. DAMBRAUSKAS, T., DAVIDOVICIENE, D., BALTAKYS, K., EISINAS, A., JASKUNAS, A., SILER, P., RUDELIS, V. and SVEDAITE, E. Effect of intercalated metal ions on the specific surface area and porosity of dibasic calcium silicate hydrate. *Surfaces and Interfaces*. 1 October 2022. Vol. 33, p. 102243. DOI 10.1016/J.SURFIN.2022.102243.
153. LEBEDEVAITE, Migle, TALACKA, Vaidas and OSTRAUSKAITE, Jolita. High biorenewable content acrylate photocurable resins for DLP 3D printing. *Journal of Applied Polymer Science*. 20 April 2021. Vol. 138, no. 16, p. 50233. DOI 10.1002/APP.50233.
154. SMALAKYS, G. and SIAUCIUNAS, R. Peculiarities of xonotlite synthesis from the raw materials with different SiO2 activities. *Journal of Thermal Analysis and Calorimetry*. 1 December 2020. Vol. 142, no. 5, p. 1671–1679. DOI 10.1007/s10973-020-09744-2.
155. BLACK, L., GARBEV, K. and STUMM, A. Structure, bonding and morphology of hydrothermally synthesised xonotlite. *Advances in Applied Ceramics*. 2009. Vol. 108, no. 3, p. 137–144. DOI 10.1179/174367608X353638.
156. SHAW, S., CLARK, S. M. and HENDERSON, C. M.B. Hydrothermal formation of the calcium silicate hydrates, tobermorite (Ca5Si6O16(OH)2 · 4H2O) and xonotlite (Ca6Si6O17(OH)2): An in situ synchrotron study. *Chemical Geology*. 2000. Vol. 167, no. 1–2, p. 129–140. DOI 10.1016/S0009-2541(99)00205-3.
157. TAYLOR, H. F. W. The transformation of tobermorite into xonotlite. *Mineralogical Magazine and Journal of the Mineralogical Society*. 1959. Vol. 32, no. 245, p. 110–116. DOI 10.1180/minmag.1959.32.245.03.
158. KUBÁTOVÁ, Dana, ZEZULOVÁ, Anežka, RYBOVÁ, Alexandra and NEČAS, Radovan. Application of dilatometric analysis to the study of autoclaved calcium silicate materials. *Journal of Thermal Analysis and Calorimetry*. 1 July 2018. Vol. 133, no. 1, p. 399–404. DOI 10.1007/s10973-017-6882-3.
159. TAJUELO RODRIGUEZ, Elena, GARBEV, Krassimir, MERZ, Daniela, BLACK, Leon and RICHARDSON, Ian G. Thermal stability of C-S-H phases and applicability of Richardson and Groves' and Richardson C-(A)-S-H(I) models to synthetic C-S-H. *Cement and Concrete Research*. 1 March 2017. Vol. 93, p. 45–56.

DOI 10.1016/j.cemconres.2016.12.005.
160. SHAW, S., HENDERSON, C. M.B. and KOMANSCHEK, B. U. Dehydration/recrystallization mechanisms, energetics, and kinetics of hydrated calcium silicate minerals: An in situ TGA/DSC and synchrotron radiation SAXS/WAXS study. *Chemical Geology*. 5 June 2000. Vol. 167, no. 1–2, p. 141–159. DOI 10.1016/S0009-2541(99)00206-5.
161. BAILEY, Donald A. A note on the conversion of amorphous silica to quartz. *American Mineralogist*. 1 August 1949. Vol. 34, no. 7–8, p. 601–605.
162. HOSSAIN, Sk S. and ROY, P. K. Study of physical and dielectric properties of bio-waste-derived synthetic wollastonite. *Journal of Asian Ceramic Societies*. 3 July 2018. Vol. 6, no. 3, p. 289–298. DOI 10.1080/21870764.2018.1508549.
163. SIAUCIUNAS, R., SMALAKYS, G., EISINAS, A. and PRICHOCKIENE, E. Synthesis of High Crystallinity 1.13 nm Tobermorite and Xonotlite from Natural Rocks, Their Properties and Application for Heat-Resistant Products. *Materials*. 12 May 2022. Vol. 15, no. 10, p. 3474. DOI 10.3390/ma15103474.
164. DIAMOND, Sidney. *Tobermorite and Tobermorite-like Calcium Silicate Hydrates: Their Properties and Relationships to Clay Minerals*. Lafayette, 1963.
165. KALOUSEK, G.L. Crystal Chemistry of Hydrous Calcium Silicates: I, Substitution of Aluminum in Lattice of Tobermorite. *Journal of The American Ceramic Society*. 1956. Vol. 40, no. 3, p. 74–80. DOI https://doi.org/10.1111/j.1151-2916.1957.tb12579.x.
166. GUO, Xiaolu, MENG, Fanjie and SHI, Huisheng. Microstructure and characterization of hydrothermal synthesis of Al-substituted tobermorite. *Construction and Building Materials*. 15 February 2017. Vol. 133, p. 253–260. DOI 10.1016/j.conbuildmat.2016.12.059.
167. LI, Qiu, HURT, Andrew P. and COLEMAN, Nichola J. The application of 29Si NMR spectroscopy to the analysis of calcium silicate-based cement using Biodentine™ as an example. *Journal of Functional Biomaterials*. 2019. Vol. 10, no. 2. DOI 10.3390/jfb10020025.
168. MUSUMECI, Valentina, GORACCI, Guido, SANZ CAMACHO, Paula, DOLADO, Jorge S. and AYMONIER, Cyril. Correlation between the Dynamics of Nanoconfined Water and the Local Chemical Environment in Calcium Silicate Hydrate Nanominerals. *Chemistry - A European Journal*. 2021. Vol. 27, no. 44, p. 11309–11318. DOI 10.1002/chem.202100098.
169. LEE, Yuan Ling, WANG, Wen Hsi, LIN, Feng Huie and LIN, Chun Pin. Hydration behaviors of calcium silicate-based biomaterials. *Journal of the Formosan Medical Association*. 1 June 2017. Vol. 116, no. 6, p. 424–431. DOI 10.1016/j.jfma.2016.07.009.
170. TIAN, Quanzhi and SASAKI, Keiko. Characterizations of calcium silicate hydrates derived from coal fly ash and their mechanisms for phosphate removal. *Desalination and Water Treatment*. 2019. Vol. 156, p. 78–86. DOI 10.5004/dwt.2019.24135.
171. DIEZ-GARCIA, Marta, GAITERO, Juan J., SANTOS, Jose I., DOLADO, Jorge S. and AYMONIER, Cyril. Supercritical hydrothermal flow synthesis of xonotlite nanofibers. *Journal of Flow Chemistry*. 1 June 2018. Vol. 8, no. 2, p. 89–

95. DOI 10.1007/s41981-018-0012-7.
172. NADERI, Majid. Surface Area: Brunauer-Emmett-Teller (BET). In : *Progress in Filtration and Separation*. Elsevier Ltd, 2015. p. 585–608. ISBN 9780123983077.
173. ROUQUEROL, Françoise, ROUQUEROL, Jean and SING, Kenneth. Assessment of Surface Area. In : *Adsorption by Powders and Porous Solids*. Elsevier, 1999. p. 165–189.
174. THOMMES, Matthias, KANEKO, Katsumi, NEIMARK, Alexander V, OLIVIER, James P, RODRIGUEZ-REINOSO, Francisco, ROUQUEROL, Jean and SING, Kenneth S W. IUPAC Technical Report Physisorption of gases, with special reference to the evaluation of surface area and pore size distribution (IUPAC Technical Report). *Pure Appl. Chem*. 2015. P. aop. DOI 10.1515/pac-2014-1117.
175. DAMBRAUSKAS, T., BALTAKYS, K., EISINAS, A. and KITRYS, S. The specific surface area and porosity of synthetic and calcined α-C2SH, kilchoanite and hydroxyledgrewite. *Powder Technology*. 1 October 2019. Vol. 355, p. 504–513. DOI 10.1016/j.powtec.2019.07.078.
176. RUDELIS, Valdas, DAMBRAUSKAS, Tadas, GRINEVICIENE, Agne and BALTAKYS, Kestutis. The Prospective Approach for the Reduction of Fluoride Ions Mobility in Industrial Waste by Creating Products of Commercial Value. *Sustainability*. 25 January 2019. Vol. 11, no. 3, p. 634. DOI 10.3390/su11030634.
177. DAMBRAUSKAS, Tadas, BALTAKYS, Kestutis, GRINEVICIENE, Agne and RUDELIS, Valdas. The effect of various hydroxide and salt additives on the reduction of fluoride ion mobility in industrial waste. *Sustainability (Switzerland)*. Online. 1 February 2021. Vol. 13, no. 3, p. 1–17. DOI 10.3390/su13031554.
178. EISINAS, A., DAMBRAUSKAS, T., BALTAKYS, K. and RUGINYTE, K. The peculiarities of mayenite formation from synthetic katoite and calcium monocarboaluminate samples in temperature range 25–1150 °C. *Journal of Thermal Analysis and Calorimetry*. 1 November 2019. Vol. 138, no. 3, p. 2275–2282. DOI 10.1007/s10973-019-08482-4.
179. VAN VALKENBURG, A and RYNDERS, G. F. Synthetic Cuspidine. *The american mineralogist*. 1958. Vol. 43, p. 1195–1202.
180. LIAO, Wei, LI, Wenqing, FANG, Zhenggang, LU, Chunhua and XU, Zhongzi. Effect of Different Aluminum Substitution Rates on the Structure of Tobermorite. *Materials (Basel)*. 2019. Vol. 12, no. 22, p. 3765–3774. DOI 10.3390/ma12223765.
181. SMALAKYS, Giedrius and SIAUCIUNAS, Raimundas. The Hydrothermal Synthesis of 1.13 nm Tobermorite from Granite Sawing Powder Waste. *Ceramics-Silikáty*. 2020. Vol. 64, no. 3, p. 239–248. DOI 10.13168/cs.2020.0013.
182. RIVAS-MERCURY, J. M., PENA, P., DE AZA, A. H. and TURRILLAS, X. Dehydration of Ca3Al2(SiO4)y(OH)4(3-y) (0 < y < 0.176) studied by neutron thermodiffractometry. *Journal of the European Ceramic Society*. 2008. Vol. 28, no. 9, p. 1737–1748. DOI 10.1016/j.jeurceramsoc.2007.12.038.
183. BALTAKYS, Kestutis, ILJINA, Aliona and BANKAUSKAITE, Agne. Thermal properties and application of silica gel waste contaminated with F- ions for C-S-H synthesis. *Journal of Thermal Analysis and Calorimetry*. 2015. Vol. 121, no. 1, p. 145–154. DOI 10.1007/s10973-015-4663-4.

184. ZARZUELA, Rafael, LUNA, Manuel, CARRASCOSA, Luis M., YESTE, María P., GARCIA-LODEIRO, Inés, BLANCO-VARELA, M. Teresa, CAUQUI, Miguel A., RODRÍGUEZ-IZQUIERDO, José M. and MOSQUERA, María J. Producing C-S-H gel by reaction between silica oligomers and portlandite: A promising approach to repair cementitious materials. *Cement and Concrete Research*. 1 April 2020. Vol. 130, p. 106008. DOI 10.1016/j.cemconres.2020.106008.
185. TINIO, Jessica Ven G., SIMFROSO, Key T., PEGUIT, Amber Dea Marie V. and CANDIDATO, Rolando T. Influence of OH- ion concentration on the surface morphology of znO-siO2 nanostructure. *Journal of Nanotechnology*. 2015. Vol. 2015. DOI 10.1155/2015/686021.
186. ESTRADA-FLORES, S., MARTÍNEZ-LUÉVANOS, A., BARTOLO-PÉREZ, P., GARCÍA-CERDA, L. A., FLORES-GUIA, T. E. and AGUILERA-GONZÁLEZ, E. N. Facile synthesis of novel calcium silicate hydrated-nylon 6/66 nanocomposites by solution mixing method. *RSC Advances*. 12 December 2018. Vol. 8, no. 73, p. 41818–41827. DOI 10.1039/c8ra07116k.
187. GIRAUDO, Nicolas, BERGDOLT, Samuel, WOHLGEMUTH, Jonas, WELLE, Alexander, SCHUHMANN, Rainer, KÖNIGER, Franz and THISSEN, Peter. Calcium Silicate Phases Explained by High-Temperature-Resistant Phosphate Probe Molecules. *Langmuir*. 2016. Vol. 32, no. 51, p. 13577–13584. DOI 10.1021/acs.langmuir.6b03218.
188. ASHRAF, Warda and OLEK, Jan. Carbonation behavior of hydraulic and non-hydraulic calcium silicates: potential of utilizing low-lime calcium silicates in cement-based materials. *Journal of Materials Science*. 1 July 2016. Vol. 51, no. 13, p. 6173–6191. DOI 10.1007/s10853-016-9909-4.
189. HUBER, Matthias, STARK, Wendelin J., LOHER, Stefan, MACIEJEWSKI, Marek, KRUMEICH, Frank and BAIKER, Alfons. Flame synthesis of calcium carbonate nanoparticles. *Chemical Communications*. Online. 7 February 2005. No. 5, p. 648–650. [Accessed 3 December 2020]. DOI 10.1039/b411725e.
190. SMIGELSKYTE, A. and SIAUCIUNAS, R. Parameter influence on the rankinite binder paste and mortar accelerated carbonation curing. *Journal of Thermal Analysis and Calorimetry*. Online. 1 November 2019. Vol. 138, no. 4, p. 2651–2659. DOI 10.1007/s10973-019-08590-1.
191. SUGUNAN, Abhijith and KURIAN, Shilpa Sara. Non Uniform Corrosion of Carbon Cure RC Beam and Conventional RC Beam. *International Research Journal of Engineering and Technology(IRJET)*. 2017. Vol. 4, no. 4, p. 3560–3563.
192. STEINOUR H. Some effects of carbon dioxide on mortars and concrete-discussion. *Journal of American Concrete Institute*. 1959. Vol. 30, no. 2, p. 905–907.
193. HOU, Guihua, CHEN, Jianan, LU, Bao, CHEN, Sijia, CUI, Entian, NAGUIB, Hamdy M., GUO, Ming-Zhi and ZHANG, Qinfang. Composition design and pilot study of an advanced energy-saving and low-carbon rankinite clinker. *Cement and Concrete Research*. 1 January 2020. Vol. 127, p. 105926. DOI 10.1016/j.cemconres.2019.105926.
194. MU, Yuandong, LIU, Zhichao, WANG, Fazhou and HUANG, Xiao.

Carbonation characteristics of γ-dicalcium silicate for low-carbon building material. *Construction and Building Materials*. 20 July 2018. Vol. 177, p. 322–331. DOI 10.1016/j.conbuildmat.2018.05.087.
195. ENG, Chern Chiet, IBRAHIM, Nor Azowa, ZAINUDDIN, Norhazlin, ARIFFIN, Hidayah and YUNUS, Wan Md Zin Wan. Impact strength and flexural properties enhancement of methacrylate silane treated oil palm mesocarp fiber reinforced biodegradable hybrid composites. *Scientific World Journal*. 2014. Vol. 2014, p. 1–8. DOI 10.1155/2014/213180.
196. LEBEDEVAITE, Migle and OSTRAUSKAITE, Jolita. Influence of photoinitiator and temperature on photocross-linking kinetics of acrylated epoxidized soybean oil and properties of the resulting polymers. *Industrial Crops and Products*. 1 March 2021. Vol. 161, p. 113210. DOI 10.1016/J.INDCROP.2020.113210.
197. LOPES, Isabela M.F., ABERSFELDER, Kai, OLIVEIRA, Peter W., MOUSAVI, S. H. and JUNQUEIRA, Rosa M.R. Flower-like silicon dioxide/polymer composite particles synthesized by dispersion polymerization route. *Journal of Materials Science*. 1 August 2018. Vol. 53, no. 16, p. 11367–11377. DOI 10.1007/s10853-018-2378-1.
198. PANTOJA, M, VELASCO, F, BROEKEMA, D, ABENOJAR, J, DEL REAL, J C and DEL, J C. The Influence of pH on the Hydrolysis Process of γ-Methacryloxypropyltrimethoxysilane, Analyzed by FT-IR, and the Silanization of Electrogalvanized Steel. *Journal of Adhesion Science and Technology*. 2010. Vol. 24, p. 1131–1143. DOI 10.1163/016942409X12586283821559.
199. BEE, Soo Ling, ABDULLAH, M. A.A., BEE, Soo Tueen, SIN, Lee Tin and RAHMAT, A. R. Polymer nanocomposites based on silylated-montmorillonite: A review. *Progress in Polymer Science*. 1 October 2018. Vol. 85, p. 57–82. DOI 10.1016/j.progpolymsci.2018.07.003.
200. VENTURA-HUNTER, Carolina, LECHUGA-ISLAS, Victor D., ULBRICH, Jens, KELLNER, Carolin, SCHUBERT, Ulrich S., SALDÍVAR-GUERRA, Enrique, ROSALES-GUZMÁN, Miguel and GUERRERO-SÁNCHEZ, Carlos. Glycerol methacrylate-based copolymers: Reactivity ratios, physicochemical characterization and cytotoxicity. *European Polymer Journal*. 5 September 2022. Vol. 178, p. 111478. DOI 10.1016/J.EURPOLYMJ.2022.111478.
201. CHERIFI, Zakaria, BOUKOUSSA, Bouhadjar, MOKHTAR, Adel, HACHEMAOUI, Mohammed, ZEGGAI, Fatima Zohra, ZAOUI, Aniss, BACHARI, Khaldoun and MEGHABAR, Rachid. Preparation of new nanocomposite poly(GDMA)/mesoporous silica and its adsorption behavior towards cationic dye. *Reactive and Functional Polymers*. 1 August 2020. Vol. 153, p. 104611. DOI 10.1016/J.REACTFUNCTPOLYM.2020.104611.
202. CHEN, Xiaojing, CHEN, Xiaohui, PEDONE, Alfonso, APPERLEY, David, HILL, Robert G. and KARPUKHINA, Natalia. New Insight into Mixing Fluoride and Chloride in Bioactive Silicate Glasses. *Scientific Reports*. 1 December 2018. Vol. 8, no. 1. DOI 10.1038/S41598-018-19544-2.
203. BRAUER, Delia S., HILL, Robert G. and O'DONNELL, Mathew D. Crystallisation of fluoride-containing bioactive glasses. *Physics and Chemistry of*

Glasses: European Journal of Glass Science and Technology Part B. 2012. Vol. 53, no. 2, p. 27–30.
204. MADDALENA, Riccardo, LI, Kefei, CHATER, Philip A., MICHALIK, Stefan and HAMILTON, Andrea. Direct synthesis of a solid calcium-silicate-hydrate (C-S-H). *Construction and Building Materials*. 30 October 2019. Vol. 223, p. 554–565. DOI 10.1016/j.conbuildmat.2019.06.024.
205. BEHERI, Hanan H., MOHAMED, Khaled R. and EL-BASSYOUNI, Gehan T. Mechanical and microstructure of reinforced hydroxyapatite/calcium silicate nano-composites materials. *Materials & Design*. 1 February 2013. Vol. 44, p. 461–468. DOI 10.1016/J.MATDES.2012.08.020.
206. GALVÁN-RUIZ, Miguel, HERNÁNDEZ, Juan, BAÑOS, Leticia, NORIEGA-MONTES, Joaquín and RODRÍGUEZ-GARCÍA, Mario E. Characterization of Calcium Carbonate, Calcium Oxide, and Calcium Hydroxide as Starting Point to the Improvement of Lime for Their Use in Construction. *Journal of Materials in Civil Engineering*. November 2009. Vol. 21, no. 11, p. 694–698. DOI 10.1061/(ASCE)0899-1561(2009)21:11(694).
207. ZEA-GARCIA, Jesus D., DE LA TORRE, Angeles G., ARANDA, Miguel A.G. and SANTACRUZ, Isabel. Processing and characterisation of standard and doped alite-belite-ye'elimite ecocement pastes and mortars. *Cement and Concrete Research*. 1 January 2020. Vol. 127, p. 105911. DOI 10.1016/J.CEMCONRES.2019.105911.
208. WANG, Zhelin, JIANG, Xuewei, PAN, Mao and SHI, Yongmin. Nano-Scale Pore Structure and Its Multi-Fractal Characteristics of Tight Sandstone by N2 Adsorption/Desorption Analyses: A Case Study of Shihezi Formation from the Sulige Gas Filed, Ordos Basin, China. *Minerals*. 22 April 2020. Vol. 10, no. 4, p. 377. DOI 10.3390/min10040377.
209. MYERS, Rupert J., L'HÔPITAL, Emilie, PROVIS, John L. and LOTHENBACH, Barbara. Effect of temperature and aluminium on calcium (alumino)silicate hydrate chemistry under equilibrium conditions. *Cement and Concrete Research*. 1 February 2015. Vol. 68, p. 83–93. DOI 10.1016/j.cemconres.2014.10.015.
210. COOK, Rachel, MA, Hongyan, OKORONKWO, Monday, SANT, Gaurav and KUMAR, Aditya. Influence of water activity on belite (β-C 2 S) hydration. *Journal of the American Ceramic Society*. 20 April 2021. Vol. 104, no. 4, p. 1831–1840. DOI 10.1111/jace.17608.
211. BOHÁČ, Martin, STANĚK, Theodor, ZEZULOVÁ, Anežka, RYBOVÁ, Alexandra, KUBÁTOVÁ, Dana and NOVOTNÝ, Radoslav. Early Hydration of Activated Belite-Rich Cement. *Advanced Materials Research*. March 2019. Vol. 1151, p. 23–27. DOI 10.4028/www.scientific.net/AMR.1151.23.
212. EISINAS, Anatolijus and VASILIAUSKIENE, Kristina. Effect of $Cu2+/SO42-$ ions concentration on the adsorption capacity of synthetic mayenite, its application for secondary adsorption process and utilization in cement samples. *Ceramics International*. 4 August 2022. DOI 10.1016/j.ceramint.2022.07.261.
213. WANG, Fang, KONG, Xiangming, JIANG, Lingfei and WANG, Dongmin. The acceleration mechanism of nano-C-S-H particles on OPC hydration.

Construction and Building Materials. 20 July 2020. Vol. 249, p. 118734. DOI 10.1016/j.conbuildmat.2020.118734.
214. DU, Xuelian, WANG, Yanqin, SU, Xinghua and LI, Jiangong. Influences of pH value on the microstructure and phase transformation of aluminum hydroxide. *Powder Technology*. 15 May 2009. Vol. 192, no. 1, p. 40–46. DOI 10.1016/j.powtec.2008.11.008.
215. ASHRAF, Warda and OLEK, Jan. Carbonation behavior of hydraulic and non-hydraulic calcium silicates: potential of utilizing low-lime calcium silicates in cement-based materials. *Journal of Materials Science*. 1 July 2016. Vol. 51, no. 13, p. 6173–6191. DOI 10.1007/s10853-016-9909-4.
216. WANG, Kai, REN, Liang and YANG, Luqing. Excellent Carbonation Behavior of Rankinite Prepared by Calcining the C-S-H: Potential Recycling of Waste Concrete Powders for Prefabricated Building Products. *Materials*. 19 August 2018. Vol. 11, no. 8, p. 1474. DOI 10.3390/ma11081474.
217. KARPOVA, Ekaterina, SKRIPKIŪNAS, Gintautas, BARAUSKAS, Irmantas, BARAUSKIENĖ, Ieva and HODUL, Jakub. Influence of carbon nanotubes and polycarboxylate superplasticiser on the Portland cement hydration process. *Construction and Building Materials*. 18 October 2021. Vol. 304, p. 124648. DOI 10.1016/j.conbuildmat.2021.124648.
218. HE, Zhen and LI, Yang. The Influence of Mayenite Employed as a Functional Component on Hydration Properties of Ordinary Portland Cement. *Materials*. 12 October 2018. Vol. 11, no. 10, p. 1958. DOI 10.3390/ma11101958.
219. ZHANG, Xiuzhen, LIU, Zhichao and WANG, Fazhou. Effect of coral powder on the carbonation behavior of γ-C2S. *Construction and Building Materials*. 12 September 2022. Vol. 347, p. 128251. DOI 10.1016/j.conbuildmat.2022.128251.
220. WANG, Dan and CHANG, Jun. Comparison on accelerated carbonation of β-C2S, Ca(OH)2, and C4AF: Reaction degree, multi-properties, and products. *Construction and Building Materials*. 10 November 2019. Vol. 224, p. 336–347. DOI 10.1016/j.conbuildmat.2019.07.056.
221. ASTM. Standard Test Methods for Chemical Analysis of Limestone , Quicklime , and Hydrated Lime. *Annual Book of ASTM Standards*. 2011. Vol. ASTMC25-11, no. Reapproved 2014, p. 1–38. DOI 10.1520/C0025-11E02.Carbon.

Curriculum Vitae

Name, surname: Andrius Gineika
E-mail: andrius.gineika@hotmail.com

Education

1998–2010
Secondary education at Kaunas Palemonas Secondary School, Lithuania

2010–2011 – 2014–2017
Bachelor's degree in Applied Chemistry, Kaunas University of Technology, Kaunas, Lithuania

2017–2019
Master's degree in Applied Chemistry, Kaunas University of Technology, Kaunas, Lithuania

2019–2023
PhD in Chemical Engineering, Kaunas University of Technology, Kaunas, Lithuania

Work experience

2017–
Engineer at Kaunas University of Technology

2019
Junior researcher in the project *Synthesis of Calcium Silicates with Intercalated Metal Ions and Their Application in Production of Alternative Cementitious Materials*

2020–2023
Junior researcher in the project *Centre of Excellence in Chemical Engineering and Bioprocesses*

List of scientific publications

Articles published in journals indexed in the Clarivate Analytics Web of Science with Impact Factor

1. Gineika, Andrius; Baltakys, Kęstutis. The effect of hydrothermal treatment conditions and silica source on the formation of cuspidine // Journal of thermal analysis and calorimetry. Dordrecht: Springer. ISSN 1388-6150. eISSN 1588-2926. 2023, Vol. 148, iss. 10, p. 3965-3974. DOI: 10.1007/s10973-023-12022-6;
2. Gineika, Andrius; Baltakys, Kęstutis; Dambrauskas, Tadas; Siauciunas, Raimundas. Hydration properties and CO_2-curing of synthetic cuspidine samples // *Journal of Thermal Analysis and Calorimetry*. Dordrecht: Springer. ISSN 1388-6150. eISSN 1588-2926. 2023, Vol. 148, iss. 4, p. 1511–1521. DOI: 10.1007/s10973-022-11843-1;
3. Gineika, Andrius; Dambrauskas, Tadas; Baltakys, Kestutis. Synthesis and characterisation of wollastonite with aluminium and fluoride ions // *Ceramics International*. Oxford: Elsevier. ISSN 0272-8842. eISSN 1873-3956. 2021, Vol. 47, iss. 16, p. 22900–22910. DOI: 10.1016/j.ceramint.2021.05.003;
4. Gineika, Andrius; Siauciunas, Raimundas; Baltakys, Kestutis. Synthesis of wollastonite from AlF3-rich silica gel and its hardening in the CO_2 atmosphere // *Scientific Reports*. London: Springer Nature. ISSN 2045-2322. 2019, vol. 9, art. No. 18063, p. 1–10. DOI: 10.1038/s41598-019-54219-6.

Articles published in conference proceedings

1. Gineika, Andrius; Baltakys, Kęstutis; Navaruckienė, Auksė; Skliutas, Edvinas; Malinauskas, Mangirdas. Application of synthetic wollastonite for 3D-printed scaffolds // *Chemistry and Chemical Technology: Proceedings of International Scientific Conference*, Kaunas, 2022. Kaunas: Kaunas University of Technology. ISSN 2538-7359. 2022, p. 82;
2. Gineika, Andrius; Baltakys, Kęstutis. Influence of calcination temperature on morphology of synthetic cuspidine // *Advanced Materials and Technologies: Book of Abstracts of 24th International Conference-school*, 22–26 August 2022, Palanga, Lithuania. Kaunas: Kaunas University of Technology. ISSN 2669-1930. 2022, B-P76, p. 114;
3. Gineika, A.; Baltakys, K. Influence of temperature on formation of precursor for cuspidine // *ICTAC 2020: 17th International Congress on Thermal Analysis and Calorimetry*, 29 Aug. – 2 Sept. 2021 / edited by: A. Łącz, M. Środa. Kraków: Akapit, 2021, S3_P-07. ISBN 9788365955524. p. 78;

4. Baltakys, Kestutis; Dambrauskas, Tadas; Gineika, Andrius; Svedaite, Evelina; Rudelis, Valdas. The effect of mechanochemical treatment on the structure of silica gel waste // *6th Central and Eastern European Conference on Thermal Analysis and Calorimetry* (CEEC-TAC6) and *15th Mediterranean Conference on Calorimetry and Thermal Analysis* (Medicta2021), 20-24 July 2021, Split, Croatia: book of abstracts / A. Rotaru, M. Erceg (eds.). București : SITECH, 2021, PS3.010. ISBN 9786061178612. p. 206;
5. Baltakys, K.; Gineika, A.; Dambrauskas, T.; Eisinas, A. The influence of Al^{3+} and F^{-} ions on formation and thermal stability of calcium silicate hydrates // *3rd International Conference on the Chemistry of the Construction Materials*, ICCCM, March 15–17, 2021, online. Frankfurt am Main: Deutsche Bauchemie. 2021, p. 38;
6. Gineika, A.; Dambrauskas, T.; Baltakys, K. Two-step synthesis of wollastonite from aluminium fluoride rich silica-gel waste: poster presentation // *International Conference on Energy, Environment and Storage of Energy*, ICEESEN 2020, 19–21 November 2020, Kayseri, Turkey: conference proceedings / editor in chief S.O. Akansu, co-editor S. Unalan. Kayseri: Erciyes University, 2020. ISBN 9786254091476. p. 565-566.

Acknowledgments

I would like to thank my long-time supervisor professor **Kęstutis Baltakys** and appreciate his enthusiastic and encouraging supervision. My supervisor has provided me with invaluable guidance on the thesis, and has also consistently and persistently shown confidence in me.

A sincere *THANK YOU* goes to all the colleagues at the Departments of Silicate technology and Polymer Chemistry and Technology for their assistance and support.

Appendices

Appendix No. 1. Material Test Report

INHUS Prefab, UAB
Žarijų g. 6
02300 Vilnius, Lietuva

prefab@inhus.eu
T. +370 700 80000

GAMYBINIO
IŠBANDYMO AKTAS

2023/04/10

GAMYBINIO IŠBANDYMO AKTAS

Užpildų prototipų bandinių panaudojimas baltojo betono plokščių gamyboje

INHUS Prefab, UAB su Kauno technologijos universiteto Silikatų technologijos katedros darbuotojais (prof. K. Baltakys, dokt. A. Gineika, doc. T. Dambrauskas, doc. A. Eisinas, prof. R. Šiaučiūnas) 2022 m. gruodžio-2023 m. kovo mėnesiais atliko gamybinius bandymus, kurių tikslas – parengti kalcio silikatų ir/ar kalcio hidrosilikatų kietėjančių CO_2 aplinkoje užpildų prototipų bandinių gamybos technologines rekomendacijos ir juos panaudoti baltojo betono plokščių gamyboje.

Keičiant dviejų stadijų sintezės, susidedančios iš hidroterminės ir kietafazės sintezių sąlygas, kontroliuojant į junginių struktūrą įterpiamų priedų kiekį bei prigimtį, nustatyta, kad optimalios tikslinės paskirties užpildų prototipų bandinių gamybos sąlygos yra: pirmoji stadija – hidroterminė sintezė 200 °C temperatūroje 12 h suspensijos nemaišant, o antroji stadija – prekursorių degimas 900 °C temperatūroje 1 h. Pirmos stadijos metu iš CaO ir Si-Al-F:37-2,1-1,5 mišinio pagaminamas kalcio hidrosilikatų pagrindų prototipas XD, kurio techninės specifikacijos duomenys pateikti priede Nr.1. Antrosios stadijos metu pagaminamas kalcio silikatų prototipas WD, kurio techninės specifikacijos duomenys pateikti priede Nr.2.

Baltojo betono plokščių gamybinio bandymo metu standartiniuose mišiniuose mikroužpildą keičiant prototipais XD ir WD pagamintos plokštės: 1 – White A, 2 – White A+, 3 – su priedu XD, 4 – su priedu WD (1 pav.).

www.inhusprefab.eu

INHUS Prefab, UAB
Įmonės kodas
121559766
PVM kodas
LT100000009017

Atsiskaitomoji sąsk.
LT41 7300 0100 9432 6580
AB „Swedbank"
Banko kodas
73000
SWIFT kodas
HABALT22

INHUS Prefab, UAB
Žarijų g. 6
02300 Vilnius, Lietuva

prefab@inhus.eu
T. +370 700 80000

GAMYBINIO
IŠBANDYMO AKTAS

2023/04/10



1 pav. Gamybinio bandymo metu pagamintos plokštės: 1 – White A, 2 – White A+, 3 – su priedu XD, 4 – su priedu WD

Gamybinio bandymo metu tirta karbonizacijos parametrų įtaka iš kalcio silikatinės (priedo WD) rišamosios medžiagos pagamintų dirbinių kietėjimo proceso kinetikai. Tyrimo metu nustatyta, kad mažiausiai CO_2 buvo sugerta bandinius kietinant vandenyje – 0,87-0,95 %, be to nedaug didesnės vertės gautos bandinius kietinant ore – 0,92-0,97 %. Kietinant 0,8 bar CO_2 aplinkoje, sugerto anglies dioksido kiekis padidėjo iki ~1,6 %. Šiomis sąlygomis aiškių skirtumų tarp bandinių nenustatyta, nes verčių skirtumai paklaidos ribose. Po kietinimo 25 bar CO_2 aplinkoje, nustatyta, bandinyje su 10 % WD priedo susidarė ~3,8 % anglies dioksido, t. y. 38 % daugiau nei baltojo betono bandinyje be priedo ir plastifikatoriaus arba 18 % daugiau nei baltojo betono bandinyje be priedo, bet su plastifikatoriumi (2 pav.).

www.inhusprefab.eu

INHUS Prefab, UAB
Įmonės kodas
121559766
PVM kodas
LT100000009017

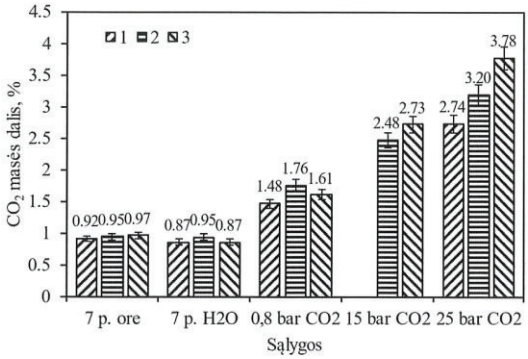
Atsiskaitomoji sąsk.
LT41 7300 0100 9432 6580
AB „Swedbank"
Banko kodas
73000
SWIFT kodas
HABALT22

INHUS Prefab, UAB
Žarijų g. 6
02300 Vilnius, Lietuva

prefab@inhus.eu
T. +370 700 80000

GAMYBINIO
IŠBANDYMO AKTAS

2023/04/10



2 pav. Skirtingomis kietinimo sąlygomis sugerto anglies dioksido masės dalis bandiniuose: 1 – baltasis cementas, smėlis ir vanduo, 2 – baltasis cementas, smėlis ir vanduo su plastifikatoriumi (1 %), 3 – baltasis cementas su 10 % WD priedu, smėlis ir vanduo su plastifikatoriumi (1 %)

Gamybinio bandymo metu nustatyta, kad atskiromis kietinimo sąlygomis didžiausią gniuždomąjį stiprį pasiekė baltojo betono bandiniai be WD priedo, bet su plastifikatoriumi (1 lentelė).

1 lentelė. Gamybinio bandymo metu pagamintų plokščių parametrai.

Bandinio Nr.	V/C santykis	Pasklida po 5 min, mm	Pasklida po 30 min, mm	Po 1 paros, MPa	Tankis, kg/m^3	Po 7 parų, MPa	Tankis, kg/m^3	Po 28 parų, MPa	Tankis, kg/m^3
su XD	0,41	410	-	29,78	2360	51,94	2415	63,60	2402
su WD	0,37	520	410	37,33	2412	56,94	2430	70,63	2425
White A	0,34	600	470	42,73	2461	68,79	2458	81,03	2475
White A+	0,34	520	400	36,33	2447	66,13	2446	75,70	2465

Didžiausia vertė pasiekta kietinant 25 bar CO2 slėgyje: baltojo betono bandiniai tik su plastifikatoriumi pasiekė 76,9 MPa gniuždomąjį stiprį, tuo tarpu baltojo betono bandiniai su 10 % WD priedo pasiekė ~25 %

www.inhusprefab.eu

INHUS Prefab, UAB
Įmonės kodas
121559766
PVM kodas
LT100000009017

Atsiskaitomoji sąsk.
LT41 7300 0100 9432 6580
AB „Swedbank"
Banko kodas
73000
SWIFT kodas
HABALT22

INHUS Prefab, UAB
Žarijų g. 6
02300 Vilnius, Lietuva

prefab@inhus.eu
T. +370 700 80000

GAMYBINIO 2023/04/10
IŠBANDYMO AKTAS

mažesnę, o baltojo betono be priedų – tik 2 % mažesnę vertę. Kitomis sąlygomis bandinių be priedų ir su WD priedu gniuždomojo stiprio vertės skiriasi nedaug. Mažiausios vertės pasiektos kietinant 0,8 bar CO_2 slėgyje: baltojo betono bandiniai tik su plastifikatoriumi pasiekė 54,5 MPa, bandiniai be priedų – ~3 % mažiau, o su 10 % WD priedo pasiekė ~15 % mažiau.

INHUS Prefab, UAB
Kokybės kontrolės skyriaus vadovas
Audrius Norkus, 2023 balandžio 10 d.

Kauno technologijos universitetas
Silikatų technologijos katedra
Prof. Kęstutis Baltakys, 2023 balandžio 10 d.

Concretus Group, UAB, UAB
Technologijų ir Inovacijų vadovas
Eugenijus Janavičius, 2023 balandžio 10 d.

dr. Eugenijus Janavičius
Technologijų ir inovacijų vadovas

www.inhusprefab.eu

INHUS Prefab, UAB
Įmonės kodas
121559766
PVM kodas
LT100000009017

Atsiskaitomoji sąsk.
LT41 7300 0100 9432 6580
AB „Swedbank"
Banko kodas
73000
SWIFT kodas
HABALT22

INHUS Prefab, UAB
Žarijų g. 6
02300 Vilnius, Lietuva

prefab@inhus.eu
T. +370 700 80000

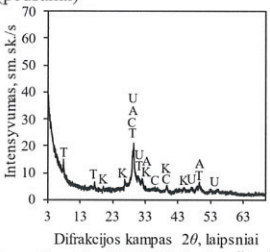
GAMYBINIO
IŠBANDYMO AKTAS

2023/04/10

Priedas Nr. 1 **2023 balandžio 10 d.**

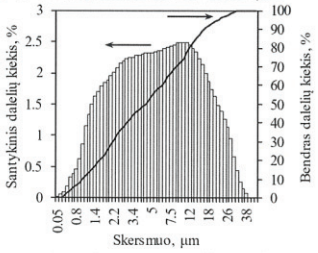
Prototipo XD techninė specifikacija

Cheminė sudėtis	SiO_2 42,29 % CaO 41,67 % Al_2O_3 2,51 % F^- 0,56 % Kaitmenys (1000 °C) ~ 12,97 %
Mineralinė sudėtis	Tobermoritas, kuspidinas, katoitas, C-S-H(I), kalcitas (pėdsakai)



1 pav. Prototipo XD RSDA kreivė. Čia: Čia: T – tobermoritas, K – katoitas, A – C-S-H(I), U – kuspidinas, C – kalcitas

Spalva	Balta (baltumas – 91,49; RGB koordinatės – 235-230-224)
Smulkumas	Vidutinis dalelių skersmuo 6,33 µm 90 % dalelių mažesnės nei 15,65 µm



2 pav. Prototipo XD granuliometrinė sudėtis

Tankis	2900-3000 kg/m^3
Savitasis paviršiaus plotas, m^2/kg	732

www.inhusprefab.eu

INHUS Prefab, UAB
Įmonės kodas
121559766
PVM kodas
LT100000009017

Atsiskaitomoji sąsk.
LT41 7300 0100 9432 6580
AB „Swedbank"
Banko kodas
73000
SWIFT kodas
HABALT22

INHUS Prefab, UAB
Žarijų g. 6
02300 Vilnius, Lietuva

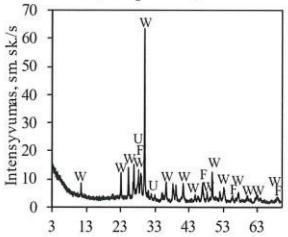
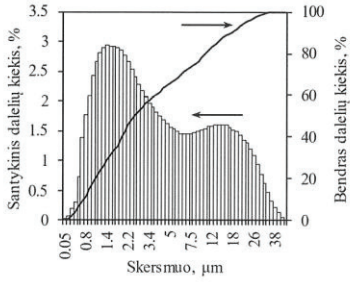
prefab@inhus.eu
T. +370 700 80000

GAMYBINIO
IŠBANDYMO AKTAS

2023/04/10

Priedas Nr. 2 **2023 balandžio 10 d.**

Prototipo WD techninė specifikacija techninė specifikacija

Cheminė sudėtis	SiO_2 48,59 % CaO 47,88 % Al_2O_3 2,88 % F^- 0,64 % Kaitmenys (1000 °C) ~ 0 %
Mineralinė sudėtis	Volastonitas, kuspidinas, fluoritas  **1 pav.** Prototipo WD RSDA kreivė.
Spalva	Balta (baltumas – 95,26; RGB koordinatės – 248-240-235)
Smulkumas	Vidutinis dalelių skersmuo 6,39 µm 90 % dalelių mažesnės nei 18,26 µm  **2 pav.** Prototipo WD granuliometrinė sudėtis
Tankis	2800-2900 kg/m^3
Savitasis paviršiaus plotas, m^2/kg	635

www.inhusprefab.eu

INHUS Prefab, UAB
Įmonės kodas
121559766
PVM kodas
LT100000009017

Atsiskaitomoji sąsk.
LT41 7300 0100 9432 6580
AB „Swedbank"
Banko kodas
73000
SWIFT kodas
HABALT22

UDK 549.642.41+661.842+666.965](043.3)

SL 344. 2023-07-12, 24,25 leidyb. apsk. l. Tiražas 14 egz. Užsakymas 113.
Išleido Kauno technologijos universitetas, K. Donelaičio g. 73, 44249 Kaunas
Spausdino leidyklos „Technologija“ spaustuvė, Studentų g. 54, 51424 Kaunas